Technische Universität München

Fakultät für Maschinenwesen

Lehrstuhl für Fahrzeugtechnik

Compensation of Drivetrain Oscillations in Electric Vehicles

Matthias Förth, M.Sc.

Vollständiger Abdruck der von der Fakultät für Maschinenwesen der
Technischen Universität München zur Erlangung des akademischen Grades eines

Doktor-Ingenieurs

genehmigten Dissertation.

Vorsitzender:	Priv.-Doz. Dr.-Ing. habil. Kian K. Sepahvand
Prüfer der Dissertation:	1. Prof. Dr.-Ing. Markus Lienkamp
	2. Prof. Dr.-Ing. Timo Oksanen

Die Dissertation wurde am 28. Mai 2020 bei der Technischen Universität München eingereicht und durch die Fakultät für Maschinenwesen am 03. September 2020 angenommen.

Acknowledgement

During the years from 2016 to 2019 I worked as a research assistant at the Institute of Automotive Technology of the Technical University of Munich. This work was carried out in these years in cooperation with the Advanced R&D and Engineering Company of the Toyota Motor Corporation.

Foremost, I want to thank my advisor Professor Markus Lienkamp for the support whenever I needed it and the freedom to explore different approaches and collaborate with other researchers. In this regard, I want to thank Professor Hakan Hjalmarsson and Riccardo Sven Risuleo for the four weeks I could spend at the KTH Royal Institute of Technology in Stockholm with the Division of Decision and Control Systems. The discussions on nonlinear system identification have been very valuable for me.

At the Institute of Automotive Technology I was able to use the prototype vehicle Visio.M which was designed and built by numerous students and faculty staff. Without their work my dissertation would not have been possible. In particular I want to thank Dr. Michael Baumann, Dr. Jörn Adermann, Dr. Johannes Betz, Thomas Zehelein and, most of all, Dr. Thorsten Helfrich for their assistance during my time at the institute. Further, I am extraordinarily grateful to the staff of the electrical and mechanical workshops of the Institute of Automotive Technology, most notably Florian Biechl.

The collaboration with the Toyota Motor Corporation was a superb experience for me and I want to thank all the people who made this possible. Each visit to Japan was a pleasure and source of great inspiration. I want to thank Mr. Hayashi in particular for his work for the project and the discussions on torque vectoring differential design. Last but not least, I want to express my deepest gratitude to Junya Ota who accompanied me on this journey. We made it through ups and downs and through it all you were not just a colleague but a friend to me.

I want to thank all my colleagues at the Institute of Automotive Technology for the great discussions and team spirit. I also owe much appreciation to Dr. rer. nat. Matthias Kronenwett who generously used his spare time for regular in depth discussions with me. Further, I want to thank my family for their unlimited support throughout my life. Finally, I want to thank my girlfriend Sophie for her motivation and being a role model in terms of dedication and endurance.

Munich, in April 2020

Matthias Förth

Contents

List of Abbreviations

ABS	Anti-lock Braking System
arctan	arcus tangens
BEV	Battery Electric Vehicle
CAN	Control Area Network
EKF	Extended Kalman Filter
ESP	Electronic Stability Program
EV	Electric Vehicle
FCEV	Fuel Cell Electric Vehicle
FFT	Fast Fourier Transformation
HEV	Hybrid Electric Vehicle
HIL	Hardware in the loop
ICE	Internal Combustion Engine
ICEV	Internal Combustion Engine Vehicle
IEA	International Energy Agency
LQR	Linear Quadratic Regulator
LTR	Loop Transfer Recovery
MIMO	multi-input multi-output
MPC	Model Predictive Control
ODE	Ordinary Differential Equation
OECD	Organization for Economic Cooperation and Development
PID	Proportional-Integral-Derivative
SISO	single-input single-output
tanh	tangens hyperbolicus
TMC	Toyota Motor Corporation
TRC	Traction Control
TUM	Technical University of Munich
TV	Torque Vectoring
TVD	Torque Vectoring Differential

Formula Symbols

Formula Symbols	Unit	Description
a_{veh}	$\mathrm{m}\,/\,\mathrm{s}^2$	Vehicle acceleration
A_{s}		Dynamics matrix of linear continuous state-space model
A_{z}		Dynamics matrix of linear discrete state-space model
α	rad	Backlash angle of shaft j
b_{veh}	m	Vehicle track width
B_{pac}		Pacejka Magic Formula coefficient
$\boldsymbol{b}_{\text{d,s}}$		Disturbance input vector of linear continuous state-space model
$\boldsymbol{b}_{\text{d,z}}$		Disturbance input vector of linear discrete state-space model
$B_{\text{u,s}}$		Input matrix of linear continuous state-space model
$B_{\text{u,z}}$		Input matrix of linear discrete state-space model
C		Output matrix of linear state-space models
c_1	N m / rad	Stiffness of actuator oscillation model
c_{12}	N m / rad	Stiffness of shaft in two-inertia model
$c_{12,\text{ flat}}$	N m / rad	Stiffness of shaft in flat two-inertia model
c_2	N m / rad	Stiffness of load oscillation model
c_{h}	N m / rad	Combined bushing stiffness of TVD mounting
C_{pac}		Pacejka Magic Formula coefficient
c_{sh}	N m / rad	Stiffness of shaft j
c_{sx}	N m	Tire slip stiffness
d		Disturbance of the state-space model
d_1	N m s / rad	Damping coefficient of actuator oscillation model
d_{12}	N m s / rad	Damping coefficient of shaft in two-inertia model
$d_{12,\text{ flat}}$	N m s / rad	Damping coefficient of shaft in flat two-inertia model
d_2	N m s / rad	Damping coefficient of load oscillation model
$d_{1,\text{opt}}$	N m s / rad	Aperiodic damping coefficient of actuator oscillation model

$d_{2,\mathrm{opt}}$	$\mathrm{N\,m\,s\,/\,rad}$	Aperiodic damping coefficient of load oscillation model
d_{α}	$\mathrm{N\,m\,s\,/\,rad}$	Damping coefficient inside the backlash gap
d_{h}	$\mathrm{N\,m\,s\,/\,rad}$	Combined bushing damping of TVD mounting
d_{sh}	$\mathrm{N\,m\,s\,/\,rad}$	Damping coefficient of shaft j
D_{pac}	N	Pacejka Magic Formula coefficient
$d(s)$		Disturbance acting on control system
$\Delta(s)$		Structured uncertainty
E_{pac}		Pacejka Magic Formula coefficient
$e(s)$		True tracking error
$\hat{e}(s)$		Estimated tracking error
F_{z}	N	Vertical tire load
f_{pac}	$\mathrm{N\,m}$	Pacejka Magic Formula
$\boldsymbol{f}(\boldsymbol{x}, u)$		Smooth nonlinear state space system in flatness definition
$\boldsymbol{g}_{\mathrm{x}}$		Smooth nonlinear state function in flatness definition
$\boldsymbol{g}_{\mathrm{u}}$		Smooth nonlinear input function in flatness definition
$G(s)$		System transfer function for the input
$G_{\mathrm{d}}(s)$		System transfer function for the disturbance
$G_{\Delta}(s)$		Perturbed system transfer function
$h(\boldsymbol{x})$		Nonlinear output function for virtual output
i_{trc}		Gear ratio of the traction motor
i_{tv}		Gear ratio of the TV motor
I_{TVD}		Gear ratio matrix of the TVD
i_{ξ}		Coefficient of unit-free twist speed curve ξ
j	l,r	Variable to distinguish between left and right side
J_1	$\mathrm{kg\,m^2}$	Inertia of actuator in two-inertia model
J_2	$\mathrm{kg\,m^2}$	Inertia of load in two-inertia model
$J_{2,0}$	$\mathrm{kg\,m^2}$	Load inertia at slip stiffness of zero
$J_{2,\infty}$	$\mathrm{kg\,m^2}$	Load inertia at infinite slip stiffness
J_{h}	$\mathrm{kg\,m^2}$	Pitch inertia of the TVD
J_{trc}	$\mathrm{kg\,m^2}$	Inertia of the traction motor
J_{tv}	$\mathrm{kg\,m^2}$	Inertia of the TV motor
J_{w}	$\mathrm{kg\,m^2}$	Inertia of one wheel
J_{yaw}	$\mathrm{kg\,m^2}$	Vehicle yaw inertia around the center of the rear axle

κ_1		Relative contribution of the actuator in the oscillation motion
κ_2		Relative contribution of the load in the oscillation motion
$k_{12,0}$	rad / s	Trajectory twist speed at $y_{\text{traj}} = 0$
$k_{12,\alpha}$	rad / s	Trajectory twist speed at $y_{\text{traj}} = \pm\alpha$
k_α	1 / rad	Tuning parameter of arctan backlash model
k_{D}	s	Derivative gain of shaft torque feedback
k'_{D}	s	Derivative gain of actuator speed feedback
k_{Fb}	N m s / rad	Gain of feedback damping in flat model
k_{P}		Proportional gain of shaft torque feedback
k'_{P}		Proportional gain of actuator speed feedback
k_{req}		Tuning parameter for smooth set-point approach in feedforward trajectory
k_σ		Slip coefficient in tire relaxation length model
k_{spd}	N m s / rad	Gain of twist speed feedback
k_{traj}	1 / rad	Gain of speed feedback in feedforward trajectory
k_ξ		Tuning parameter for ξ
$K(s)$		Controller transfer function
λ_i		Eigenvalue of eigenmode i
Λ		Diagonal matrix of eigenvalues
l_σ	m	Tire relaxation length
$l_{\sigma,0}$	m	Tire relaxation length at zero slip
$L(s)$		Open loop transfer function
L_i^k		Closed loop transfer function of optimization goal i and model k
L_j^k		Closed loop transfer function of optimization constraint j and model k
m_{veh}	kg	Vehicle mass
μ_{x}		Surface friction coefficient
$n(s)$		Measurement noise
ω_{b}	rad / s	Feedback controller bandwidth
ω_{Fb}	rad / s	Minimum operation frequency of feedback control
ω_1	rad / s	Oscillation frequency of the actuator oscillation model without damping
$\omega_{\text{nat},i}$	rad / s	Natural oscillation frequency of eigenmode i
φ_{12}	rad	Rotational twist angle of shaft in two-inertia model
$\varphi_{12,\text{req}}$	rad	Set point for trajectory of flatness based feedfordward control

$\varphi_{12,\text{Throttle}}$	rad	Rotational twist angle of shaft equivalent to throttle request
φ_{h}	rad	Rotational twist angle of TVD mounting
$\varphi_{j,\text{sh}}$	rad	Rotational twist angle of shaft j
$\varphi_{j,\text{out}}$	rad	Rotational angle of TVD output j
$\varphi_{j,\text{w}}$	rad	Rotational angle of wheel j
$\dot{\varphi}_1$	rad / s	Rotational speed of the actuator in two-inertia model
$\dot{\varphi}_{12}$	rad / s	Rotational twist speed of the shaft in two-inertia model
$\dot{\varphi}_2$	rad / s	Rotational speed of the load in two-inertia model
$\dot{\varphi}_{\text{anti,w}}$	rad / s	Anti-phase wheel twist speed (left and ride side turn in opposite direction)
$\dot{\varphi}_{\text{h}}$	rad / s	Rotational twist speed of TVD mounting
$\dot{\varphi}_{\text{in,w}}$	rad / s	In-phase wheel twist speed (left and ride side turn in same direction)
$\dot{\varphi}_{j,\text{sh}}$	rad / s	Rotational twist speed of shaft j
$\dot{\varphi}_{j,\text{out}}$	rad / s	Rotational speed of the TVD output j
$\dot{\varphi}_{j,\text{w}}$	rad / s	Rotational speed of wheel j
$\dot{\varphi}_{j,\text{veh}}$	rad / s	Rotational vehicle speed around the wheel axis at wheel j
$\dot{\varphi}_{\text{s,0}}$	rad / s	Rotational speed reference for slip calculation
$\dot{\varphi}_{\text{trc}}$	rad / s	Rotational speed of the traction motor
$\dot{\varphi}_{\text{tv}}$	rad / s	Rotational speed of the TV motor
$\dot{\varphi}_{\text{veh}}$	rad / s	Rotational vehicle speed around the wheel axis
$\dot{\varphi}_{\text{veh,0}}$	rad / s	Steady-state vehicle speed
$\dot{\varphi}_{\text{w,0}}$	rad / s	Steady-state wheel speed
$\dot{\varphi}_{\text{yaw}}$	rad / s	Yaw rate of the vehicle
$\ddot{\varphi}_1$	rad / s^2	Rotational acceleration of the actuator in two-inertia model
$\ddot{\varphi}_2$	rad / s^2	Rotational acceleration of the load in two-inertia model
$\ddot{\varphi}_{j,\text{out}}$	rad / s^2	Rotational acceleration of the TVD output j
$\ddot{\varphi}_{j,\text{w}}$	rad / s^2	Rotational acceleration of wheel j
$\ddot{\varphi}_{\text{yaw}}$	rad / s^2	Yaw acceleration of the vehicle
$\boldsymbol{p}$		Vector of control parameter for optimization
p	1 / rad	Tuning parameter of tanh backlash model
q		Tuning parameter of tanh backlash model
r_{w}	m	Dynamic tire radius
$r(s)$		Reference signal

r	N m	Reference torque for feedback control
$s_{\mathrm{s,0}}$		Steady-state wheel slip
s_{x}		Longitudinal wheel slip
$s_{j,\mathrm{x}}$		Longitudinal wheel slip at tire j
$\dot{s}_{\mathrm{x}}$		Derivative of longitudinal wheel slip
$\dot{s}_{j,\mathrm{x}}$		Derivative of longitudinal wheel slip at tire j
$S(s)$		Sensitivity function
$S_{\Delta}(s)$		Perturbed sensitivity function
T_1	N m	Actuator torque in two-inertia model
T_{12}	N m	Shaft torque in two-inertia model
$\hat{T}_{12}$	N m	Estimated shaft torque in two-inertia model
T_{Fb}	N m	Feedback torque
$T_{\mathrm{Fb},\dot{\varphi}_{12}}$	N m	Feedback torque of twist speed feedback
$T_{\mathrm{Fb},\hat{e}}$	N m	Feedback torque of shaft torque feedback with P-gain
$T_{\mathrm{Fb,PD}}$	N m	Feedback torque of shaft torque feedback with PD-gain
$T_{j,\mathrm{sh}}$	N m	Torque of shaft j
$T_{j,\mathrm{out}}$	N m	Torque of the TVD output j
$T_{j,\mathrm{tire}}$	N m	Torque of the tire j
T_{pac}	N m	Tire torque of Pacejka Magic Formula model
T_{req}	N m	Torque request in flat model
T_{Throttle}	N m	Driver's torque request via the throttle
T_{trc}	N m	Torque of the traction motor
T_{tv}	N m	Torque of the TV motor
$T(s)$		Complementary sensitivity function
$\Delta T_{j,\mathrm{tire}}$	N m	Disturbance torque at tire j
$\dot{T}_{\mathrm{trc}}$	N m / s	Torque derivative of the traction motor
$\dot{T}_{\mathrm{tv}}$	N m / s	Torque derivative of the TV motor
τ_{trc}	s	Torque time constant of the traction motor
τ_{tv}	s	Torque time constant of the TV motor
τ_{DT1}	s	Filter time constant of the torque estimator
τ_{D}	s	Filter time constant of the D-gain in shaft torque feedback
τ'_{D}	s	Filter time constant of the D-gain in actuator speed feedback
$\boldsymbol{u}$		Input of state-space model

u_{trc}	N m	Torque request of the traction motor
u_{tv}	N m	Torque request of the TV motor
$u(s)$		System input
$\boldsymbol{v}_i$		Eigenvector of the eigenmode i
V		Matrix of eigenvectors
W_i		Weight for optimization cost function i
W_j		Weight for optimization constraint j
$W_{\text{r,e}}(s)$		Weight for reference tracking
$W_{\text{d,e}}(s)$		Weight for disturbance rejection
$W_{r,T_{\text{Fb}}}(s)$		Weight to limit control torque in reference tracking
$W_{d,T_{\text{Fb}}}(s)$		Weight to limit control torque in disturbance rejection
ξ		Unit-free twist speed for feedforward trajectory
$\boldsymbol{x}$		State vector of state-space model
$\boldsymbol{y}$		Output of state-space model
$y(s)$		System output
$\dot{y}_{\text{ref}}$		Reference speed for feedforward trajectory
$\ddot{y}_{\text{ref}}$		Reference acceleration for feedforward trajectory
y_{traj}		Trajectory angle for feedforward control
$\dot{y}_{\text{traj}}$		Trajectory speed for feedforward control
$\ddot{y}_{\text{traj}}$		Trajectory acceleration for feedforward control
y_{v}		Virtual system output
ζ_1		Damping ratio of actuator oscillation model
$\zeta_{\text{nat},i}$		Damping ratio of eigenmode i

1 Introduction

Climate change and emissions caused by humans are a major challenge our society must urgently address. The magnitude of climate change is so overwhelming that only a combination of solutions has the power to solve the problem. Part of the solution could be electric mobility [1]. Today, individual mobility is a fundamental need people want satisfied. In wealthy countries the passenger vehicle density is between 400 and 800 vehicles per 1000 citizens [2, p. 36], [3, p. 1].

In OECD countries, transport is the largest final energy consumer and also the fastest growing energy sector. It increases consistently and across the world. Currently, one third of the total final energy is allocated to transport [4, p. 12]. Within the transport sector of International Energy Agency (IEA) countries, passenger vehicles take up 60 % [5, p. 5]. With countries like China and India on the rise to a wealthier society, the passenger vehicle density in these countries will increase as well [2, p. 36], [3, p. 1]. Therefore, any improvement in the passenger transport sector will have an increased leverage due to the rising vehicle stock worldwide. Today, passenger transport relies heavily on diesel and gasoline driven Internal Combustion Engine Vehicles (ICEVs) [5, p. 5]. The resulting pollutants emitted by the transport sector lead to the global problem of climate change and the local problem of air pollution impairing public health [6–8]. Therefore, reducing emissions and improving efficiency is one of the most urgent goals our society faces today [1], [3, p. V].

In order to reduce emissions, people should change their mobility behavior. For short distances, walking and cycling are energy efficient and healthy alternatives to passenger vehicles [9, p. 1087]. For longer distances, buses and trains can carry a high capacity of passengers and, thereby, use a smaller amount of energy per passenger kilometer than individual passenger cars [5, p. 5]. Kuhnimhof et al. [10, p. 447 f.] reported that Germany has seen a diversification of the transport modes used by young adults which reduced the share of individual passenger vehicles. Besides shifting the transportation mode to alternatives, it is essential to improve passenger cars in energy consumption and environmental aspects [11, p. 1932].

In recent years, innovations in ICEVs and new technologies, such as Hybrid Electric Vehicles (HEVs) and Electric Vehicles (EVs), have focused on this task. Especially the potential of energy recovery during braking is an important benefit of electrified drivetrains [12–14]. In contrast to HEVs, EVs produce no tailpipe emissions improving the air quality at the point of operation. This is an important factor solving air pollution on a local level [7], [15, p. 57]. With respect to the global problem of climate change, the complete energy path from well to wheel and the vehicles life cycle have to be analyzed. A well to wheel comparison of Fuel Cell Electric Vehicles (FCEVs), Battery Electric Vehicles (BEVs) and currently available ICEVs and HEVs was presented in [12]. A full life cycle analysis including production and end-of-life for BEVs and ICEVs was conducted in [7]. These studies demonstrate the possible benefits of EVs regarding climate change. However, the improvements depend on several factors, for e.g. electric energy mix, battery or fuel cell technology and the desired vehicle range. Therefore, continuous research is necessary in order to tackle remaining drawbacks. Nevertheless, EVs yield the potential to

conquer global and local emission problems.

1.1 Motivation

In order for EVs to have a significant impact on global and local emission problems, they have to be widely adopted. Yet, the following three barriers limit the adoption of electric mobility significantly [16, p. 184 f.]:

1. Purchase price and lifetime cost are key factors for customers looking to acquire a new vehicle and EVs must surpass ICEVs in this category.
2. Knowledge spillover discourages manufacturers to invest in research of EV technology, since they fear competitors will benefit from their innovations.
3. Innovative EVs need to satisfy the customers' high demands regarding comfort and performance, which are driven by well established ICEVs.

Barrier 1 is affected by multiple factors. Purchase price and lifetime cost are subject to government policies, manufacturing costs and fuel prices. Many countries employ subsidies for EV buyers and owners in order to increase adoption rates [15, p. 23 ff.]. Also, the rise of production volumes reduces manufacturing costs. Especially battery prices have been falling, which is the most expensive component in BEVs [15, p. 71 ff.], [16, p. 185]. Further, the lifetime benefit of an EV over an ICEV depends on fuel prices. They are difficult to predict, since political decisions and technological advances strongly effect fuel prices [17, p. 9 ff.]. For a high EV adoption rate high fossil fuel prices are desirable [15, p. 67]. Barrier 2 limits the choice possible EV buyers have. To create the necessary supply of EVs, manufacturer investments are increased by government policies. Legislature pressures the automobile industry to provide the necessary vehicle lineup [15, p. 23 ff.]. Recently, manufacturers have announced further electrification of vehicles and buses, which proves that electric mobility is gaining momentum and the implemented policies work [18, p. 4].

Barrier 3 results from the continuous improvement of ICEVs for decades. Therefore, customers expect certain performance characteristics from a vehicle. A key characteristic is the driving range [16, p. 185]. To meet customer expectations, the average battery size of BEVs increases to meet customer expectations [18, p. 129]. But customers also expect easy access to refueling and low refueling times. Therefore, charging infrastructure for BEVs and fuel stations for FCEVs are important factors for EV adoption [16, p. 185].

Further performance criteria are ride comfort and vehicle dynamics. Customers are becoming increasingly demanding in these categories [19, 20] and EVs need to be competitive in this field as well [21, p. 2]. The implementation of electric motors to the drivetrain yields new capabilities for improvement, possibly giving EVs an edge over ICEVs. EVs can apply the same amount of torque in positive direction as well as in negative direction, which is not possible in ICEVs. In addition, the electric motor's torque response is faster and smoother compared to an Internal Combustion Engine (ICE). This may lead to an increase in safety due to improved Anti-lock Braking System (ABS), Traction Control (TRC) and Electronic Stability Program (ESP) performance [13, 14, 22–24]. However, such improvements in vehicle dynamics control rely on an accurate wheel torque control by the electric motors.

Yet, in most vehicle drivetrains the motor's torque is transmitted through elastic steel shafts to the wheels. The shafts act as springs between the motor and the wheels, which tend to low

frequency oscillations below 20 Hz. In dynamic driving situations, the wheel torque is not equal to the motor's output torque. The torque oscillations disturb the vehicle dynamics controllers [22–25], harm the durability of components [26, 27] and impair the passengers comfort of the vehicle [28–31]. In order to achieve an accurate wheel torque control, a compensation of these oscillations is required.

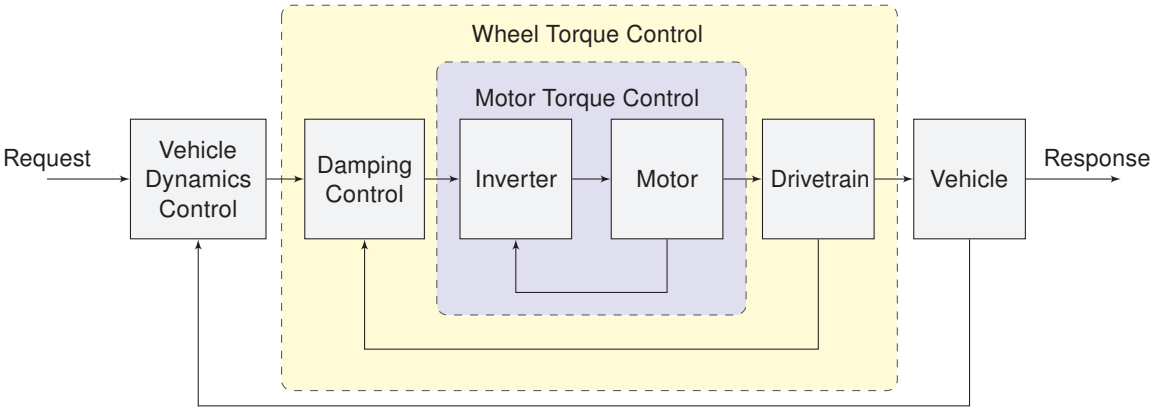

Figure 1.1: Basic control architecture of the vehicle dynamics controllers

Due to the advantages in motor torque control, the electric motor also yields a good foundation for the active damping of drivetrain oscillations. The active damping approach is illustrated in Fig. 1.1. The "Drivetrain" block contains the mechanical components, required to propel the vehicle. The "Vehicle Dynamics Control" block combines measurement feedback from the vehicle and the driver's request. It outputs a wheel torque request to the "Damping Control" block, which ensures the realization of the desired wheel torque by setting an appropriate motor torque request. At the heart of the diagram lies the motor torque control. Because of the nested structure, the outer control loop always relies on the performance of the inner loop [32, p. 462]. Any possible benefit of improved motor torque control is only available to the vehicle dynamics control, if the performance of the damping control is sufficient. In other words, a well designed drivetrain and damping control is the foundation for improved performance, comfort and safety of EVs.

1.2 Scope

Since active damping forms the basis for improvements in comfort and safety, this study focuses on the oscillations in EV drivetrains and possible control strategies to compensate them. However, the variable size and the simple connection by electric cables enables a variety of drivetrain topologies for EVs. Therefore, the following paragraphs summarize the benefits and drawbacks of the different topologies in order to narrow down the research area of this dissertation.

The most straight forward approach to building an EV is replacing the ICE with an electric motor. The advantageous torque characteristic of the electric motor renders components such as clutch, fly-wheel and shifting gearbox obsolete. However, since an electric drivetrain is less complex than its ICE counterpart, completely new topologies are possible. Recently, research has shifted to multiple motors in the vehicle, driving individual wheels. The addition of more motors enables further improvements in vehicle dynamics control by changing the torque split between the left and right vehicle side. The procedure is called Torque Vectoring (TV) [13, 14, 33].

With respect to wheel torque control and drivetrain oscillations, the best solution is placing the motor directly inside the wheel. Since there are no long shafts transmitting the torque, there are no low frequency oscillations. The wheel torque can be controlled directly with the motor. These are called in-wheel motors. However, in-wheel motors increase the unsprung mass, which may cause drawbacks in passenger comfort, and causes difficulties for vehicle suspension and package [13, 14, 34].

Each motor can also drive a single wheel through a shaft, placing the motor inside the chassis. This setup does not increase the unsprung masses but still enables individual wheel torque control. Since the motors are on-board they are called on-board motors [22]. The decision between on-board motors and in-wheel motors depends on the weighting of the drivetrain oscillations on one side (on-board motors) and the comfort and package drawbacks on the other side (in-wheel motors).

For in-wheel motor and on-board motor drivetrains, equally sized motors need to be placed on both sides of the vehicle and have to operate simultaneously most of the time. An active differential or Torque Vectoring Differential (TVD) can control the wheel torque individually but only uses a single traction motor most of the time. The torque of the traction motor is split evenly between the wheels. The individual wheel torque control is conducted with a second smaller TV motor. It is only used, when the torque distribution between the left and the right side has to be adapted. Since only the TV motor is responsible for the torque shift, traction is unaffected by the TV capabilities, which is an advantage compared to in-wheel motors and on-board motors [35–38]. There are also mechanical TVDs, which use clutches instead of an electric motor [39–41]. However, such mechanical TVDs can not match the efficiency of electric TVDs [42, 43].

Because of these benefits, this dissertation focuses on the active damping of oscillations in EVs with electric TVDs. They are referred to as TVDs, omitting the explicit reference to the electric actuation. When referring to the clutch-based actuation, it is explicitly stated. For such TVD drivetrains, only the low frequency oscillation modes up to 20 Hz are analyzed because these frequencies are critical for vehicle dynamics control and vehicle driveability [20, 22]. Since the performance of ABS, ESP and TRC are especially important on low friction surfaces, the analysis of low frequency oscillations has to include such surface conditions [25].

1.3 Introduction to torque vectoring drivetrains

As established in section 1.2, the TVD is superior to other topologies with respect to comfort and the sizing of the motors. However, its mechanical design is more complex than in-wheel motor or on-board motor topologies. Therefore, this section contains a brief introduction to the prototype vehicles and the integrated TVDs used in this study. The goal is to generate a basic understanding of the scale and the design of this drivetrain topology. First, the research vehicle of the Technical University of Munich (TUM) is described. Subsequently, a second prototype constructed by the Toyota Motor Corporation (TMC) is introduced.

At the TUM a small sized EV was developed in recent years. In the projects a new type of active differential was developed. The initial project was the MUTE, which was presented at the International Motor Show in 2011. Afterwards, the Visio.M followed. It appeared at the International Motor Show in 2014. Both vehicles are in the subcompact class L7e. The net weight in this class is below 450 kg. This excludes the traction battery and payload. The driving

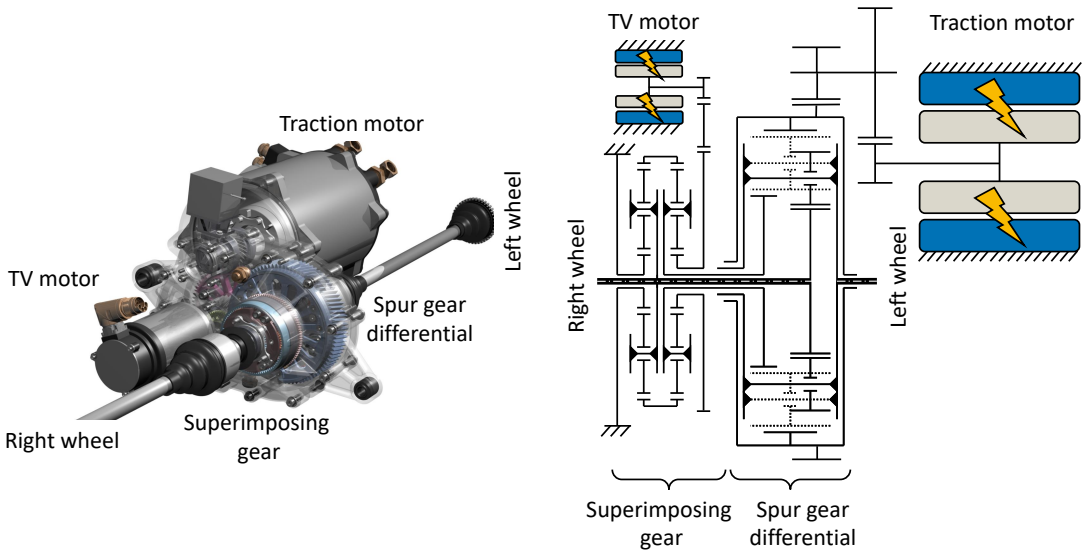

(a) Assembled TVD including wheel shafts (b) Drawing of the TVD's gear stages

Figure 1.2: TVD drivetrain of the Visio.M [36]

range of the two-seater vehicles is at least 100 km with a battery capacity of 10 kWh in the MUTE and 13.5 kWh in the Visio.M. The continuous traction power is limited to 15 kW. During both research projects, an innovative drivetrain topology with TV capability was developed [36, 38]. This study focuses on the Visio.M since it contains the latest version of the TVD. Its drivetrain is displayed in Fig. 1.2. The rendering in Fig. 1.2(a) shows the assembled system with labels for the most important components. The large squirrel-cage traction motor propels the vehicle and produces a peak torque of 80 Nm. The spur gear differential splits its torque evenly to both wheels. In contrast to clutch based TV systems, an electric TV motor shifts the torque split through a superimposing gear stage, which is added to the spur gear differential. In straight line driving, the TV motor is in standstill. Only when left and right wheel rotate at different speeds, the TV motor turns. The assembly illustrates the difference in size between traction and TV motor as well as the compact design of the superimposing gear stage compared to the spur gear differential. The diagram in Fig. 1.2(b) demonstrates the complex set of gear stages to accomplish the TVD's functionality. A pre-stage connects traction motor to the TVD. It has a gear ratio of 10.15, which allows a vehicle top speed of 120 kph at a motor speed of 12000 rpm. The pre-stage of the TV system has a gear ratio of 48. Therefore, a small-sized synchronous TV motor with a peak power of 6.5 Nm is sufficient to enable a torque shift of 312 Nm at the wheels. In cornering scenarios the TV motor turns with up to 1200 rpm [36].

The second vehicle is a research prototype developed at the TMC. It is based on a small sized four seater production car. In this study the vehicle is referred to as Prototype Two. Its TVD drives the rear axle, analogue to the Visio.M. Even though the TVD's design is completely different, it uses the same superimposing principle as the Visio.M. Nevertheless, the TVD is constructed to output more torque than the Visio.M. Prototype Two's traction motor creates a maximum torque of 250 Nm and its gear stage has a gear ratio of 10. The TV motor produces a maximum of 30 Nm in torque. The gear ratio of the TV unit is 60. The difference between both vehicles and their TVDs is a solid foundation to analyze this drivetrain topology.

1.4 Outline

After the introduction and motivation for active damping in TVD drivetrains, the related work is analyzed in chapter 2. Since the damping of low frequency oscillations has been an important task in ensuring good performance and safety, researchers have produced a large number of publications in this field. However, TVD drivetrains are rarely investigated. Therefore, the related work survey starts with an investigation of previously used models representing the main phenomena in section 2.1. Based on this fundamental understanding of the problem, the variety of proposed controllers is categorized according to the methods they apply in section 2.2. At the end in section 2.3, the active damping approach of this dissertation is chosen and research questions are formulated.

Following the choice of a control approach, chapter 3 presents the models required for the control design. The selection of components in section 3.1 is strongly connected to section 2.1. The validation of the model in section 3.2 is split into frequency and time domain. The frequency domain focuses on the changing behavior in different tire and surface conditions. The time domain validation aims at the evaluation of delays and nonlinear effects.

Since the active damping control must perform in regular operation but also in ABS, ESP and TRC scenarios, the changing behavior due to tire dynamics is of high importance. Therefore, chapter 4 presents a detailed analysis of the validated linear model with respect to changing tire conditions. The methodology as well as the results are separated into an investigation based on a two-inertia model (section 4.1.1 and 4.2.1) and modal analysis of the complete linear model (section 4.1.2 and 4.2.2). The main contribution of this chapter are guidelines presented at the end of section 4.3. These guidelines on the physical design of the drivetrain intend to ensure a beneficial behavior already without an active controller.

The active damping of low frequency oscillations in the drivetrain is split into two controllers, a linear feedback controller for damping and a nonlinear feedforward controller for the compensation of backlash. The feedback controller is discussed in chapter 5. Its main contribution is the combination of well understood classic controllers, summarized in section 2.2.2, and automated optimization based on the linear models. The model based optimization targets the robust performance of the active damping control in various driving conditions. In contrast, the feedforward backlash compensation in chapter 6 addresses a phenomenon, which only occurs in load changes. However, it is an important component for further improvement in the driver's perception of the vehicle. The main contributions of the backlash compensation are in modeling and trajectory generation for the backlash. Finally, chapter 7 contains a summary of the results and an outlook to future work.

2 Related Work

The focal point of this work is control design. This design process contains multiple steps. Doyle [44, p. 1] identifies eleven steps for control design in general, while Mackenroth [45, p. 12] separates the process of robust control design into nine steps. The different steps are part of two main tasks. The initial task is model building. Based on an initial investigation of the physical system, a mathematical model is created, evaluated and analyzed. These steps yield the foundation for the subsequent implementation of the controller. The objective of this task is to create a controller, which meets certain design goals. Various control schemes and tuning methods are available to achieve the objective. In case the defined goals are not met, the controller, the mathematical model or even the physical system may have to be adapted.

Following these general tasks of the control design process, this chapter is structured in two review sections and an overall conclusion section. First, section 2.1 focuses on mathematical models previously used in the field of drivetrain oscillations to form a fundamental understanding of the control problem. Afterwards, section 2.2 reviews the control schemes applied to active oscillation damping in drivetrains. Finally, research objectives are deducted in section 2.3 based on the reviewed literature.

Even though this dissertation focuses on EV drivetrains with TVDs other drivetrain topologies are considered as well, since the general phenomenon of wheel shaft oscillations is common to most vehicle drivetrains. The literature review excludes the in-wheel motor topology because it does not possess wheel shafts. Further, ICEVs experience oscillations caused by the combustion process in the engine. Additional electric actuators in the drivetrain can be used for active damping of such oscillations as well [46–49]. However, since these oscillations are of a different nature, they are also excluded from this survey.

2.1 Drivetrain Oscillation Modeling and Analysis

There are two approaches to modeling, namely experimental and theoretical modeling. In experimental modeling, also called system identification, a certain model structure is assumed, correlating to the process being modeled. The necessary model parameters are automatically identified based on input-output measurement signals. Such a model is called a black-box model because the internal dynamics are unknown. Since identification relies on measurements, the physical system has to exist prior to modeling and the model is only valid for this specific system in the examined operation range. The parameters of a black-box model do not possess a physical meaning. They are coefficients of a function. In contrast, white box models describe a system based on theoretical modeling, physical laws and their mathematical equations. Therefore, the model is applicable to various systems of the same class by changing its parameters. The parameters connect to physical components such as the stiffness of a steel shaft or the inertia of the motor's rotor. Such a model is called a white-box model, because the model is completely

known. However, theoretical modeling may be a complex engineering task and finding the correct model parameters for the physical system can be difficult. Grey-box models combine benefits of white- and black-box models by using automated model parameter estimation for models based on physical laws [50, p. 6 f].

Stewart et al. [51] apply the black-box approach to identify the parameters of second-order transfer functions resembling drivetrain oscillations in the different gears and at various vehicle speeds. Goetting et al. [26] fit a general model with two oscillation modes to measurement data of the drivetrain. The grey-box approach is used in [52, 53]. However, in most publications regarding vehicle drivetrain oscillations white-box models are presented. Since the model in this dissertation is used on multiple vehicles and should predict the behavior of future prototypes, a white-box model is used.

This section is organized as follows. First, in section 2.1.1 previous literature shows that different drivetrain topologies may be reduced to a general model. In section 2.1.2 the key phenomenon of low-frequency drivetrain oscillations is discussed by reviewing the fundamental models presented in literature. Several additions to the models are summarized afterwards. In section 2.1.3 the nonlinear backlash is addressed. Different modeling approaches to tire dynamics are summarized in section 2.1.4. The connection of the drivetrain to the chassis by the motor mounts and the wheel suspension is discussed in section 2.1.5. In section 2.1.6 actuator dynamics and communication delays are reviewed. For ICE drivetrains, the dual mass fly wheel and the clutch dynamics are often considered as in [54–56]. However, since electric drivetrains lack these components, they are not discussed in the following paragraphs. Further, ideal gearing without friction is assumed and gear stiffness is neglected as its contribution to low frequency oscillations is insignificant, demonstrated in [21, p. 51], [57, p. 76].

2.1.1 Creating Comparable Models for Different Topologies

In order to reduce the model's size and complexity, the vehicle drivetrain is often converted to a single unbranched strand. The example in Fig. 2.1(a) contains an actuator, a wheel and a vehicle inertia. The input torque on the left, represented by the double arrow, acts on the actuator inertia. A single gear stage and a wheel shaft connect actuator and wheel. One tire links the wheel to the vehicle inertia. Different publications may differ in the components included in the unbranched model. However, this section reviews the general conversion of the different topologies into such an unbranched model. It forms the basis for comparing publications with different drivetrains.

The block diagram in Fig. 2.1(b) shows a drivetrain with a single motor and a standard differential gear stage, splitting the torque evenly to both sides. There are two approaches to convert the standard drivetrain of Fig. 2.1(b) to the unbranched strand in Fig. 2.1(a). Barta et al. [58–60] cut the drivetrain on a horizontal line between the two shafts. The result are two unbranched strands with half of the actuator and differential gear stage on the left and half of the vehicle on the right. Therefore, the properties of shaft, wheel and tire remain unchanged. The properties of actuator, differential gear stage and vehicle have to be adjusted. In contrast, most publications combine the two shafts, wheels and tires by adding their properties. The actuator, gear stage and vehicle remain unchanged. This approach results in a single unbranched strand. It is applied to EVs in [21, 26, 52, 57, 61–65] and ICEVs in [54, 66–82].

The on-board motor topology is portrayed in Fig. 2.1(c). Only the vehicle block connects the two single IBMs. Therefore, cutting the vehicle inertia in half separates both on-board motor

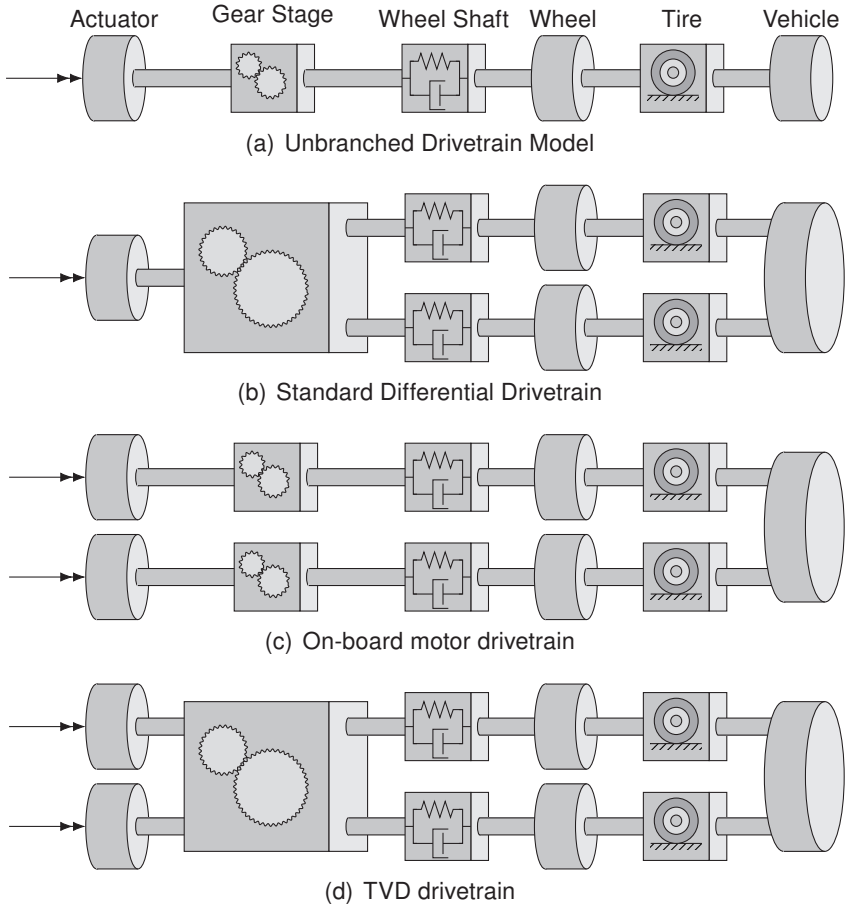

(a) Unbranched Drivetrain Model

(b) Standard Differential Drivetrain

(c) On-board motor drivetrain

(d) TVD drivetrain

Figure 2.1: Drivetrain block diagrams

strands, which creates two unbranched models. The example in Fig. 2.1(c) resembles a vehicle with two driven wheels. In case of a four wheel drive vehicle, the vehicle inertia needs to be scaled accordingly. The conversion is used in [83–87]. In contrast to on-board motors, the two motors of a TVD drivetrain are interconnected by the TVD, visualized by the gear stage with two inputs and two outputs in Fig. 2.1(d). To the author's knowledge, the interconnected structure of TVD drivetrains has not been converted to an unbranched structure, yet. However, the investigation of complex models has revealed that coupling due to the TVD is small [35, 88]. Small coupling allows a separation of the TVD drivetrain into two transfer functions, one for the traction motor and one for the TV motor response [35]. This is similar to creating two unbranched models for the dynamics of the traction and the TV system.

There are two benefits of the conversion to an unbranched strand. First, it reduces complexity. Second, since many publications reduce the specific drivetrain to a single strand, the presented results are easily transferred to other topologies.

2.1.2 Fundamental Oscillator

The unbranched drivetrain model in Fig. 2.1(a) contains three inertias. In order to reduce complexity and provide analytic solutions, several publications applied further simplifications. An initial simplification is the elimination of the gear stage by transferring the actuator inertia to the wheel level or vice versa, e.g. in [27, 52, 87]. The wheel shaft is commonly represented by a linear spring-damper element, e.g. in [27, 58, 67, 72]. Further, the load side, including wheel,

tire and vehicle, is often simplified by neglecting tire dynamics. The resulting models require fewer parameters and yield analytic solutions for the oscillation frequency and damping. They are portrayed in Fig. 2.2.

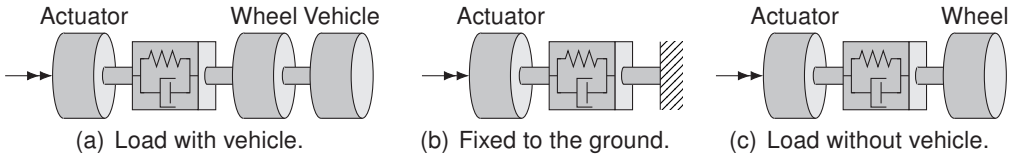

Figure 2.2: Fundamental oscillation models without tire dynamics

Investigations focusing on dry roads commonly lock the wheel to the vehicle, illustrated in Fig. 2.2(a). This fixed link between wheel and vehicle also creates a two-inertia system. The approach assumes that there is no tire slip and is used in [57, 62, 67–72, 74, 76, 77, 79, 80, 89–91]. These studies all focus on the drivetrain's behavior on high-friction surfaces with limited wheel slip. Rosenberger et al. [87] calculate analytic boundary values for the drivetrain's oscillation frequency in different operation points. For the case of a launch from standstill on dry roads, they assume that the wheel is locked to the ground by the tire because of the high friction-coefficient of dry roads. This creates a single-inertia oscillator, including the actuator inertia and the shaft. This case is depicted in Fig. 2.2(b). For the case of braking on low-friction surfaces, the wheel inertia is disconnected from the vehicle as the tire can not transmit any traction force. This creates a two-inertia oscillator with actuator and wheel inertia connected by the shaft, displayed in Fig. 2.2(c).

Neglecting tire dynamics is a strong simplification. Therefore, two methods have been presented to include a tire model in a two-inertia oscillator. The first method takes the model from Fig. 2.2(c) and applies a tire torque to the wheel inertia, similar to the actuator torque on the left. Yeap et al. [27, 92] use this approach in combination with a nonlinear tire model. They linearize the model and conduct a detailed analytic analysis considering different operation points. The linearization assumes a constant vehicle speed. Therefore, the vehicle inertia can be neglected. A similar but less detailed numeric analysis was presented in [83]. The second method extends the model displayed in Fig. 2.2(a) and is presented by Templin et al. [93–95]. They neglect the wheel inertia and replace it with a linear damper, modeling the tire. The connection between actuator and vehicle consists of a spring-damper element with an additional damper element in series. These studies focus on dry roads and heavy duty trucks, with a high vehicle mass. The wheel inertia may be insignificant to the drivetrain oscillations in such conditions.

One- and two-inertia models require only few parameters and yield the possibility of analytic analysis. These fundamental oscillators demonstrate that the shafts in the drivetrain are always key to the low-frequency oscillation phenomenon. In more complex models and changing conditions, the contribution of components may change. However, the importance of the wheel shafts persists. However, their foundation are strong assumptions, which are only valid in a certain operation point. Therefore, the fundamental two-inertia oscillator is extended in the following sections.

2.1.3 Backlash

Since drivetrains consist of several components transmitting the torque, backlash is always included due to production tolerances and assembly requirements. During load changes, the backlash gap must be traversed, displayed in Fig. 2.3 by a wishbone. Inside the backlash

gap, the actuator and the load are disconnected. Therefore, the backlash creates a nonlinear system with different dynamics in contact and during the traverse. The total backlash size is the combination of several smaller backlash gaps, which are combined for simplification [96, 97]. Transmission gears and cardan shaft joints mainly contribute to backlash [52, 61, 80]. Backlash is studied in many industrial applications especially when high precision in position control is necessary. The backlash can cause limit cycles in such applications [97, 98]. In vehicle drivetrains the main problem caused by backlash is the change in oscillation frequency and the increase in amplitude [80, 90].

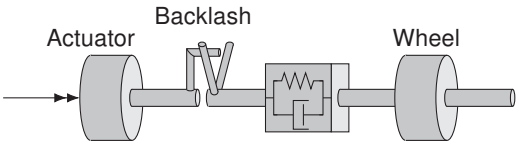

Figure 2.3: Block diagram including backlash between actuator and wheel inertia

There are two approaches to modeling the backlash, switching models and continuous nonlinear models. A switching model approximates the backlash with two models corresponding to the contact and the traverse. The switching is state-dependent and autonomous, which means that there is no direct control over the switching mechanism [99]. Nordin et al. [100] studied three switching models. The so called physical model was adopted by [64, 65, 74, 77, 82, 91, 93, 95, 101, 102] for vehicle drivetrains. However, since the damping of steel shafts is low [26], the simpler dead-zone model is also widely used for vehicle drivetrains, e.g. [19, 52, 61, 66, 76, 90, 91, 103, 104]. The previously cited literature shows that, for steel shafts, linear models approximate the contact and traverse operation regions well. Therefore, apart from the switching mechanism, the shaft model remains linear and eligible to a wide range of analysis methods [105].

In contrast to switching models, Merzouki et al. [106–108] represent the backlash with a single nonlinear continuous model to the backlash. The shaft torque is a smooth nonlinear function which resembles the backlash characteristic of the experimental test bench used. This approach does not rely on discrete switches but rather creates a smooth transition from contact to traverse and vice versa. Pham et al. [80] employ a similar approach to vehicle drivetrains. A tangens hyperbolicus (tanh) function approximates the backlash characteristic with two tuning parameters. They are not related to physical properties like the backlash gap size and have to be fitted. Further, the linear relation between shaft angle and torque does not hold in the tanh approximation.

In summary, the switching linear model is parametrized more easily and may be analyzed with well understood linear methods in its separate operation regions. Its drawback is the switching mechanism. The tanh model eliminates this drawback. However, it is not suitable for the well established linear control and analysis methods. In addition, it is more of an approximation than a model of the physical phenomenon. Therefore, the choice of the backlash model is postponed until the control approaches are discussed.

2.1.4 Tire Dynamics

Modeling tire dynamics is an important field for various applications in vehicle dynamics. Therefore, a variety of tire models exists with different complexity and accuracy [109]. Tuononen [110] conducted a detailed experimental study of rubber friction and the detaching process in stick-slip situations. It illustrates the complexity of the physical phenomenon. Regarding low frequency drivetrain oscillations, three approaches to tire modeling are favored in literature, which have

been summarized in [111] and depicted in Fig. 2.4. They are all approximations at best and do not represent the actual physical process.

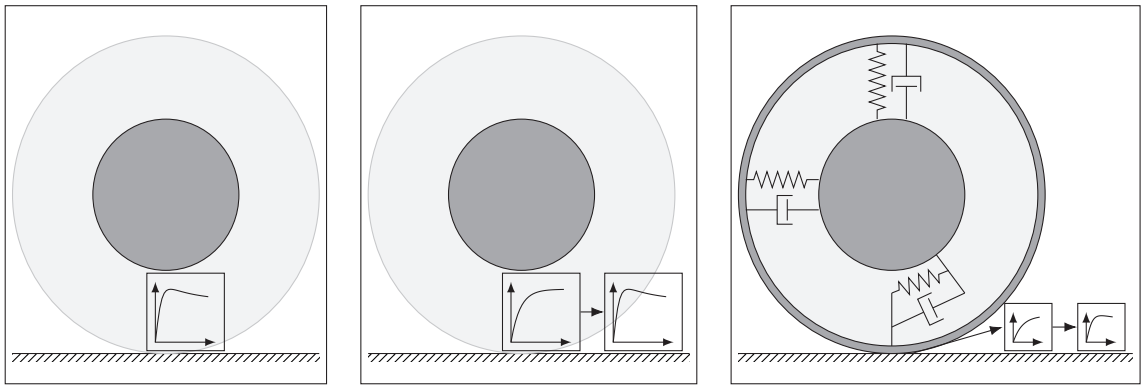

(a) Steady-state model (b) Relaxation-length model (c) Rigid-ring model

Figure 2.4: Different tire models for low frequency drivetrain oscillations

Steady-state Model Displayed on the left in Fig. 2.4(a), the most widespread and simplest tire model is the steady-state model. The most common steady-state model is the magic formula presented by Pacejka et al. [112]. The tire's steady-state characteristic is a nonlinear relation between the tire's slip, vertical and longitudinal load. In addition, the road friction coefficient μ effects the transmittable longitudinal force. The nonlinear curve at the bottom of Fig. 2.4(a) symbolizes this relation. At low tire slip, the relation is close to linear. However, with increasing slip the nonlinear characteristic dominates. At high slip levels, the longitudinal force decreases with increasing tire slip. This creates an unstable system [27]. However, since it is a steady-state model it does not replicate transient tire dynamics and is therefore hardly reliable for high and fast changing slip values [113] as well as oscillations above 10 Hz [111]. The investigations of drivetrain oscillations in [64–66, 114, 115] adopted the steady-state tire model. They all study oscillations on high μ surfaces with a frequency below 10 Hz. Yeap et al. [27] presented a detailed analysis of the tire's steady-state characteristics in combination with drivetrain oscillations. The tire's operation point changes oscillation frequency and damping of the drivetrain depending on vehicle speed, slip and surface condition. The shift in frequency ranges from 10 Hz to 15 Hz, the damping ratio varies by a factor close to five. These results emphasize the strong effect of the tire characteristic on the drivetrain's oscillations.

Relaxation-length Model Displayed in Fig. 2.4(b), the tire's transient dynamics are included through a first-order transfer function in front of the nonlinear steady-state characteristics. This approach is called the relaxation-length tire model. It represents the tire's carcass compliance. The relaxation-length parameter depends on tire slip, vertical and longitudinal tire force [116, p. 127 ff.]. Since it is also an approximation of physical effects, it is only valid up to 30 Hz [111]. Especially at low vehicle speed, the relaxation-length model demonstrates a resonance peak at low frequency, which enhances oscillations [117, 118]. The relaxation-length model is applied to low-frequency drivetrain oscillations on high μ surfaces in [55, 59]. The publications [58, 83–85] also consider low μ surfaces. However, these studies do not explicitly evaluate the relaxation-length model's contribution to the oscillations. Nevertheless, Castellazzi et al. [55] confirm the steady-state effect that damping increases with increasing vehicle speed also for the relaxation-length model.

Rigid-ring Model The tire's carcass is approximated by three spring-damper elements separating the tire's outer belt inertia and the inner rim inertia, illustrated in Fig. 2.4(c). This rigid-ring model contains the vertical, longitudinal and rotational motion between tire belt and rim. The connection between tire belt and ground is represented by a first-order transfer function and the steady-state model. The first-order transfer function approximates the contact dynamics between ground and tire belt, similar to the relaxation-length model. However, in this case, the first-order transfer function only models the tread dynamics, excluding the carcass [116, p. 154 ff.]. Regarding the investigation of drivetrain oscillations, Hao et al. [119] conclude, based on a simulation study, that the tires' torsional stiffness plays a key role for low-frequency oscillations. Tuononen et al. [120] conduct experiments with road and ABS excitation. They state that the longitudinal motion is located at a lower frequency than the rotational motion of the tire, closer to the drivetrain's oscillation frequency. Rosenberger [24, p. 69, p. 71] states that the torsional tire mode is located at a high frequency and does barely contribute to the important low-frequency oscillations. Nevertheless, Rosenberger et al. [24, 86, 87] consider the tire's torsional stiffness in their model. Regarding vertical tire dynamics, Killian et al. [56] concluded from high speed video footage that the vertical tire dynamics are insignificant to drivetrain oscillations.

In summary, previous literature demonstrates that, except for low speed and small tire slip on high friction, tire dynamics influence the drivetrains behavior significantly. The importance of the steady-state characteristic at varying slip, vehicle speed and surface condition is emphasized in different studies. However, tire dynamics are complex and not all tire modes are important to low-frequency oscillations. The reports on the contribution of each rigid-ring mode to low frequency drivetrain oscillations are inconclusive. Therefore, the relaxation-length tire model appears to be the best choice, regarding low-frequency drivetrain oscillations.

2.1.5 Suspension and Chassis Mounting

The torque produced and transmitted in the drivetrain acts on the chassis mainly in two points, the mounting of the motor and the suspension of the wheel. Both contain elastic components which may contribute to drivetrain oscillations.

The publications [21, 24, 55, 82, 87] consider mounting dynamics and report that the twist motion around the output shaft axis is the most critical. In these publications this motion is the pitch motion of the mounting. The pitch angle of the mounting adds to the twist angle of the shafts and thereby contributes to the drivetrain oscillations. Rosenberger [24, p. 72] demonstrates in measurements that the mounting oscillates with the low frequency of the drivetrain oscillations. The mounting's eigenfrequency of about 30 Hz is insignificant. In addition to the pitch motion, Goetting [21, p. 32 f., p. 55 ff.] considers the yaw motion of the mounting, because measurement results show an excitation of the yaw mode. However, after further analysis, only the pitch motion is used for control design. Castellazzi et al. [55, 121] incorporates pitch, longitudinal and vertical motion of the ICE in their simulation and validate the model's frequency response with measurement data. They show that all mounting modes are in an important frequency interval (3 Hz - 15 Hz), but only the pitch motion contributes to the first natural frequency of the drivetrain. Zemke [82, p. 92 ff.] identifies the necessary parameters for the pitch dynamics but states that the addition of the pitch motion did not improve the simulation model's accuracy significantly.

The publications [55, 56, 118–120, 122] consider suspension dynamics. In the vertical direction, the shock absorber and the spring define the vertical dynamics of the unsprung mass. The vertical dynamics effect the vertical force on the tire, which effects the load torque on the

drivetrain. In longitudinal direction, the suspension bushings, similar to the bushings of the motor mounting, transmit the traction force. Therefore, the combination of unsprung mass and suspension bushings act as an additional mass-spring-damper element in the block diagram. Tuononen et al. [120] locate the longitudinal and vertical suspension mode close to 10 Hz with measurement data, which is a critical area for drivetrain oscillations. However, an explicit evaluation of the contribution to drivetrain oscillation is missing since the study focuses on ABS braking. Castellazzi et al. [55] include longitudinal and vertical suspension dynamics in their study but the contribution to drivetrain oscillations is insignificant. In addition, these dynamics are outside the reliable frequency range of the measurements and could not be validated. Killian et al. [56] state, based on high speed video footage, that only the longitudinal motion of the suspension contributes to low-frequency drivetrain oscillations. This is confirmed by [119, 122] in simulation studies for high μ surfaces.

Previous studies demonstrate that the pitch motion of the mounting and the longitudinal motion of the suspension may contribute to low-frequency drivetrain oscillations. However, compared to the large number of studies investigating drivetrain oscillations, only few studies include mounting and suspension dynamics in the control scheme. Based on literature, the mounting appears to be more relevant than the suspension.

2.1.6 Actuator Response and Communication Delays

In addition to the mechanical properties of the drivetrain, communication and the actuator's control are important system properties as well. Large sampling intervals and other delays increase the controller's sensitivity to parameter errors [123, p. 461]. The actuator has its own control loop. Therefore, the combination of a damping controller and an actuator torque controller forms a cascaded control structure, portrayed in Fig. 1.1. In such a structure the dynamics of the inner loop are critical for the overall performance [32, p. 462].

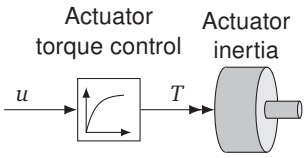

Figure 2.5: Block diagram including motor dynamics

In vehicle drivetrains, the input torque is not set directly. Instead, it is a request to the actuator's torque control. The actual applied torque is subject to the actuator's dynamics, represented by a first-order transfer function in Fig. 2.5. The first-order approximation is the most common in literature regarding EVs. However, the reported values of the time constant spreads according to Tab. 2.1. Bottiglione et al. [83] also include the first-order motor dynamics but only state that the time constant is small without mentioning a specific value. Similar, Lv et al. [64] label their time constant as small. Nevertheless, the time constant used by Lv et al. [65] is over 20 times larger than the one used by Rodriguez et al. [84], which is part of the same research group as Bottiglione et al. [83]. Instead of a first-order approximation, Amann et al. [52] model motor dynamics with a second-order transfer function but do not specify the parameters. Pham et al. [124] apply a zero-order hold to include the electric motor's dead time of 20 ms in a HEV. Regarding ICEVs, the engine dynamics are speed dependent since they are affected by the combustion process. At low engine speed the torque response is reduced. In [19, 91], a fourth order pade-approximation represents the engine's torque delay, which is in the range of 20 ms to 200 ms. The approximation assumes the worst case delay time of 200 ms.

Table 2.1: Time constant of first-order electric motor dynamics approximation

Source	Time constant
Li et al. [102]	10 ms
Lv et al. [65] citing [125]	50 ms
Rodriguez et al. [84]	2.2 ms
Rosenberger et al. [24, 87]	12 ms

In addition to the actuator's torque dynamics, communication delays effect sensor measurements and the torque request. Rosenberger et al. [86] investigate the sampling rate and measurement delays in a simulation study. They conclude that a sampling rate of 5 ms is common to passenger vehicles and sufficient for damping control. However, delays of 10 ms degrade the control performance and delays of 15 ms already destabilize the system. Pham et al. [124] include a sampling rate of 10 ms and a measurement and request delay of 20 ms each in their simulation study of a HEV. The study shows that considering the delays improves performance significantly.

Although surveys regarding vehicle dynamics control expect rapid torque response by the electric motor, e.g. [13, 14, 22], the time constant assumed in literature varies in a wide range. Depending on the specific system, an evaluation is necessary whether actuator dynamics need to be considered in the model. A general guideline on cascaded controllers states that the inner loop should be three times as fast as the outer loop [32]. This means the actuator's bandwidth needs to be three times as high as the oscillation frequency to guarantee a sufficient damping performance. The sampling frequency should be 20 times higher than the oscillation frequency to be controlled [123, p. 474 f.].

2.2 Control Methods

In general, the main design goals for a controller are performance, namely a small tracking error and high bandwidth, as well as robustness against parameter uncertainties and neglected dynamics. However, performance and robustness are often contradictory control objectives [44, p. 9], [45, p. 5]. With respect to active damping control in vehicle drivetrains these two goals translate into the following specifications. The active damping control has to minimize the deviation between the actual wheel torque and the requested wheel torque by the ABS, ESP and TRC controllers. The bandwidth of the torque transfer through the drivetrain has to outperform the torque modulation by the friction brakes in order to create an improvement for ABS, ESP and TRC. Therefore, the bandwidth should be close to or above 10 Hz [22]. The controller's robustness has to be sufficient to cope with the different phenomena discussed in the previous section 2.1. As literature demonstrates, the changing system dynamics due to nonlinear tire characteristics are the most important phenomenon in this regard.

Section 2.1.2 demonstrates that the fundamental phenomenon of low-frequency drivetrain oscillations is represented by a two-inertia oscillator. For this basic system, active damping is studied in various fields, such as industrial plants and laboratory test benches. The publications [126, 127] explicitly show that a two-inertia test bench can emulate vehicle drivetrain oscillations. Therefore, studies from other fields are included in the following literature survey. First, input filters are discussed in section 2.2.1, which reduce the excitation of oscillations by the input signal. Second, the application of classic control methods is reviewed in section 2.2.2. Third,

section 2.2.3 summarizes approaches relying on system models. Section 2.2.4 extends this by focusing on algorithms, which create an optimal control for a given model. Nonlinear control methods are summarized in section 2.2.5.

2.2.1 Pre-Filter

A pre-filter reduces the excitation of oscillations by the input signal. Since it does not include any feedback from the system, it is a pure feedforward method. The simplest filter is a rate limiter, which is the benchmark in [80, 128]. The reduction of oscillations corresponds to the reduction in torque rate. However, limiting the torque input directly limits the vehicles response to a torque request by the driver or the vehicle dynamics control. Therefore, this approach is limited. The notch filter eliminates only a specified frequency from a signal. It is applied to damping of industrial plants in [129–131]. Valenzuela et al. [130] demonstrate that the notch filter shows good performance even with a parameter variation of 20 % and can compete with a more complex model-based control scheme. Schmidt et al. [129] adapt the frequency of the notch filter with a online Fast Fourier Transformation (FFT) of the system's output signal. This ensures that the notch filter is tuned to the correct frequency. However, the method relies on a short trial run to identify the frequency which delays the adaptation. Park et al. [128] apply input shaping to vehicle drivetrain damping. It outperforms the rate limiter but requires knowledge of the system's oscillation frequency in its design. Rosenberger et al. [87] use a pre-filter to enhance the torque dynamics for an on-board motor drivetrain. Zemke [82, p. 125 f.] creates a pre-filter based on a drivetrain model with similar characteristics as the notch filter. Previously summarized literature from section 2.1.4 shows that the oscillation frequency of vehicle drivetrains changes in a wide range quickly due to tire dynamics. Stewart et al. [51] use a response surface, to tune the pre-filter according to the current vehicles operation point. However, measuring the response surface is time consuming. They only focus on high μ surfaces.

However, because of unknown disturbances and uncertainties in the system's dynamics, the feedforward control is insufficient for damping oscillations. It can only act as a supplement to a feedback controller [132].

2.2.2 Classic Linear Control

In order to react to the system's response, a feedback of measured outputs is necessary. At the heart of classic feedback theory is the Proportional-Integral-Derivative (PID) controller for single-input single-output (SISO) systems. Classic tuning procedures are the Nyquist criterion and the root-locus method. The PID controller is widely adopted because of its simplicity and often sufficient performance [45, p. 4]. The P gain mimics the intuitive action of increasing the control to counter an increasing error. The I gain forces the steady-state error of the control loop to zero in a sufficiently long time period. The D gain creates a faster control response since the derivative evaluates the trend of the error [133, p. 10]. In the field of drivetrain oscillation damping, the PD controller attracts a lot of attention. Because the system's input is the actuator torque and the system's output is a rotational speed or angle, an integrator already exists in the system. Therefore, a PD controller is sufficient to ensure a steady-state error of zero [133]. In the following paragraphs, the D controller is discussed prior to the P controller. For these classic feedback controllers, time delays pose a possible problem. Therefore, the Smith predictor aims at the compensation of delays [133]. It is discussed after the controllers.

D Controller The most basic classic approach is the feedback of the motor speed with a D controller. In order to create a numerically stable transfer function of the controller, the derivative is combined with a first-order low-pass filter (PT1). This combination is called a DT1 controller or high pass filter. In normal operation conditions the derivative of the motor speed, the acceleration, is minor compared to when oscillations occur. Therefore, D gain and filter time constant are tuned to reduce oscillations but allow a desired acceleration. This approach is used in [127, 134] producing good results. Hori et al. [135] enhance the DT1 approach by using the motor inertia and torque constant to create a disturbance torque observer for an industrial drive. The approach falls into the general category of a disturbance observer [136]. Berriri [19] uses the disturbance torque observer in combination with a Bandpass-Filter. Sugiura and Hori [137] extend the method with an additional DT1 block to feedback the torque derivative. A drawback of the DT1 controller is the necessary filtering, because it has to reduce signal noise but cause only a limited phase shift in the control signal at the same time [21, p. 98]. Nordin and Gutman [97] survey damping controllers in industrial systems when only the motor speed is available for feedback. They state that slow actuators, high resonance frequencies and a low load inertia are possibly dangerous to classic motor-speed controllers. As reported in section 2.1.4, the load inertia in vehicle drivetrains changes depending on the surface condition and tire slip. The phenomenon has to be considered when only the motor speed is fed back.

P Controller Since the wheel speed is available in production vehicles today, the speed difference between motor and wheel resembles the shaft's twist speed. Therefore, a P gain feeding back the speed difference adds damping to the drivetrain. The publications [84, 86] report good performance of the P controller in simulation. In order to compensate the speed-dependent tire dynamics, they adapt the P gain accordingly. This is called gain scheduling. Novellis et al. [138] prove the good damping performance in vehicle tests on high μ surfaces. Bruce et al. [68] apply a PD controller to the speed difference between motor and wheel, which shows good performance with a diesel truck on dry roads. Zech et al. [81] achieve a reduction in oscillation amplitude of close to 50 % in tip-in tests on low μ surfaces with an ICE drivetrain. However, the controllers are sensitive to delays and parameter uncertainties [68, 81]. Further, Goetting [21, p. 125] proves in measurements on a test bench that the selection of the P gain is a compromise between high damping and fast system response. Rosenberger [24, p. 81 ff.] shows that an additional high-pass filter improves the speed feedback with the P controller. The high-pass partly compensates slow actuator dynamics of the electric motor. The resulting controller is similar to the PD controller of Bruce et al. [68]. In [24, p. 77 ff.], a reference model calculates an ideal speed difference for the controller to track. This improves the system's step response. The controller is tuned for the ABS maneuver at 100 kph [24, p. 68]. It shows good performance in ABS braking tests on dry and wet roads, strongly reducing the oscillations of the on-board motor drivetrain [24, p. 103 ff.]. The foundation for this good performance is an interrupt based communication scheme. It ensures a minimum time delay. Further, the high sampling rate of 1000 Hz benefits the controller. In addition the sensor resolution is analyzed and because of the limited wheel speed signal quality the damping control is deactivated below 5 rad/s [24, p. 97 f.].

Smith Predictor Significant dead times reduce control performance. An approach to compensate delays is the Smith predictor. Essentially it is a model of the system without delays which predicts the output of the actual system ahead of time. With the Smith predictor, the controller can adapt the input signal before the system response is measured. However, this makes

the controller rely heavily on the underlying model. Therefore, high control gains should be avoided [133]. Baumann et al. [67] implement a Smith predictor to estimate the speed difference in advance. A PD controller, designed by root-locus, uses the prediction to create a damping torque. The Smith predictor's inputs are the requested torque and the drivetrain's state, which is provided by a Luenberger observer. It is explained in section 2.2.3. The study considers dry roads only and uses a two-inertia model. Measurement data proves the benefit of the Smith predictor in an ICEV during tip-in and tip-out maneuvers.

Summary The benefit of classic methods is their simplicity and often satisfying performance. The DT1 controller enables damping based on the motor speed only. However, the signal noise and unavoidable filtering must not affect the control. The PD feedback of the speed difference between motor and wheel adds damping but can also compensate slow actuator dynamics to a certain degree. Nevertheless, robustness is a concern for classic methods, especially in the presence of limited sampling rates and delays. The Smith predictor is an attempt to compensate delays. However, it is sensitive to modeling errors.

2.2.3 State Feedback through Pole Placement

In contrast to classic methods, pole placement enables the control engineer to specify the closed-loop dynamics freely to meet the design goals. The technique relies on a linear state space model of the system. The calculated gain matrix feeds back the complete state of the system. Thereby, the system's poles are shifted to the predefined location, chosen by the control engineer. In case not all system states are measurable, observers, also called estimators, provide an estimate of the system's state. Pole placement is applicable to both the controller and the observer separately. Observers designed by pole placement are called Luenberger observers [45, p. 139].

Goetting [21, p. 127 ff.] demonstrates that a simple two-inertia model is sufficient for the Luenberger observer since the control shows good performance and robustness. He employs the Luenberger observer to estimate wheel speed and shaft twist angle for an EV drivetrain. The necessary measurement signal is only the motor speed. The damping controller feeds the estimated speed difference back through a P gain. Because of model uncertainties and difficulties in determining the correct pole location, the root-locus method is used instead of pole placement, for the controller. The observer-based approach outperforms the previously discussed classic methods in test bench experiments, emulating high- and low μ surfaces. Even though the two-inertia observer assumes high μ conditions it performs well in low μ scenarios. Since the observer's error reduces the torque request on low μ, the wheel slip is automatically reduced, which creates a correct behavior by the control even though the actual state estimate is inaccurate. The additional feedback of the shaft's twist angle, which is proportional to the shaft torque, corresponds to a full state feedback and enhances the system's response. However, nonlinearities such as backlash, reduce the effectiveness of the shaft angle feedback. The control system is implemented with a sampling rate of 5 ms, which is a reasonable value for production vehicles according to the findings in section 2.1.6. Full state feedback with pole placement is used in [84, 89] with a Luenberger observer and a two-inertia model. Further, Rodriguez et al. [84] extend the control scheme with a wheel torque feedback. The wheel torque is estimated as a constant disturbance in the observer. This approach is different to the disturbance observer presented by [135] because it incorporates the disturbance estimation directly in the state space system. Therefore, it is labeled as an unknown input observer [136].

State feedback yields potential to improve performance. However, especially Goetting [21, p. 87] raises concerns about model uncertainties and robustness of the feedback design with pole placement. Also, the tuning procedure is iterative since the pole locations have to be adjusted to meet performance and robustness goals [21, p. 87]. In addition, the control effort is not recognized, which means that the controller may request excessive torque from the actuator to ensure the dynamics of the pole placement design [45, p. 5].

2.2.4 Optimal Linear Control

Optimal control focuses on the optimization of a cost function. Therefore, the tuning procedure is a mathematical optimization of the cost function. However, the cost has to be specified by the control engineer. There are two general approaches for this specification. In the time domain, the cost function evaluates performance in the state space over time. In the frequency domain, design goals are formulated based on transfer functions [139, p. 1 ff.], [45, p. 5 ff.].

Time Domain In the time domain, the cost function is a weighted integral or sum of the system's state and control variables. The cost function can include a limited receding horizon or an infinite horizon. There are two main representatives of time domain optimization. On the one hand, the Linear Quadratic Regulator (LQR) and the Kalman filter are the solutions to quadratic cost functions with an infinite horizon and no constraints. On the other hand, Model Predictive Control (MPC) uses a receding horizon and optimizes the control strategy online including constraints [140, p. 89 f.]. Both methods have been applied to drivetrain damping. First, the LQR and Kalman Filter approaches are reviewed. Second, publications studying MPC are summarized.

The LQR and the Kalman filter represent the counterparts to the previously discussed pole placement state feedback and Luenberger observer. Instead of choosing pole locations the design is governed by the weights of the cost function. In the controller design, the weights represent scaling factors of state and control variables. The controller's constant feedback matrix minimizes the cost function for an infinite time horizon. In the Kalman filter design, the weights represent the noise covariance of a gaussian process. There are two implementations of the Kalman filter. The steady-state implementation possesses constant gains [141, p. 193 f.]. The time-varying implementation adapts the gains according to the estimation's accuracy [45, p. 238], [141, p. 128]. The LQR control design ensures certain robustness properties when all system states are known. However, these properties are not guaranteed in combination with a state observer [142, p. 383]. Instead, there is a trade off between the recovery of robustness properties and measurement noise rejection. One possible tuning procedure for the Kalman filter is called Loop Transfer Recovery (LTR) [143]. Pettersson [78] uses LQR/LTR for drivetrain damping and investigates the influence of the sensor position. Due to the trade off between noise rejection and robustness in LTR the poor quality of the 20 Hz wheel-speed signal prohibits the complete robustness recovery. Higher signal quality enables improved results. The LQR/LTR approaches outperform a P controller even though only a simple two-inertia model is used. Similarly, Fredriksson et al. [72] demonstrate that the combination of LQR and LTR with a steady-state Kalman filter is superior to a PID motor-speed feedback and a pole placement controller. The comparison is based on simulation. Subsequently, measurement results prove the performance of the LQR/LTR controller. The advantage in robustness of the LQR/LTR method is emphasized. In both publications the LQR tracks a reference speed. Bruce et al. [69] present two calculation methods for the reference signal and test them in simulation. Templin

and Egardt [94] propose a LQR/LTR controller limiting the shaft jerk, which does not require a reference signal. The underlying model is a two-inertia model with a linear damper for the tire in series to the shaft, presented in [93]. Measurements prove the effectiveness of this approach in [95]. All these studies focus on dry roads and heavy duty trucks with ICEs. Rosenberger et al. [85] use a mix of optimal and classic methods. A Kalman filter estimates the shaft torque based on a three-inertia model with linear tire. To compensate the nonlinear tire characteristic, the tire's damping coefficient in the linear Kalman filter model is updated according to the vehicle speed. However, the steady-state gain of the Kalman-filter is not adapted. The estimated shaft torque is compared to the desired value and fed back by a PD controller. The feedback is designed by the root-locus method. In [87], the torque controller is extended with speed feedback, pre-filter and a four-inertia Kalman filter including actuator dynamics. The simulations show good damping performance on changing road conditions with an EV. However, the parameter adaptation creates an undesired coupling between the drivetrain oscillations and the Kalman filter's dynamics. For this reason, the method is discarded for experimental tests in [24, p. 68]. Caruntu et al. [70, 71] use MPC to include time varying Control Area Network (CAN) bus delays in the damping controller. The underlying model is a linear two-inertia system without a tire model. However, the large number of possible delay combinations causes a large number of constraints. The optimization problem is formulated as a linear program. Simulations and Hardware in the loop (HIL) tests show good results.

Linear optimal control demonstrates promising experimental results but they are limited to high μ surfaces and low speed. Different investigations include low μ surfaces. They use an update of the linear model according to the tire's operation point. However, the method is confined to simulation and explicitly not included in experimental tests. This indicates that the LQR and Kalman filter are designed for a specific linear model, which cannot represent the drivetrain's behavior in all necessary operation points.

Frequency Domain In contrast to the LQR and Kalman filter, the H_∞ control design is based on weights in the frequency domain. These weights define closed-loop performance and robustness criteria. Using the H_∞ norm as the cost function results in a worst-case controller, since the H_∞ norm evaluates the supremum of the weighted closed-loop transfer function [139, p. 83], [45, p. 180]. Similarly, μ-analysis evaluates the robustness of a controller with respect to uncertainties. An extension to the analysis procedure are design methods based on the singular value μ. If model uncertainties are defined, optimization algorithms tune the controller to satisfy the design goals for the given uncertainties. Controllers based on H_∞ and μ design are usually of high order, since weights and uncertainties are added to the system model for the control design. The controller's order is that of this so called extended system [45, p. 6 ff.].

Lefebvre et al. [91] implement an H_∞ controller for an ICEV in simulation. In addition, the paper yields a detailed guideline for tuning the controller weights. The controller is composed of a feedback and a feedforward part. It is of 11th order and based on a two-inertia drivetrain model without tire dynamics. The simulations demonstrate good damping performance in tip-in maneuvers on dry roads. A μ-analysis illustrates the parameter bounds for which the controller ensures stability and performance requirements. Berriri et al. [19] use μ-analysis to investigate the robustness of their classic control approach. The controller is similar to the DT1 disturbance torque observer by Hori et al. [135]. A band-pass filter replaces the previously used low-pass. In addition, a Smith predictor compensates the delay caused by the ICE. The nonlinear backlash is one of the main causes for uncertainties in this study and measurements show good damping performance for the robust linear controller. Zemke [82] demonstrates in an ICEV that a robust

H_∞ control is superior to the Smith predictor for delay compensation. Especially, the sensitivity to modeling errors harms the Smith predictor. Not even online parameter estimation techniques based on the Kalman filter compensate this drawback. Koenig et al. [90] design an H_∞ controller as well as controllers based on μ-optimization. The H_∞ controller is evaluated in simulations and experiments with an EV. It shows good damping performance. The experimental results match the simulation results closely. Three design methods based on μ-optimization are studied. The resulting controllers are more complex but directly account for the uncertainties in the model. All controllers rely on a two-inertia drivetrain without tire model. The test case is a launch from standstill on dry roads.

2.2.5 Nonlinear Control

The previously discussed design of linear controllers addresses nonlinearities in the system by requiring a certain robustness or considering them as a disturbance. However, the literature survey in section 2.1 shows that the two main nonlinearities in vehicle drivetrains are tire dynamics and backlash. Robustness and performance are often antagonists [44, p. 9], [45, p. 5], [139, p. 52 f.]. Therefore, including the nonlinearities in the control may reduce the robustness requirements thus improving performance. Since backlash and tire dynamics are different in nature, they are incorporated differently. This section is separated accordingly. First, backlash compensation is summarized. Second, controllers including tire dynamics are reviewed.

Backlash

Analogue to backlash modeling in section 2.1.3, there are two main approaches to backlash compensation, namely switching controllers and differential flatness. Since the backlash creates a switching linear system, a natural approach to control the system is a linear switching controller [99, p. 75]. Lagerberg [144] identifies switching controllers to be the most promising for backlash compensation in a literature survey. The simulation study in [74] shows that a switching control strategy outperforms a standard PID controller and a PID controller with disturbance observer, similar to [135]. However, such switching controllers rely on an accurate estimation of the backlash state because this variable determines the switching mechanism. A false estimate creates a false change in control dynamics.

In order to observe the state of nonlinear systems, variations of the Kalman filter exist. The nonlinear system can be linearized prior to the Kalman filter design, if the nominal trajectory during operation is known ahead of time [141, p. 397 ff.]. Amann et al. [52] take this approach to incorporate the backlash with a dead-zone model into the state observer. The nonlinear tire dynamics are not considered. Instead, an unknown input observer with a constant disturbance dynamic accounts for the tire torque. The Kalman filter gains are constant. However, two sets of steady-state gains are required since the wheel speed signal is not available at low speed. One set of gains uses motor and wheel speed measurements. The other set uses only the motor speed. In order to compensate the drivetrain's oscillations, a third order linear controller feeds back the estimated shaft torque. The control parameters are designed with the root-locus method. Measurement results prove the control performance in tests on dry roads. However, potential for improvement remains during the backlash traverse. Haschka and Krebs [96] create a linear steady-state Kalman filter with an external backlash compensation based on a lookup table. The system loses its observability in the backlash, when no torque is transmitted. However, the authors argue that in a real system there is no perfect disengagement between load and

motor. A minor modification of the backlash model reestablishes observability for the system. In addition, the stability of the linear steady-state Kalman filter is proven with the Popov-criterion. A simulation study proves good results for the observer. Similar detailed stability analysis are conducted in [145] for position control, which is less relevant for automotive drivetrains.

The most widely used nonlinear state estimation technique is the Extended Kalman Filter (EKF). The nonlinear system is linearized at the current state estimate. This linearized system is then used in a new state estimation by the Kalman filter. The essential difference to the previously discussed method is the repeated linearization during operation [141, p. 400 ff.]. Lagerberg and Egardt [77, 101] use an EKF for the state estimation considering backlash. However, in a linear switching system, the linearization of the EKF corresponds to the switching mechanism depending on the estimated backlash state. Therefore, the EKF is simplified to a switching steady-state Kalman filter in [77]. An additional switching Kalman filter estimates the backlash size with the unknown constant input approach. Measurement results prove the observers' performance in open loop. In addition, direct position measurement at the motor and wheel improves the estimation compared to the regular speed sensors [77]. Lv et al. [64] also use an EKF for drivetrain damping with backlash to enable good regenerative braking and hydraulic braking blending in a simulation study. However the study focuses on energy efficiency and the damping control analysis is less detailed. Similar to Lagerberg and Egardt [77, 101], the EKF from [64] is replaced by a switching Luenberger observer in [65]. The concept is taken from Balluchi et al. [146] who propose a hybrid discrete-continuous observer for gear shift detection. The discrete part observes the switching mechanism and the continuous part observes the system's state. In [65] the damping performance is proven in a simulation study. Ferrari and Gati [103] implement a switching observer, which relies on a simulation of the drivetrain in the backlash traverse. The approach was proposed in combination with an observability study. When only motor and wheel speed sensors are available, observability is lost during the backlash traverse, also stated by [96]. Therefore, an observer is ineffective and an open-loop simulation predicts the drivetrain's state. A similar approach is taken by [147] in which the load side of the system has no sensor and loses observability in the backlash. Templin and Egardt [93, 95] implement the approach for a heavy duty diesel truck. In contact, a LQR/LTR controller compensates oscillations. Inside the backlash gap, a constant torque limits the transition jerk. The experimental study in [95] demonstrates a good damping performance.

Caruntu et al. [148] extend the CAN delay compensation from [70, 71] to account for drivetrain backlash. Similar to the switched observers and controllers, the MPC relies on a piecewise affine model. The approach is evaluated on a test bench. In [149, 150] Caruntu et al. address clutch characteristics, which are similar to the backlash. In [76] the piecewise affine MPC is solved offline and the optimal control laws are stored in lookup tables. Therefore, the time consuming online optimization is avoided. However, the lookup tables are large, since they have to account for most driving situations. A LQR serves as a backup in case an operation point is not included in the tables. A simulation study proves the strategy's effectiveness for load changes in vehicles. A more detailed description of the offline calculation of the optimal trajectory through the backlash is presented in [75]. Best [54] compares a general nonlinear MPC to a LQR in a simulation study of an ICE drivetrain with backlash. The results are mixed and it is concluded that a MPC is unlikely to outperform a LQR in any practical implementation.

Pham et al. [80] employ the concept of differential flatness to create a feedforward controller compensating the drivetrains backlash. Fliess et al. [151, 152] presented the concept of differential flatness, or short, flatness, which is a system property. In contrast to switching feedback controllers, it requires a smooth mathematical representation. The goal of flatness-

based control is to find an output such that the system's states and inputs are fully described by the output and a finite number of its derivatives. With such an output available, a control law can be derived that computes the necessary input to track a desired output [153, p. 48]. In case of vehicle drivetrains, the flat output is the shaft's twist angle, which is directly linked to the drivetrain's torque. Pham et al. [79] demonstrated this for linear models and for a model with backlash in [80]. Based on these results, the feedforward flatness-based control tracks a predefined trajectory to ensure a smooth transition from one torque demand to the next. An additional feedback controller compensates disturbances and model errors. The feedback is independent of the flatness-based feedforward path. It consists of a LQR with an integral part in [79] and a P controller in [80]. Both studies evaluate the control strategy in simulation. The results in [80] demonstrate the potential of differential flatness in backlash compensation.

Tire Dynamics

Previously reviewed approaches tackle changes in tire dynamics by robustness or unknown input disturbance estimation. The later assumes a constant disturbance. However, the tire's torque depends on the system's state and is not constant, as discussed in section 2.1.4. Such modeling errors may reduce the estimation accuracy [141, p. 140 f.]. Therefore, Bottiglione et al. [83] apply an EKF to drivetrain state estimation including nonlinear tire dynamics represented by the Pacejka Magic Formula. As mentioned in section 2.1.4, the tire's longitudinal force depends on tire slip, vertical load and the road friction coefficient. Therefore, in order to include the nonlinear tire characteristic, friction coefficient and vertical load have to be estimated. Simulations with parameter variations show that the EKF is robust against incorrect friction estimation and changes in the tire's parameters. Therefore simple estimation methods are sufficient. The friction coefficient is estimated according to [154] similar to the DT1 disturbance torque observer. The vertical tire load estimation neglects suspension dynamics and approximates the vehicle as a rigid body. The PID controller, feeding back the shaft torque estimate, is designed to satisfy robust phase and gain margins at a speed of 50 kph. A tip-in maneuver at 50 kph on a slippery surface demonstrates the control performance of the system.

Similar to the model in the EKF, Batra et al. [58, 60] implement a MPC based on a three-inertia model with nonlinear transient dynamics, which is linearized in its current operation point. The MPC optimizes a quadratic program with input constraints. The control objective is a cost function combining energy efficiency, damping and tracking of a desired tire slip. Simulations and HIL tests demonstrate the performance. However, since oscillation damping is only one of three control objectives, the results are not as good as in other publications. In [59] the repeated linearization of the tire is replaced by the regular Pacejka Magic Formula, which converts the quadratic program to a general nonlinear optimization problem for the MPC.

2.3 Summary

In summary, the approach by Pham et al. [80] to separate damping control by feedback and backlash compensation by feedforward appears to be the most reasonable. With a sufficient damping controller, the backlash traverse occurs only in load changes induced by the driver. Therefore, a feedforward control is legitimate. When relying solely on feedforward, the issue of observing the backlash position is avoided. Many studies have demonstrated the difficulty of this task and the sensitivity of feedback controllers to estimation errors regarding backlash

position. Therefore, avoiding this issue is the biggest benefit of the feedforward approach.

With the backlash addressed, the main task of the feedback controller is to guarantee sufficient damping in all driving conditions. This goal focuses on the nonlinear tire dynamics. These dynamics rapidly cause severe changes to the drivetrain's dynamics. Tire dynamics are mainly handled by demanding sufficient robustness for the control loop. However, the biggest uncertainty is known. It is the damping coefficient of the linearized tire model. The gain scheduling approach of Rosenberger et al. [85, 87] used this knowledge. Yet, Rosenberger [24, p. 68] stated clearly that the changes in the tire's damping coefficient create problems because oscillations feed into the observers dynamics. Instead of an online scheduling of the control, this knowledge should be incorporated into the offline control design. The optimization techniques based on H_∞ and the singular value μ integrate design goals and uncertainties. The method has been used by Koenig et al. [90] but they do not consider the full operation range of the tire. Nevertheless, this framework appears to be the most promising to ensure the performance goals of the controller for the full operation region. The main drawback of the method is the complex nature of the resulting optimal controllers. However, abandoning optimality for simpler sufficient control structures could pose a solution to this drawback [155, 156]. This approach requires a linear model and the knowledge of the parameter uncertainty. Therefore, a linear parameter-varying model needs to be constructed for the TVD drivetrain. The varying parameters must represent the nonlinear tire dynamics sufficiently. The model's accuracy has to be proven with measurement results. In the search for a simple control structure, the transformation of the TVD drivetrain into simplified models is an open topic. Addressing this should make the TVD drivetrain comparable to other topologies as described in section 2.1.1. These simplified parameter-varying linear models pose the foundation for the optimization of classic well-understood control approaches. The novelty in this area is the connection of classic approaches with an optimization for various operation conditions.

Based on this summary, this thesis seeks to answer the following research questions:

1. Which dynamics of TVD drivetrains are common to vehicle drivetrains in general and which are unique to TVDs?
2. Can simple controllers satisfy performance and robustness goals in a variety of tire operation points?
3. How effective is a flatness-based backlash compensation compared to other feedforward approaches in vehicle experiments?

3 Modeling

The two main aspects of low-frequency drivetrain damping are backlash compensation and robustness against tire dynamics. Therefore, the overall objective of this chapter is the construction of mathematical models, which resemble the behavior of the physical system in this regard and fit the control design approaches. The goal is to avoid any unnecessary complexity [157, p. 4]. The focus is on the drivetrain itself and not on a full vehicle model. However, the models derived in this chapter may be included in a detailed full vehicle model as a subsystem if required. The choice, which components are necessary to simulate the drivetrain's behavior, is based on the literature review of section 2.1. In literature, the main focus of modeling is on straight line driving. In order to build on previous publications, this study neglects severe cornering and lateral dynamics. This allows certain simplifications during the modeling process and in the experimental design. Nevertheless, the results demonstrate that the models match the key dynamics of cornering with the TVD.

The foundation of this chapter are the student theses by Yang [158], Hoecher [159], Grilli [160] and Pech [161]. It is organized as follows. First, the equations of the models are discussed in section 3.1. Subsequently, the model is evaluated in section 3.2 with measurement data of various vehicle operation points for the two vehicles. The discussion in section 3.3 focuses on the validity of the model and its underlying assumptions.

3.1 Methodology

The contribution of the different components to the low-frequency oscillations is summarized in section 2.1 based on previous publications. The identified key components are displayed in Fig. 3.1. The block diagram shows all components included in the models. Inertias carry their label above. Blocks symbolize connecting elements without mass. The labels of blocks are below the corresponding entity. Section 2.1 demonstrates that some components in the drivetrain generally show linear behavior while others are nonlinear. In Fig. 3.1, the nonlinear curve of the steady-state tire characteristics is visible in the right part of the tire block. The shafts contain backlash. The model is derived from the left side of Fig. 3.1 to the right side with the exception of the tire. Since the tire is such a crucial component, it is discussed at the end in section 3.1.4 in detail. Section 3.1.5 summarizes the final model representation. The method for the model validation is outlined in section 3.1.6.

3.1.1 Torque Vectoring Differential

Based on the theoretical simulation results from the publications [35, 88], the TVD model condenses to the following relations. Equation 3.1 holds the relation between the TVD's input speeds to its output speeds. The input contains $\dot{\varphi}_{\mathrm{trc}}$ for the traction motor and $\dot{\varphi}_{\mathrm{tv}}$ for the

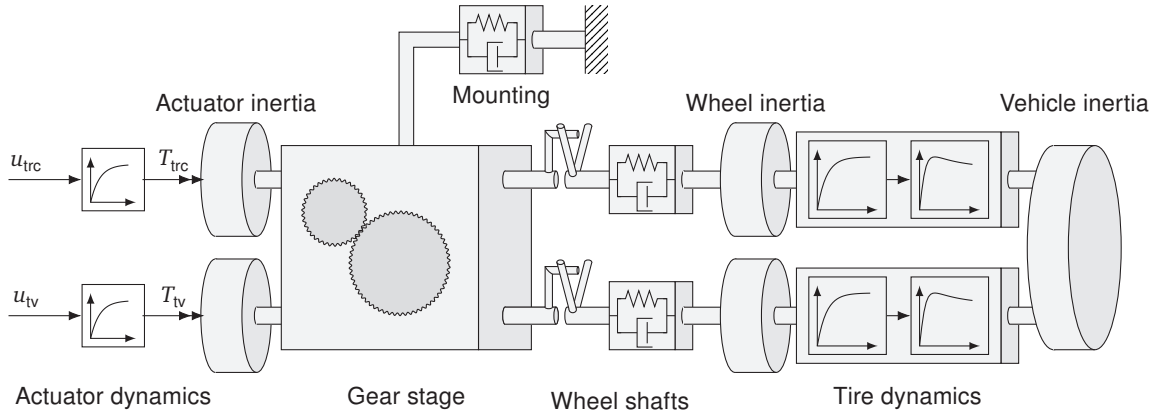

Figure 3.1: Block diagram of the complete TVD drivetrain model containing the components with a significant contribution to the oscillations as summarized in section 2.1

TV-motor. The outputs hold $\dot{\varphi}_{\mathrm{l,out}}$ for the left side and $\dot{\varphi}_{\mathrm{r,out}}$ for the right side. The transformation matrix I_{tvd} stores the gear ratios i_{trc} and i_{tv} for the speed conversion. The torque split from input to output is given in Eq. 3.2, with T_{trc} and T_{tv} corresponding to traction and TV-motor, as well as $T_{\mathrm{l,sh}}$ and $T_{\mathrm{r,sh}}$, corresponding to the left and right shafts.

$$\begin{bmatrix} \dot{\varphi}_{\mathrm{l,out}} \\ \dot{\varphi}_{\mathrm{r,out}} \end{bmatrix} = \begin{bmatrix} \frac{1}{i_{\mathrm{trc}}} & \frac{1}{i_{\mathrm{tv}}} \\ \frac{1}{i_{\mathrm{trc}}} & -\frac{1}{i_{\mathrm{tv}}} \end{bmatrix} \begin{bmatrix} \dot{\varphi}_{\mathrm{trc}} \\ \dot{\varphi}_{\mathrm{tv}} \end{bmatrix} = I_{\mathrm{tvd}} \begin{bmatrix} \dot{\boldsymbol{\varphi}}_{\mathrm{trc}} \\ \dot{\boldsymbol{\varphi}}_{\mathrm{tv}} \end{bmatrix} \tag{3.1}$$

$$\begin{bmatrix} T_{\mathrm{l,out}} \\ T_{\mathrm{r,out}} \end{bmatrix} = \frac{1}{2} \begin{bmatrix} i_{\mathrm{trc}} & i_{\mathrm{tv}} \\ i_{\mathrm{trc}} & -i_{\mathrm{tv}} \end{bmatrix} \begin{bmatrix} T_{\mathrm{trc}} \\ T_{\mathrm{tv}} \end{bmatrix} = I_{\mathrm{tvd}}^{-T} \begin{bmatrix} \boldsymbol{T}_{\mathrm{trc}} \\ \boldsymbol{T}_{\mathrm{tv}} \end{bmatrix} \tag{3.2}$$

The rotational impulse for the TVD is given by Eq. 3.3.

$$\left(\boldsymbol{I}_{\mathrm{tvd}}^{-T} \begin{bmatrix} \boldsymbol{J}_{\mathrm{trc}} & \boldsymbol{0} \\ \boldsymbol{0} & \boldsymbol{J}_{\mathrm{tv}} \end{bmatrix} \boldsymbol{I}_{\mathrm{tvd}}^{-1} \right) \begin{bmatrix} \ddot{\varphi}_{\mathrm{l,out}} \\ \ddot{\varphi}_{\mathrm{r,out}} \end{bmatrix} = \boldsymbol{I}_{\mathrm{tvd}}^{-T} \begin{bmatrix} \boldsymbol{T}_{\mathrm{trc}} \\ \boldsymbol{T}_{\mathrm{tv}} \end{bmatrix} - \begin{bmatrix} \boldsymbol{T}_{\mathrm{l,sh}} \\ \boldsymbol{T}_{\mathrm{r,sh}} \end{bmatrix} \tag{3.3}$$

The torques provided by the motors, T_{trc} and T_{tv}, are subject to the corresponding motor dynamics of Eq. 3.4 and Eq. 3.5, respectively. The time constants τ_{trc} and τ_{tv} define the response of the motors to the requests u_{trc} and u_{tv}. These first-order dynamics are an approximation of the physical behavior of the motors and the control by the inverters.

$$\dot{T}_{\mathrm{trc}} = \frac{1}{\tau_{\mathrm{trc}}} \left(u_{\mathrm{trc}} - T_{\mathrm{trc}} \right) \tag{3.4}$$

$$\dot{T}_{\mathrm{tv}} = \frac{1}{\tau_{\mathrm{tv}}} \left(u_{\mathrm{tv}} - T_{\mathrm{tv}} \right) \tag{3.5}$$

3.1.2 Wheel Shafts and TVD Mounting

As discussed in section 2.1.2, the elasticity of the steel shafts causes the low-frequency oscillations. A linear parallel spring-damper element is the most basic representation for this elasticity, given in Eq. 3.6. The stiffness c_{sh} and damping coefficient d_{sh} are constant and identical for the left and right side. For steel shafts, d_{sh} is small compared to c_{sh} and may be neglected [26]. Since the left and the right drivetrain side are identical the index $j \in [\mathrm{l}, \mathrm{r}]$ is used.

$$T_{j,\mathrm{sh}} = c_{\mathrm{sh}} \, \varphi_{j,\mathrm{sh}} + d_{\mathrm{sh}} \, \dot{\varphi}_{j,\mathrm{sh}} \tag{3.6}$$

However, the wheel shafts in the Visio.M have considerable backlash in the joints. According to the literature review in section 2.1.3, switching and continuous backlash models are available. The final goal is to control the backlash based on differential flatness. Hence, a continuous model is necessary. Nevertheless, switching models are widespread and the comparison between switching and continuous models is important. For this purpose, the dead zone model of Eq. 3.7 according to [100] is used. The model requires only the backlash angle α in addition to the linear model of Eq. 3.6. The continuous representation by Pham et al. [80], represented by Eq. 3.8, relies on the two tuning parameters p and q. They do not possess a physical meaning, but Pham [162] suggests to select $q \approx \frac{1}{\alpha}$. The resulting nonlinear characteristic implemented by the tanh function is similar to a nonlinear spring and damper coefficient.

$$T_{j,\mathrm{sh}} = \begin{cases} c_{\mathrm{sh}}\left(\varphi_{j,\mathrm{sh}} - \alpha\right) + d_{\mathrm{sh}}\ \dot{\varphi}_{j,\mathrm{sh}} & \varphi_{j,\mathrm{sh}} > \alpha \\ c_{\mathrm{sh}}\left(\varphi_{j,\mathrm{sh}} + \alpha\right) + d_{\mathrm{sh}}\ \dot{\varphi}_{j,\mathrm{sh}} & \varphi_{j,\mathrm{sh}} < -\alpha \\ 0 & -\alpha \leq \varphi_{j,\mathrm{sh}} \leq \alpha \end{cases} \tag{3.7}$$

$$T_{j,\mathrm{sh}} = \left(c_{\mathrm{sh}}\ \varphi_{j,\mathrm{sh}} + d_{\mathrm{sh}}\ \dot{\varphi}_{j,\mathrm{sh}}\right)\ q\ \tanh\left(p\ \left|\varphi_{j,\mathrm{sh}}\right|\right) \tag{3.8}$$

However, in the tanh model of Eq. 3.7 a significant relation between $T_{j,\mathrm{sh}}$ and $\varphi_{j,\mathrm{sh}}$ remains inside the backlash gap. Therefore, Pham [162] introduces an additional exponent to the model and another hyperbolic function to subtract α from $\varphi_{j,\mathrm{sh}}$.

Since the final model requires additional complexity to generate a sufficient approximation, a new continuous backlash model is proposed, which reflects the switching nature of the backlash more closely with only a single tuning parameter k_α. The model of Eq. 3.9 replaces the switching logic of the dead zone model with an arcus tangens (arctan) function. It relies on the physical parameter α and the scaling factor k_α, which defines the slope of the transition from contact to traverse and vice versa. In addition, the damping factor d_α incorporates viscous damping inside the backlash gap in order to capture friction during the backlash transition. In comparison to the tanh model, the arctan-model resembles the dead zone model more closely and sticks to physical parameters. However, the equation of the tanh model is leaner than the one by the arctan-model.

$$\begin{aligned} T_{j,\mathrm{sh}} = {} & \left(c_{\mathrm{sh}}\left(\varphi_{j,\mathrm{sh}} - \alpha\right) + d_{\mathrm{sh}}\ \dot{\varphi}_{j,\mathrm{sh}}\right)\left(\frac{1}{2} + \frac{\arctan\left(k_\alpha\left(\varphi_{j,\mathrm{sh}} - \alpha\right)\right)}{\pi}\right) \\ & + \left(c_{\mathrm{sh}}\left(\varphi_{j,\mathrm{sh}} + \alpha\right) + d_{\mathrm{sh}}\ \dot{\varphi}_{j,\mathrm{sh}}\right)\left(\frac{1}{2} - \frac{\arctan\left(k_\alpha\left(\varphi_{j,\mathrm{sh}} + \alpha\right)\right)}{\pi}\right) \\ & + d_\alpha\ \dot{\varphi}_{j,\mathrm{sh}}\left(-\frac{\arctan\left(k_\alpha\left(\varphi_{j,\mathrm{sh}} - \alpha\right)\right)}{\pi} + \frac{\arctan\left(k_\alpha\left(\varphi_{j,\mathrm{sh}} + \alpha\right)\right)}{\pi}\right) \end{aligned} \tag{3.9}$$

The difference between the backlash models is depicted in Fig. 3.2. In general, as demonstrated by most of the publications reviewed in section 2.1.3, it is assumed that inside the backlash gap actuator and load are disconnected. The dead zone model represents complete disconnection. The arctan model approximates the disconnection. In the transition area at $\varphi_{j,\mathrm{sh}} = \pm\alpha$, the arctan model deviates the most from the hard-switching dead zone model. The scaling factor k_α determines the deviation. The higher the value of k_α is, the closer is the approximation of the dead zone. The tanh model does not fully disconnect actuator and load. Pham et al. [80] acknowledge this fact and justify it with the presence of multiple backlashes in a real vehicle drivetrain. The argument has been previously presented by [96]. In addition, the tanh model shows a small deviation from the linear behavior in contact at $\left|\varphi_{j,\mathrm{sh}}\right| > |2\alpha|$. Pham [162, p. 78 ff.]

extends the tanh model, which increases its complexity but also improves the fit. In case of

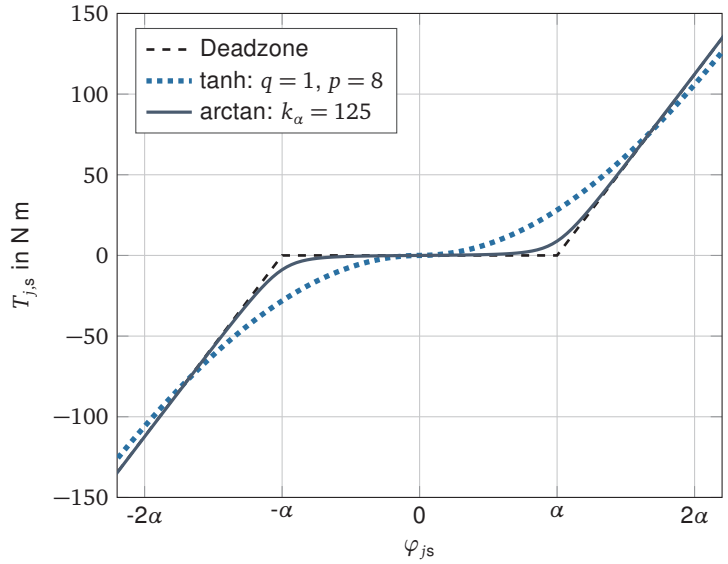

Figure 3.2: Comparison of backlash models without damping ($d_{sh} = 0$ Nms/rad, $d_\alpha = 0$ Nms/rad) based on the parameters given in Tab. 3.1

the Visio.M, the wheel-shaft joints account for most of the backlash. The gear stages in the TVD have no significant influence. Hence, the argument for the tanh model with a distributed backlash is inappropriate. Nevertheless, all these models are approximations of the physical system. Therefore, the tanh and arctan model are compared to experiments in section 3.2.2.

The literature reviewed in section 2.1.5 and the sensitivity analysis in [88] show a possibly significant influence of the TVD's mounting to the chassis to low-frequency oscillations. Therefore, the approach by [21, p. 52 ff.] is adopted by including the motion of the housing in its pitch direction φ_h. Equation 3.10 describes the rotational impulse of the housing inertia J_h. It has to support the TVD's output torques $T_{l,sh}$ and $T_{r,sh}$ through the combined bushing stiffness c_h and damping d_h. Superposition adds the housing motion to the twist of both shafts in Eq. 3.11.

$$J_h \ddot{\varphi}_h = -T_{r,sh} - T_{l,sh} - c_h \varphi_h - d_h \dot{\varphi}_h \tag{3.10}$$

$$\varphi_{j,sh} = \varphi_{j,out} + \varphi_h - \varphi_{j,w} \tag{3.11}$$

The calculation of the shaft's twist angle requires the wheel angle $\varphi_{j,w}$. Therefore, the next step is setting up the rotational impulse at the wheels.

3.1.3 Wheel and Vehicle Dynamics

The rotational impulse at the wheel in Eq. 3.12 yields the wheel's acceleration $\ddot{\varphi}_{j,w}$ according to the difference between shaft torque $T_{j,sh}$ and tire torque $T_{j,tire}$. The tire has a strong influence on the drivetrain's dynamics, which was summarized in section 2.1.4. Therefore, tire dynamics are discussed in detail separately. At this point, the tire torques $T_{j,tire}$ are assumed to be known.

$$J_w \ddot{\varphi}_{j,w} = T_{j,sh} - T_{j,tire} \tag{3.12}$$

Suspension dynamics rarely contribute to low-frequency drivetrain oscillations, according to the literature review in section 2.1.5. Especially for the Visio.M, but also for Prototype Two, the unsprung mass is small and suspension bushings are stiff. Preliminary analysis showed

that for this combination of low mass and stiff compliance the contribution of the suspension to the low-frequency drivetrain oscillations is insignificant. Therefore, suspension dynamics are neglected and the tire torques propel the vehicle directly. The sum of both $T_{\text{r,tire}}$ and $T_{\text{l,tire}}$ cause the longitudinal motion of the vehicle. The angular acceleration $\ddot{\varphi}_{\text{veh}}$ in Eq. 3.13 expresses the longitudinal motion in the rotational coordinate around the wheel axis. In order to set up the rotational impulse equation, the wheel radius r_{w} converts the vehicle mass m_{veh} to an inertia. Since the longitudinal acceleration a_{veh} is an important measurement signal, it is defined by Eq. 3.14 based on $\ddot{\varphi}_{\text{veh}}$.

$$m_{\text{veh}}\, r_{\text{w}}^2\, \ddot{\varphi}_{\text{veh}} = T_{\text{r,tire}} + T_{\text{l,tire}} \tag{3.13}$$

$$a_{\text{veh}} = r_{\text{w}}\, \ddot{\varphi}_{\text{veh}} \tag{3.14}$$

Any difference between $T_{\text{r,tire}}$ and $T_{\text{l,tire}}$ results in a yaw acceleration of the vehicle, expressed by $\ddot{\varphi}_{\text{yaw}}$ in Eq. 3.15. The ratio of track width b_{veh} to wheel radius r_{w} represents the conversion from the wheel coordinate to yaw coordinate, which is the vertical axis at the center of the drivetrain. Therefore, the yaw inertia J_{yaw} includes a term to account for the offset between vehicle center-of-mass and drivetrain center. The coordinate transformation in Eq. 3.16 and Eq. 3.17 converts vehicle speed and yaw rate to the road speed on the left side $\dot{\varphi}_{\text{l,veh}}$ and the right side $\dot{\varphi}_{r,veh}$ of the vehicle, which is necessary for the tire models.

$$J_{\text{yaw}}\, \ddot{\varphi}_{\text{yaw}} = \frac{b_{\text{veh}}}{2\, r_{\text{w}}} \left(T_{\text{r,tire}} - T_{\text{l,tire}} \right) \tag{3.15}$$

$$\dot{\varphi}_{\text{l,veh}} = \dot{\varphi}_{\text{veh}} - \frac{b_{\text{veh}}}{2\, r_{\text{w}}} \dot{\varphi}_{\text{yaw}} \tag{3.16}$$

$$\dot{\varphi}_{\text{r,veh}} = \dot{\varphi}_{\text{veh}} + \frac{b_{\text{veh}}}{2\, r_{\text{w}}} \dot{\varphi}_{\text{yaw}} \tag{3.17}$$

The TVD connects the traction motor with a motion of the left and right outputs in the same direction. This motion is referred to as the in-phase motion of the left and right side. The TV-motor connects to the anti-phase motion, with the left output turning in opposite direction to the right output. Because of this mapping by the TVD, the in-phase wheel motion $\dot{\varphi}_{\text{in,w}}$ and the anti-phase wheel motion $\dot{\varphi}_{\text{anti,w}}$ are introduced. They create the counterpart to the corresponding motor speeds. The in-phase motion is the mean value of both wheel speeds while the anti-phase motion is the difference between the two wheels, given by Eq. 3.18 and Eq. 3.19 respectively. This mapping helps to analyze the different oscillation modes in the TVD drivetrain. Usually, in standard drivetrains only the in-phase motion is investigated.

$$\dot{\varphi}_{\text{in,w}} = \frac{\dot{\varphi}_{\text{l,w}} + \dot{\varphi}_{\text{r,w}}}{2} \tag{3.18}$$

$$\dot{\varphi}_{\text{anti,w}} = \frac{\dot{\varphi}_{\text{l,w}} - \dot{\varphi}_{\text{r,w}}}{2} \tag{3.19}$$

Next, a relation for the tire torque is derived in order to link vehicle and wheel.

3.1.4 Tire Dynamics

The tire is a highly nonlinear component and has great effect on drivetrain dynamics. Zegelaar [116] presented a detailed summary of steady-state and transient dynamics. The following paragraphs are mainly based on his dissertation. In a steady-state tire model, Eq. 3.20 represents the slip. The steady-state slip is denoted by $s_{\text{x,0}}$. Some publications distinguish between braking

and traction slip, e.g. [163]. This is also recognized in [109, p. 4]. Therefore, the general rotational speed $\dot{\varphi}_{s,0}$ is used and Eq. 3.21 defines the switching. For braking conditions $\dot{\varphi}_{s,0}$ is the vehicle speed and for acceleration conditions $\dot{\varphi}_{s,0}$ is the wheel speed.

$$s_{x,0} = \frac{\dot{\varphi}_{w,0} - \dot{\varphi}_{veh,0}}{\dot{\varphi}_{s,0}} \tag{3.20}$$

$$\dot{\varphi}_s = \begin{cases} \dot{\varphi}_{veh} & \dot{\varphi}_{veh} > \dot{\varphi}_w \\ \dot{\varphi}_w & \dot{\varphi}_{veh} \leq \dot{\varphi}_w \end{cases} \tag{3.21}$$

The steady-state slip to torque characteristic is given by Eq. 3.22 according to the Pacejka Magic Formula with its parameters B_{pac}, C_{pac}, D_{pac} and E_{pac}. The parameters of the Pacejka Magic Formula depend on the vertical load F_z and the surface friction coefficient μ. Therefore, the tire torque is a function of s_x, F_z and μ expressed by Eq. 3.23. In this study, the vertical dynamics are neglected and F_z is constant. The surface friction coefficient μ is also constant and set according to the test scenario. The tire torque of the Pacejka model T_{pac} is displayed over tire slip s_x in Fig. 3.3 for two different values of μ. At low slip values, the slope of the curves is steep. At high slip values, the curves are nearly flat. For the energy saving tire used on both prototype vehicles, the steady-state characteristic creates only a minor peak. The maximum of T_{pac} decreases strongly when μ is reduced.

$$T_{pac} = r_w \, D_{pac} \sin\left(C_{pac} \arctan\left(B_{pac} \, s_x - E_{pac}\left[B_{pac} \, s_x - \arctan\left(B_{pac} \, s_x\right)\right]\right)\right) \tag{3.22}$$

$$T_{pac} = f_{pac}\left(s_x, F_z, \mu\right) \tag{3.23}$$

Standard tire models are nonlinear but robust control design relies on linear models. Therefore, a linearization of the tire dynamics is necessary. Any real system is locally linear around an operation point. Therefore, it can be linearized at this point [164, p. 5], [45, p. 2 f.]. The variables vehicle speed, tire slip and friction coefficient define the operation point. In order to cover the vehicle's operation range, several operation points are required, which creates a linear parameter-varying model. In the subsequent paragraphs the linear tire model is derived in general. The model contains the final equations for the left and right side.

The linearization of a function f in the operation point x_0 is given by Eq. 3.24. It approximates the dynamics of the system based on the Taylor series expansion but only considers the constant and first-order terms. This is justified, since higher-order terms in a Taylor series are small for small deviations from the operation point and for sufficiently smooth functions, which the tire model satisfies. The first term $f(x_0)$ is an offset with the constant value in the operation point. The second term is the linear slope tangent to f in x_0 multiplied by the deviation of x from x_0 [141, p. 22 ff.]. Applying Eq. 3.24 to Eq. 3.23 results in 3.25. However, the linear model only considers dynamic effects. Therefore, the constants are insignificant. Further, Eq. 3.26 defines the slip stiffness c_{sx} for a given operation point. The reduction yields Eq. 3.27, which contains only the product of s_x and c_{sx}.

$$y = f\left(x\right) \approx f\left(x_0\right) + \left.\frac{\partial f\left(x\right)}{\partial x}\right|_{x=x_0} \left(x - x_0\right) \tag{3.24}$$

$$T_{pac} \approx \left.\frac{\partial f_{pac}\left(s_x, F_z, \mu\right)}{\partial s_x}\right|_{s_x = s_{x,0}} \left(s_x - s_{x,0}\right) + f_{pac}\left(s_{x,0}, F_z, \mu\right) \tag{3.25}$$

$$c_{sx} = \left.\frac{\partial f_{pac}\left(s_x, F_z, \mu\right)}{\partial s_x}\right|_{s_x = s_{x,0}} \tag{3.26}$$

In order to investigate the effect of disturbances, $\Delta T_{j,\text{tire}}$ represents an additional input to the system. However, $\Delta T_{j,\text{tire}}$ can not resemble the changes in system dynamics, caused by changes in μ. For cornering an extension of the model is reasonable.

$$T_{j,\text{tire}} = c_{\text{sx}}\, s_{j,\text{x}} + \Delta T_{j,\text{tire}} \tag{3.27}$$

Even though c_{sx} is commonly referred to as a slip stiffness, it acts as a damping coefficient. The slip $s_{\text{x,0}}$ relates to angular velocities of the system and not to angular positions. Therefore, the product of c_{sx} and $s_{\text{x,0}}$ is a damping torque, which is demonstrated by Eq. 3.28. Since c_{sx} is already a function of $s_{\text{x,0}}$, F_{z} and μ, the damping coefficient d_{tire} in Eq. 3.29 is a function of s_{x}, F_{z}, μ and $\dot{\varphi}_{\text{s}}$. Especially this speed dependence has been investigated and used for gain scheduling in controllers, e.g. [138, p. 5], [87, p. 10] or [51, p. 739]. However, Fig. 3.3 demonstrates the strong decline of c_{sx} with increasing slip. On low μ, the decline is steeper than on high μ. The derivative of c_{sx} over s_{x} demonstrates that the steepest descent occurs well below $s_{\text{x}} = 25$ %.

$$T_{j,\text{tire}} = \frac{c_{\text{sx}}}{\dot{\varphi}_{\text{s}}} \left(\dot{\varphi}_{\text{w,0}} - \dot{\varphi}_{\text{veh,0}}\right) + \Delta T_{j,\text{tire}} \tag{3.28}$$

$$T_{j,\text{tire}} = d_{\text{tire}} \left(\dot{\varphi}_{\text{w,0}} - \dot{\varphi}_{\text{veh,0}}\right) + \Delta T_{j,\text{tire}} \tag{3.29}$$

Since traction and straight line driving is the focus of this research, c_{sx} is assumed to be equal for the left and right side. This reduces the number of parameters in the model. Disturbances, large TV torques and extreme cornering conditions may lead to a violation of this assumption. Up to this point, only steady-state tire dynamics have been considered. Zegelaar [116, p. 129 ff.]

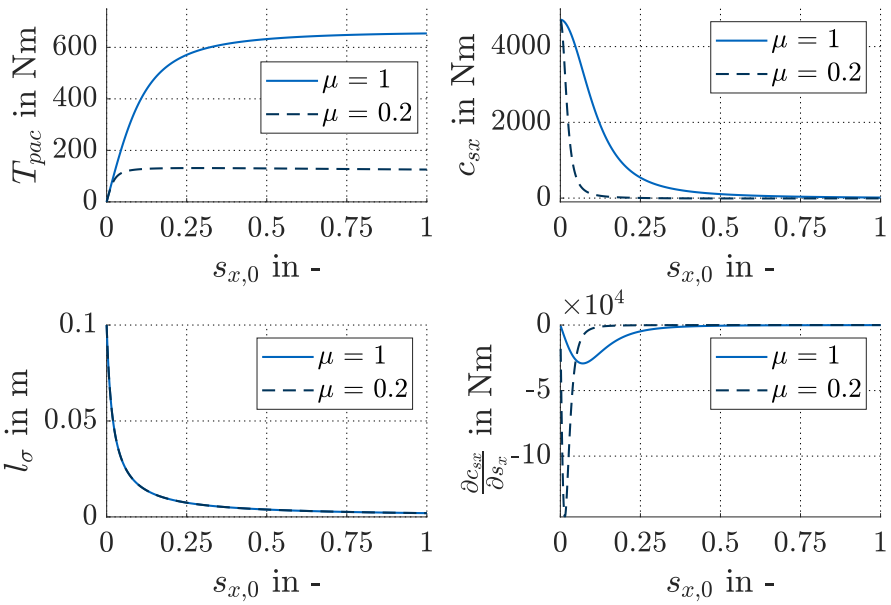

Figure 3.3: Nonlinear tire characteristics over tire slip

presents several pragmatic transient tire models. Filtering s_{x} through a first-order transfer function is well suited for this study, because it separates steady-state and transient characteristics. In the transient relaxation-length model of Eq. 3.30, the transient slip s_{x} responds with a lag to changes in $\dot{\varphi}_{\text{w}}$ and $\dot{\varphi}_{\text{veh}}$. The dynamics of the response depend on $\dot{\varphi}_{\text{veh}}$ and s_{x} itself. Therefore,

the linearization of Eq. 3.30 is necessary.

$$\dot{s}_\mathrm{x} = \frac{r_\mathrm{w}\left|\dot{\varphi}_\mathrm{s}\right|}{l_\sigma\left(s_\mathrm{x}\right)}\left(\frac{\dot{\varphi}_\mathrm{w}-\dot{\varphi}_\mathrm{veh}}{\left|\dot{\varphi}_\mathrm{s}\right|}-s_\mathrm{x}\right) \tag{3.30}$$

Before linearizing Eq. 3.30, a function of l_σ over s_x is required. Plots in [116, p. 131] show a strong decrease of l_σ when s_x increases. The behavior is illustrated by the bottom left plot of Fig. 3.3. This inverse proportional relation is approximated by Eq. 3.31. The parameter k_σ determines the decline rate starting from the initial value $l_{\sigma,0}$. A large value of $k_\sigma \gg 1$ ensures a high descent rate. Prior to the linearization, a couple of simplifications are possible. First, only positive vehicle speeds are considered, which makes the absolute value operator obsolete. Second, the main focus is on acceleration. Therefore, $\dot{\varphi}_\mathrm{w}$ replaces $\dot{\varphi}_\mathrm{s}$. In addition, $\dot{\varphi}_\mathrm{s}$ is factored into the bracket, eliminating the fraction. Third, Eq. 3.31 replaces the general expression of $l_\sigma\left(s_\mathrm{x}\right)$. The result is Eq. 3.32.

$$l_\sigma\left(s_\mathrm{x}\right) = \frac{l_{\sigma,0}}{1+k_\sigma\, s_\mathrm{x}} \tag{3.31}$$

$$\dot{s}_\mathrm{x} = \frac{r_\mathrm{w}}{l_{\sigma,0}}\left(1+k_\sigma\, s_\mathrm{x}\right)\left(\dot{\varphi}_\mathrm{w}-\dot{\varphi}_\mathrm{veh}-\dot{\varphi}_\mathrm{w}\, s_\mathrm{x}\right) \tag{3.32}$$

Applying the linearization of Eq. 3.24 to Eq. 3.32 yields Eq. 3.33.

$$\begin{aligned}\dot{s}_\mathrm{x} \approx \frac{r_\mathrm{w}}{l_{\sigma,0}}\Bigg[\; & k_\sigma\left(\dot{\varphi}_\mathrm{w}-\dot{\varphi}_\mathrm{veh}-\dot{\varphi}_\mathrm{w}\, s_\mathrm{x}\right)\Big|_{s_{\mathrm{x},0},\dot{\varphi}_{\mathrm{veh},0},\dot{\varphi}_{\mathrm{w},0}}\left(s_\mathrm{x}-s_{\mathrm{x},0}\right)\\ & -\dot{\varphi}_\mathrm{w}\left(1+k_\sigma\, s_\mathrm{x}\right)\Big|_{s_{\mathrm{x},0},\dot{\varphi}_{\mathrm{w},0}}\left(s_\mathrm{x}-s_{\mathrm{x},0}\right)\\ & -\left(1+k_\sigma\, s_\mathrm{x}\right)\Big|_{s_{\mathrm{x},0}}\left(\dot{\varphi}_\mathrm{veh}-\dot{\varphi}_{\mathrm{veh},0}\right)\\ & +\left(1+k_\sigma\, s_\mathrm{x}\right)\left(1-s_\mathrm{x}\right)\Big|_{s_{\mathrm{x},0}}\left(\dot{\varphi}_\mathrm{w}-\dot{\varphi}_{\mathrm{w},0}\right)\\ & +\left(1+k_\sigma\, s_{\mathrm{x},0}\right)\left(\dot{\varphi}_{\mathrm{w},0}-\dot{\varphi}_{\mathrm{veh},0}-\dot{\varphi}_{\mathrm{w},0}\, s_{\mathrm{x},0}\right)\;\Bigg]\end{aligned} \tag{3.33}$$

In order to reduce the large expression of Eq. 3.33, two simplifications are possible. First, the constant terms are neglected for the linear model. Second, Eq. 3.34 links $\dot{\varphi}_{\mathrm{w},0}$ to $\dot{\varphi}_{\mathrm{veh},0}$ and $s_{\mathrm{x},0}$ based on the steady-state slip from Eq. 3.20. Inserting Eq. 3.34 in Eq. 3.33 eliminates the first term $\left(\dot{\varphi}_\mathrm{w}-\dot{\varphi}_\mathrm{veh}-\dot{\varphi}_\mathrm{w}\, s_\mathrm{x}\right)$.

$$\dot{\varphi}_{\mathrm{veh},0} = \dot{\varphi}_{\mathrm{w},0}+\dot{\varphi}_{\mathrm{w},0}\, s_{\mathrm{x},0} \tag{3.34}$$

Without the constant terms, Eq. 3.35 remains. Further, the factor $\left(1+k_\sigma\, s_{\mathrm{x},0}\right)$ is common to all terms and, therefore, placed in front of the brackets to form Eq. 3.36. The transient dynamics of Eq. 3.36 are implemented into the linear model.

$$\dot{s}_\mathrm{x} \approx \frac{r_\mathrm{w}}{l_{\sigma,0}}\left[-\dot{\varphi}_{\mathrm{w},0}\left(1+k_\sigma\, s_{\mathrm{x},0}\right)s_\mathrm{x}-\left(1+k_\sigma\, s_{\mathrm{x},0}\right)\dot{\varphi}_\mathrm{veh}+\left(1+k_\sigma\, s_{\mathrm{x},0}\right)\left(1-s_{\mathrm{x},0}\right)\dot{\varphi}_\mathrm{w}\right] \tag{3.35}$$

$$\dot{s}_{j,\mathrm{x}} = \frac{r_\mathrm{w}\left(1+k_\sigma\, s_{\mathrm{x},0}\right)}{l_{\sigma,0}}\left[-\dot{\varphi}_{\mathrm{w},0}\, s_{j,\mathrm{x}}+\left(1-s_{\mathrm{x},0}\right)\dot{\varphi}_{j,\mathrm{w}}-\dot{\varphi}_{j,\mathrm{veh}}\right] \tag{3.36}$$

For a more detailed understanding, Eq. 3.38 represents a rewritten form of Eq. 3.36. The

first-order transfer function of Eq. 3.37 serves as a reference model. The term in front of $\dot{s}_{\mathrm{x}}$ is the time constant τ. It decreases with $s_{\mathrm{x,0}}$ and $\dot{\varphi}_{\mathrm{w,0}}$. This means that the transient slip responds faster at higher wheel speeds and slip values. On the right hand side of Eq. 3.38, the first term represents the slip ratio for the transient values of $\dot{\varphi}_{\mathrm{w}}$ and $\dot{\varphi}_{\mathrm{veh}}$ at the predefined operation point $\dot{\varphi}_{\mathrm{w,0}}$. In case of $\tau \to 0$ s, the first term acts as a relative damper between wheel and vehicle. The gain K for the relative speed difference $\dot{\varphi}_{\mathrm{w}} - \dot{\varphi}_{\mathrm{veh}}$ decreases with increasing wheel speed, as $\dot{\varphi}_{\mathrm{w,0}}$ is in the denominator. The second term on the right hand side accounts for the steady-state slip of the chosen operation point. In case of $\tau \to 0$ s, it acts as a viscous friction on the wheel. Its gain also decreases with increasing $\dot{\varphi}_{\mathrm{w,0}}$. Appendix A.1 shows that the main difference between the two steady-state slip definitions of Eq. 3.21, brake and traction slip, is the location of the viscous friction in the second term. For brake slip, the friction acts on the vehicle instead of the wheel.

$$\tau\ \dot{y}(t) + y(t) = K\ u(t) \tag{3.37}$$

$$\frac{l_{\sigma,0}}{r_{\mathrm{w}}\ \dot{\varphi}_{\mathrm{w,0}}\left(1 + k_{\sigma}\ s_{\mathrm{x,0}}\right)}\dot{s}_{j,\mathrm{x}} + s_{j,\mathrm{x}} = \frac{1}{\dot{\varphi}_{\mathrm{w,0}}}\left(\dot{\varphi}_{j,\mathrm{w}} - \dot{\varphi}_{j,\mathrm{veh}}\right) - \frac{s_{\mathrm{x,0}}}{\dot{\varphi}_{\mathrm{w,0}}}\dot{\varphi}_{j,\mathrm{w}} \tag{3.38}$$

In summary, the tire acts as a damper with a damping coefficient c_{sx}, which depends on μ, $s_{\mathrm{x,0}}$ and $\dot{\varphi}_{\mathrm{w,0}}$. The tire's slip dynamics are a first-order low-pass. Its time constant varies with $s_{\mathrm{x,0}}$ and $\dot{\varphi}_{\mathrm{w,0}}$. For the implementation in the linear model, the left and right side tire have the same operation point. Differences in tire torque are analyzed with the disturbance torques $\Delta T_{j,\mathrm{tire}}$.

3.1.5 Model Representation

After the previous sections contain the necessary equations for different components, the overall representation of these equations defines the model and applicable methods. In engineering, state-space models are common. Their behavior solely depends on the state variables $\boldsymbol{x}_0$ at some initial time t_0, called the initial condition of the system, and the history of inputs $\boldsymbol{u}(t)$ and external disturbances $d(t)$ over time [157, p. 9 ff.], [105, p. 4. f.]. In case of the drivetrain model, $\boldsymbol{x}$ contains fourteen variables. The input vector $\boldsymbol{u}$ holds the two motor torque requests while $\Delta T_{\mathrm{l,tire}}$ is the specified disturbance d. Outputs of the drivetrain are the signals produced by the sensors at the motors, wheels and the vehicle. In addition, y contains $\dot{\varphi}_{\mathrm{in,w}}$ and $\dot{\varphi}_{\mathrm{anti,w}}$, which are calculated from the wheel speeds.

$$\boldsymbol{x} = \left[\ \varphi_{\mathrm{l,sh}},\ \varphi_{\mathrm{r,sh}},\ \varphi_{\mathrm{h}},\ \dot{\varphi}_{\mathrm{l,out}},\ \dot{\varphi}_{\mathrm{r,out}},\ \dot{\varphi}_{\mathrm{h}},\ \dot{\varphi}_{\mathrm{l,w}},\ \dot{\varphi}_{\mathrm{r,w}},\ s_{\mathrm{l,x}},\ s_{\mathrm{r,x}},\ \dot{\varphi}_{\mathrm{veh}},\ \dot{\varphi}_{\mathrm{yaw}},\ T_{\mathrm{trc}},\ T_{\mathrm{tv}}\ \right]^T \tag{3.39}$$

$$\boldsymbol{u} = \left[\ u_{\mathrm{trc}},\ u_{\mathrm{tv}}\ \right]^T \tag{3.40}$$

$$d = \Delta T_{\mathrm{l,tire}} \tag{3.41}$$

$$\boldsymbol{y} = \left[\ \dot{\varphi}_{\mathrm{trc}},\ \dot{\varphi}_{\mathrm{tv}},\ \dot{\varphi}_{\mathrm{l,w}},\ \dot{\varphi}_{\mathrm{r,w}},\ \dot{\varphi}_{\mathrm{veh}},\ \dot{\varphi}_{\mathrm{yaw}},\ a_{\mathrm{veh}},\ T_{\mathrm{trc}},\ T_{\mathrm{tv}},\ \dot{\varphi}_{\mathrm{in,w}},\ \dot{\varphi}_{\mathrm{anti,w}}\ \right]^T \tag{3.42}$$

First-order Ordinary Differential Equations (ODEs) describe the evolution of the state variables. If any component in the model is nonlinear, the complete model is nonlinear [157, p. 11]. In case of the drivetrain model, backlash as well as nonlinear tire dynamics form a nonlinear model. In general, Eq. 3.43 and Eq. 3.44 represent a nonlinear system in state-space form. The function $\boldsymbol{f}$ contains the state-variables' dynamics while $\boldsymbol{g}$ maps $\boldsymbol{x}$ to the outputs $\boldsymbol{y}$ [45, p. 86], [141, p. 22]. In the particular case of the presented drivetrain model, $\boldsymbol{g}$ does not possess a feedthrough from $\boldsymbol{u}$ or d to $\boldsymbol{y}$. The nonlinear drivetrain model is used to assess the effects of backlash and

nonlinear tire dynamics. In addition, it forms the foundation for the backlash compensation.

$$\dot{\boldsymbol{x}}(t) = \boldsymbol{f}\left(\boldsymbol{x}(t), \boldsymbol{u}(t), d(t)\right) \tag{3.43}$$

$$\boldsymbol{y}(t) = \boldsymbol{g}\left(\boldsymbol{x}(t)\right) \tag{3.44}$$

Even though most physical systems are nonlinear, a great number of analysis and control design methods requires linear ODE models [45, p. 2 f.], [157, p. 11 f.]. For the shaft in section 3.1.2 and the tire in section 3.1.4, linear as well as nonlinear equations exist. The robust control methods rely on a linear model. Therefore, the feedback control model neglects backlash and uses the tire linearization. The resulting linear model is expressed by Eq. 3.45 and Eq. 3.46. It only considers changes around an equilibrium operation point. The matrix $\boldsymbol{A}_{\mathrm{s}}$ defines the internal dynamics of the model. The vector $\boldsymbol{b}_{\mathrm{d,s}}$ describes the impact of the disturbance d. The inputs $\boldsymbol{u}$ feed into the model through the matrix $\boldsymbol{B}_{\mathrm{u,s}}$. The matrix C maps $\boldsymbol{x}$ to $\boldsymbol{y}$ [45, p. 86 ff.]. The index "s" distinguishes the continuous-time model, which is used in the same context as the Laplace variable "s", from the subsequently defined discrete-time model, which is used along with the discrete variable "z". Parameter uncertainties alter these matrices and include the changes in the tires' operation point in the linear model. Due to the uncertainties, the model is a continuous linear parameter varying model. The parameter variation addresses the tire nonlinearity indirectly [45, p. 3, p. 55].

$$\dot{\boldsymbol{x}}(t) = A_{\mathrm{s}}\, \boldsymbol{x}(t) + \boldsymbol{b}_{\mathrm{d,s}}\, d(t) + B_{\mathrm{u,s}}\, \boldsymbol{u}(t) \tag{3.45}$$

$$\boldsymbol{y}(t) = C\, \boldsymbol{x}(t) \tag{3.46}$$

Most control applications are implemented in digital electronics. Even though, physical systems are part of the continuous time domain, a digital controller receives information from the physical system at discrete sampling instances and sends inputs to the physical system at discrete sampling instances. Therefore, a discrete model is more appropriate for control design since it acknowledges the digital nature of the control system [141, p. 26 f., p. 45, p. 111]. The necessary transformation from continuous to discrete is given in [141, p. 26 f.]. The discrete time k is an integer representing the discrete sampling steps [105, p. 4. f.]. Due to the transformation, the matrix $\boldsymbol{A}_{\mathrm{z}}$ and $\boldsymbol{B}_{\mathrm{u,z}}$ as well as the vector $\boldsymbol{b}_{\mathrm{d,z}}$ differ from their continuous counterparts. So does the nature of the equation itself. Instead of $\dot{\boldsymbol{x}}(t)$, Eq. 3.47 directly delivers the state at the next time step $\boldsymbol{x}[k+1]$. The outputs remain a linear combination of the state-vector.

$$\boldsymbol{x}[k+1] = A_{\mathrm{z}}\, \boldsymbol{x}[k] + \boldsymbol{b}_{\mathrm{d,z}}\, d[k] + B_{\mathrm{u,z}}\, \boldsymbol{u}[k] \tag{3.47}$$

$$\boldsymbol{y}[k] = C\, \boldsymbol{x}[k] \tag{3.48}$$

In case the sampling rate is sufficiently high (50 times the bandwidth of the model), the discrete signals are similar to their continuous counterparts. However, for lower sampling rates, the discretization of signals results in delays [123, p. 4 f.]. Such sampling delays may reduce the stability margin of a control loop. Therefore, it is important to acknowledge this effect in the control design. Additional delays may arise due to the communication between several digital control units. The physical sensors might be connected to individual micro controllers processing the sensor's data before it is sent to the main control unit. This processing is a source for additional output delays. The same holds for delays on input signals caused by individual actuator control units. Additional state variables can incorporate additional input and output delays into the discrete model [123, p. 337 ff.].

In summary, the three models serve different purposes. The nonlinear model is the most

comprehensive representation. It serves as the foundation for the linear models and forms the basis for the backlash compensation. The continuous-time linear model enables the investigation of the physical system with frequency response tools and eigenmode analysis. It forms the foundation for the discrete-time linear model, which forms the basis of the feedback control design.

3.1.6 Model Validation

An objective validation of the model requires a predefined objective evaluation measure assessing the quality of the model [165, 166]. However, modeling and controlling a physical system are two inseparable problems. They have to be solved in an iterative way, since the nature of the input force - in drivetrain control: the motor torque - effects the validity of the given model. Further, arbitrarily small modeling errors may cause arbitrarily large control errors, or even instability [167, p. 1741 f]. Therefore, there is no prior objective measure for the open-loop behavior guaranteeing model validity for all possible controllers. Hence, instead of an objective model validation, the goal is to explain the important effects in the measurement with the model behavior. Therefore, the validation is only qualitative. Previous literature provides a solid foundation for the definition of test cases. The next paragraph reviews the initial condition of the vehicle and the environment of previous studies. Afterwards, common procedures to excite drivetrain oscillations are summarized. The subsequent paragraph recaps measurement equipment to record the necessary data. Finally, possible analysis methods are surveyed.

The operation range of passenger vehicles is wide since the vehicles travel at high speed on highways but also low speed in urban areas and surface conditions change depending on the weather or road type. The importance of good damping performance on different surface conditions was discussed in section 1.1. Therefore, the vehicle drivetrain has to be evaluated on different surface conditions. Yeap and Mueller [27, p. 8 ff.] demonstrate that the oscillations are least damped at low speed on any surface condition. This is also stated for high μ in [52]. Consequently, low speed poses a worst case test scenario regarding oscillation damping. Tests are conducted on dry roads where $\mu \geq 0.8$, which is the standard case for tip-in tip-out tests, and on surfaces with $0.1 \leq \mu \leq 0.4$ representing low μ road conditions. Since the vehicles are located at different sites, they cannot be tested on exactly the same surfaces, which leads to the spread of $0.1 \leq \mu \leq 0.4$.

The basis of experimental design are the fundamentals in control theory on the input to output behavior of dynamical systems. In order to investigate this behavior, a test input should be simple and reproducible. It has to be suitable for the actuators and applicable to the process of interest. Also, the input signal needs to excite all the necessary system dynamics [50, p. 21]. For the class of linear time-invariant (LTI) systems, the response to an impulse excitation completely defines the system's behavior. However, because of actuator limitations, the impulse can only be approximated in experiments. Due to the electric motor's constraints, the impulse excitation of a vehicle drivetrain is limited. In order to avoid the disadvantages of the impulse, the unit step can be applied, which is the integral of the impulse [168, p. 111]. A torque step is a common maneuver for vehicle drivetrains, since drivers regularly step on the accelerator pedal during every day driving. The maneuver is so common that, in literature, pressing and releasing the accelerator pedal rapidly is called a tip-in and tip-out maneuver [19, 31, 51, 52, 93]. In addition, the vehicle's operation limits are easily monitored during a tip-in test, which is especially important on low μ [27, p. 2]. An extension to the tip-in tip-out maneuvers are pseudo random binary signals. They are a sequence of steps with various magnitude. In [52, 53, 82] pseudo

random binary signals are used to analyze vehicle drivetrain oscillations. Alternatives to the step input are white noise [168, p. 111] and sine sweeps, which are a sinusoidal oscillations with a gradually increasing frequency [123, p. 487 f.]. The sweep across a whole range of frequencies shows directly the response to each excitation and points out resonance peaks. The sine sweep is applied to vehicle drivetrains in [21, 53, 55, 138]. These publications use the pseudo random binary and sine sweep signal only on high μ, on which a safe operation is maintained more easily than on low μ. To the author's knowledge, white noise has not been used in this field. Because this study focuses on high- and low μ, the tip-in maneuver is best suited for the experiments due to its simplicity and safety.

In order to measure the vehicle's response to the input signal, the signals on the vehicle's CAN are available. The electric motor relies on accurate sensors for its current control. Therefore, the motor's speed measurement is available in a high resolution. The electric motor also sends out a torque estimation based on its current control [52, 61]. In addition, today, all production vehicles are equipped with ESP, which holds sensors for wheel speed, vehicle acceleration and yaw rate. However, the wheel speed signals are of poor accuracy, especially at low speed [52, 61, 77, 101]. Some publications neglect the wheel speed sensor completely and take only the motor speed signal into account, e.g. [26]. In contrast to relying solely on the standard CAN data, Lagerberg et al. [77, 101] use direct measurement of the pulses generated by the wheel speed sensors to bypass the ESP's control unit. This reduces delay and enables measuring the wheel's position. In [25, 52] the test vehicle was equipped with special measurement wheels to record the transmitted wheel torque. Goetting [21, p. 21 f.] adds strain gauges to the wheel shafts and accelerometers to the drive unit. Such measures provide improvements in accuracy. However, this study includes multiple vehicles. Any additional sensors must be implemented and maintained in all vehicles. Therefore, standard sensors are primarily used.

The measurement analysis may be conducted in the time and the frequency domain. Control theory yields several tools to analyze a system's response in the frequency domain [50]. However, the resolution of frequency analysis depends on the length of the measurement and the sampling frequency [169, p. 681]. Therefore, the short tip-in maneuvers are a drawback for frequency domain analysis. Time-domain analysis of the step response can yield sufficient and transparent results, if disturbances are small and the process is sufficiently approximated by a simple model [50, p. 59]. A thorough analysis should consider both, time and frequency-domain [165]. Especially on low μ, disturbances affect the system's response strongly. For example, disturbances such as small changes in μ cause a similar frequency response, but occur at different times during the measurement. The main focus of the frequency analysis lies in the number and the location of resonance frequencies. Time domain validation will be limited to the high μ test case for the identification of delays and nonlinear effects.

3.2 Validation Results

As stated at the beginning of this chapter, the validation focuses on straight-line driving since this is the main test case for low-frequency drivetrain oscillations in literature. Appendix B.2 covers experiments regarding cornering with the TV-unit. This section spotlights the most important oscillation phenomena of both vehicles. Therefore, the results are presented for the vehicle with the stronger occurrence of the particular phenomenon. Further experiments are added in the appendix. The physical parameters for the models of both prototypes are given in Tab. 3.1.

The vehicles' specification of the CAN communication is summarized in Tab. 3.2. In case of the Visio.M, the communication to the traction motor is limited to 12 ms, which is the slowest rate and therefore chosen as the discrete model's sampling rate. Both motor speed signals are delayed by one sampling interval. The ESP's signals are sent every 10 ms but experience significantly higher delays than the motor signals. In case of the Prototype Two, the TV and traction motor torque may only be requested with a sampling rate of 20 ms. This is the bottle neck in the communication. Therefore, the linear model is discretized with this sampling rate but no additional delays are added. First, the frequency-domain validation is presented. The measurements are compared to the nonlinear model, since it is the most comprehensive model. The frequency domain validation focuses on the general oscillation behavior. Afterwards, the time-domain validation pinpoints to specific effects such as backlash, delays and discretization. In all these different cases, the models are compared with multiple runs for each test case. The number of runs varies for each test case and vehicle because a test may be harmful to the vehicle, limiting the number of runs, or it may be of special interest, increasing the number of runs. Also, the length of the individual runs is different for the test cases. On high μ, the motor accelerates slowly, staying well below its operation limit. On low μ, however, the motor accelerates quickly, limiting the maneuver time. Nevertheless, within a test case, all runs are cut to the same length to compare them. A short measurement length impairs especially the resolution of the frequency analysis.

Table 3.1: Model parameters for the two prototype vehicles

		Prototype vehicle	
Description	Parameter	Visio.M	Prototype Two
Traction motor inertia	J_{trc}	0.0124 kgm^2	0.039 kgm^2
TV motor inertia	J_{tv}	9.54×10^{-5} kgm^2	0.01 kgm^2
Traction motor gear ratio	i_{trc}	10.15	9
TV motor gear ratio	i_{tv}	48	60
Traction motor time constant	τ_{trc}	0.006 s	0.025 s
TV motor time constant	τ_{tv}	0.002 s	0.01 s
Shaft stiffness	c_{sh}	2100 $\frac{\text{Nm}}{\text{rad}}$	6300 $\frac{\text{Nm}}{\text{rad}}$
Shaft damping	d_{sh}	0.5 $\frac{\text{Nms}}{\text{rad}}$	0.6 $\frac{\text{Nms}}{\text{rad}}$
TVD pitch inertia	J_{h}	1.4 kgm^2	1.0 kgm^2
Mounting stiffness	c_{h}	30000 $\frac{\text{Nm}}{\text{rad}}$	30000 $\frac{\text{Nm}}{\text{rad}}$
Mounting damping	d_{h}	100 $\frac{\text{Nm}}{\text{rad}}$	400 $\frac{\text{Nm}}{\text{rad}}$
Wheel inertia	J_{w}	0.349 kgm^2	1.18 kgm^2
Wheel radius	r_{w}	0.276 m	0.32 m
Relaxation length	$l_{\sigma,0}$	0.1 m	0.15 m
Relaxation length coefficient	k_{σ}	50	100
Vehicle mass	m_{veh}	850 kg	1750 kg
Yaw inertia at rear axle	J_{yaw}	1467 kgm^2	3450 kgm^2
Track width	b_{veh}	1.4 m	1.6 m

Table 3.2: Communication parameters for the two prototype vehicles

	Prototype vehicle	
Description	Visio.M	Prototype Two
Overall sampling rate	0.012 s	0.02 s
Delay of $\dot{\varphi}_{\text{l,w}}$, $\dot{\varphi}_{\text{r,w}}$, a_{veh} and $\dot{\varphi}_{\text{yaw}}$	0.036 s	-

3.2.1 Frequency Domain Validation

The measurement results are compared to a single simulation of the nonlinear model with the same input as in the experiments. Prior to the frequency analysis of the measurement using the FFT, the signals are preprocessed with a detrend function, removing offsets and linear trends. A Butterworth filter reduces aliasing effects and focuses the frequency analysis on the region of interest below 30 Hz. The frequency domain validation should answer the following key points:

- Does the model capture the peak location and shape of the main oscillation modes?
- Does the model capture the occurrence of the oscillation mode in the different signals accurately?

The frequency-domain validation starts with the in-phase motion in regular tip-in maneuvers because it is the main area of interest for standard drivetrains and has been widely studied. High- and low μ conditions are directly compared for both prototypes. Afterwards, the anti-phase response to a regular tip-in is investigated, since it poses a special effect for the TVD drivetrain.

In-phase response to tip-ins

For the in-phase motion, the Visio.M's behavior is evaluated in ten test runs for the high- and low μ condition each. The tip-in maneuvers start from stand still on high- and low μ. In case of high μ, u_{trc} steps from 0 Nm to 40 Nm, which is 50 % of the maximum torque. The tire remains well within its close-to-linear operation region with $s_{\text{x,0}}$ near 0.5 %. In case of low μ, u_{trc} steps from 0 Nm to 60 Nm to ensure the tires slip. Therefore, $s_{\text{x,0}}$ varies in a wide range. In order to account for small changes in surface conditions on low μ, white noise with 0 Nm mean and a standard deviation of 8 Nm is fed to the model via $\Delta T_{\text{l,tire}}$. This choice is arbitrary because the exact disturbance is unknown. The disturbance is added to test, whether the system responds with additional dynamics except the main in-phase oscillations, excited by the tip-in.

Since the tip-in maneuver is a step input to u_{trc}, it is natural to start with the response of $\dot{\varphi}_{\text{trc}}$, followed by $\dot{\varphi}_{\text{in,w}}$ and finally a_{veh}. In this order, the analysis follows the path of the traction torque.

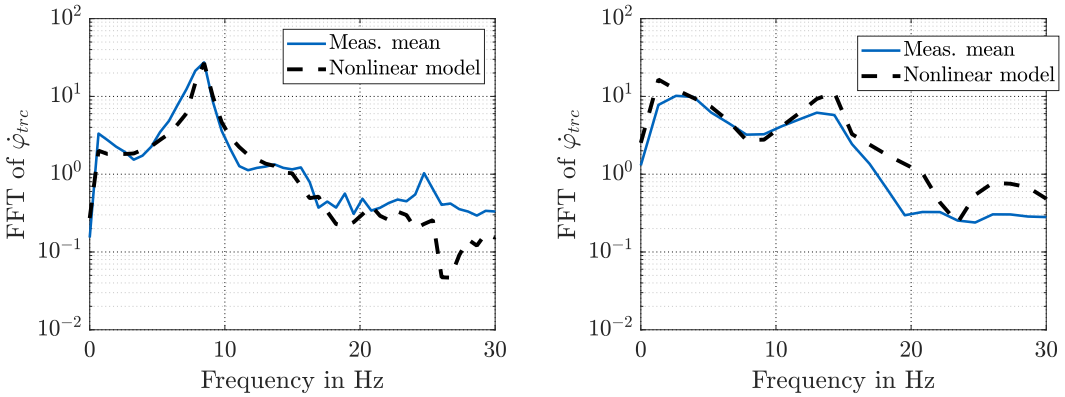

(a) High μ (b) Low μ

Figure 3.4: Comparison of frequency response of measurement and nonlinear model for $\dot{\varphi}_{\text{trc}}$ of the Visio.M in tip-in maneuvers with a step input to u_{trc}

The results of the frequency analysis for $\dot{\varphi}_{\text{trc}}$ are plotted in Fig. 3.4 and summarized in Tab. 3.3. On the left, in Fig. 3.4(a), the measurements on high μ show a dominant resonance peak at 8.4 Hz. The peak's standard deviations for frequency and magnitude in Tab. 3.3 are small, since

surface condition and slip ratio do not change significantly during the experiments. In these conditions, the nonlinear model matches the peak's frequency and amplitude closely.

On the right, in Fig. 3.4(b), the measurements for low μ do not demonstrate a single strong peak. They rather form a plateau below 15 Hz with two small peaks at 2.6 Hz and 14 Hz. However, due to the short measurement length, the resolution of the FFT is limited to 1.6 Hz intervals. Since the two peaks are rather flat compared to the high μ test case, the oscillations in the low μ measurements experience stronger damping. The peak at 2.6 Hz in the frequency analysis resembles an initial sine wave right after launch in the time domain. This wave vanishes quickly. The 14 Hz peak refers to an oscillation similar to the single high μ peak. On low μ, the tire operation point changes quickly, which changes to oscillation behavior of the drivetrain. Therefore, Tab. 3.3 contains a larger standard deviation for the frequency on low μ than on high μ. The model simulates the general behavior well. However, the model's peak location and especially its magnitude do not fit as accurately on low μ as on high μ.

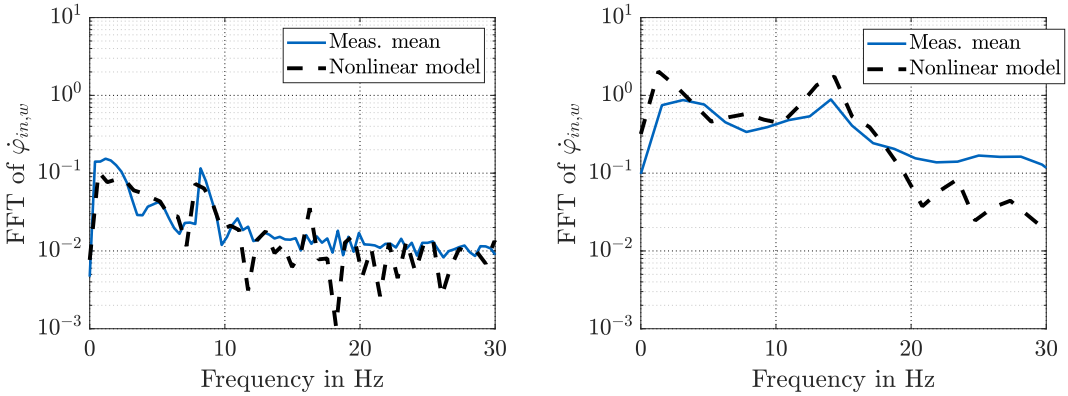

(a) High μ (b) Low μ

Figure 3.5: Comparison of frequency response of measurement and nonlinear model for $\dot{\varphi}_{\text{in,w}}$ of the Visio.M in tip-in maneuvers with a step input to u_{trc}

Fig. 3.5 and Tab. 3.3 represent the wheels response to the tip-ins. In contrast to $\dot{\varphi}_{\text{trc}}$, the response of $\dot{\varphi}_{\text{in,w}}$ in Fig. 3.5(a) shows only a small peak in the high μ surface experiments in Fig. 3.5(a). Its frequency is at 8.2 Hz without any deviation between the measurement. This means that the changes between experiments are less than the frequency analysis' resolution of 0.39 Hz. Differences in frequency between $\dot{\varphi}_{\text{trc}}$ and $\dot{\varphi}_{\text{in,w}}$ in Tab. 3.3 are the result of measurement inaccuracies. The high value of c_{sx} on high μ at small tire slip locks the wheels strongly to the

Table 3.3: Result summary for frequency analysis for in-phase motion of Visio.M

	Frequency				Magnitude		
$\dot{\varphi}_{\text{trc}}$	model	mean	std	res.	model	mean	std
High μ	8.5	8.4	0.21	0.65	27	27	3.1
Low μ	14	13	0.63	1.3	11	6.3	0.57
$\dot{\varphi}_{\text{in,w}}$	model	mean	std	res.	model	mean	std
High μ	7.8	8.2	0	0.39	0.073	0.12	0.02
Low μ	14	14	0	1.6	1.8	0.89	0.24
a_{veh}	model	mean	std	res.	model	mean	std
High μ	8.5	8.2	0	0.39	0.8	1.1	0.13
Low μ	-	-	-	-	-	-	-

ground, which suppresses oscillations.

However, on low μ the wheels can spin almost freely. Therefore, the curves for $\dot{\varphi}_{\text{in,w}}$ on low μ illustrated in Fig. 3.5(b) are similar to the ones for $\dot{\varphi}_{\text{trc}}$ in Fig. 3.4(b). This means that on low μ the wheels oscillate with the motor whereas on high μ the wheels barely participate in the motor's oscillation. The model follows the behavior of the measurements closely. Similar to $\dot{\varphi}_{\text{trc}}$ before, the model reenacts the high μ behavior more precisely than the low μ behavior.

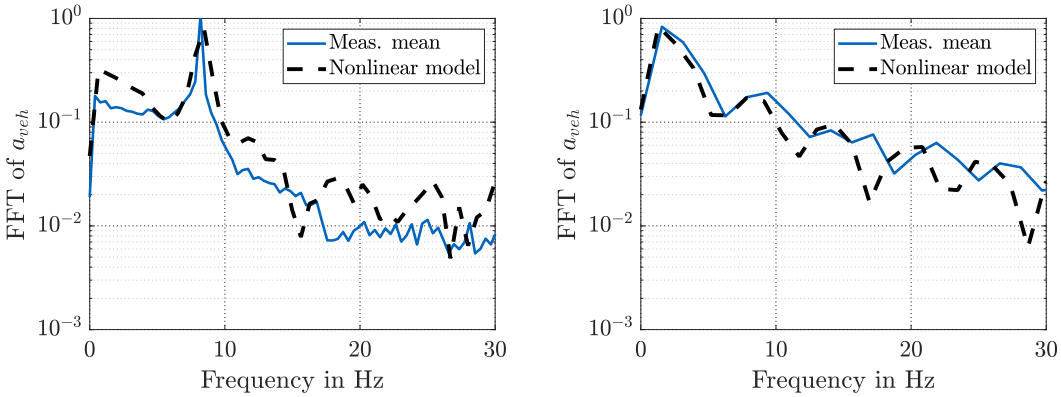

(a) High μ (b) Low μ

Figure 3.6: Comparison of frequency response of measurement and nonlinear model for a_{veh} of the Visio.M in tip-in maneuvers with a step input to u_{trc}

Finally, the sum of the longitudinal tire forces propel the vehicle. Therefore, oscillations in the tire force cause oscillations in the vehicle's acceleration. On high μ in Fig. 3.6, the longitudinal acceleration demonstrates a clear peak at 8.5 Hz. The behavior of a_{veh} strongly resembles the shape of $\dot{\varphi}_{\text{trc}}$ in Fig. 3.4. While the high value of c_{sx} limits oscillations of the wheel, it creates high amplitudes in the acceleration because of the strong torque transfer from the drivetrain to the vehicle. In contrast, on low μ no distinct peak is visible since the low values of c_{sx} detach drivetrain and vehicle. Both phenomena are captured by the nonlinear model. Since there are no peaks on low μ Tab. 3.3 only holds numbers for the high μ case.

Appendix B.1 contains the figures for Prototype Two. In essence, Prototype Two demonstrates the same behavior with a peak at 6.5 Hz on high μ. However, the oscillations are highly damped. Therefore, no significant oscillations occur on low μ as these conditions create additional damping compared to high μ. Further, Appendix B.2 holds the validation of the anti-phase motion for Prototype Two on high μ. Due to the large TV-motor inertia, the oscillation frequency is at 2.6 Hz lower and the anti-phase wheel contribution is larger than for the in-phase oscillation. Nevertheless, the data shows that in principle the TV-unit is subject to the same phenomena as the traction unit. Due to technical difficulties, such a measurement was not possible with the Visio.M.

Anti-phase response to tip-ins

The TVD is designed to separate the in-phase traction motion from the anti-phase TV motion. However, in the in-phase tip-in experiments of Appendix B.1 anti-phase oscillations occur on Prototype Two. In the twelve experiments, the anti-phase oscillations occurred at various speeds but changed depending on the tire slip level. This behavior is limited to Prototype Two and could not be replicated on the Visio.M. Since the TVD decouples in- and anti-phase motion, disturbances at the tire are the suspected cause for these oscillations. The following paragraphs

investigate this phenomenon further. In order to compare results, the disturbance on high and low μ is the same, white gausian noise with 0 Nm mean and 20 Nm standard deviation.

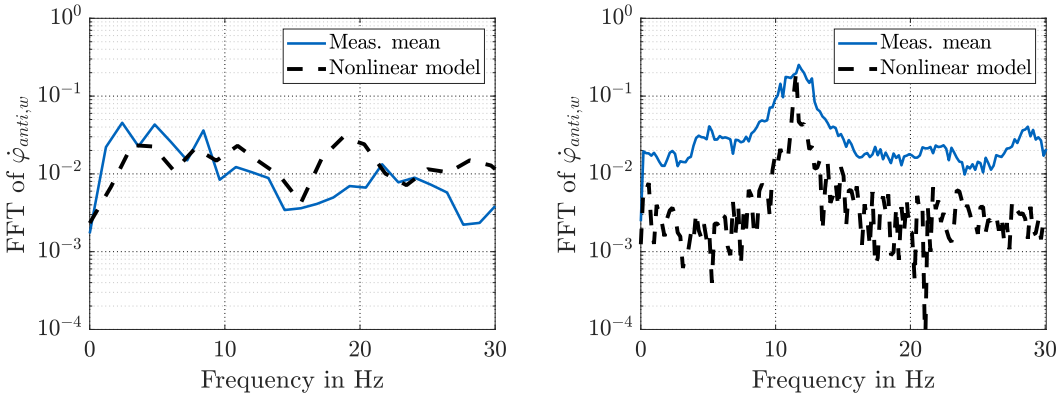

(a) High μ (b) Low μ

Figure 3.7: Comparison of frequency response of measurement and nonlinear model for $\dot{\varphi}_{\text{anti,w}}$ of Prototype Two in tip-in maneuvers with a step input to u_{trc} and white noise in $\Delta T_{\text{l,tire}}$

Figure 3.7 shows the response of $\dot{\varphi}_{\text{anti,w}}$ to $\Delta T_{\text{l,tire}}$ during u_{trc} tip-ins. On high μ in Fig. 3.7(a), no distinct peaks are visible. However, on low μ, a strong resonance peak occurs at 12 Hz. Since the oscillations are excited by disturbances and not a well defined step input, the magnitude varies from measurement to measurement. The standard deviation in Tab. 3.4 expresses the variation. The model meets the peak location precisely. Its peak shape is sharper than the measurement mean. In the measurements the tires slip is controlled by the driver and changing tire operation points widen the peak. In the open-loop simulation of the model, the tire operation point remains at high slip values.

Fig. 3.8 shows the results for $\dot{\varphi}_{\text{tv}}$. On high μ, the model has a small peak at 2.6 Hz, which is not present in the measurement. Since this peak is inconsistent it is not included in Tab. 3.4. On low μ, however, the 12 Hz peak is clearly captured in the measurements and the model. Nevertheless, the difference in magnitude between the high μ and low μ curves is small compared to the resonance peak of $\dot{\varphi}_{\text{anti,w}}$ before. With the gear ratio of 60 between TV motor and wheels accounted for, the mean magnitude of $\dot{\varphi}_{\text{anti,w}}$ would produce a mean peak of 22 in $\dot{\varphi}_{\text{tv}}$. However, the measurements show only a magnitude of 1.4. This means that the oscillations are not evenly distributed between motor and wheels but occur mainly at the wheels. The TV motor is barely affected.

Table 3.4: Result summary for frequency analysis of anti-phase motion of Prototype Two

	Frequency				Magnitude		
$\dot{\varphi}_{\text{anti,w}}$	model	mean	std	res.	model	mean	std
High μ	-	-	-	-	-	-	-
Low μ	12	12	0.6	0.20	0.21	0.37	0.16
$\dot{\varphi}_{\text{tv}}$	model	mean	std	res.	model	mean	std
High μ	-	-	-	-	-	-	-
Low μ	12	12	0.71	0.16	0.82	1.4	0.66

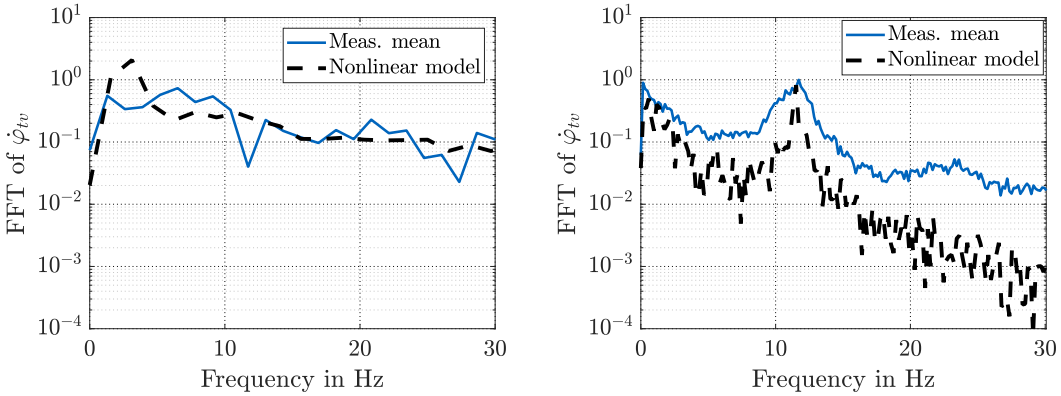

(a) High μ (b) Low μ

Figure 3.8: Comparison of frequency response of measurement and nonlinear model for $\dot{\varphi}_{\text{tv}}$ in tip-in maneuvers with a step input to u_{trc} and white noise in $\Delta T_{\text{l,tire}}$

Summary

Based on the results in section 3.2.1, the model captures the peak location and shape of the dominant low-frequency oscillations modes sufficiently. Further, the model resembles the changes in the oscillations' distribution throughout the drivetrain, which is important for the control design. On high μ, the motor speed signals record the dominant low-frequency mode best. The wheels are tightly connected to the vehicle speed by a high c_{sx}, especially at low speed. Due to the high value of c_{sx}, the torque oscillations in the drivetrain directly transfer to a_{veh}. Therefore, the driver can feel the oscillations strongly. On low μ, c_{sx} is low and the wheels are disconnected from the vehicle speed. Therefore, the drivetrain oscillations are distributed between wheels and motors. The oscillations do not transfer to a_{veh}. In addition, the anti-phase oscillations illustrate the shifting influence of u_{trc} and $\Delta T_{\text{l,tire}}$ depending on the tire operation point. On high μ, the excitation by the motors explains the measurements well. On low μ, especially with respect to the anti-phase oscillations, disturbances at the tire can cause strong oscillations.

Significant coupling from the traction to the TV system and vice versa was found neither in measurements nor in the models. The anti-phase effects during in-phase tip-ins are explained by the disturbance response on low μ. The absence of coupling is important since it proves that the two systems are separable. This is further demonstrated in Appendix A.2 based on the linear model.

3.2.2 Time Domain Validation

The frequency domain validation has proven that the nonlinear model resembles the general oscillation behavior of the drivetrain sufficiently. The goal of the time domain validation is the evaluation of signal delays and scarce nonlinear dynamics, such as the backlash, which are difficult to spot in the frequency domain. For a time domain validation with step inputs, it is important to choose test cases in which the disturbance has limited effect [50, p. 59]. The high μ surface experiments satisfy this assumption. However, on low μ disturbances at the tire have great effect and occur regularly during the experiments. Therefore, experiments for low μ are conducted with the vehicle on a lift. Since the vehicle is in the air, the lift eliminates any tire forces and disturbances. The time domain validation is limited to the Visio.M because the frequency domain validation has proven that the Visio.M responds to tip-ins with stronger in-phase oscillations than Prototype Two. Further, the Visio.M's measurement signals have

significant time delays, which makes the time-domain validation all the more important. The time domain validation should answer the following key points:

- Are delays correctly represented by the models?
- How big is the effect of nonlinear phenomena?
- How much do the models deviate from measurements over time?

Tip-ins on dry roads

The gray area encloses the minimum and maximum of the ten test runs previously used for the frequency domain validation. Thereby, the variation among measurements is illustrated. The measurements are compared to the nonlinear model and the discrete linear model. The nonlinear model contains the arctan backlash model and the nonlinear tire model. The discrete linear model shall demonstrate effects of the linearization. The stairs in the signals represent the sampling of both models.

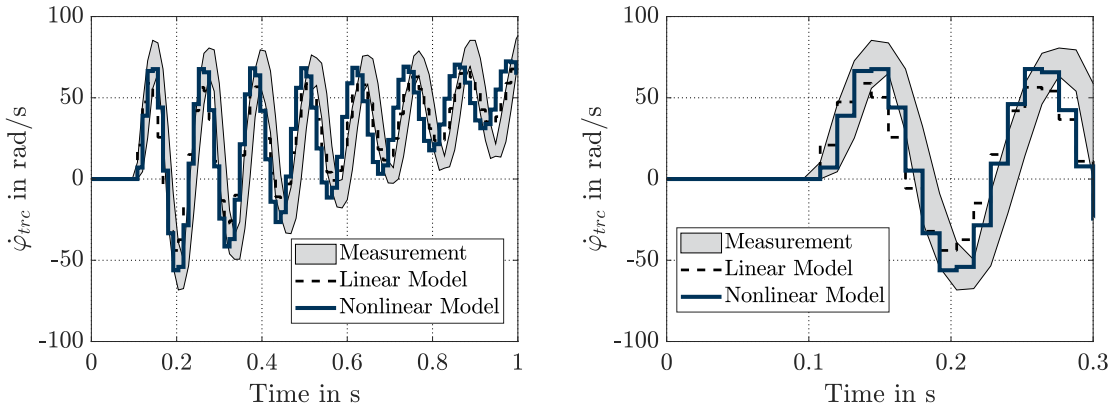

(a) Full one second validation window

(b) Initial 0.2 s after launch

Figure 3.9: Step response of Visio.M's motor speed for tip-in maneuver on dry roads

The area created by the measurements in Fig. 3.9 is narrow, which proves that random disturbances have a minor effect in this test case. The full one second horizon of Fig. 3.9(a) demonstrates that both models match the amplitude of the measurements closely. However, the models overestimate the system's damping and frequency slightly. This results in an increasing deviation over time. To scrutinize the models' fit further, Fig. 3.9(b) focuses on the launch. It contains the backlash transition, which occurs only once at the beginning. The discrete linear model underestimates the oscillation peak. The nonlinear model matches peak size and time better because it acknowledges the backlash. Overall both models fit the measurements well considering the respective simplifications.

Starting with a_{veh} in Fig. 3.10(b), the general behavior is similar to the $\dot{\varphi}_{\text{trc}}$ in Fig. 3.9. Both models predict the initial amplitude well. Because of the neglected backlash, the linear model underestimates the oscillation peaks slightly more than the nonlinear model. However, due to the mismatch in damping, the amplitudes differ from the measurements near the end, analogue to $\dot{\varphi}_{\text{trc}}$. The delays of ESP signals is set to 36 ms, which is a worst case estimation for a_{veh}, because it shifts the initial rise of both models to the right of the measurement area. In contrast to the $\dot{\varphi}_{\text{trc}}$, $\dot{\varphi}_{\text{in,w}}$ in Fig. 3.10(a) matches better at the end of the horizon than at the launch. In addition to the 36 ms delay, the wheel speed signals are not available below 0.7 rad/s. Further,

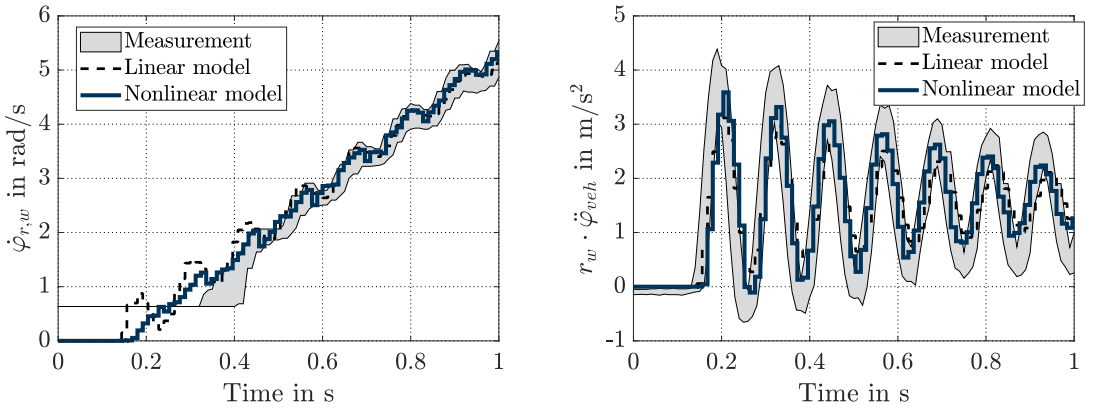

(a) $\dot{\varphi}_{r,w}$ (b) a_{veh}

Figure 3.10: Step response of Visio.M's wheel speed and vehicle acceleration for tip-in maneuvers on dry roads

at low speed, the resolution is poor because only 42 teeth per revolution are available. Therefore, the measurement at one second is more reliable than in the beginning. Regarding the linear model, the wheel speed oscillates strongest right after launch. However, the nonlinear model predicts only a small ripple. After 0.4 s both models reflect the measurement in oscillation magnitude. The shape of the oscillation is matched closer by the nonlinear model.

Tip-ins on a lift

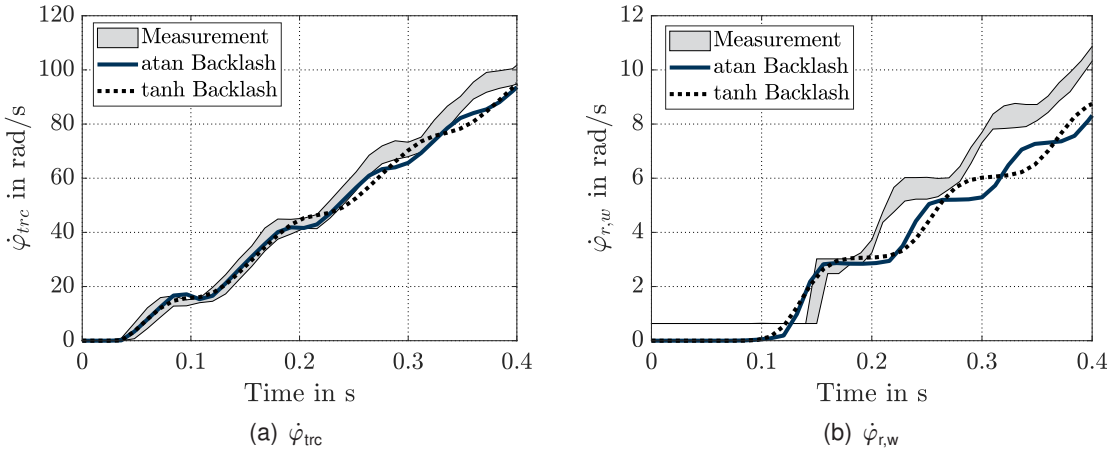

(a) $\dot{\varphi}_{trc}$ (b) $\dot{\varphi}_{r,w}$

Figure 3.11: Step response of Visio.M for tip-in maneuver on the lift

Since the vehicle is on the lift, a torque step of 5 Nm is sufficient to accelerate the drivetrain quickly. The three conducted measurements are compared to two nonlinear models, one for the arctan and one for the tanh backlash representation. In order to highlight the backlash effect in both models, the raw signals from the continuous ODE solver are plotted here. The linear discrete model is omitted, since the backlash effects the system dynamics strongly in this test case. This is visible in the measurements of Fig. 3.11. The motor in Fig. 3.11(a) shows longer increases in speed separated by short plateau-like segments. This behavior is even stronger in the wheel speed with clearly defined plateaus in Fig. 3.11(b). In both signals the phenomenon is strongest at the beginning of the measurement and fades out over time. The reason for the

behavior is that the motor spins up freely inside the backlash until it reaches the contact side. Once the shaft is in contact again, the shaft transfers energy from the motor to the wheels. Since the motor torque is low in this experiment, the shaft torque is sufficient to throw the motor back into the backlash gap. The process repeats. Initially, the speed difference between motor and wheel is largest. Over time, both speeds converge.

Both models capture the general behavior of the backlash. Overall, the real system accelerates faster than the models predict. Due to the low motor torque, a misrepresentation of friction in the models leads to a significant deviation from the measurements. The difference between the arctan and the tanh backlash models also arises because of the low traction torque. Since the Visio.M's backlash is not distributed but rather concentrated at the wheel shafts, there is no load on the motor inside the backlash gap. However, the tanh representation always assumes at least a small shaft torque, even inside the gap. This is illustrated in Fig. 3.2. Further, for small twist angles, the stiffness of the shaft is smaller c_{sh} because of the gradual transition of the tanh model. This leads to a smaller oscillation frequency with three peaks for the tanh model and four peaks in the measurement of $\dot{\varphi}_{\mathrm{trc}}$. The arctan model does decouple motor and wheels inside the gap and transitions to c_{sh} in contact quicker than the tanh model. Therefore, it shows four peaks, similar to the measurement. However, the oscillation periods are shorter than displayed by the measurement. Even though both models deviate from the measurements, fitting them closer to the measurements is not straight forward. The unknown initial backlash position makes replicating the measurements exactly difficult. This leads to deviations from one measurement to the next, which creates the wider gray area near the plateaus of $\dot{\varphi}_{\mathrm{r,w}}$. Overall, both backlash models reenact the general dynamics. However, the arctan model requires less tuning parameters. The validation proves that it is difficult to predict the drivetrains' behavior in these low torque conditions. Therefore, it is advisable to avoid these regions in the every day operation of the vehicle.

Summary

Beyond the results in the frequency domain, the time domain validation of section 3.2.2 has proven that the discrete linear model as well as the nonlinear models capture the key dynamics of the drivetrain sufficiently. The nonlinear effect of the tire is most visible on high μ right at the launch. The discrepancy between discrete linear and nonlinear model illustrates this. Unfortunately, the ESP signals are least reliable or even unavailable in this region. The backlash is also strongest near the launch. Because of the low torque in the drivetrain, neglected effects cause deviations between models and measurements. Therefore, neither the arctan and nor the tanh backlash model can predict the traverse through the backlash precisely in open loop.

3.3 Discussion

The overall objective of this chapter was the design of models which resemble the drivetrains' dominant low-frequency oscillation modes. The validation proves that the nonlinear model resembles the oscillation behavior adequately for this task. However, the models' validity is limited. The models are constructed to represent the first dominant eigenmode. Especially the tire model is responsible for this limitation. It is not a physical model but rather an empirical one. The choice of the relaxation length model and Pacejka Magic Formula aims to reproduce the first dominant tire mode and the nonlinear slip characteristic. Therefore, the presented models

cannot explain more than one tire mode. This is especially important when the parameters are varied and eigenmodes move in the complex plain. Due to this movement, an eigenmode might move out of the model's area of validity. This study focuses on the first dominant oscillation mode. For more detailed studies, at least a rigid ring tire model is necessary. Regarding the backlash, the tanh model presented by Pham et al. [80] and the newly presented arctan model are similar in their accuracy. The arctan model is used further, because it is more easily parametrized when the backlash angle is known. An important conclusion from the lift experiments is that the models are less reliable when only little torque is applied to the drivetrain. Therefore, any strategy for backlash compensation should try to leave this region quickly. Nevertheless, little torque input is required to pass the backlash smoothly [97, p. 1646].

Further, the validation method has several shortcomings in itself. Experiments were conducted at low vehicle speed only. However, vehicle speed has great effect on the oscillation behavior. The reduction of d_{tire}, caused by higher vehicle speeds, is assumed to be similar to the effects on low μ. The comparison between the results of section 3.2.1 and the general results in [27, p. 8 ff.] and [51, p. 739] affirm this assumption. Also, the importance of $\Delta T_{\text{l,tire}}$ on low μ calls for investigations with a known disturbance input, similar to the cleats used by Tuononen [120]. This could show the impact of a sole disturbance excitation. In addition, increased sampling rate and wheel speed sensors with a higher resolution would improve the quality of the measurements. This would create a better resolution of the frequency analysis. It would also allow a better investigation of the nonlinear effects of backlash and tire. In addition, the different sensors and test conditions of the two vehicles create challenges in comparing their results.

3.4 Conclusion

The goal of this chapter was to provide mathematical models for robust linear control design and nonlinear backlash compensation. In this regard, the effects of backlash and tire dynamics were considered in a nonlinear model. Based on this nonlinear model, a linear model was derived for the modal analysis and robust design of a damping controller in the following chapters. Parameter variation accounts for simplifications caused by the linearization of the tire dynamics. The frequency domain validation in section 3.2.1 proves that the nonlinear model resembles the oscillation behavior adequately. The time domain validation shows that the discrete model also incorporates the characteristics of the CAN communication correctly. The measurements with the two prototype vehicles and their TVD drivetrains are a major contribution of this dissertation. Especially the different disturbance responses of the TV-units is a novel finding. The models and their validation, presented in this chapter, compose an important foundation for the robust control design in chapter 5. Further, the validated linear model provides guidance in chapter 4 on the design of drivetrains suitable for driving dynamics control at the tire's performance peak. Finally, the nonlinear model enables the backlash compensation discussed in chapter 6.

4 Model Analysis

The model validation of the previous chapter demonstrates that the Visio.M and Prototype Two show similar behavior in some test cases (tire slip stiffness $c_{sx} \to \infty$, in-phase excitation) but also different behavior in other test cases (tire slip stiffness $c_{sx} = 0$, disturbance excitation). These differences take shape in the oscillations' frequency and damping as well as the changing contribution of various components in the drivetrain. In order to understand the similarities and differences, an appropriate analysis method must provide information on these three characteristics, namely frequency, damping and contribution. Therefore, this chapter aims to answer research question 1 ("Which dynamics of TVD drivetrains are common to vehicle drivetrains in general and which are unique to TVDs?") and provides guidelines on electric vehicle drivetrain design. On the one hand, extensive model reduction yields analytic solutions to the low-frequency oscillation problem. On the other hand, modal analysis provides the required oscillation characteristics for continuous linear models independent of their size. These two approaches are discussed in section 4.1. They are applied to the low-frequency oscillation problem in section 4.2. Results are presented, summarized and discussed. In section 4.3, research question 1 is answered and guidelines for the physical system and the control design are derived.

4.1 Methodology

The validation of section 3.2.1 points out that there are two boundary conditions, $c_{sx} \to \infty$ and $c_{sx} = 0$, for the oscillation phenomena. Rosenberger et al. [87, p. 6 f.] as well as Yeap and Mueller [27, p. 13 ff.] already investigated these two boundary cases with simplified models. Such a model reduction is possible for the TVD drivetrain, when in-phase and anti-phase motion are considered separately. The necessary equations are presented in section 4.1.1. Due to the simplifications, it is possible to analyze the oscillation phenomenon analytically with few parameters. Therefore, the method is available early in the design process and points out possible drawbacks of a specific design. Section 4.1.2 focuses on the transition in between the boundary cases. Parameter variation and modal analysis yield insight to the effects of changing operation points. In order to track certain oscillation modes through the parameter space, a mapping method is required.

4.1.1 High and Low Grip Conditions as Two-Inertia-Oscillators

The goal of this section is the representation of the TVD drivetrain's oscillation phenomenon in the most simple equations with the least parameters possible. The fundamental model, used by most publications summarized in section 2.1.2, is a two-inertia oscillator. Once the drivetrain is reduced to this general oscillation model, the two-inertia oscillation modes can be investigated by splitting the model into two single-inertia oscillators. In this form, simple relations yield the

results for oscillation frequency, damping and contribution.

Starting with the complex TVD drivetrain, it separates into two unbranched strands, one for the in-phase motion and one for the anti-phase motion. These strands are comparable to other drivetrain topologies, as mentioned in the literature review of section 2.1.1. Each strand is simplified to the most important components. These components are the shaft, the actuator and the load. The actuator includes the motor and the gear stage, expressed by J_1 in Eq. 4.1 for the traction and the TV case. The load changes depending on the driving condition. In case of $c_{\mathrm{sx}} = 0$, the load inertia $J_{2,0}$ includes only the two driven wheels, given by Eq. 4.2. In case of $c_{\mathrm{sx}} \to \infty$, $J_{2,\infty}$ also contains the vehicle mass for the traction drivetrain and the vehicle yaw inertia for the TV drivetrain.

$$J_1 = \begin{cases} i_{\mathrm{trc}}^2 \, J_{\mathrm{trc}} & \text{Traction unit} \\ i_{\mathrm{tv}}^2 \, J_{\mathrm{tv}} & \text{TV unit} \end{cases} \tag{4.1}$$

$$J_{2,0} = 2 \, J_{\mathrm{w}} \tag{4.2}$$

$$J_{2,\infty} = \begin{cases} 2J_{\mathrm{w}} + m_{\mathrm{veh}} \, r_{\mathrm{w}}^2 & \text{Traction unit} \\ 2J_{\mathrm{w}} + \frac{2 \, r_{\mathrm{w}}}{b_{\mathrm{veh}}} \, J_{\mathrm{yaw}} & \text{TV} \end{cases} \tag{4.3}$$

The motion of J_1 is connected to the motor of the corresponding unit by Eq. 4.4. Analogue, Eq. 4.5 converts the input torque. The impulse in Eq. 4.6 combines actuator acceleration, input torque and the shaft torque T_{12}.

$$\dot{\varphi}_1 = \begin{cases} \frac{\dot{\varphi}_{\mathrm{trc}}}{i_{\mathrm{trc}}} & \text{Traction unit} \\ \frac{\dot{\varphi}_{\mathrm{tv}}}{i_{\mathrm{tv}}} & \text{TV unit} \end{cases} \tag{4.4}$$

$$T_1 = \begin{cases} i_{\mathrm{trc}} \, T_{\mathrm{trc}} & \text{Traction unit} \\ i_{\mathrm{tv}} \, T_{\mathrm{tv}} & \text{TV unit} \end{cases} \tag{4.5}$$

$$J_1 \, \ddot{\varphi}_1 = T_1 - T_{12} \tag{4.6}$$

Similar to the actuator, Eq. 4.7 defines the motion of the load and Eq. 4.8 the impulse. Instead of T_1, the disturbance acts on the load. For the analysis in this chapter, the disturbance is represented by a torque at the left tire $\Delta T_{\mathrm{l,tire}}$.

$$\dot{\varphi}_2 = \begin{cases} \dot{\varphi}_{\mathrm{in,w}} & \text{Traction unit} \\ \dot{\varphi}_{\mathrm{anti,w}} & \text{TV unit} \end{cases} \tag{4.7}$$

$$J_2 \, \ddot{\varphi}_2 = T_{12} - \Delta T_{\mathrm{l,tire}} \tag{4.8}$$

In an unbranched strand model, the two shafts merge into one shaft with twice the stiffness c_{12} and damping d_{12}, represented by Eq. 4.9 and Eq. 4.10. The twist speed $\dot{\varphi}_{12}$ in Eq. 4.11 is the relative speed between J_1 and J_2. Integration yields the corresponding angle. The torque of this virtual shaft is labeled T_{12} and given by Eq. 4.12.

$$c_{12} = 2 \, c_{\mathrm{s}} \tag{4.9}$$

$$d_{12} = 2 \, d_{\mathrm{s}} \tag{4.10}$$

$$\dot{\varphi}_{12} = \dot{\varphi}_1 - \dot{\varphi}_2 \tag{4.11}$$

$$T_{12} = c_{12} \, \varphi_{12} + d_{12} \, \dot{\varphi}_{12} \tag{4.12}$$

The next step in the model reduction is the split of the two-inertia system into two single-inertia

system. To create a simple image for the separation, Fig. 4.1 illustrates the two-inertia oscillator as an oscillating system in longitudinal direction. The actuator mass m_1 moves in x_1 direction, corresponding to J_1 and φ_1, the load mass m_2 in x_2 direction, corresponding to J_2 and φ_2. The oscillation of the system is excited by an initial displacement of the spring. No external forces act on the system. Therefore, the center of mass has to stay in place. This is represented by the separation plane between the two masses. The longitudinal motion of Fig. 4.1 and the concept of the center of mass are only an instrument to envision the separation of the two-inertia system. However, they must not be confused with the actual rotational dynamics of the system.

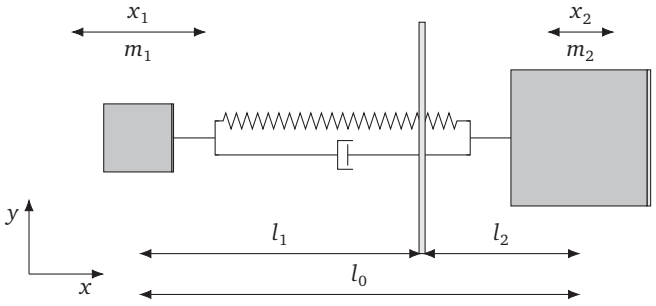

Figure 4.1: Longitudinal Two-Mass Oscillator

In the relaxed state, the initial length l_0 in Eq. 4.13 is the sum of the distances from m_1 and m_2 to the separation plane, l_1 and l_2 respectively. Using the torque equilibrium about the z-axis in Eq. 4.14 at m_2, l_1 and l_2 are expressed by l_0, m_1 and m_2 in Eq. 4.16 and Eq. 4.15.

$$l_0 = l_1 + l_2 \tag{4.13}$$

$$0 = l_0\ g\ m_1 - l_2\ g\ (m_1 + m_2) \tag{4.14}$$

$$l_2 = \frac{m_1}{m_1 + m_2}\ l_0 \tag{4.15}$$

$$l_1 = \frac{m_2}{m_1 + m_2}\ l_0 \tag{4.16}$$

Because the center of mass remains at rest, the oscillation amplitude of the two masses has to be related to their mass in such a way that a displacement of m_1 by x_1 balances a displacement of m_2 by x_2. The torque equilibrium about the z-axis in the center of mass yields Eq. 4.17. Based on the equilibrium assumption, the relation between x_1 and x_2 is given by Eq. 4.20, whereas Eq. 4.21 expresses the relative contribution of x_1 to the complete motion between m_1 and m_2. This relative contribution equals the relative mass and is given by the ratio κ_1.

$$m_1\ g\ (l_1 - x_1) = m_2\ g\ (l_2 + x_2) \tag{4.17}$$

$$m_1\ l_1 - m_1\ x_1 = m_2\ l_2 + m_2\ x_2 \tag{4.18}$$

$$\frac{m_1\ m_2}{m_1 + m_2}\ l_0 - m_1\ x_1 = m_2\ x_2 + \frac{m_2\ m_1}{m_1 + m_2}\ l_0 \tag{4.19}$$

$$x_2 = -\frac{m_1}{m_2} x_1 \tag{4.20}$$

$$\frac{x_1}{x_1 - x_2} = \frac{x_1}{x_1 + \frac{m_1}{m_2} x_1} = \frac{m_2}{m_2 + m_1} = \kappa_1 \tag{4.21}$$

Returning to the original two-inertia system, the link through the spring connects the rotational impulse of both J_1 and J_2 in Eq. 4.22. This connection is based on the assumption that there are no external inputs to the system. Therefore, T_1 and d are neglected. This link yields the same result for the rotational acceleration in Eq. 4.23 as for the longitudinal displacement in

Eq. 4.20. Integration of both sides returns the necessary results for rotational speed and position. Therefore, analogue to Eq. 4.21 of the longitudinal example, κ_1 also represents the relative contribution for the rotational example, summarized by Eq. 4.26.

$$J_1\ \ddot{\varphi}_1 = c\,(\varphi_1 - \varphi_2) = -J_2\ \ddot{\varphi}_2 \tag{4.22}$$

$$\ddot{\varphi}_2 = -\frac{J_1}{J_2}\ddot{\varphi}_1 \tag{4.23}$$

$$\dot{\varphi}_2 = -\frac{J_1}{J_2}\dot{\varphi}_1 \tag{4.24}$$

$$\varphi_2 = -\frac{J_1}{J_2}\varphi_1 \tag{4.25}$$

$$\kappa_1 = \frac{\varphi_1}{\varphi_1 - \varphi_2} = \frac{J_2}{J_2 + J_1} \tag{4.26}$$

$$\kappa_2 = \frac{\varphi_2}{\varphi_1 - \varphi_2} = \frac{J_1}{J_2 + J_1} = 1 - \kappa_1 \tag{4.27}$$

Based on the relation between φ_1 and φ_2, the spring stiffness c_{12} is separated into c_1 and c_2, corresponding to J_1 and J_2. The resulting systems must satisfy the following two conditions. On the one hand, both separated systems must store the same amount of potential energy as the original system. On the other hand, both spring forces must offset at the connection point. In the longitudinal analogy, the offsetting forces ensure that the separation plane remains at rest. Based on this condition, Appendix A.3 contains the derivation of the spring stiffnesses c_1 and c_2. The results are summarized by Eq. 4.28 and Eq. 4.29.

$$c_1 = \frac{c_{12}}{\kappa_1} \tag{4.28}$$

$$c_2 = \frac{c_{12}}{\kappa_2} \tag{4.29}$$

The converted spring stiffness c_1 allows the approximation of the eigenfrequency of the single-inertia system with Eq. 4.30. Further, the combination of inertia and stiffness yield the dimensionless damping ratio ζ_1, given in Eq. 4.31 [170, p. 1191]. An aperiodically damped system requires a damping ratio of one [157, p. 232]. In order to achieve this condition, the optimal damping coefficient $d_{1,\text{opt}}$ must satisfy Eq. 4.32. Analogue to the separated spring, the addition of $d_{1,\text{opt}}$ to system one must be matched by a damper $d_{2,\text{opt}}$ in system two.

$$\omega_1 = \sqrt{\frac{c_1}{J_1}} \tag{4.30}$$

$$\zeta_1 = \frac{d_1}{2\sqrt{c_1\ J_1}} \tag{4.31}$$

$$d_{1,\text{opt}} = 2\sqrt{c_1\ J_1} \tag{4.32}$$

In summary, the two-inertia model allows the estimation of the oscillation frequency, distribution and the required damping for the boundary conditions of $c_{\text{sx}} \to \infty$ and $c_{\text{sx}} = 0$.

4.1.2 Modal Analysis

Section 4.1.1 focused on the boundary cases of $c_{\text{sx}} \to \infty$ and $c_{\text{sx}} = 0$. However, the transition between the two extreme cases is just as important for understanding the dynamics and for

control design. Therefore, this section presents methods to investigate the intermediate cases between the two boundaries. First, modal analysis links frequency, damping and contribution to the modal properties of the continuous linear system. Subsequently, the variation of tire operation parameters mimics the transition between the two boundary cases.

The modal properties describe the oscillation behavior of the system. These properties are primarily eigenvalues, which contain damping and frequency information, and eigenvectors, which reflect the mode shape. The mode shape determines the spatial distribution of an eigenmode, meaning the contribution of each state to the mode. The eigenvalue decomposition produces the modal properties based on the structural properties, such as stiffness, inertia and damping [171, p. 3 f.]. The dynamic matrix A_s from Eq. 3.45 contains these structural properties. It is transformed to the diagonal matrix Λ holding the eigenvalues $\lambda_1, \lambda_2, ..., \lambda_n$. The eigenvectors $\boldsymbol{v}_1, \boldsymbol{v}_2, ..., \boldsymbol{v}_n$ form the transformation between the original and the diagonal form. Matrix V resembles this transformation basis [171, p. 112].

$$\Lambda = V^{-1} A_\mathrm{c}\, V \tag{4.33}$$

$$V = \begin{bmatrix} \boldsymbol{v}_1, & \boldsymbol{v}_2, & ..., & \boldsymbol{v}_n \end{bmatrix} \tag{4.34}$$

$$\Lambda = \mathrm{diag}(\lambda_1, \lambda_2, ..., \lambda_n) \tag{4.35}$$

The eigenvalue λ_i of the i-th eigenmode defines the natural frequency $\omega_{\mathrm{nat},i}$ with Eq. 4.36. The real part of λ_i defines the damping ratio $\zeta_{\mathrm{nat},i}$ with Eq. 4.37 [157, p. 232], [171, p. 114].

$$\omega_{\mathrm{nat},i} = |\lambda_i| \tag{4.36}$$

$$\zeta_{\mathrm{nat},i} = \frac{|\Re(\lambda_i)|}{\omega_{\mathrm{nat},i}} \tag{4.37}$$

The individual elements of the eigenvector $\boldsymbol{v}_i$ define the relative contribution of the corresponding state-variable to the i-th eigenmode [171, p. 113 f.]. However, in contrast to κ_1 and κ_2, the elements of the eigenvectors are not normalized to sum up to one. Instead, the eigenvectors are commonly scaled to be of unit length with respect to the euclidean norm, the H_2-norm. Nevertheless, this is a matter of scaling and does not affect the relative relation between the elements [171, p. 88]. In case A_s is real, all complex eigenmodes appear in complex conjugate pairs of eigenvalues and eigenvectors. If λ_i has a positive imaginary part, there must be a conjugate complex λ_j with a matching negative imaginary part. The same holds for the eigenvectors $\boldsymbol{v}_i$ and $\boldsymbol{v}_j$ corresponding to λ_i and λ_j [168, p. 43].

Since the modal analysis provides the modal properties for a single system, the following paragraphs discuss the extension to multiple systems. First, the parameter variation is discussed. Afterwards, the mapping algorithm is presented. The parameters $s_{\mathrm{x},0}$, $\dot{\varphi}_{\mathrm{w},0}$ and μ are continuous variables. Hence, the parameter space between the two boundary cases contains an infinite amount of possible parameter values. The transition from one boundary to the other is approximated by an evenly spaced finite number of samples. The parameter variation is conducted one variable at a time. For example, when $s_{\mathrm{x},0}$ changes then $\dot{\varphi}_{\mathrm{w},0}$ and μ are fixed. This way, the different effects are separated and clearly traceable. Further, only $s_{\mathrm{x},0}$ and $\dot{\varphi}_{\mathrm{w},0}$ are varied because these variations correspond to the tip-in experiments in which slip and speed change due to the torque step. The lower bound of $s_{\mathrm{x},0}$ and $\dot{\varphi}_{\mathrm{w},0}$ is zero since this produces the largest value for c_{sx}. The upper bound of $s_{\mathrm{x},0}$ is the point at which $c_{\mathrm{sx}} = 0$ Nm. The upper bound of $\dot{\varphi}_{\mathrm{w},0}$ is not clearly defined because d_{tire} approaches its minimum only for $\dot{\varphi}_{\mathrm{w},0} \to \infty$. Therefore, $\dot{\varphi}_{\mathrm{w},0}$ is limited to reasonable operation speeds of the vehicles.

Since each parameter sample creates a new linear model with a new dynamic matrix A_c, each sample creates a new set of modal properties, which are calculated by the "eig" function in Matlab. However, there is no guarantee that the i-th eigenmode of the new model corresponds to the i-th eigenmode of the previous model [172]. Therefore, tracking individual oscillation modes through the transition requires a mapping algorithm for the eigenmodes. In general, different eigenmodes may possess identical eigenvalues. However, even in such a case, the eigenvectors are unique because in structural dynamic problems, such as the drivetrain, the eigenvectors are always linear independent [171, p. 89]. For example, in the drivetrain, in-phase and anti-phase dynamics are already dominated by the same wheel shaft and tire properties. If the in-phase and anti-phase actuators also have an identical inertia, oscillation frequency and damping might be identical, which results in identical eigenvalues. However, the eigenvectors differ. The in-phase eigenmodes oscillate in the same direction on the left and right vehicle side, which results in eigenvector elements of the same sign for these state-variables. The anti-phase eigenmodes oscillate in opposite direction resulting in an opposite sign. Therefore, the eigenvectors V of the current sample k are mapped to the eigenvectors W of the previous sample $k-1$. In case two eigenvectors in W are equally close to an eigenvector $\boldsymbol{v}_i$, the eigenvalues are compared to find the correct mapping. Algorithm 1 summarizes the procedure.

for *k = 1; k <= max. sample; k++* **do**
  generate A_s, Λ and V for the parameter values of the k-th sample;
  if *k == 1* **then**
    initialize $W = V$ and $\Gamma = \Lambda$ for the first sample;
  else
    initialize $searchSet = [1, ..., n]$;
    for *i = 1; i <= n; i++* **do**
      find all $j \in searchSet$ which maximize $\left|\boldsymbol{v}_i \cdot \boldsymbol{w}_j\right|$;
      if *there is more than one* j **then**
        find j which minimizes $\left|\lambda_i - \gamma_j\right|$;
      end
      save the mapping $i \rightarrow j$;
      pop j from $searchSet$;
    end
    map V, Λ to W, Γ for the next iteration;
  end
end

Algorithm 1: Mapping algorithm for eigenmodes

At the start of Algorithm 1, the state space model for the parameter set of the current sample k is created and its modal properties are calculated from its A_s matrix. The first sample defines the order of the modes. All following samples are mapped to the previous sample. Therefore, if the mapping fails, increasing the number of samples helps the algorithm, since the step size decreases. The mapping of the eigenvectors is based on the inner product. The inner product measures the similarity of two vectors in a scalar number. Since the eig-function normalized the eigenvectors by default [172], the maximum value is one, which means that the two vectors are identical [173, p. 168 ff.]. However, eigenvectors are independent of scaling [174, p. 106] but the inner product is not [173, p. 164 ff.]. An eigenvector $\boldsymbol{w}_j$ pointing in the opposite direction of $\boldsymbol{v}_i$, which is equivalent to a scaling by -1, must result in a mapping of $j \rightarrow i$. Therefore, the absolute value of the inner product is used [173, p. 164 ff.]. But, due to the parameter variation, two eigenvectors of the sample k might produce the same inner product with $\boldsymbol{v}_i$ of sample $k-1$. In case the eigenvectors do not produce a distinct mapping, the distance between the eigenvalues

distinguishes the remaining candidates [175, p. 192]. After the mapping, the index j is removed from the search set to avoid duplicate mappings. Finally, V and Λ of sample k are reordered with the generated mapping and form the basis W and Γ for the next sample $k+1$.

4.2 Results

The results for the two-inertia model are presented first. They focus on the quantification of the changes in inertia. Subsequently, the modal analysis is discussed with the focus on the transition between $c_{sx} \to \infty$ and $c_{sx} = 0$ Nm and the contribution of the mounting.

4.2.1 Boundary Cases

The reduced inertias and relative contribution of actuator and load are given in Tab. 4.1. Comparing the top line for J_1 demonstrates the big differences between the two vehicles and their TVDs. In the Visio.M, the traction unit's inertia is over six times higher than the TV-unit's. The situation is the opposite in Prototype Two. The traction unit is over twelve times smaller than the TV-unit's inertia. The big difference between the two vehicles is caused by the great difference in their TV-motor inertias due to their different designs. This difference is further amplified due to the large gear ratios in both TV-units.

First, the relative contribution to the oscillation is analyzed. Tab. 4.1 demonstrates the effect of the inertia distribution. In case of $c_{sx} \to \infty$, the load inertia is so large that the main oscillation occurs at the motor for all four configurations. The heavy TV-unit in Prototype Two shows the smallest value with a 95 % relative magnitude in the motor.

However, for $c_{sx} = 0$, without the overwhelming load inertia, the values of κ_1 vary in a wide range. The light weight TV-unit in the Visio.M oscillates mainly on the actuator side even though the load was greatly reduced. The traction systems in Visio.M and Prototype Two distribute the oscillations between motor and wheel, shifting a significant contribution to the wheels. Finally, the TV-unit in Prototype Two flips the result from $c_{sx} \to \infty$ to $c_{sx} = 0$ with the oscillations occurring

Table 4.1: Results of two-inertia model for infinite and zero tire slip stiffness

Vehicle	Visio.M		Prototype Two	
Subsystem	Traction	TV	Traction	TV
c_{12} in Nm/rad	4200	4200	12600	12600
J_1 in kgm^2	1.3	0.2	3.2	38.5
$J_{2,0}$ in kgm^2	0.7	0.7	2.6	2.6
$J_{2,\infty}$ in kgm^2	65.4	309.4	180.3	679.8
κ_1 for $c_{sx} \to \infty$	0.98	0.9992	0.98	0.95
κ_1 for $c_{sx} = 0$	0.36	0.76	0.45	0.06
ω_1 in Hz for $c_{sx} \to \infty$	9.2	22	10	3.0
ω_1 in Hz for $c_{sx} = 0$	15	25	15	12
ω_1 in Hz from meas. on high μ	8.2	-	7.8	2.6
ω_1 in Hz from meas. on low μ	14	-	-	12
$d_{1,opt}$ in Nms/rad for $c_{sx} \to \infty$	141	58	401	1431
$d_{1,opt}$ in Nms/rad for $c_{sx} = 0$	234	66	594	5577
$d_{2,opt}$ in Nms/rad for $c_{sx} \to \infty$	7567	85565	23047	25292
$d_{2,opt}$ in Nms/rad for $c_{sx} = 0$	135	221	484	371

nearly fully at the wheels.

The changes in κ_1 are an important information for sensing and damping the drivetrains oscillation. The best sensors are at the actuator and the actuator supplies the damping torque requested by the controller. Therefore, high values of κ_1 are beneficial. Goetting [21, p. 100 f.] in particular justifies the feedback of only the motor's oscillation by the high values of κ_1. Overall, κ_1 reflects the measurement results of section 3.2.1 proving that the two-inertia model captures the key effects in the boundary cases. The trend in the boundary cases matches the findings [170, p. 1196 ff.], which shows that ω_1 increases when κ_2 increases.

Next, the quality of the two-inertia model is evaluated with the estimated eigenfrequency of the system. Table 4.1 contains the results for all cases. A comparison is made for the Visio.M's traction-unit and Prototype Two's TV-unit with the measurements of section 3.2 and Appendix B, because the measurements are of the best quality for these two. For the Visio.M, ω_1 for $c_{sx} \to \infty$ is 9.2 Hz. The frequency response measurement showed a peak at 8.2 Hz. This deviation is reasonable since the two-inertia model neglects tire and housing elasticity, which moves the eigenfrequency to lower values. For the TV-unit of Prototype Two, the estimate of ω_1 is 3 Hz. Again, the estimate is above the measured frequency of 2.6 Hz. In case of $c_{sx} = 0$, the single-inertia system meets the measurement results even better. The estimate for the traction unit of the Visio.M is 15 Hz with the measured value at 14 Hz. In case of Prototype Two, estimate and measurement match exactly at 12 Hz. Therefore, the two-inertia model is a sufficient approximation of the oscillation in the two boundary cases.

Table 4.1 holds the aperiodic damping coefficients. In case of $c_{sx} \to \infty$, all systems display small values in $d_{1,opt}$ compared to their $d_{2,opt}$ counterparts. Since the oscillations show high magnitudes at J_1, proven by the high values of κ_1, a small damping coefficient is sufficient to generate the required damping torque. On the wheel side, with the small amplitudes, only a large value of $d_{2,opt}$ can match $d_{1,opt}$. With $c_{sx} \to \infty$, the tire provides at least in part the required strong damping. In case of $c_{sx} = 0$, the ratio between $d_{1,opt}$ and $d_{2,opt}$ varies strongly, depending on the system. In general, the values of $d_{1,opt}$ increase while $d_{2,opt}$ declines by a large margin compared to the high-grip case. In all cases, the Visio.M's TV-unit needs the smallest values of $d_{1,opt}$ to achieve aperiodic damping of the oscillations and Prototype Two's TV-unit needs the largest values of $d_{1,opt}$. This is natural, since the Visio.M's TV-unit has the smallest overall inertia and Prototype Two's TV-unit has the largest. Since the damping power is the product of the damping torque and the oscillation speed, a small oscillation magnitude requires high damping torques to achieve the same power. However, high damping torques are a problem for the control since high gains are necessary and the actuators can only provide limited magnitudes of torque. In addition, the low values of $d_{2,opt}$ for $c_{sx} = 0$ show that oscillations occurring at the peak of the tire slip-torque curve can be damped by moving the operation point in a region with $c_{sx} > 0$. Thereby, the tire contributes to the damping again. With the small required values of $d_{2,opt}$, a small change in operation point should be sufficient. The measurement results back this suggestion because the strong anti-phase oscillations in Prototype Two only occur at low values of μ in combination with high slip values.

Summary and Discussion

Already the two-inertia model predicts the shift in frequency and distribution of the oscillations. It is an appropriate tool to evaluate early design drafts. However, the analysis with the two-inertia model requires strong simplifications. The modal analysis demonstrates that the mounting may have a significant contribution. Such effects are completely neglected by the reduced two-inertia

model. Further, the ideal damping coefficients $d_{1,\text{opt}}$ and $d_{2,\text{opt}}$ depend on the stiffness and the inertias of the system. Therefore, it is difficult to compare different systems. Since the overall inertia changes between $c_{\text{sx}} \to \infty$ and $c_{\text{sx}} = 0$, even a comparison of the same system on different surfaces is difficult. It is important to acknowledge these changes in any conclusions.

4.2.2 Modal Analysis

The modal analysis focuses on the motor speed, housing twist speed and wheel speed. These state-variables are the main contributors to the low-frequency oscillation modes, proven by [88]. First, the Visio.M's in-phase motion is investigated. Therefore, only in-phase modes are selected for the analysis. The top-left complex plane is displayed in Fig. 4.2 for different operation points on low μ. The main region of interest is near the imaginary axis below 20 Hz. This region contains poorly damped oscillations between 0 Hz and 15 Hz, which were observed in measurements. In order to assess the movement of modes in and out of this region, the plots display also values outside 20 Hz. However, when modes move outside the 20 Hz region the model, and subsequently the analysis, starts to loose its validity.

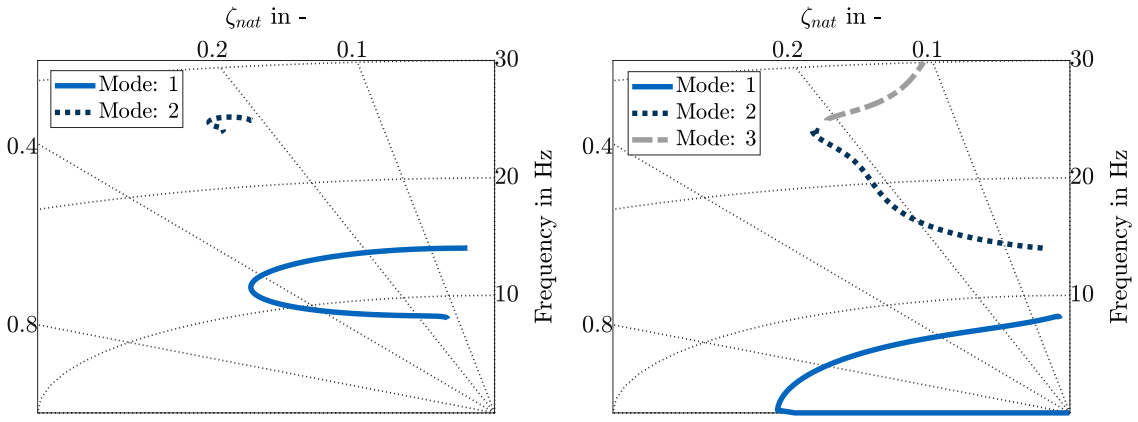

(a) $\dot{\varphi}_{\text{w,0}} = 30$ rad/s (b) $\dot{\varphi}_{\text{w,0}} = 3$ rad/s

Figure 4.2: Eigenvalues for the in-phase motion of the Visio.M at different slip values with $\mu = 0.4$ at two different operation speeds

On the left in Fig. 4.2(a), the two modes both move in a half circle. Mode 2 remains on the top left with high frequency and damping. Therefore, mode 2 is not relevant for the main oscillation phenomenon in this operation region. The two ends of mode 1 are located at an imaginary part of 8 Hz and at 14 Hz. The ends correspond to an 8 Hz and a 14 Hz oscillation, which are the eigenfrequencies of the traction system with $c_{\text{sx}} \to \infty$ and $c_{\text{sx}} = 0$. On the right in Fig. 4.2(b), however, three modes are visible in the excerpt of the complex plane. Mode 1 shows a half circle but, in contrast to $\dot{\varphi}_{\text{w,0}} = 30$ rad/s, one end is placed at the origin. Mode 2 moves along a line between the top left and a location near 14 Hz. The third mode stays outside the main region of interest. The comparison of both Fig. 4.2(a) and Fig. 4.2(b) demonstrates that the tire operation points cause drastic and different changes to the oscillation behavior.

The plots in Fig. 4.2 do not show the direction of the eigenmodes' motion and which states contribute. The plots in Fig. 4.3 address these questions. First, Fig. 4.3(a) demonstrates the contribution to the oscillation by the main components. This contribution changes along with the operation point. At the top, mode 1 starts out as a motor oscillation with minor contributions by housing and wheel. However, the contribution shifts quickly to a mixed wheel-motor oscillation.

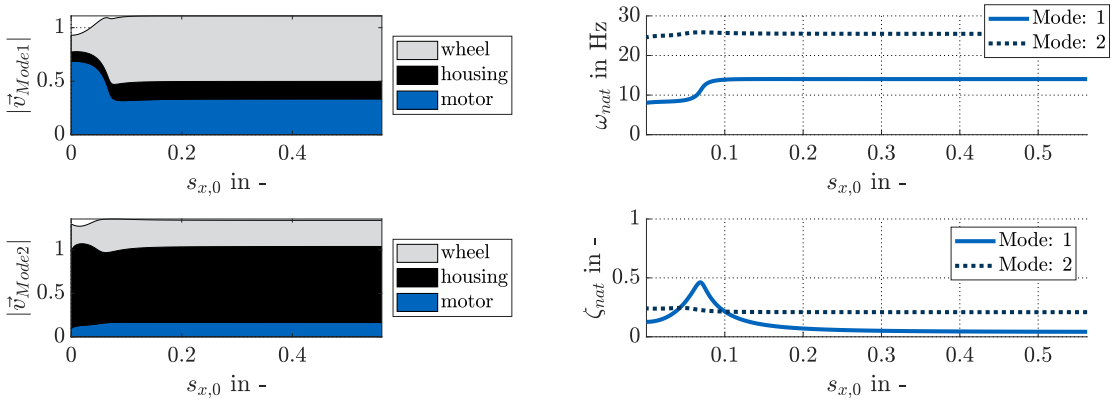

(a) Contribution of wheel, housing and motor to the oscillation modes.

(b) Eigenfrequency and damping ratio of the oscillation modes

Figure 4.3: Oscillation modes in the in-phase motion of the Visio.M at different slip values at $\mu = 0.4$ and $\dot{\varphi}_{w,0} = 30$ rad/s

This configuration remains nearly constant for $s_{s,x} > 0.1$. At the bottom, mode 2 shows minor changes in contribution. The mode is mainly a housing-mode for all operation points. Second, Fig. 4.3(b) displays the changes in frequency ω_{nat} and damping ratio ζ_{nat}. Analogue to the contribution, mode 1 shows the biggest changes for $s_{s,x} < 0.1$. This means that most of the half circle in the complex plane of Fig. 4.2(a) is passed quickly. Mode 2 experiences only minor changes since it remains confined to a small area of the complex plane.

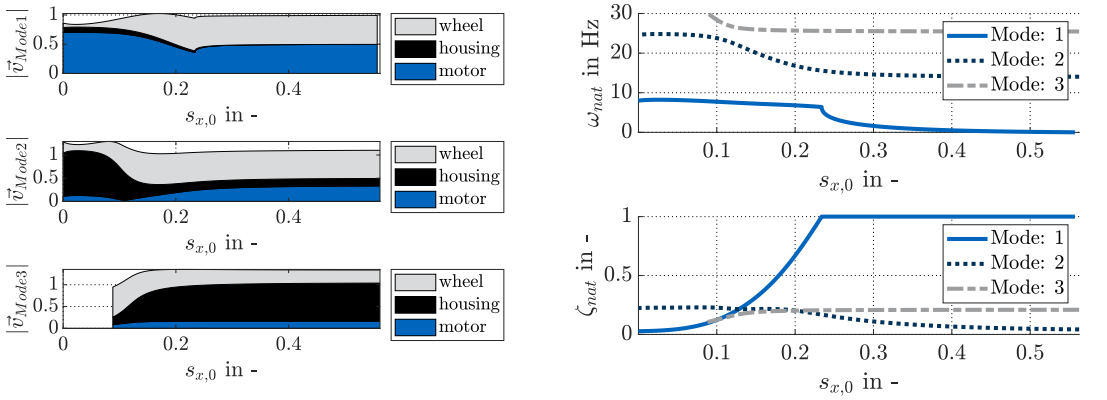

(a) Contribution of wheel, housing and motor to the oscillation modes.

(b) Eigenfrequency and damping ratio of the oscillation modes

Figure 4.4: Oscillation modes in the in-phase motion of the Visio.M at different slip values at $\mu = 0.4$ and $\dot{\varphi}_{w,0} = 3$ rad/s

In Fig. 4.4 for $\dot{\varphi}_{w,0} = 3$ rad/s, both, mode 1 and mode 2, enter the main region of interest. Similar to $\dot{\varphi}_{w,0} = 30$ rad/s, they both start out as a motor-mode (mode 1) and a housing-mode (mode 2), demonstrated by Fig. 4.4(a). With increasing $s_{x,0}$, mode 1 gradually incorporates an increasing amount of wheel motion. So does mode 2 in the region of $0.05 < s_{x,0} < 0.15$. At the end, mode 2 is rather a wheel mode than a housing-mode. For further increasing tire slip, the motor contribution in mode 2 rises slightly. Nevertheless, mode 2 remains mainly a wheel mode for $s_{x,0} > 0.15$. As the housing contribution falls in mode 2 it rises in mode 3. Mode 3 enters the 30 Hz region at $s_{x,0} \approx 0.09$ mainly as a wheel mode. However, at $s_{x,0} \approx 0.2$ it is the main housing-mode replacing mode 2. The importance of this shift is demonstrated in

Fig. 4.4(b). Mode 3 remains at high frequencies and is therefore not significant. The damping of mode 1 increases steadily until the oscillation is annihilated with $\zeta_{\text{nat}} = 1$. Mode 2 is well damped initially but ζ_{nat} decreases for $s_{\text{x,0}} > 0.2$. This proves that mode 1 moves out of the main interest region near the imaginary axis in Fig. 4.2(b) while mode 2 moves into it. For a short window in Fig. 4.4(b), mode 1 and mode 2 are inside the 20 Hz region simultaneously prior to the annihilation of mode 1. This means that in contrast to $\dot{\varphi}_{\text{w,0}} = 30$ rad/s, two low-frequency oscillation modes exist for $\dot{\varphi}_{\text{w,0}} = 3$ rad/s. However, in this narrow slip window, both modes are well damped. Nevertheless, this behavior in part explains the plateau, which is visible in the measurements of the Visio.M on low μ in section 3.2.1. In both cases, $\dot{\varphi}_{\text{w,0}} = 30$ rad/s and $\dot{\varphi}_{\text{w,0}} = 3$ rad/s, the dominant oscillation mode at high values of $s_{\text{x,0}}$ includes at least in part the housing. Therefore, it should not be neglected. Further, there is a slip region in both cases for which the overall damping of oscillations below 15 Hz is maximized. This means that for high slip conditions reducing slip with a TRC system could reduce oscillations.

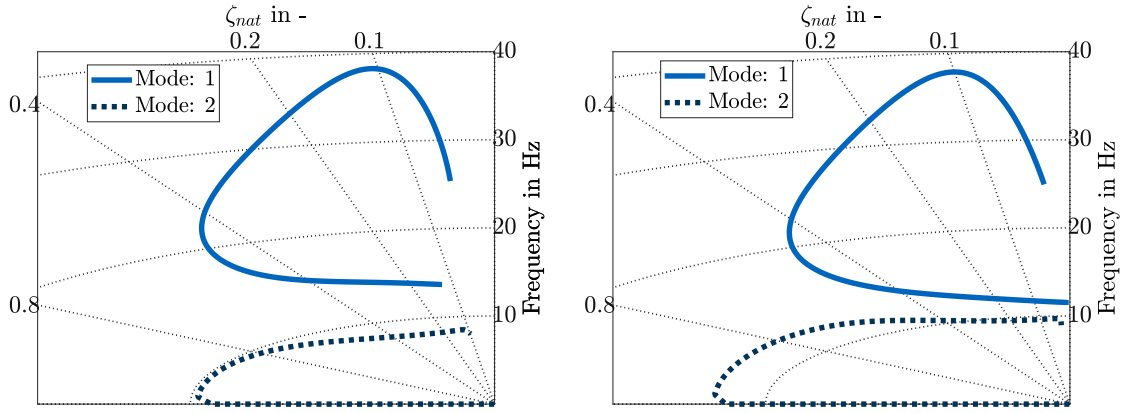

(a) Standard mounting (b) Rigid mounting

Figure 4.5: Eigenvalues in the complex plane for the in-phase motion of Prototype Two at different slip values with $\mu = 0.4$ at $\dot{\varphi}_{\text{w,0}} = 6$ rad/s

Prototype Two emphasizes the importance of the drivetrain's mounting further. The measurement data on low μ shows that the in-phase motion is well damped while the anti-phase motion experiences strong oscillations. A major difference between in- and anti-phase motion is the coupling between the housing pitch motion and the in-phase motion of the drivetrain. Therefore, the in-phase motion of Prototype Two is analyzed with two different mounting configurations. The modal analysis in Fig. 4.5 demonstrates the difference between the regular mounting on the left and a rigid mounting with a stiffness of $c_{\text{h}} = 10^9$ Nm/rad on the right. To the top, Fig. 4.5(a) and Fig. 4.5(b) show two modes. Comparing their paths, especially the end points, indicates that the modes with a rigid mounting experience less damping since they reach closer to the imaginary axis.

Damping and eigenfrequencies in Fig. 4.6(a) and Fig. 4.6(b) prove that the modes move in a counter-clockwise direction in the complex plane. Further, mode 2 is the dominant low-frequency mode up to $s_{\text{x,0}} \approx 0.13$. At this point mode 2 is fully damped and mode 1 enters the region of $\omega_{\text{nat}} < 20$ Hz. The damping ratio, at the bottom of Fig. 4.6(a) and Fig. 4.6(b), proves that with a rigid mounting the dominant oscillation mode at low and at high slip values experiences less damping. The contributions in Fig. 4.7(a) illustrate that the dominant mode contains a significant housing contribution at all slip values. However, the modes in Fig. 4.7(b) for the rigid mounting show no housing contribution. This means that the housing contributes to the damping of the in-phase oscillations of Prototype two. These results oppose the finding by Goetting [21, p. 77 f.].

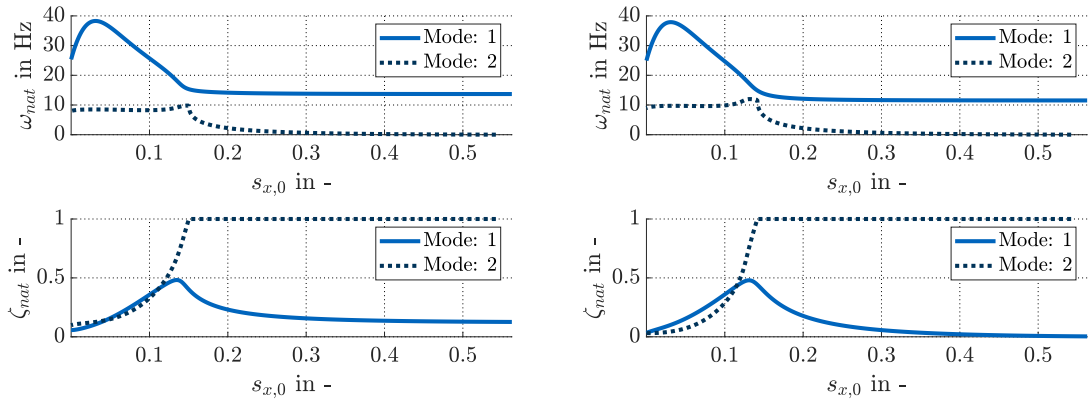

(a) Standard mounting (b) Rigid mounting

Figure 4.6: Eigenfrequency and damping ratio for the in-phase motion of Prototype Two at different slip values with $\mu = 0.4$ at $\dot{\varphi}_{w,0} = 6$ rad/s

However, the mounting model of Prototype Two has a significantly larger damping coefficient, which creates an overly damped mounting system ($\zeta > 1$). The behavior of Prototype Two is an important finding because it shows that soft bushing with sufficient damping can improve comfort and oscillation damping. In contrast, the parameter configuration of the Visio.M and Goetting [21] create a conflict in the design guideline. In these vehicles, soft bushings improve comfort but harm the oscillation behavior.

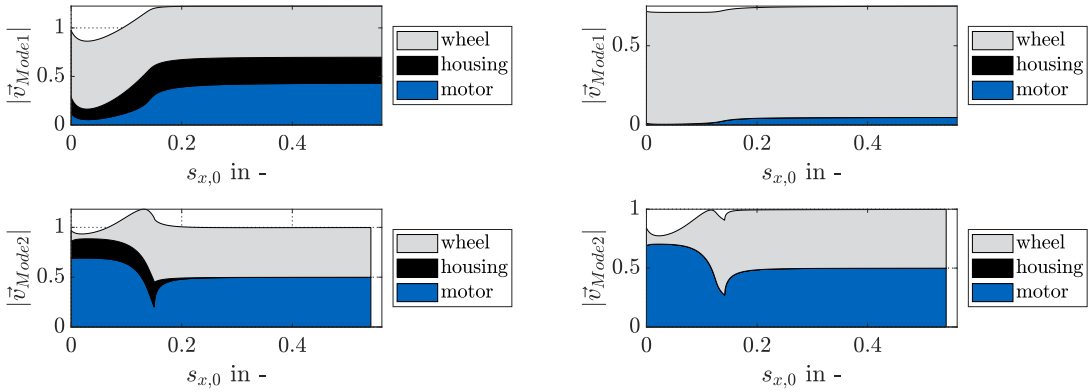

(a) Standard mounting (b) Rigid mounting

Figure 4.7: Contribution of motor, housing and wheel for the in-phase motion of Prototype Two at different slip values with $\mu = 0.4$ at $\dot{\varphi}_{w,0} = 6$ rad/s

Next, the continuous effects of $\dot{\varphi}_{w,0}$ are examined with the anti-phase motion of Prototype Two on high μ. The anti-phase motion does not connect to the housing pitch motion and tire modes are above 15 Hz and do not enter the region of interest. Therefore, only one mode accounts for the anti-phase dynamics in Prototype Two. Figure 4.8 contains the area charts for the contribution as well as the frequency and damping plots for two different slip values. At the top right, Fig. 4.8(b) shows the path which the mode takes for increasing speed. The frequency remains nearly constant around 2.9 Hz but the damping increases steadily until the oscillations are fully damped at 65 rad/s. In the following zone of $\zeta_{nat} = 1$, the frequency rises sharply until the damping starts to decrease again. The re-appearance of the oscillation happens at 85 rad/s. The oscillation frequency moves from initially 16 Hz down to 12 Hz and ζ_{nat} keeps

declining. In the measurement of section 3.2, the TV-unit experienced a 2.6 Hz oscillation on high μ and low speeds and a 12 hz oscillation on low μ and high tire slip. The results of the modal analysis demonstrate the same oscillations. Since an increase in $\dot{\varphi}_{w,0}$ reduces the tire's linearized damping coefficient analogue to a reduction of c_{sx} by increased $s_{x,0}$ or μ, the effect on the eigenmodes is similar. Further, the results show that for a certain speed interval the low-frequency anti-phase oscillations are fully damped. The contribution in Fig. 4.8(a) shows that the transition from the motor-mode at low speed to the tire-mode at high speed occurs gradually up to the point of full damping at 65 rad/s. Inside the zone of $\zeta_{nat} = 1$, the motor contribution declines rapidly. At the re-appearance, mode 1 is fully a tire mode.

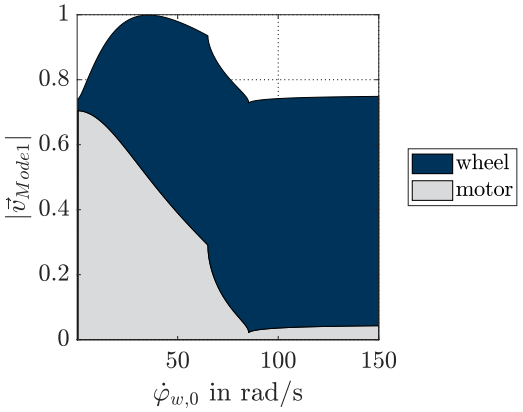

(a) Contribution of wheel and motor to the oscillation modes at $s_{x,0} = 0.01$

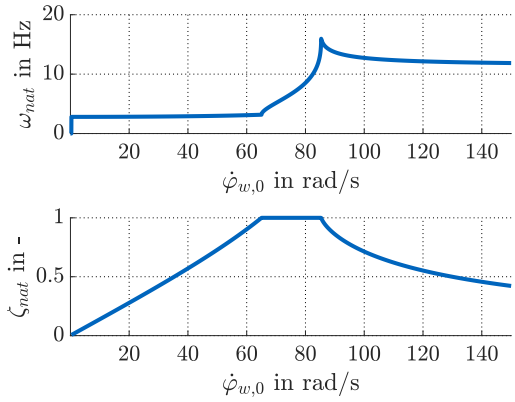

(b) Eigenfrequency and damping ratio of the oscillation modes at $s_{x,0} = 0.01$

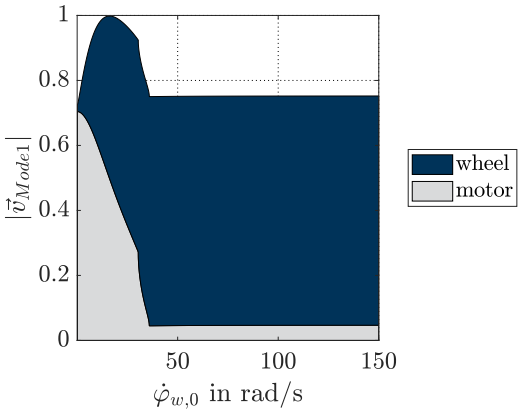

(c) Contribution of wheel and motor to the oscillation modes at $s_{x,0} = 0.1$

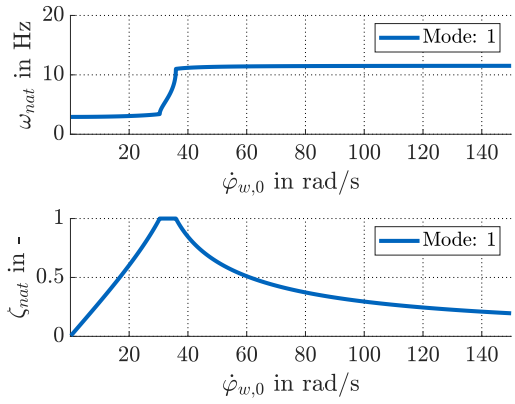

(d) Eigenfrequency and damping ratio of the oscillation modes at $s_{x,0} = 0.1$

Figure 4.8: Oscillation modes in the anti-phase motion of Prototype Two at different operation speeds on high μ ($\mu = 1$)

At the bottom in Fig. 4.8(c) and Fig. 4.8(d), $s_{x,0}$ is set to 10 %. This increase results in a shift of the phenomenon to lower speeds. In general, the shift of the curves is similar to the 1 % slip case. However, the fully damped zone is shorter and located between 30 rad/s and 36 rad/s. The oscillation frequency before and after the zone experiences only minor changes. So does the contribution of actuator and wheel. In this regard, Fig. 4.8(c) is simply a compressed version of Fig. 4.8(a). These findings are important since the oscillations prior to the zone of $\zeta_{nat} = 1$ are damped more easily by the actuator than the oscillations to the right of the zone. In addition, low speed poses the worst case scenario to the left of $\zeta_{nat} = 1$ while the oscillations to the right are less damped at high speed. Further, to the left of the zone, higher slip values add damping while

to the right of the zone higher slip reduces damping.

Summary and Discussion

A more detailed investigation of the boundary cases as well as the transition between the two is available with modal analysis. In case of changes in s_x, the transition occurs quickly and in the area of the steepest decline of c_{sx}, which is illustrated in Fig. 3.3. In case of changes in $\dot{\varphi}_{w,0}$, the transition is slower but also depends on the value of s_x. The tempo of the transition influences the choice of control approaches. Gain scheduling may be feasible for $\dot{\varphi}_{w,0}$ but seems inappropriate for s_x. This underlines that a robust control design is the more promising approach, as already proposed by Yeap and Mueller [27, p. 14]. Further, the modal analysis shows that, depending on the current speed, a single eigenmode or two different eigenmodes explain the shifting frequency and contribution. The changes of a single eigenmode have been widely studied for in-phase dynamics with respect to frequency, damping ratio and eigenvalue-location [27, 51]. Since the housing generates the second relevant eigenmode, it is not included in the detailed study of Yeap and Mueller [27]. The most important contribution of the modal analysis is the damping effect of the rubber bushings in the mounting. Since the pitch motion of the mounting is overdamped in Prototype Two it significantly dissipates oscillation energy. Therefore, it is one reason for the highly damped in-phase oscillation of Prototype Two on low and on high μ.

The modal analysis of internal dynamics is based on two assumptions. First, the model's input-to-output behavior was validated, not the internal dynamics themselves. Therefore, it has to be assumed that an input-output validation contains sufficient information about the validity of the internal model dynamics. Even though placing sensors for example on the mounting or the suspension is possible, a validation is difficult. The mounting contribution is in general small and rises only in rare operation points. Second, tire models are empiric and do not explain the physics behind tire dynamics. Therefore, any interpretation of the system's dynamics with respect to the tire operation point has to acknowledge this shortcoming of the model. The true tire dynamics, especially on low μ are far more complex than the linear model can replicate [110]. Therefore, the model is valid only for the low-frequency oscillations, which essentially limits the validity to the first dominant eigenfrequency. However, the modal analysis shows the shifts of different eigenmodes. Some of these modes pass through frequency regions in which the model is not valid anymore. This is proven by the in-phase oscillation analysis of Prototype Two. This shows that for any analysis, which focuses on more than the main low-frequency mode, a more complex model is required. However, this is not the goal of this study and the validation of such a model requires additional measurements.

4.3 Conclusion

Overall, this chapter answers research question 1. In general, the dynamics of a TVD drivetrain are common to regular vehicle drivetrains because the TVD drivetrains include two separate drivetrains, a traction unit and a TV-unit. The traction unit is common to all vehicles considered in chapter 2. The analysis of the traction unit in a TVD drivetrain does not show any significant difference to previously reported results in this regard, e.g. Rosenberger et al. [87, p. 6 f.], Yeap and Mueller [27, p. 13 ff.] and Goetting [21, p. 77 f.]. The TV-unit acts similar to the traction unit and regular drivetrains in most parts. However, if a high TV inertia is added to the drivetrain, dynamics appear which are unique to TVDs because a normal differential does not have a large

anti-phase inertia. This has to be acknowledged in the TVD's design and the control. High actuator inertias result in wheel oscillations when the slip-stiffness of the tire is low. These oscillations are difficult to control. When the tire's slip stiffness is high this special phenomenon does not appear. One reason for the strong oscillation in the TV-unit is that it does not interact with the pitch-motion of the housing, which can contribute to the damping of in-phase oscillations. The findings regarding the disturbance response of the TV-unit are one of the main contributions of this thesis.

In general, a low actuator inertia is desirable since this increases the actuator's contribution to the oscillation. Hence, oscillations are measured and damped directly at the actuator. However, convenient oscillation behavior may not be the only design goal for an electric drive. Therefore, two different design goals are examined, if they align with favorable oscillation behavior. In case of industrial drives, a fast responding load with maximum acceleration is achieved with a gear ratio that creates an even distribution of the inertias ($J_1 = J_2$) [176, p. 40 ff.]. For the TVD, slippery conditions require the fastest response because ABS, ESP and TRC try to operate the drivetrain in its optimal operation point with maximum grip. Therefore, traction and TV-unit should meet $J_1 \leq J_{2,0}$. In case of vehicle drivetrains, a low energy consumption for propelling the vehicle is a key design goal. The traction units inertia adds to the overall vehicle mass, increasing energy consumption during acceleration. Therefore, the smaller J_1 the better [177, p. 228 f.], [178, p. 18, p. 21]. Among the TVDs of this study, the traction unit of Prototype Two is closest to meeting these guidelines. However, its TV-unit is also furthest away from satisfying the guidelines.

5 Active Damping by Feedback Control

At the end of section 1.1 the overall objective of this study was stated as follows: In order to give EVs an edge over ICEVs in driving dynamics, the performance of the wheel torque control is essential. Based on this general formulation and the results of chapter 3 and chapter 4, more specific requirements are derived for the control design in the following paragraphs.

First of all, the torques transmitted to the wheels are the shaft torques, $T_{\mathrm{l,s}}$ and $T_{\mathrm{r,s}}$. Both are the superposition of the traction and the TV-units' virtual shaft torques T_{12}. This superposition and the absence of significant coupling allows the design of two separate controllers, one for the traction unit and one for the TV-unit. This separation reduces the complexity of the design. Both controllers must ensure predefined performance requirements. Because the terminology must apply to traction and TV-unit, the labeling of the two-inertia model is best suited. Its definition in section 4.1.1 already accounts for the two units. Therefore, the two-inertia model provides variables which relate to traction and TV-unit, such as $\dot{\varphi}_1$, $\dot{\varphi}_2$ or T_{12}. Further, it provides simple expressions for the key dynamics in the systems. Therefore, it is an ideal foundation to derive damping controllers for the drivetrain.

In the terminology of control theory, key performance requirements are reference tracking and disturbance rejection. For both, the control error is the measure in focus. Ideally, the steady-state control error is zero, which means that T_{12} matches the reference torque once the system reaches a steady-state [45, p. 48]. If friction on the actuator side is negligible, the drivetrain naturally satisfies this goal. This is proven by the actuator's impulse in Eq. 4.6, which remains steady only if the shaft torque matches the input torque. This fact will be discussed in more detail in section 5.1.2. Nevertheless, it is important for the definition of design goals, since it proves that the controller can focus on transient dynamics. The oscillations in the drivetrain are the main transient concern. Beyond the oscillations, the wheel torque control must possess a sufficient bandwidth. The bandwidth implies that the wheel torque reaches a desired value in a certain period of time. Previous results show that the transient dynamics change strongly with the tires' operation point, defined by μ, $s_{\mathrm{x,0}}$ and $\dot{\varphi}_{\mathrm{w,0}}$ (as well as other factors effecting the tire's slip stiffness, which are not considered in this study). This variation in the model's parameters creates a whole set of models. The performance requirements apply to all models in this set. Therefore, the controller must demonstrate robust performance, which means that its performance holds for all models in the set [139, p. 57], [44, p. 53].

To achieve this, the motor and wheel speed signals are available to the controller. Among the standard sensor signals, these carry the main information about the oscillations. Signals, such as a_{veh}, might be considered in advanced controllers but provide less information than the speed sensors. Further constraints to the control design are actuator limits since the motors cannot provide an infinite amount of torque. In addition, the discrete nature of the controller must be acknowledged, since the implementation relies on digital computers [141, p. 26]. Also, the control loop must be internally stable and ensure robust stability of the control loop. However, the controller is not responsible to ensure the drivetrains or the vehicles stable and safe

operation. The damping controller is part of a cascaded control structure and other controllers are responsible for these tasks.

In order to create a controller, which performs well in the different driving conditions, it should rely only on model parameters which are well known and are not subject to changes during driving. Further, the controllers implementation should be straightforward and computationally inexpensive. It should contain few and well defined tuning parameters for engineers to adjust in the field [155]. The student thesis of Berthold [179], Bennett [180], Himpsl [181], Hoffmann [182] and Schwarz [183] contain investigations on Kalman filter, neuronal networks, LQR, LTR and MPC. However, these rather complex approaches could not produce satisfactory robustness and their computational load was too high.

In this context, the chapter aims to answer research question 2 (Can simple controllers satisfy performance and robustness goals in a variety of tire operation points?), by applying simple control structures to the problem. Robust control design and optimization address the task systematically. The approach is explained in section 5.1. It explores which control structures are least complex but capable of solving the task of active damping. Further, the performance goals and system limitations are transformed into a mathematical representation for the optimization framework. The results for the traction unit of the Visio.M and of the TV-unit of Prototype Two are given in section 5.2. Limitations of the approach are discussed in section 5.4.

5.1 Methodology

Preliminary investigations on simple control structures were made in the student thesis by Woellhaf [184] and Mosch [185]. Krusch [186] reviewed H∞ control designs for drivetrain damping. These three student thesis contributed to the basic idea behind the following methodology.

To combine the different goals, tire operation points and actuator constraints into a systematic design procedure, an optimization framework is appropriate [45, p. 84]. Optimization has the benefit that it is highly flexible in its application since the procedure automatically produces a new solution for a new model or requirement systematically [155]. It also quantifies the performance of a certain control design with an absolute scale, making different design directly comparable [139, p. 2]. Nevertheless, elaborate robust design methods root in classic control design [45, p. 8]. Therefore, section 5.1.1 reviews the basic design principles for SISO systems. On the foundation of these fundamentals, H_∞ design and μ synthesis achieve optimal performance and robustness with complex, high-order controllers [45, p. 6 ff.]. For the implementation in the vehicle, simple and fixed control structures are easier to implement and adjust in the field [155, 156]. Section 5.1.2 surveys different control structures in order to derive two candidates appropriate for the active damping of drivetrain oscillations. The optimization procedure is described in section 5.1.3 along with the mathematic description of design goals, constraints and uncertainties.

5.1.1 Classic SISO Design Fundamentals

The feedback fundamentals are mainly based on [45, p. 41 ff.]. They are essential to understand general objectives and compromises in control design. The goal of this section is the explanation of these basic design principles based on a SISO system. The theory is linked to the two-inertia model of section 4.1.1. This comparison shall demonstrate similarities and differences between

the basic SISO control and active drivetrain damping.

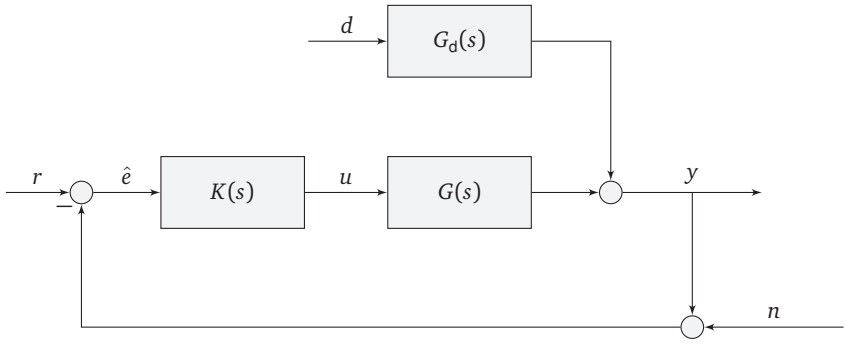

Figure 5.1: Basic feedback system

In the SISO control system of Fig. 5.1, u defines the single input and y the single output. If this structure was applied to drivetrain damping, u would be the torque request to the motor and y would be the shaft torque. In Eq. 5.1, the transfer function $G(s)$ describes the system's response of y to u. Further, the disturbance d influences y through the transfer function $G_d(s)$. In case of the drivetrain, d contains most importantly tire disturbances. In order to track r, a controller $K(s)$ feeds back the control error $\hat{e}$. According to Eq. 5.2, this error is the deviation of y from the reference r including the measurement inaccuracies n. The hat of $\hat{e}$ symbolizes that it is not the true error but rather an estimate. The essential difference between this basic feedback structure and drivetrain damping is that $\hat{e}$ is unknown because the shaft torque is unknown. In the general example, the feedback of the measured output y through $\hat{e}$ and $K(s)$ creates a loop. The dynamics of this open-loop is captured in the transfer function $L(s)$, which is the product of $K(s)$ and $G(s)$ in Eq. 5.4.

$$y(s) = G(s)\, u(s) + G_d(s)\, d(s) \tag{5.1}$$

$$\hat{e}(s) = r(s) - y(s) - n(s) \tag{5.2}$$

$$u(s) = K(s)\, \hat{e}(s) \tag{5.3}$$

$$L(s) = K(s)\, G(s) \tag{5.4}$$

The implementation of the controller requires certain properties. The controller must be realizable, which means it must be proper [45, p. 44]. A proper transfer function has a numerator degree that is equal to or less than its denominator degree [45, p. 23]. The system is already proper because it is the model of a real physical system. Further, the combination of controller and system must be internally stable [45, p. 44 f.].

Beyond these properties for the implementation, the equations of the control loop demonstrate further requirements. The goal of the control design is the minimization of the control error. Therefore, the subsequent paragraphs present expressions to analyze the behavior of the control error and derive further requirements. Due to the feedback of $\hat{e}$, $y(s)$ appears on both sides of Eq. 5.5. Reordering the terms yields Eq. 5.6.

$$y(s) = L(s)\,(r(s) - y(s) - n(s)) + G_d(s)\, d(s) \tag{5.5}$$

$$y(s) = \frac{L(s)}{1+L(s)}\, r(s) - \frac{L(s)}{1+L(s)}\, n(s) + \frac{1}{1+L(s)}\, G_d(s)\, d(s) \tag{5.6}$$

In order to evaluate the tracking and disturbance rejection performance, the true control error e in Eq. 5.7 assumes a measurement without noise. In Eq. 5.9, the repeated terms are encapsulated. This shows that the true tracking error is shaped by two functions, the sensitivity function $S(s)$

and the complementary sensitivity function $T(s)$. The two functions $S(s)$ and $T(s)$ are defined in Eq. 5.10 and Eq. 5.11 respectively.

$$e(s) = r(s) - y(s) \tag{5.7}$$

$$e(s) = r(s) - \frac{L(s)}{1+L(s)}\ r(s) + \frac{L(s)}{1+L(s)}\ n(s) - \frac{1}{1+L(s)}\ G_\mathrm{d}(s)\ d(s) \tag{5.8}$$

$$e(s) = S(s)\ r(s) + T(s)\ n(s) - S(s)\ G_\mathrm{d}(s)\ d(s) \tag{5.9}$$

with

$$S(s) = \frac{1}{1+L(s)} \tag{5.10}$$

$$T(s) = \frac{L(s)}{1+L(s)} \tag{5.11}$$

$$T(s) + S(s) = 1 \tag{5.12}$$

The transfer function $G_\mathrm{d}(s)$ of the disturbance is outside the loop and, therefore, not included in $L(s)$. Shaping $S(s)$ and $T(s)$ with $K(s)$ changes the dynamics of $e(s)$. To minimize $e(s)$, Eq. 5.9 shows that for good tracking and disturbance rejection $S(s)$ and $S(s)\ G_\mathrm{d}(s)$ have to be small [45, p. 188]. Putting a performance specification on $e(s)$, tracking or disturbance rejection, places a condition on $S(s)$ [44, p. 42]. However, performance alone is insufficient since changing system behavior requires robustness. Therefore, analogue to [45, p. 189 f.], the structured uncertainty $\Delta(s)$ incorporates these changes into the perturbed transfer function $G_\Delta(s)$ in Eq. 5.13. The addition of $\Delta(s)$ also creates a perturbed loop transfer function $L_\Delta(s)$.

$$G_\Delta(s) = (I + \Delta(s))\, G(s) \tag{5.13}$$

$$L_\Delta(s) = K(s)\ (I + \Delta(s))\, G(s) = (I + \Delta(s))\, L(s) \tag{5.14}$$

The performance of the perturbed system depends on the perturbed sensitivity function $S_\Delta(s)$. In $S_\Delta(s)$, the effect of $\Delta(s)$ should be as small as possible. This ensures that the performance stays within a narrow range around the desired specification. Based on Eq. 5.15, $\Delta(s)$ is singled out in Eq. 5.16. The scaling term of $\Delta(s)$ is the unperturbed complementary sensitivity function $T(s)$.

$$S_\Delta(s) = \frac{1}{1 + (I + \Delta(s))\, L(s)} = \frac{1}{1 + L(s) + \Delta(s) L(s)} \tag{5.15}$$

$$S_\Delta(s) = \frac{1}{(1+L(s))\ \left(1 + \Delta(s)\ \frac{L(s)}{1+L(s)}\right)} \tag{5.16}$$

$$S_\Delta(s) = \frac{1}{(1+L(s))\ (1 + \Delta(s)\ T(s))} \tag{5.17}$$

Eq. 5.17 proves that, in order to diminish the effects of $\Delta(s)$ on $S(s)$, $T(s)$ has to be small at the frequency where $\Delta(s)$ is large [45, p. 190]. However, following their definition in Eq. 5.12, $T(s)$ and $S(s)$ must equal one at all frequencies. This results in the contradictory design goals of good performance with a small $S(s)$ and good robustness with a small $T(s)$ [45, p. 5]. But robustness specifications are not the only reason for compromise. High magnitudes of the control signal u may lead to actuator saturation. Therefore, the actuator's limitations should be considered in the design [45, p. 83 f.]. In contrast to performance specifications on e which result in requirements on $S(s)$, performance specifications on u result in requirements on $T(s)$ [44, p. 42]. In addition, $T(s)$ has to be small to suppress the effects of sensor noise [45, p. 189], demonstrated by

Eq. 5.9.

$$||W_1(s)\,S(s)||_\infty = \sup_{\omega\in\mathbb{R}} |W_1(i\omega)\,S(i\omega)| \tag{5.18}$$

$$||W_1(s)\,S(s)||_\infty \leq 1 \tag{5.19}$$

Frequency dependent weight functions capture these requirements in mathematical form. The formulation is explained with $S(s)$ as an example but applies directly to $T(s)$ as well. It uses the H_∞ norm which is the supremum of the transfer functions for all complex frequencies $i\omega$, given in Eq. 5.18. The weight $W_1(s)$ scales $S(s)$ in such a way that the control system satisfies the performance requirement based on the inequality condition of Eq. 5.19. Since $S(s)$ must be less or equal to one according to Eq. 5.12, the supremum of the product $W_1(s)\,S(s)$ is chosen to be less or equal to one. Therefore, $W_1(s)$ must be large in frequency regions with strict performance requirements in order to force a small $S(s)$ [45, p. 55 f.], [44, p. 41 f.], [139, p. 99]. Apart from the design specifications, the weight function and its inverse must be stable [139, p. 107].

The fundamentals of SISO feedback systems demonstrate that compromises are necessary in control design. In summary, performance specifications for e create requirements for $S(s)$ to be small. Robustness, noise rejection and limitations for u create requirements for $T(s)$ to be small. Further, the control loop must be stable and the controller must be proper. In general, high gains benefit performance but cause noise amplification and actuator saturation, in some cases even instability [139, p. 52 f.]. However, the control structure in this section assumes that the desired tracking output is measurable. This is not the case for drivetrain oscillations since the shaft torque is unknown. Therefore, the following sections present control structures suitable for active drivetrain damping.

5.1.2 Definition of Control Structures

The main goal of this section is the presentation of control structures for the drivetrain which do not rely on a comparison of reference and shaft torque. Since the control design focuses on traction and TV-unit separately, Fig. 5.2 displays the discrete system of section 3.1.5 with a single input u but multiple measured outputs $\boldsymbol{y}$. In terms of the two-inertia model, the input u is the torque request for the actuator. The measured outputs are the actuator speed at the shaft level $\dot{\varphi}_1$ and the load speed $\dot{\varphi}_2$ which corresponds to the wheels. The unknown output z represents T_{12} which is available for the evaluation of a controller but not for feedback. At the core of the block diagram is the discrete state space model. The matrices C and $\boldsymbol{c}_\mathsf{T}$ map the state $\boldsymbol{x}$ to $\boldsymbol{y}$ and T_{12}. On the left side, $\boldsymbol{b}_{\mathsf{d,z}}$ and $\boldsymbol{b}_{\mathsf{u,z}}$ define the effect of u and d on the system. In contrast to the SISO diagram of Fig. 5.1, $K[z]$ uses the outputs directly because the control error is not available. The calculated feedback torque T_{Fb} adds to r. Similar control structures are used in [52, 85, 87]. In this configuration, the driver's reference r has a direct impact on u. The role of the feedback is to control transient dynamics with T_{Fb} but preserve the vehicle's steady-state characteristics. Therefore, T_{Fb} must vanish over time [52]. Even though, the structure is different, the open loop system may be encapsulated to form an open-loop transfer function $L[z]$. The goal is the optimization of $L[z]$ in a similar fashion, as previously discussed in section 5.1.1.

It is important to distinguish between explanations and derivations based on the reduced two inertia model and the actual control optimization. Nevertheless, the final optimization utilizes the full discrete linear state space model which was validated in section 3.2. The controllers are presented in the continuous domain equations because most publications use this domain. The controllers are discretized prior to the control optimization with the sampling rate of the model.

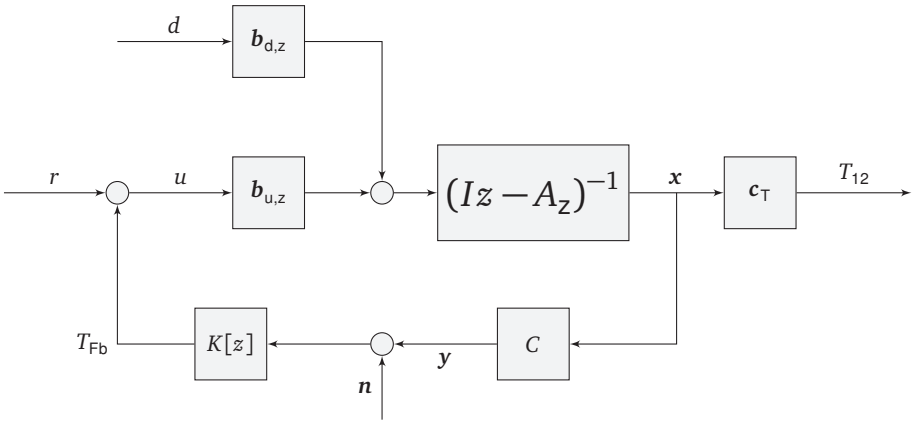

Figure 5.2: Single-input multi-output feedback system

For the following derivation of the controller, the actuator's impulse of Eq. 4.6 and the shaft torque's Eq. 4.12 are repeated to improve readability. The two equations explain the foundation of different control structures in simple terms. For example, the impulse demonstrates that in a steady-state, with $\ddot{\varphi}_1 = 0$ rad/s^2, the shaft torque T_{12} equals the actuator torque T_1. Therefore, if the actuator does not saturate, $T_1 = u$ and, if T_{Fb} vanishes over time, $u = r$ holds. The result is $T_{12} = r$, which emphasizes that T_{Fb} must decline to zero in the steady-state case. However, most of the time the test cases are transient maneuvers, such as tip-ins and tip-outs. In high grip conditions, it is expected that the oscillations vanish within the first few seconds of a tip-in while reaching the steady-state may require a multiple of this time. During such maneuvers, J_1 creates a deviation between T_1 and T_{12}, because $\ddot{\varphi}_1 \neq 0$ rad/s^2. The magnitude of the deviation depends on how much J_1 contributes to the total inertia (κ_2), which is accelerated by the actuator. It is not the goal of the control design to compensate J_1 or change the steady-state behavior of the system.

$$J_1 \ \ddot{\varphi}_1 = T_1 - T_{12}$$
$$T_{12} = c_{12} \ \varphi_{12} + d_{12} \ \dot{\varphi}_{12}$$

Initially, the twist speed feedback is discussed because $\dot{\varphi}_{12}$ directly appears as part of the shaft's natural damping. Therefore, it is an obvious choice for a damping controller and previous publications have stated its good performance [68, 81, 84, 86]. Apart from the twist speed, oscillations in the shaft cause a deviation between r and T_{12}. Therefore, a feedback, which eliminates the tracking error between r and T_{12} over time, is an eligible damping controller. Nevertheless, T_{12} is not measured. In order to calculate a control error, a shaft torque estimate, $\hat{T}_{12}$, is required. Because $\hat{T}_{12}$ is the key element, the estimation is discussed first. Subsequently, different feedback methods of the tracking error are reviewed. Finally, limiting the derivative of $\hat{T}_{12}$ also generates damping of the oscillations.

Twist Speed Feedback

The main goal of the control is oscillation damping. Because the shaft's twist speed $\dot{\varphi}_{12}$ appears in the damping term of the shaft torque, a feedback of $\dot{\varphi}_{12}$ increases damping of the shaft's oscillations. Since the feedback acts through u on T_1, the feedback torque $T_{Fb,\dot{\varphi}_{12}}$ in Eq. 5.20 must be negative ($k_{Spd} \leq 0$). With the negative sign, $T_{Fb,\dot{\varphi}_{12}}$ affects the impulse of J_1 in the same direction as T_{12}. Therefore, the control gain k_{Spd} adds to the damping coefficient d_{12} of the shaft

[21, p. 88 ff.].

$$T_{\mathrm{Fb},\dot{\varphi}_{12}} = k_{\mathrm{Spd}}\ \dot{\varphi}_{12} = k_{\mathrm{Spd}}\ (\dot{\varphi}_1 - \dot{\varphi}_2) \tag{5.20}$$

Because $\dot{\varphi}_1$ and $\dot{\varphi}_2$ are measurements, implementation of the twist speed feedback is simple. In Eq. 4.11, $\dot{\varphi}_{12}$ is defined as the difference between $\dot{\varphi}_1$ and $\dot{\varphi}_2$. It even incorporates the housing pitch motion because this motion is inherent in the measured rotor speed of the actuator [21, p. 92]. Once the oscillations vanish, $T_{\mathrm{Fb},\dot{\varphi}_{12}}$ should decline to zero because there is no relative motion between $\dot{\varphi}_1$ and $\dot{\varphi}_2$. However, in the discrete implementation with communication delays, the difference between the measured signals $\dot{\varphi}_1$ and $\dot{\varphi}_2$ may not vanish. In transient driving maneuvers, both, $\dot{\varphi}_1$ and $\dot{\varphi}_2$, change over time even after the oscillations have disappeared. Due to different signal qualities, one sensor is ahead of the other. In such a case, the twist speed feedback does not vanish until the drivetrain reaches a steady-state. Overall, the benefit of this approach is the simple implementation. Its drawback is the strong dependency on the quality of the measurement signals. Because the simplicity of the P-controller is the main benefit, the option of a high-pass or PD controller, as in Bruce et al. [68] and Rosenberger [24, p. 81 ff.], is passed here.

Shaft Torque Estimation

There are three possibilities for the estimation of the shaft torque. Since the damping of steel shafts is minor [26], T_{12} mainly depends on φ_{12}. Its derivative, $\dot{\varphi}_{12}$, is available from the measurements of $\dot{\varphi}_1$ and $\dot{\varphi}_2$. However, the integration of $\dot{\varphi}_{12}$ is not advisable, especially regarding the generally poor resolution of the wheel speed information [52, 94, 101]. The integral accumulates deviations caused by measurement errors and delays in the speed signals. Since $\dot{\varphi}_{12} \gg \varphi_{12}$, already small deviations of the measured signals from the true value lead to a significant error of φ_{12}. In order to avoid the integration, different observers have been presented to calculate $\hat{T}_{12}$. State observers are common but rely on a state space model of the dynamic system. Even though the shaft torque estimate is the goal, these observers must address the complex tire dynamics in their mathematical models. The three most important approaches are discussed briefly.

The three publications are considered to be the most relevant out of the more detailed literature review in section 2.2. Bottiglione et al. [83] estimate T_{12} with an EKF, which accounts for the nonlinear tire dynamics in the state space model. It is the most accurate approach but also the most complex. Rodriguez et al. [84] use an unknown input observer. This linear state observer assumes that the tire torque is a constant input to the model. This assumption simplifies the observer but ignores that the tire's response is an important dynamic of the drivetrain. Rosenberger et al. [87] add a linearized tire model to the linear Kalman filter. Gain scheduling adapts the parameter to the operation point of the vehicle. The feedback of measurement signals into the observer's model by the gain scheduling causes problems when oscillations occur [24, p. 68]. This demonstrates that addressing the tire dynamics is a common drawback to state space observers. In contrast to the state space models, Hori et al. [135] create an observer for $\hat{T}_{12}$ solely with the impulse equation of J_1. The shaft torque T_{12} is considered a disturbance to the actuator system. To form an observer, first, the impulse in Eq. 4.6 is transferred into the Laplace domain. Next, the terms are reordered to create an expression for T_{12}. Finally, a low-pass filter is added to create a proper transfer function for the derivative. The result is

Eq. 5.21.

$$\hat{T}_{12} = T_1 - J_1 \, \frac{s}{\tau_{\mathrm{DT1}} s + 1} \, \dot{\varphi}_1 \tag{5.21}$$

The major benefit of this approach is that it focuses on the actuator and does not need a tire model. Since it relies on the actuator, it requires only a few measurements, T_1 and $\dot{\varphi}_1$. These measurements are typically of the best quality among the sensors in the drivetrain. Its drawback is the derivative of $\dot{\varphi}_1$, which amplifies signal noise. For the vehicles considered in this dissertation, the disturbance observer based on the actuator impulse is the best option because signal noise is small.

Tracking Error Feedback

Once the shaft torque is estimated, it is possible to calculate the control error $\hat{e}$ with $\hat{T}_{12}$ as y and feed it back. The PID controller is the most important feedback controller in classic control design [45, p. 41]. The role of its parameters are well understood. In contrast to more complex controllers, engineers can often retune the PID controller to improve results [45, p. 9]. The I-gain forces the steady-state error of the control loop to zero in a sufficiently long time period [133, p. 10]. However, in case of the drivetrain, this occurs naturally. In the feedback structure of Fig. 5.2, [83, 87] use an I-gain. Rosenberger et al. [87] explicitly state that the I-gain is unnecessary for damping but rather compensates the actuator's inertia. Since this compensation is not a primary goal here, the I-gain is neglected. The subsequent paragraphs start with a pure proportional feedback. Afterwards, a PD is investigated. The torque control law in Eq. 5.22 feeds back the difference between $\hat{T}_{12}$ and r with the gain k_{P}.

$$T_{\mathrm{Fb},\hat{e}} = k_{\mathrm{P}} \left(r - \hat{T}_{12} \right) = k_{\mathrm{P}} \left(r - T_1 + J_1 \, \frac{s}{\tau_{\mathrm{DT1}} \, s + 1} \, \dot{\varphi}_1 \right) \tag{5.22}$$

The feedback law in Eq. 5.22 requires the actuator torque and speed. However, in general, T_1 follows the request u with a first order transfer function, which was previously discussed in section 2.1.6. Analogue to Rosenberger [24, p. 81 f.], the control law may be simplified even further. The first order relation is defined in Eq. 5.23. Prior, Eq. 5.23 and Eq. 5.24 set up the switching for the traction and the TV-unit.

$$u = \begin{cases} i_{\mathrm{trc}} \, u_{\mathrm{trc}} & \text{Traction} \\ i_{\mathrm{tv}} \, u_{\mathrm{tv}} & \text{TV} \end{cases} \tag{5.23}$$

$$\tau_1 = \begin{cases} \tau_{\mathrm{trc}} & \text{Traction} \\ \tau_{\mathrm{tv}} & \text{TV} \end{cases} \tag{5.24}$$

$$T_1 = \frac{1}{\tau_1 \, s + 1} u \tag{5.25}$$

Starting with Eq. 5.26, which resembles the sum block on the left of Fig. 5.2, an expression for u is derived. First, the relation for the actuator torque in Eq. 5.25 replaces T_1 in the feedback law of Eq. 5.22. The result substitutes the general feedback torque T_{Fb} in Eq. 5.26. This yields Eq. 5.27, which has u on both sides. Therefore, reordering is necessary. The terms are rearranged and u appears only on the left-hand side in Eq. 5.28. Before isolating u, the bracket on the left-hand side is converted to a common denominator in Eq. 5.29. The fraction in front of u is transferred to the right-hand side. In Eq. 5.31, the transfer function scaling r and the feedback of $\dot{\varphi}_1$ is

rearranged to a more familiar format.

$$u = r + T_{\mathrm{Fb}} \tag{5.26}$$

$$u = r + k_{\mathrm{P}} \left(r - \frac{1}{\tau_1\, s + 1}\, u + J_1\, \frac{s}{\tau_{\mathrm{DT1}}\, s + 1}\, \dot{\varphi}_1 \right) \tag{5.27}$$

$$\left(1 + \frac{k_{\mathrm{P}}}{\tau_1\, s + 1} \right) u = (1 + k_{\mathrm{P}})\; r + k_{\mathrm{P}}\, J_1\, \frac{s}{\tau_{\mathrm{DT1}}\, s + 1}\, \dot{\varphi}_1 \tag{5.28}$$

$$\frac{\tau_1\, s + 1 + k_{\mathrm{P}}}{\tau_1\, s + 1} u = (1 + k_{\mathrm{P}})\; r + k_{\mathrm{P}}\, J_1\, \frac{s}{\tau_{\mathrm{DT1}}\, s + 1}\, \dot{\varphi}_1 \tag{5.29}$$

$$u = \frac{(1 + k_{\mathrm{P}})(\tau_1\, s + 1)}{\tau_1\, s + 1 + k_{\mathrm{P}}}\, r + k_{\mathrm{P}}\, J_1\, \frac{\tau_1\, s + 1}{\tau_1\, s + 1 + k_{\mathrm{P}}}\, \frac{s}{\tau_{\mathrm{DT1}}\, s + 1}\, \dot{\varphi}_1 \tag{5.30}$$

$$u = \frac{\tau_1\, s + 1}{\frac{\tau_1}{1 + k_{\mathrm{P}}}\, s + 1}\, r + \frac{k_{\mathrm{P}}\, J_1}{1 + k_{\mathrm{P}}}\, \frac{\tau_1\, s + 1}{\frac{\tau_1}{1 + k_{\mathrm{P}}}\, s + 1}\, \frac{s}{\tau_{\mathrm{DT1}}\, s + 1}\, \dot{\varphi}_1 \tag{5.31}$$

The transfer function in front of r is a high-pass pre-filter. It compensates the declining gain of the actuator response in a feedforward approach. The high-pass is also included in the feedback loop. However, τ_1 is close to or even smaller than the sampling intervals and far from the oscillations' frequency in both vehicles. Therefore, it is neglected, which results in the feedback law of Eq. 5.32. The proportional feedback of the torque error results in a DT1 feedback of $\dot{\varphi}_1$ in Eq. 5.33, similar to Hori et al. [135] or Syrnik [134, p. 83].

$$T_{\mathrm{Fb},\hat{e}} = \frac{k_{\mathrm{P}}}{1 + k_{\mathrm{P}}}\, \frac{J_1\, s}{\tau_{\mathrm{DT1}}\, s + 1}\, \dot{\varphi}_1 \tag{5.32}$$

$$T_{\mathrm{Fb},\hat{e}} = k'_{\mathrm{P}}\, \frac{J_1\, s}{\tau_{\mathrm{DT1}}\, s + 1}\, \dot{\varphi}_1 \tag{5.33}$$

with

$$k'_{\mathrm{P}} = \frac{k_{\mathrm{P}}}{1 + k_{\mathrm{P}}} \tag{5.34}$$

If the actuator spins up rapidly, $T_{\mathrm{Fb},\hat{e}}$ adds torque to u. This results in an even higher actuator acceleration but also in a faster twisting motion of the shaft and, therefore, in an increase in shaft torque. This allows the change of the system's eigenfrequency, which corresponds to a virtual increase in stiffness. Feeding back the torque estimate is similar to feeding back φ_{12} [21, p. 94 ff.], [135]. The final feedback law relies solely on $\dot{\varphi}_1$, which is a further improvement over the torque estimation of Eq. 5.21. The combination of $T_{\mathrm{Fb},\hat{e}}$ and $T_{\mathrm{Fb},\dot{\varphi}_{12}}$ can increase damping and bandwidth of the wheel torque control loop based on $\dot{\varphi}_1$ and $\dot{\varphi}_2$. However, if d_{12} is minor, the twist speed feedback is equivalent to a feedback of the shaft torque derivative $\dot{T}_{12}$ [21, p. 97 f.]. Therefore, a PD feedback of the torque error promises increased damping and bandwidth with only $\dot{\varphi}_1$. The previous studies [94, 137] prove that limiting $\dot{T}_{12}$ successfully damps drivetrain oscillations. On the one hand, Templin and Egardt [94] use this approach in a sophisticated LQR/LTR design. On the other hand, Sugiura and Hori [137] simply subtract $\dot{T}_{12}$ from r. An additional DT1 block generates $\dot{T}_{12}$ from T_{12}. Based on this approach, Eq. 5.35 extends the previous proportional feedback of Eq. 5.22 with an additional derivative term.

$$T_{\mathrm{Fb,PD}} = \left(k_{\mathrm{P}} + \frac{k_{\mathrm{D}}\, s}{\tau_{\mathrm{D}}\, s + 1} \right) \left(r - \hat{T}_{12} \right) \tag{5.35}$$

Analogue to the exclusive P-controller, the final feedback law of the PD-controller is extracted in multiple steps. Appendix C.1 contains the transformation of the equations. The result is Eq. 5.36.

$$T_{\text{Fb,PD}} = \left(k'_{\text{P}} + \frac{k'_{\text{D}}\, s}{\tau'_{\text{D}}\, s + 1} \right) \frac{J_1\, s}{\tau_{\text{DT1}}\, s + 1}\, \dot{\varphi}_1 \tag{5.36}$$

with

$$\tau'_{\text{D}} = \frac{k_{\text{D}}}{k_{\text{P}} + 1} + \tau_{\text{D}} \tag{5.37}$$

$$k'_{\text{D}} = \frac{k_{\text{D}}}{(k_{\text{P}} + 1)^2} \tag{5.38}$$

The P-gain k'_{P} is identical to the P-controller. In addition, k'_{D} and τ'_{D} define the derivative term of the torque feedback. In order to extend the bandwidth of the drivetrain, the P-gains must satisfy $k_{\text{P}} \geq 0$ and, therefore, $k'_{\text{P}} \geq 0$. The derivative gain k_{D} must also be positive to achieve damping because $\hat{T}_{12}$ enters the control error with a negative sign. Therefore, $k_{\text{D}} \geq 0$, and accordingly $k'_{\text{D}} \geq 0$, reduces u for a positive shaft jerk $\dot{T}_{12}$. Analogue, a positive $\dot{T}_{12}$ means that the load on J_1 increases. Hence, the derivative of $\ddot{\varphi}_1$ is negative. Therefore, $k'_{\text{D}} \geq 0$ must be positive to reduce $\dot{T}_{12}$.

Summary

The main goal of this section was the derivation of control structures for the sensor/actuator setup of the drivetrain, which can achieve the damping of oscillations and, if necessary, the extension of the system's bandwidth. The feedback of $\dot{\varphi}_{12}$ or the derivative of $\hat{T}_{12}$ achieve damping. The benefit of $\dot{\varphi}_{12}$ is that a simple P-gain is sufficient while $\dot{T}_{12}$ requires the second derivative of $\dot{\varphi}_1$. However, the noise amplification in the derivatives may be less harmful than the delay and resolution issues of $\dot{\varphi}_2$. The extension of the bandwidth may be achieved with the feedback of $\hat{T}_{12}$. Therefore, two feedback structures are considered in the optimization, namely the PD-controller of Eq. 5.36 and the sum of $T_{\text{Fb},\hat{e}}$ and $T_{\text{Fb},\dot{\varphi}_{12}}$. The former possesses three tuning parameters (k'_{P}, k'_{D}, τ_{D}) while the later contains only two (k_{Spd}, k'_{P}). If the time constant of the torque estimation τ_{DT1} is included in the tuning parameters, the optimization can use it to improve results. However, this could break the tie to the physical explanations of the control structures and simply create a higher order controller.

5.1.3 Fixed-Structure Multi-Model Multi-Objective Control Optimization

The main goal of this section is the mathematical representation of the performance goals as well as the system limitations. They are required for the optimization framework, which is described in [155, 156] and implemented in the Matlab Robust Control Toolbox [172]. In the following paragraphs, the different features of the framework are discussed and translated to the drivetrain damping problem. The optimization procedure itself is a complex numeric method which is explained in [187] but outside the focus of this dissertation.

"Fixed-Structure" refers to the control structures of section 5.1.2. The controllers are predefined and possess a limited number of tuning parameters $\boldsymbol{p}$. Prior to the optimization, the controller must be discretized to the sampling rate of the control system. The term "multi-model" indicates that the optimization covers a set of models. This set is a structured representation of the system's uncertainties [44, p. 45], in particular tire dynamics. Usually, structured representations

can represent low-frequency uncertainties while high-frequency components are difficult to capture in a structured form [188, p. 6]. Further, at high-frequency, delays and model errors cause uncertainties [188, p. 6], [45, p. 190]. The investigation of tire dynamics in chapters 3 and 4 favors the approach with a set of models. However, the results already showed that the model's validity fades for frequencies above 20 Hz. These shortcomings of the uncertainty representation and the model's validity must be acknowledged when interpreting the results.

The optimization procedure separates objectives into desired (soft) and necessary (hard) goals for the closed loop system. In terms of mathematical optimization, soft goals take the form of a cost function while hard goals are constraints. As the initial paragraphs of chapter 5 demonstrate, there are multiple soft and hard goals for the damping of drivetrain oscillations. The following paragraphs discuss the framework of the optimization. Subsequently, the mathematical representation of the goals is derived. The equations relate to the continuous time domain because most books and papers cited in this dissertation use this domain. Therefore, the equations are comparable. Analogue to the controllers, the goals are discretized prior to the optimization.

The framework must optimize the controllers for multiple models with respect to multiple goals. It tackles this manifold by focusing on the worst case objective and model. The procedure is expressed by Eq. 5.39 for the cost function and by Eq. 5.40 for the constraints. The max function selects the combination of the model k and the soft goal i, which produces the largest norm of the cost function. In order to compare the different goals effectively, they must be normalized. The cost function contains the weight $W_i(s)$ and the corresponding closed-loop transfer function $L_i^k(s,\boldsymbol{p})$. The constraints are handled in similar fashion with the index j relating to the worst case constraint. The vector $\boldsymbol{p}$ contains the tuning parameters of the given controller, which are optimized by the framework.

$$\min_{p} \max_{i,k} \left\{ \left|\left| W_i(s)\, L_i^k(s,\boldsymbol{p}) \right|\right|_\infty \right\} \tag{5.39}$$

$$\text{subject to } \max_{j,k} \left\{ \left|\left| W_j(s)\, L_j^k(s,\boldsymbol{p}) \right|\right|_\infty \right\} \leq 1 \tag{5.40}$$

The soft goals contain the desired damping and bandwidth. In this regard, they represent a perfect behavior from u and d to the control error $e = r - T_{12}$. This behavior, in the form of suitable weights W_i, is chosen as follows. If the drivetrain were perfectly damped, it should perform like a first order transfer function with the specified bandwidth ω_b. However, the acceleration of the actuator inertia uses up torque, which is not transmitted through the shaft. The weights must account for this deviation in transient maneuvers. The maximum deviation occurs for $c_\mathrm{sx} = 0$ when the drivetrain spins up the fastest, without the vehicle as a load. For the tracking error (input r), $\kappa_{2,c_\mathrm{sx}=0}$ of section 4.2.1 quantifies the amount of torque consumed by J_1, which is not transferred through the shaft. For the disturbance rejection (input d), $\kappa_{2,c_\mathrm{sx}=0}$ quantifies the amount of torque which is transferred through the shaft to affect the motion of J_1, therefore, disturbing the shaft torque. The result is that both weights, $W_\mathrm{r,e}(s)$ and $W_{d,e}(s)$, are equivalent. The values for $\kappa_{2,c_\mathrm{sx}=0}$ are given in Tab. 5.1.

$$W_\mathrm{r,e}(s) = \frac{s + \omega_\mathrm{b}}{s + \kappa_{2,c_\mathrm{sx}=0}\ \omega_\mathrm{b}} \tag{5.41}$$

$$W_\mathrm{d,e}(s) = \frac{s + \omega_\mathrm{b}}{s + \kappa_{2,c_\mathrm{sx}=0}\ \omega_\mathrm{b}} \tag{5.42}$$

Fig. 5.3 compares two open loop transfer functions $G_{r,e}(s)$, one for $c_\mathrm{sx} = 0$ Nm and one for

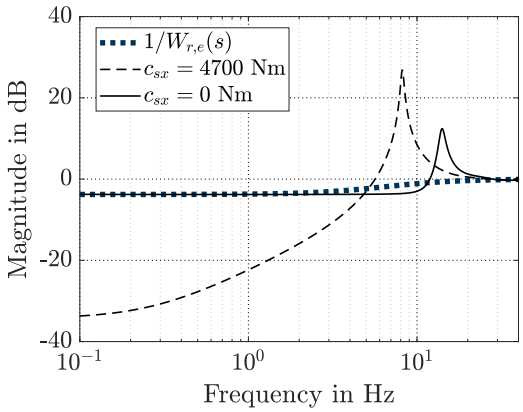

Figure 5.3: Comparison of the tracking weight $W_{r,e}(s)$ with the open loop model of the Visio.M's tracking unit ($\omega_\mathrm{b} = 8$ Hz)

$c_\mathrm{sx} = 4700$ Nm, to the corresponding weight $W_{r,e}(s)$. The inverse of the weight is plotted because it represents the limit which the transfer functions must not exceed to satisfy Eq. 5.19 [45, p. 54 f.]. It illustrates that the large low frequency error $\kappa_{2,c_\mathrm{sx}=0}$ creates a weight, which puts the main focus on damping resonance peaks. The resonances cause the largest elevation above the inverse weight and the optimization framework focuses on the peaks first. An extension of the bandwidth plays a secondary role. If the bandwidth is key, then $\kappa_{2,c_\mathrm{sx}=0}$ should be replaced with a smaller value, e.g. 10^{-3} [45, p. 316].

The hard goals contain the actuator limitations. The peak torque of the actuators are a nonlinear saturation. The linear weights cannot represent this behavior. Therefore, the weights limit T_Fb relative to r and d. In order to avoid a backlash traverse caused by the controller, the magnitude of T_Fb must be less than or equal to the magnitude of r. This means that in a tip-in maneuver, T_Fb can create an overshot of u to $2\ r$ but also reduce u to zero. Similarly, the controller should be able to compensate any effect of d on the shaft with an equivalent magnitude. However, the controller action must be limited to low-frequency oscillation damping. Therefore, below the frequency ω_Fb the control gain must decline. Based on [45, p. 316], the steady-state magnitude of T_Fb is set to 10^{-2}. The actuator limitations and the vanishing steady-state control action results in the weights W_{r,T_Fb} and W_{d,T_Fb}. A reduced actuator response at high frequencies is neglected.

$$W_{r,T_\mathrm{Fb}}(s) = \frac{s + \omega_\mathrm{Fb}}{s + 10^{-2}\ \omega_\mathrm{Fb}} \tag{5.43}$$

$$W_{d,T_\mathrm{Fb}}(s) = \frac{s + \omega_\mathrm{Fb}}{s + 10^{-2}\ \omega_\mathrm{Fb}} \tag{5.44}$$

In order to ensure internal stability, all closed-loop poles must be stable. This is an additional constraint to the optimization problem. In the Robust Control Toolbox, it is converted to a form, which aligns with the inequality condition of Eq. 5.40.

Table 5.1: Relative contribution of two-inertia oscillator for zero tire slip stiffness

Vehicle	Visio.M		Prototype Two	
Subsystem	Traction	TV	Traction	TV
$\kappa_{2,c_\mathrm{sx}=0}$	0.64	0.24	0.55	0.94

5.2 Results

The damping control optimization is applied to the Visio.M's traction unit and the TV-unit of Prototype Two. The Visio.M demonstrated the strongest oscillations on dry roads in the traction unit while Prototype Two shows a strong response to disturbances on low μ. In both cases, the desired loop bandwidth is set to $\omega_{\mathrm{b}} = 8$ Hz. The control effort is limited to $\omega_{\mathrm{Fb}} = 10^{-2}$ Hz. The controllers are compared in tables with their results for the different goals and constraints in two driving conditions. On the one hand, the high grip condition is defined by a maximum slip stiffness c_{sx}, $s_{\mathrm{x},0} = 0.01$ and $\dot{\varphi}_{\mathrm{w},0} = 1$ rad/s. On the other hand, the zero grip condition sets $c_{\mathrm{sx}} = 0$ Nm, which renders $s_{\mathrm{x},0}$ and $\dot{\varphi}_{\mathrm{w},0}$ obsolete. First, the results for Visio.M's traction unit are studied. Afterwards, Prototype Two is analyzed.

5.2.1 Traction unit of the Visio.M

The Visio.M's traction inverter contains an internal damping controller. Its exact structure is unknown but it relies fully on the measurements available from the motor. Therefore, a controller in the form of Eq. 5.36 was fitted to time-domain measurement data of tip-ins. Appendix C.6 contains the results. In this section, the worst case results are compared first since they are the main objective of the optimization. Subsequently, the individual goals in the two extreme grip cases are examined. The maximum slip stiffness for the Visio.M is $c_{\mathrm{sx}} = 4674$ Nm. Afterwards, the optimized controllers are separated into their individual components in order to investigate how they achieve their performance. Finally, the possible improvement is demonstrated by measurements.

Table 5.2: Evaluation of the optimization results for the Visio.M's traction unit

Evaluation metric	Open loop	$T_{\mathrm{Fb,PD}}$	$T_{\mathrm{Fb},\hat{e}} + T_{\mathrm{Fb},\dot{\varphi}_{12}}$	Internal Damping
Worst case	24.16	3.51	4.9	3.75
$W_{r,e}(s)$ for high grip	24.16	3.51	4.89	2.42
$W_{r,e}(s)$ for zero grip	4.07	2.59	2.69	1.8
$W_{d,e}(s)$ for high grip	2.66	2.68	2.66	3.75
$W_{d,e}(s)$ for zero grip	6.77	3.51	4.03	2.88
$W_{r,T_{\mathrm{Fb}}}(s)$ for high grip	0	0.89	0.95	1.02
$W_{r,T_{\mathrm{Fb}}}(s)$ for zero grip	0	0.53	0.44	0.96
$W_{d,T_{\mathrm{Fb}}}(s)$ for high grip	0	0.41	0.14	0.81
$W_{d,T_{\mathrm{Fb}}}(s)$ for zero grip	0	1	1	1.39

Table 5.2 compares the two feedback structures of section 5.1.2, namely the PD control $T_{\mathrm{Fb,PD}}$ and the combined torque and twist speed feedback $T_{\mathrm{Fb},\hat{e}} + T_{\mathrm{Fb},\dot{\varphi}_{12}}$, with the open loop behavior and the internal damping on the inverter. The worst case score is the final result of all models in the set. All three controllers improve the system dynamics greatly compared to the open loop starting point. In the worst case performance, $T_{\mathrm{Fb,PD}}$ shows the smallest value. Since the proportional torque feedback is common to both optimized controllers, the advantage of $T_{\mathrm{Fb,PD}}$ is within the derivative feedback and the availability of the two tuning parameters, k'_{D} and τ'_{D}, over k_{spd}. Studying the individual goals for the high and zero grip conditions reveals that $T_{\mathrm{Fb,PD}}$ performs worst in high grip tracking ($W_{r,e}(s)$) and zero grip disturbance rejection ($W_{d,e}(s)$). For $T_{\mathrm{Fb},\hat{e}} + T_{\mathrm{Fb},\dot{\varphi}_{12}}$ the maximum score is the tracking on high grip but it does not match the overall worst case score completely. This demonstrates that considering only the two boundary cases is insufficient. Nevertheless, the two values are close to each other. In contrast, the internal

damping performs worst for $W_{d,e}(s)$ on high grip. Only in this scenario, $T_{\text{Fb,PD}}$ and $T_{\text{Fb},\hat{e}} + T_{\text{Fb},\dot{\varphi}_{12}}$ outperform the internal controller. However, the defining peaks for the performance of the internal controller are above 30 Hz. Therefore, they are outside the region of interest for this dissertation and also outside the validity of the tire model. In the region of focus below 20 Hz, the internal controller outperforms the optimized controllers slightly. Regarding the constraints, both optimized controllers are limited strongest by the gain limitation for the disturbance rejection at zero grip. The internal damping controller, however, does not satisfy the constraints, since it was not optimized with the limitations in place. In the high grip case, the internal controller exceeds $W_{r,T_{\text{Fb}}}(s)$ marginally to suppress the main low-frequency mode. The internal controller shows an even larger breach of the disturbance rejection constraint $W_{d,T_{\text{Fb}}}(s)$ for the zero grip case. Similar to the high grip condition, the constraint is violated in order to reduce the low-frequency mode at 13 Hz. In essence, the internal damping controller outperforms the other two because they are limited by the constraints. In fact, if the constraints are relaxed such that the internal damping controller satisfies them, $T_{\text{Fb,PD}}$ and $T_{\text{Fb},\hat{e}} + T_{\text{Fb},\dot{\varphi}_{12}}$ approach its performance. But even though the margin decreases, the internal controller remains superior.

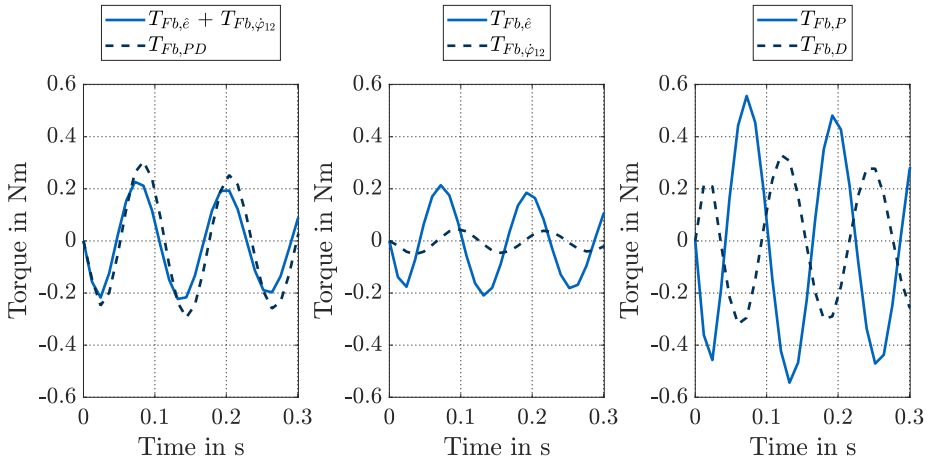

Figure 5.4: Comparison of the control torque composition for the optimized controllers for the Visio.M in a tip-in with $r = 1$ Nm in high grip conditions

Fig. 5.4 shows the control effort of both optimized controllers in an open loop tip-in from 0 Nm to 1 Nm. On the left side, $T_{\text{Fb},\hat{e}} + T_{\text{Fb},\dot{\varphi}_{12}}$ leads $T_{\text{Fb,PD}}$ slightly but $T_{\text{Fb,PD}}$ demonstrates a higher amplitude. The optimization accomplishes part of the improvement by choosing negative P-gains in the torque feedback for both $T_{\text{Fb,PD}}$ and $T_{\text{Fb},\hat{e}}$. This contradicts the sign convention at the end of section 5.1.2. However, since the oscillation frequency is roughly located between 50 rad/s and 100 rad/s, a delay between 31 ms and 16 ms is sufficient to create a 90° phase shift in the signal. Sampling and filtering cause delays for the controllers. Instead of relying on the delayed torque derivative, the controllers use the negative torque to predict the derivative ahead of time. This is demonstrated by the plot in the middle and to the right. In the middle, $T_{\text{Fb},\hat{e}}$ and $T_{\text{Fb},\dot{\varphi}_{12}}$ are separated. Both act generally in the same direction but $T_{\text{Fb},\hat{e}}$ demonstrates a much larger amplitude and leads $T_{\text{Fb},\dot{\varphi}_{12}}$, which should be the correct damping torque, according to the theory of section 5.1.2. On the right side, the individual parts of the PD controller, $T_{\text{Fb,P}}$ and $T_{\text{Fb,D}}$, almost act completely opposite to each other. The amplitudes of both signals is larger than the final feedback torque in the plot on the left. The superposition of these almost anti-phase signals creates the lag effect, which causes $T_{\text{Fb,PD}}$ to follow $T_{\text{Fb},\hat{e}} + T_{\text{Fb},\dot{\varphi}_{12}}$ in the left plot. The filter of the derivative τ'_{D} is an important parameter to tune the lag. If τ_{DT1} is available for tuning, the phase of $T_{\text{Fb},\hat{e}}$ can also be optimized. This creates a better performance but diminishes

the quality of $\hat{T}_{12}$ as a shaft torque estimate. Besides the damping effect, the negative P-gains cause a reduction in bandwidth. If the control gains are limited to positive values, the bandwidth cannot be reduced anymore, however, the performance suffers (overall score for $T_{\text{Fb},\hat{e}} + T_{\text{Fb},\dot{\varphi}_{12}}$: 8.1, overall score for $T_{\text{Fb,PD}}$: 16.4). The internal damping controller also follows this approach and reduces the bandwidth even stronger than the optimized controllers to achieve its damping performance.

Based on these results, the control structures presented in section 5.1.2 are capable to create the desired performance and robustness for the Visio.M. Among the two controllers $T_{\text{Fb,PD}}$ is the better option of the two. Nevertheless, neither optimized controller is able to outperform the internal damping controller, which would justify replacing it. Further, the internal controller has been tested with the Visio.M in numerous driving experiments on various surfaces without problems caused by disturbances on high μ or excessive torque changes on low μ. These results suggest that a revision of $W_{d,T_{\text{Fb}}}(s)$ could improve the optimization procedure. In addition, the high-frequency tire oscillations should be addressed by improving the model or accounting for them in the control design.

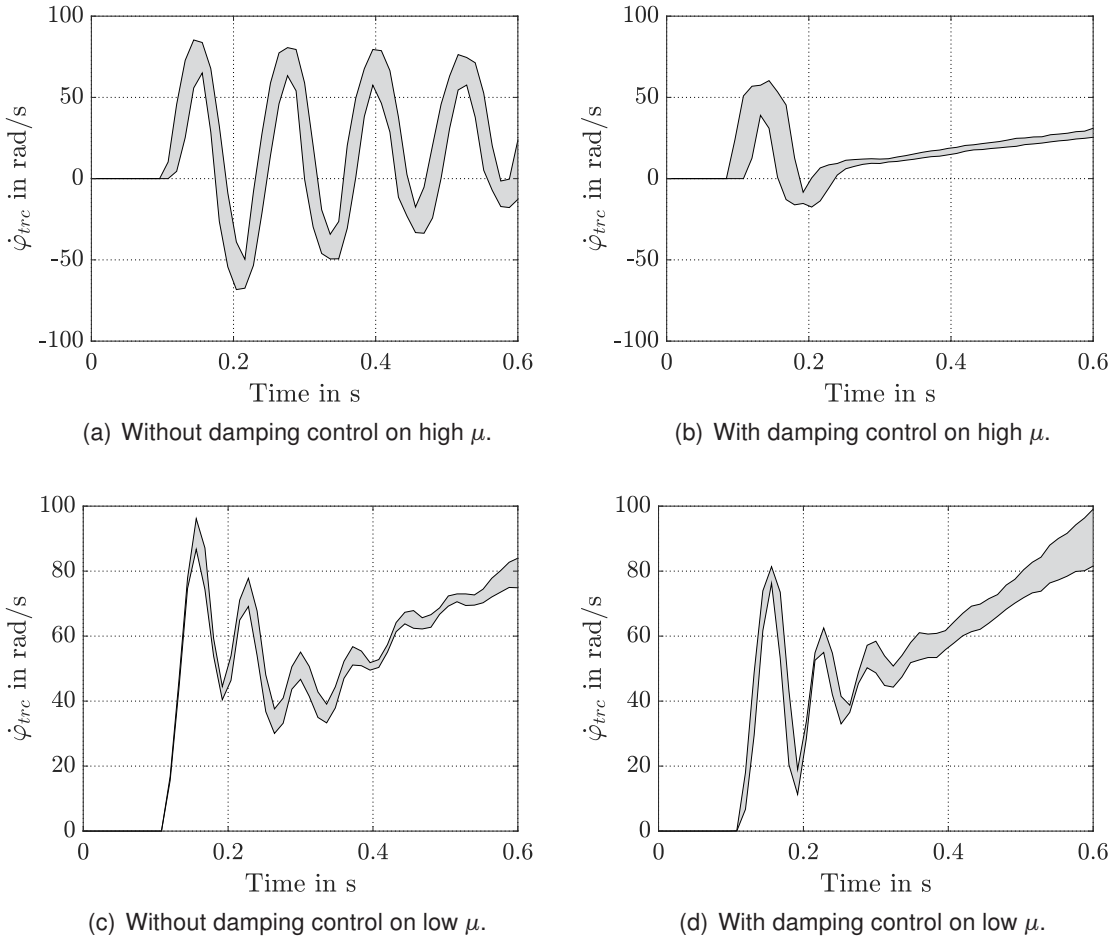

(a) Without damping control on high μ.

(b) With damping control on high μ.

(c) Without damping control on low μ.

(d) With damping control on low μ.

Figure 5.5: Evaluation of damping control with Visio.M's $\dot{\varphi}_{\text{trc}}$ for tip-in maneuvers on high and low μ surfaces

The performance of the internal controller in vehicle tests is displayed in Fig. 5.5. At the top, Fig. 5.5(a) and Fig. 5.5(b) illustrate the traction motor speed response on high μ without and with active damping control. The gray areas contain twelve measurements each. The comparison of the two figures shows that the internal damping controller effectively damps the oscillations

right after the launch. At the bottom, Fig. 5.5(c) and Fig. 5.5(d) demonstrate the behavior on low μ for four measurements each. Already without the internal controller, the oscillations on low μ are smaller in magnitude and decline faster. The improvement by the controller is less obvious. Nevertheless, in Fig. 5.5(c) small oscillations remain after 0.4 s. By that time, the damping control in Fig. 5.5(d) has eliminated the oscillations. The measurements in both test cases match the results of Tab. 5.2.

5.2.2 Torque Vectoring Unit of Prototype Two

The model analysis of section 4.2 predicted the control of Prototype Two's TV-unit to be difficult because of its special inertia distribution. The optimization results in Tab. 5.3 verify this prediction. The high grip case for Prototype Two provides a maximum slip stiffness of $c_{\mathrm{sx}} = 11676$ Nm.

Table 5.3: Evaluation of the optimization results for the Prototype Two's TV-unit

Evaluation metric	Open loop	$T_{\mathrm{Fb,PD}}$	$T_{\mathrm{Fb},\hat{e}} + T_{\mathrm{Fb},\dot{\varphi}_{12}}$
Worst case	123.06	116.45	116.44
$W_{r,e}(s)$ for high grip	33.34	31.03	30.64
$W_{r,e}(s)$ for zero grip	7.59	7.23	7.23
$W_{d,e}(s)$ for high grip	4.21	3.91	3.86
$W_{d,e}(s)$ for zero grip	122.99	116.39	116.37
$W_{r,T_{\mathrm{Fb}}}(s)$ for high grip	0	0.21	0.2
$W_{r,T_{\mathrm{Fb}}}(s)$ for zero grip	0	0.5	0.13
$W_{d,T_{\mathrm{Fb}}}(s)$ for high grip	0	0.03	0.03
$W_{d,T_{\mathrm{Fb}}}(s)$ for zero grip	0	1	1

Both control structures achieve only marginal improvements for Prototype Two because both are limited by the disturbance rejection $W_{d,e}(s)$ at low grip and the constraint on the control gain $W_{d,T_{\mathrm{Fb}}}(s)$. Due to the large actuator inertia, it is not possible to control the strong wheel oscillations caused by disturbances without unreasonably large magnitudes of T_{Fb}. The worst case results do not fully match the result for zero grip. Instead, the worst case is a scenario with c_{sx} close to but not exactly zero. When inspected in detail, the individual scores demonstrate a slight advantage for $T_{\mathrm{Fb},\hat{e}} + T_{\mathrm{Fb},\dot{\varphi}_{12}}$. However, the improvements are too small to label it the better approach. The constraints demonstrate that there would be room for higher gains and performance improvement, if the disturbance rejection at reduced grip levels were to be removed from the optimization objectives. Indeed, when the optimization focuses on high grip scenarios ($c_{\mathrm{sx}} \geq 2500$ Nm), similar improvements to Visio.M are possible with worst case scores for $T_{\mathrm{Fb},\hat{e}} + T_{\mathrm{Fb},\dot{\varphi}_{12}}$ of 12.66 and for $T_{\mathrm{Fb,PD}}$ of 3.5. The controllers act similar to the Visio.M with negative P-gains to achieve the damping. Further, analogue to the Visio.M, $T_{\mathrm{Fb,PD}}$ demonstrates a superior performance because in the high grip conditions the oscillations occur mainly at the actuator side and additional tuning parameters are better than the additional information provided by $\dot{\varphi}_2$. The approach could be used in a combination with ABS, ESP and TRC controllers which keep the tires out of the critical slip area. However, the goal of this chapter is the design of a robust controller especially for critical situations on low μ. The physical properties of Prototype Two's TV-unit prohibit the accomplishment of this goal. Therefore, it is necessary to either redesign the TV-unit itself or to abandon the goal of controlling the wheel torque near the tires' peak performance.

5.3 Discussion

On the basis of the linear parameter varying model, this chapter presents a mathematical optimization procedure for simple damping controllers of vehicle drivetrains. The term simple controller is specified in section 5.1.2. Two control structures were chosen. On the one hand, the combined feedback of $T_{\mathrm{Fb},\hat{e}}$ and $T_{\mathrm{Fb},\dot{\varphi}_{12}}$ utilizes both speed signals, $\dot{\varphi}_1$ and $\dot{\varphi}_2$. On the other hand, $T_{\mathrm{Fb,PD}}$ relies only on $\dot{\varphi}_1$ but contains an additional tuning parameter. The control parameters of each controller are tuned in an optimization procedure according to mathematically described goals and constraints, given in section 5.1.3. The procedure uses a set of linear models and uses mathematical weights to define performance requirements. While the models are validated, the weights are untested and may require further tuning themselves.

The results for the Visio.M's traction unit in section 5.2.1 demonstrate that $T_{\mathrm{Fb,PD}}$ generates the better results among the two controllers. The additional tuning parameter provides more freedom in the design for the optimization. Further, even on low μ the oscillations in the Visio.M occur mainly at the actuator and $\dot{\varphi}_1$ contains sufficient information about the oscillations. The performance of the internal damping algorithm substantiates this fact because it also relies only on $\dot{\varphi}_1$. In section 5.2.2, the TV-unit of Prototype Two proves the importance of the oscillation's distribution for the control performance. On low μ the oscillations occur nearly completely at the wheels and neither control structure is able to suppress them effectively. However, when the optimization is limited to high μ the results confirm the findings for the Visio.M.

In general, the optimization procedure is versatile, proven by the different vehicles and control structures. Nevertheless, its setup leaves room for improvement. First, measurement noise and errors are neglected because the two vehicles used in this dissertation have smooth signals but small sampling rates. Therefore, the focus was on the discrete nature of the systems. However, in vehicles with noisy signals, building derivatives may be more difficult, which would favor $T_{\mathrm{Fb},\dot{\varphi}_{12}}$. Further, the optimization evaluates the model up to half the sampling frequency, which is above 40 Hz for the Visio.M. However, the tire model is not valid for such high frequencies. The internal damping controller in the Visio.M demonstrated its worst case result at frequencies outside the valid area for disturbance rejection on high grip. This could be addressed by limiting the frequency range for the optimization, extending the model and possibly using a different uncertainty representation. Further, the internal controller violated the constraint on the control torque for disturbance rejection on low grip. Yet, the internal controller has been tested over the years in numerous driving experiments, proving its performance and robustness. Therefore, it is possible that the constraint is too strict.

5.4 Conclusion

The main focus of this chapter was to ensure a sufficient control of the wheel torque via active damping in various driving scenarios. In order to achieve this, appropriate and simple control structures were chosen and tuned with an optimization framework. In summary, the results answer research question 2. Simple control structures are capable of the required performance and robustness as long as the drivetrain does not violate the design guidelines of section 4.3 drastically. This emphasizes the importance of an early analysis with the design tools of chapter 4. Also, the results prove that it is necessary to consider a variety of operation points instead of focusing on the high μ case. Further, the optimization shows that it is not possible to achieve better results than with the already existing internal controller due to the limitations of

the CAN bus. This underlines the benefit of a simple control structure, which may be placed directly in the inverter. Future work should be conducted with an internal damping controller, which is optimized by the presented methodology.

6 Backlash Compensation

Backlash can be found in every mechanical machine in which the actuator and load are not connected directly. The transition between the two states can happen rapidly, changing the system's behavior drastically. For controllers, the backlash impairs performance and can even lead to limit cycles. For the mechanical parts in the system, a fast transition from traverse to contact causes additional strain, limiting the drivetrain's lifetime [97, 189]. For the driver, the unsteadiness or interruption in the transient acceleration build up may result in a perception of unreliability and discomfort [31]. If the damping controller works properly, the drivetrain passes the backlash only once during load changes. The backlash compensation in this chapter focuses on the improvement of the driver's perception of the vehicle and the reduction of strain in regular driving operations. It is not aimed at driving conditions near the vehicle dynamics limits, in which ABS, ESP or TRC may be necessary to ensure stability instead of comfort.

As discussed in section 2.2.5, there are numerous approaches to backlash compensation. This dissertation follows the work of Pham et al. [80, 162] and considers the backlash traverse separately from the oscillation damping in contact. A feedforward controller based on differential flatness is used for the backlash compensation. Since no feedback is required it can be applied even when state estimation of the system is difficult. Therefore, the feedforward approach poses a major advantage. However, different feedforward approaches in the form of pre-filters have been already presented, summarized in section 2.2.1. This chapter aims to address the effectiveness of a flatness-based feedforward controller over less complex pre-filter in vehicle tests and thereby answering research question 3 (How effective is a flatness-based backlash compensation compared to other feedforward approaches in vehicle experiments?).

The chapter extends the work in [80, 162] with following contributions:

1. an improved backlash approximation for the flat model based on the arctan function with straight forward parameters;
2. a trajectory for the backlash traverse based on a smooth torque derivative in the driveshafts, which is not based on offline optimization but few tunable parameters;
3. the comparison of the flatness based controller in vehicle tests with no active feedforward controller and a first-order filter.

The chapter is organized as follows: In section 6.1, the feedforward control law is derived based on a differentially flat drivetrain model. The necessary trajectory for this control scheme is presented in section 6.2. Subsequently, the measurement results, provided in section 6.3, demonstrate the benefit of the method in an electric vehicle. In section 6.4, the contributions of the chapter are summarized and future work is outlined.

6.1 Differentially Flat Drivetrain Controller

In this section the feedforward controller is derived based on the differential flatness of the drivetrain. First, the definition of differentially flat systems is introduced. Next, a drivetrain model is presented which satisfies the necessary conditions for differential flatness. Finally, the feedforward control law is derived.

6.1.1 Definition of Differentially Flat Systems

The concept of differential flatness was introduced in [151] and is explained in great detail in [190] and [153]. A continuous-time single-input single-output system in state space form represented by Eq. 6.1 and Eq. 6.2 with the state vector $\boldsymbol{x} \in \mathcal{R}^n$, the input u, the smooth vector field $\boldsymbol{f}$, and the virtual output y_v

$$\dot{\boldsymbol{x}} = \boldsymbol{f}(\boldsymbol{x}, u) \tag{6.1}$$

$$y_\mathrm{v} = h(\boldsymbol{x}) \tag{6.2}$$

is differentially flat if

1. all states and the input can be expressed by the virtual output and a finite number $r = n$ of its derivatives through the smooth functions $\boldsymbol{g}_x$ and g_u,

$$\boldsymbol{x} = \boldsymbol{g}_\mathrm{x}\left(y_\mathrm{v}, \dot{y}_\mathrm{v}, ..., y_\mathrm{v}^{(r-1)}\right) \tag{6.3}$$

$$u = g_\mathrm{u}\left(y_\mathrm{v}, \dot{y}_\mathrm{v}, ..., y_\mathrm{v}^{(r)}\right) \tag{6.4}$$

2. the system has no zero dynamics ($\boldsymbol{0} = \boldsymbol{f}(\boldsymbol{0}, 0)$).

For such a flat system the algebraic equation 6.4 yields the necessary input to track the desired trajectory of y_v. The pivotal points in designing the feedforward controller with differential flatness are identifying a flat output y_v as well as a smooth system representation.

6.1.2 Differentially Flat Drivetrain Model

Figure 6.1 shows the two-inertia model of section 4.1.1 with backlash included in the shaft. In the subsequent paragraphs, $\boldsymbol{f}(\boldsymbol{x}, u)$ is derived for this simplified drivetrain. The main dynamics of the two-inertia oscillator have been widely discussed. Therefore, this section focuses on the necessary simplifications and additions for the flatness based controller. The foundation for the flat drivetrain model are the considerations by Schwarz [183] for his MPC.

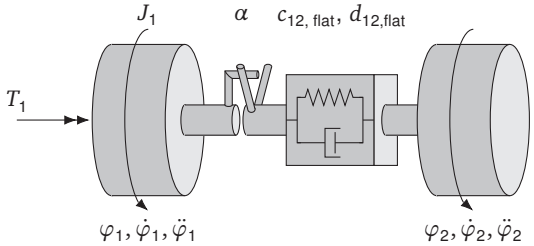

Figure 6.1: Two-inertia drivetrain model with backlash

For the flatness based controller, only the actuator side is considered. Since standard production

vehicles are equipped with stability control systems, the load speed $\dot{\varphi}_2$ is measurable. The load acceleration $\ddot{\varphi}_2$ can be calculated by numeric differentiation. Therefore, $\ddot{\varphi}_2$ demonstrates a known disturbance to the system. As a result, the model does not contain tire dynamics, which makes it easier to find an output describing all states and inputs of the model. However, neglecting tire dynamics eliminates the main source of damping from the system. Therefore, $d_{12,\,\text{flat}}$ contains not only the shaft's damping but also compensates the energy dissipation through the tire. Further, $c_{12,\,\text{flat}}$ replaces c_{12} in order to account for neglected mounting and tire compliance. The results for the two-inertia model in section 4.2.1 demonstrated that the oscillation frequency is overestimated with c_{12}. Therefore, $c_{12,\,\text{flat}}$ is smaller than c_{12}. The shaft model of Eq. 6.5 is based on the arctan approximation of Eq. 3.9. In contrast to the position dependent damping of Eq. 3.9, $d_{12,\,\text{flat}}$ acts independent of the backlash position as a linear damping element. Because the tire compensation overwhelms the shaft's damping, this reduction of complexity is justified. The compensation of the tire's energy dissipation with a constant damper is valid since the primary application of the flatness based controller is on dry roads with tire slip near zero due to load change.

$$\begin{aligned} T_{12} = {} & c_{12,\,\text{flat}}(\varphi_{12}-\alpha)\left(\frac{1}{2}+\frac{\arctan\left(k_\alpha(\varphi_{12}-\alpha)\right)}{\pi}\right) \\ & + c_{12,\,\text{flat}}(\varphi_{12}+\alpha)\left(\frac{1}{2}-\frac{\arctan\left(k_\alpha(\varphi_{12}+\alpha)\right)}{\pi}\right) \\ & + d_{12,\,\text{flat}}\,\dot{\varphi}_{12} \end{aligned} \tag{6.5}$$

The model also neglects actuator dynamics ($T_1 = u$). This avoids the additional state of the first-order transfer function, which is important for choosing a flat output. The simplification is justified by the fast actuator response. Nevertheless, the design of the trajectory must acknowledge that the real actuator cannot change T_1 arbitrarily fast. Further, the feedforward controller does not set T_1 directly. Instead the flatness based controller alters r since it is outside the damping control loop of chapter 5. In contrast to [80], the damping controller is active at all times and should be considered in the model for the feedfoward controller. In the block diagram of Fig. 5.2, feedback control torque T_{Fb} adds to the requested torque r, expressed in Eq. 5.26. Due to the neglected actuator dynamics, Eq. 6.6 represents the incorporation of the feedback loop for the drivetrain model of the feedfoward control design.

$$T_1 = r + T_{\text{Fb}} \tag{6.6}$$

Section 5.1.2 shows that the proportional feedback of $\dot{\varphi}_{12}$ creates additional damping and that it is equivalent to the higher-order feedback of $\dot{\varphi}_1$. Therefore, with the proper choice of the feedback gain k_{Fb}, Eq. 6.7 implements the effect of the damping controller in the model without additional states. Substituting Eq. 6.7 into the actuator impulse of Eq. 4.6 yields Eq. 6.8.

$$T_1 = r - k_{\text{Fb}}\,\dot{\varphi}_{12} \tag{6.7}$$

$$\ddot{\varphi}_1 = \frac{r - k_{\text{Fb}}\dot{\varphi}_{12} - T_{12}}{J_1} \tag{6.8}$$

In summary, the model in state space form with state vector $\boldsymbol{x} = [\varphi_{12}, \dot{\varphi}_{12}]^T$.

$$\begin{bmatrix} \dot{\varphi}_{12} \\ \ddot{\varphi}_{12} \end{bmatrix} = \begin{bmatrix} \dot{\varphi}_{12} \\ \frac{1}{J_1}\left(r - k_{\text{Fb}}\,\dot{\varphi}_{12} - T_{12}\right) - \ddot{\varphi}_2 \end{bmatrix} \tag{6.9}$$

6.1.3 Differentially Flat Drivetrain Controller

Following [80], the virtual output y_v is defined according to Eq. 6.10. It is differentiated twice and Eq. 6.9 is used to replace $\ddot{\varphi}_{12}$. This leads to the algebraic Eq. 6.13 connecting $\ddot{y}_\mathrm{v}$ and r.

$$y_\mathrm{v} = \varphi_{12} \tag{6.10}$$

$$\dot{y}_\mathrm{v} = \dot{\varphi}_{12} \tag{6.11}$$

$$\ddot{y}_\mathrm{v} = \ddot{\varphi}_{12} = \ddot{\varphi}_1 - \ddot{\varphi}_2 \tag{6.12}$$

$$\ddot{y}_\mathrm{v} = \frac{r - k_\mathrm{Fb}\ \dot{\varphi}_{12} - T_{12}}{J_1} - \ddot{\varphi}_2 \tag{6.13}$$

The mapping between y_v and $\boldsymbol{x}$ is given by Eq. 6.10 and Eq. 6.11. However, the disturbance $\ddot{\varphi}_2$ remains in Eq. 6.13. It cannot be expressed by y_v, $\dot{y}_\mathrm{v}$ and $\ddot{y}_\mathrm{v}$ violating the necessary conditions for a flat system. Therefore, r is replaced by the sum of the feedforward controller's output, the torque request T_req, and an additional term compensating the disturbance $\ddot{\varphi}_2$. This is possible since $\dot{\varphi}_2$ is measurable and can be differentiated numerically.

$$r = T_\mathrm{req} + J_1\ \ddot{\varphi}_2 \tag{6.14}$$

$$\ddot{y}_\mathrm{v} = \frac{T_\mathrm{req} - k_\mathrm{Fb}\ \dot{y}_\mathrm{v} - T_{12}\left(y_\mathrm{v}, \dot{y}_\mathrm{v}\right)}{J_1} \tag{6.15}$$

After the disturbance compensation in Eq. 6.14, the system is flat according to the definition stated in Section 6.1.1. The algebraic Eq. 6.15 contains the smooth shaft torque representation of Eq. 6.5 and yields the control law given in Eq. 6.16.

$$T_\mathrm{req} = J_1 \ddot{y}_\mathrm{v} + k_\mathrm{Fb} \dot{y}_\mathrm{v} + T_{12}\left(y_\mathrm{v}, \dot{y}_\mathrm{v}\right) \tag{6.16}$$

6.2 Set Point and Trajectory Generation

The control law in Eq. 6.16 defines u as a function of y_v, $\dot{y}_\mathrm{v}$, $\ddot{y}_\mathrm{v}$. This control law is used to track a trajectory from one setpoint to another ensuring a smooth transition. The setpoints represent the driver's throttle demand. However, since y_v is the twist angle φ_{12}, the setpoints and the trajectory have to be in angular units as well. Therefore, the driver's torque demand is converted to an angular setpoint for the flat output at the beginning of this section. Afterwards, a reference curve for $\dot{\varphi}_{12}$ is derived to limit the shaft's torque rate during setpoint changes. Finally, on the basis of this reference curve, a trajectory is presented, replacing y_v, $\dot{y}_\mathrm{v}$, $\ddot{y}_\mathrm{v}$ in Eq. 6.16. The approach is based on the set-point generation and jerk limitation by the MPC of Schwarz [183].

6.2.1 Setpoint Generation

Because of the sharp approximation of the double arctan backlash model, an inverted deadzone model can be used to create a set point. The driver's torque request T_Throttle is converted to a corresponding angular request $\varphi_\mathrm{12,Throttle}$ by Eq. 6.17. To account for the backlash, α is added

in Eq. 6.18 depending on the sign of $\varphi_{12,\text{Throttle}}$.

$$\varphi_{12,\text{Throttle}} = \frac{i_g}{c_{12,\text{ flat}}} T_{\text{Throttle}} \tag{6.17}$$

$$\varphi_{12,\text{req}} = \begin{cases} \varphi_{12,\text{Throttle}} + \alpha & \varphi_{12,\text{Throttle}} > 0 \\ \varphi_{12,\text{Throttle}} - \alpha & \varphi_{12,\text{Throttle}} < 0 \\ \varphi_{12,\text{Throttle}} & \varphi_{12,\text{Throttle}} = 0 \end{cases} \tag{6.18}$$

The difference between deadzone and arctan model increases when k_α decreases. Therefore, the setpoint calculation results in a steady state error between T_{Throttle} and T_1 near the transition. In such cases an offline optimization as in [80] has to be used for the setpoint generation.

6.2.2 Feedforward Trajectory

The vehicle's acceleration and its rate of change, also called jerk, are important for the driver's perception of comfort and driveability [30, 31, 191]. It has been reported that the perception of the driver depends on the relative jerk compared to the acceleration [30]. According to [191], a high initial jerk may result in a positive evaluation but, according to [30], subsequent oscillations of the jerk hinder subjective results. To reduce the jerk created by the transition into contact $\dot{\varphi}_{12}$ should be limited [76]. This is the main goal of the trajectory presented in the following paragraphs and is one of the main contributions of this chapter. The trajectory presented is only one of many possible trajectories. However, since it relies on trigonometric functions, it is continuously differentiable and a single function can cover the full operation range. However, it is not optimal in a mathematical sense and can be tuned by the application engineer. Similar to the state space model of Eq. 6.9 the dynamics of the trajectory are completely defined by $\ddot{y}_{\text{traj}}$. In the deduction of the trajectory y_{traj} and $\dot{y}_{\text{traj}}$ are assumed to be known. Just like states in a state space model, y_{traj} and $\dot{y}_{\text{traj}}$ are generated by time integration.

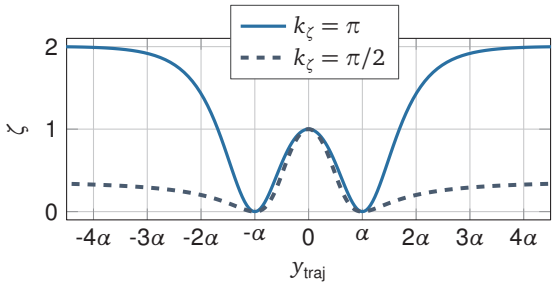

Figure 6.2: Unit-free twist speed curve ξ for two different values of k_ξ over trajectory angle y_{traj}

To limit $\dot{y}_{\text{traj}}$ a dimensionless curve, $\xi \in [0, 2]$, is created.

$$\xi = 1 - \sin\left(k_\xi \arctan\left(i_\xi \left(\frac{y_{\text{traj}}}{\alpha}\right)^2\right)\right) \tag{6.19}$$

with

$$i_\xi = \tan\left(\frac{\pi}{2k_\xi}\right) \tag{6.20}$$

Fig. 6.2 demonstrates that ξ is reduced to its minimum near the transition at $y_{\text{traj}} = \pm\alpha$. Raising

k_ξ increases ξ in contact relative backlash traverse. A reasonable range for tuning is $k_\xi \in [1, \pi]$. In order to convert ξ to a reference speed for $\dot{y}_{\text{traj}}$, a maximum traverse speed $k_{12,0}$ and a transition speed $k_{12,\alpha}$ are defined. In Eq. 6.21, ξ is scaled and shifted so the traverse speed is reached in the middle of the backlash whereas the lower transition speed reduces jerk at $y_{\text{traj}} = \pm\alpha$. For a smooth set point approach an additional arctan function scales $\dot{y}_{\text{ref}}$, reducing $\dot{y}_{\text{ref}}$ near $\varphi_{12,\text{req}}$. The arctan term also defines the sign of $\dot{y}_{\text{ref}}$.

$$\dot{y}_{\text{ref}} = \frac{2}{\pi} \arctan\left(k_{\text{req}}\left(\varphi_{12,\text{req}} - y_{\text{traj}}\right)\right)\left(\left(k_{12,0} - k_{12,\alpha}\right)\xi + k_{12,\alpha}\right) \tag{6.21}$$

The differentiation of $\dot{y}_{\text{ref}}$ yields the reference acceleration of the trajectory $\ddot{y}_{\text{ref}}$, given in Eq. 6.22. The driver's request is assumed to be constant.

$$\begin{aligned}\ddot{y}_{\text{ref}} = {} & \frac{2}{\pi} \arctan\left(k_{\text{req}}\left(\varphi_{12,\text{req}} - y_{\text{traj}}\right)\right)\left(k_{12,0} - k_{12,\alpha}\right)\dot{\xi} \\ & + \frac{2}{\pi} \frac{-k_{\text{req}}\dot{y}_{\text{traj}}}{1 + \left(k_{\text{req}}\left(\varphi_{12,\text{req}} - y_{\text{traj}}\right)\right)^2}\left(\left(k_{12,0} - k_{12,\alpha}\right)\xi + k_{12,\alpha}\right)\end{aligned} \tag{6.22}$$

with

$$\dot{\xi} = -\cos\left(k_\xi \arctan\left[i_\xi\left(\frac{y_{\text{traj}}}{\alpha}\right)^2\right]\right) \frac{k_\xi}{1 + \left[i_\xi\left(\frac{y_{\text{traj}}}{\alpha}\right)^2\right]^2} \frac{2 i_\xi}{\alpha^2} y_{\text{traj}} \dot{y}_{\text{traj}} \tag{6.23}$$

To ensure tracking, $\dot{y}_{\text{traj}}$ is compared to $\dot{y}_{\text{ref}}$ and the error is fed to $\ddot{y}_{\text{traj}}$ through the gain k_{traj}. The final trajectory defined by $\ddot{y}_{\text{traj}}$ is given by Eq. 6.24.

$$\ddot{y}_{\text{traj}} = \ddot{y}_{\text{ref}} + k_{\text{traj}}\left(\dot{y}_{\text{ref}} - \dot{y}_{\text{traj}}\right) \tag{6.24}$$

6.3 Results

The flatness-based controller is evaluated on the traction unit of the Visio.M because it has the largest backlash of the two vehicles considered in this dissertation. The controller is implemented on the main control unit. Therefore, the communication to the motor and the sensors is via CAN. This section is organized as follows. First, the drivetrain model, which is the foundation of the flatness-based controller, is compared to measurement data illustrating the open-loop model's fit. Afterwards, the flatness-based controller is evaluated, using two alternative control approaches as benchmarks. Model and controller are evaluated in tip-ins and tip-outs because they are the common load changing maneuvers in the traction unit.

6.3.1 Comparison of Flat Model and Measurements

Section 3.2 focused on the validation of the drivetrain models. The model of the flatness-based controller matches in large parts these models. Therefore, the additional simplifications, which were specifically made for the flat model derived in section 6.1.2, are validated in this section. To evaluate the fit of the drivetrain model, it is compared to measurement data with and without the feedback damping controller. The inputs to the model are the requested torque r and the wheel speed $\dot{\varphi}_2$. Since only the traction unit of the Visio.M is considered, the output is the motor speed $\dot{\varphi}_{\text{trc}}$. Most parameters of the flat model are identical to the other models' parameters in

Table 3.1. Table 6.1 shows the additional necessary parameters for the flat model.

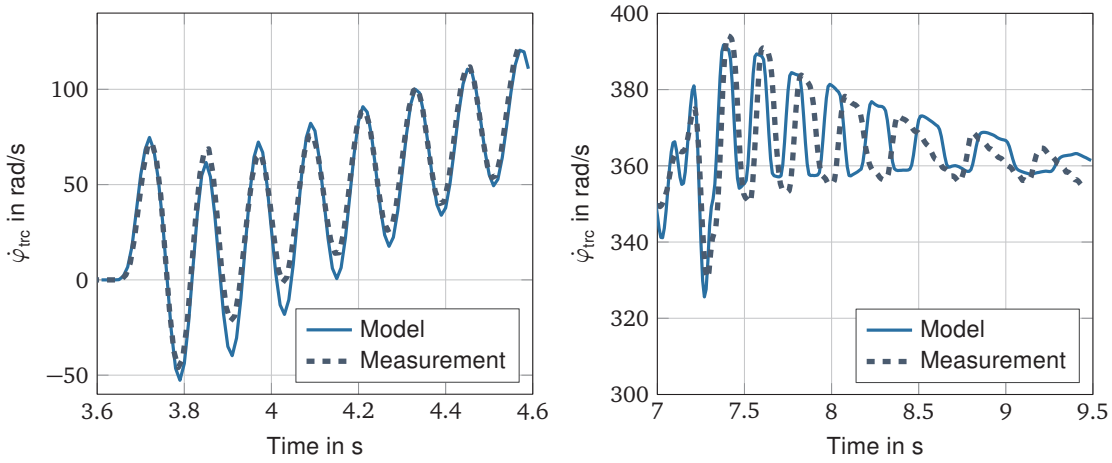

(a) Tip-in from standstill from 0 Nm to 80 Nm

(b) Tip-out from 80 Nm to 0 Nm

Figure 6.3: Evaluation of flat drivetrain model with deactivated damping controller ($k_{Fb} = 0$ Nm s/rad)

First, the damping controller is deactivated to evaluate the oscillation behavior of the model in contact and backlash. Figure 6.3 shows the results for a tip-in to the maximum torque of 80 Nm (left) followed by a tip-out to 0 Nm (right). The flat model demonstrates an even better fit than the nonlinear model in section 3.2.2. The reason is that tire dynamics are neglected and the compensation in the shaft's damping is tuned to fit specifically dry road tests at low speed. The nonlinear model of section 3.2.2, however, is applicable to multiple test cases. At about 35 kph the tip-out reduces r to zero ($t \approx 7.25$ s). Following the smooth oscillations in the acceleration phase $\dot{\varphi}_{trc}$ drops significantly during the backlash traverse. Subsequently, a nonlinear oscillation in model and measurement occurs. Since the motor is at zero torque it repeatedly traverses the backlash. In this phase, the backlash angle α and the damping constant $d_{12,\,flat}$ mainly define the model behavior. However, due to the low shaft torque in this phase, model simplifications and disturbances have a greater effect on the model fit, similar to the tip-ins on a lift in section 3.2.2. Therefore, the close match demonstrated for the tip-in could not be reproduced for the tip-out.

Second, the damping controller is activated. The tip-in maneuver on the left of Fig. 6.4 shows an initial rise in $\dot{\varphi}_{trc}$ similar to without the damping controller. This spike emphasizes the potential for improvement. However, the oscillations subsequently decline quickly in the model and the measurement. This demonstrates the good performance of the damping controller in contact. In electric vehicles releasing the accelerator pedal often results in a regenerative braking torque. The braking torque is a design variable [13]. After the behavior in the backlash at $r = 0$ Nm was examined, the tip-out maneuvers from here on are conducted with a final torque of $r = -10$ Nm. On the right of Fig. 6.4 the active deceleration of the motor results in a larger drop $\dot{\varphi}_{trc}$ than in Fig. 6.3. After this rapid backlash traverse, the damping controller quickly reduces the

Table 6.1: Parameters of the drivetrain model collected from datasheets or fitted to measurement data

Parameter	Value	Unit
k_{Fb}	4.06	Nms/rad
$d_{12,\,flat}$	1.764	Nms/rad
$c_{12,\,flat}$	3600	Nm/rad
k_{α}	250	1/rad

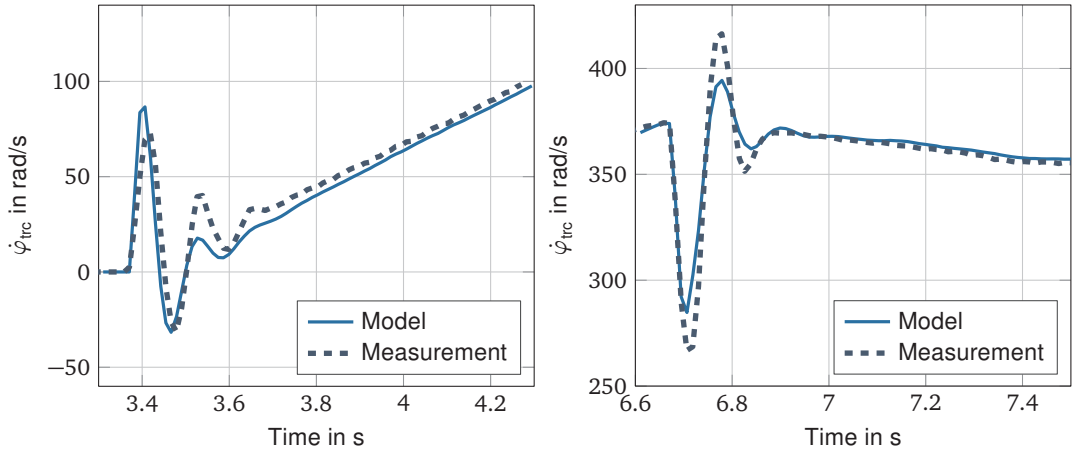

(a) Tip-in from standstill from 0 Nm to 80 Nm

(b) Tip-out from 80 Nm to -10 Nm

Figure 6.4: Evaluation of flat drivetrain model with activated damping controller ($k_{Fb} = 0.4$ Nm s/rad)

oscillations. The results prove that the simplifications made for the flat model are justified and create a satisfying fit for the test scenario of low speeds on dry roads.

6.3.2 Evaluation of the Feedforward Controller

After the model was verified, the flatness-based controller was tested. The parameters for the trajectory used in the following experiments are shown in Table 6.2. The tuning of the parameters follows two main objectives. First, leave the low torque area quickly since the models are least reliable for low shaft torques. Second, avoid strong deceleration torques prior to reaching the contact because slow communication and the unknown backlash position make a precise deceleration impossible. The second principle falls in line with the "weak action in the gap" concept, which Nordin and Gutman [97, p. 1646] identified as the best approach to passing the backlash. The trajectory for the tip-in is illustrated in Fig. 6.5 in the time domain.

At $t = 0.052$ s the torque request jumps to 80 Nm. This request is converted to a setpoint angle, displayed in the top plot, causing the spike in $\ddot{y}_{traj}$ at the bottom. The acceleration declines as y_{traj} approaches the transition point. In the middle, $\dot{y}_{traj}$ does not reach the transition speed $k_{12,\alpha}$. Because of the limitation of the CAN frequency of 167 Hz, the trajectory has to be designed conservatively. After the transition, $\ddot{y}_{traj}$ and $\dot{y}_{traj}$ increase again. Finally, the trajectory slows down for a smooth setpoint approach.

Limiting the torque gradient is a common way to reduce oscillations and jerk [73, 128]. Therefore, the flatness-based controller is compared to a regular step and a first-order filter. The time constant is set according to the time the trajectory takes to reach the setpoint. Fig. 6.6 compares the performance of the different approaches with tip-ins on the left and tip-outs on the right. To

Table 6.2: Parameters of the trajectory used for the experiments

Parameter	Value	Unit
k_{ξ}	π	-
k_{req}	15	1/rad
k_{traj}	80	1/s
$k_{12,0}$	4	rad/s
$k_{12,\alpha}$	3	rad/s

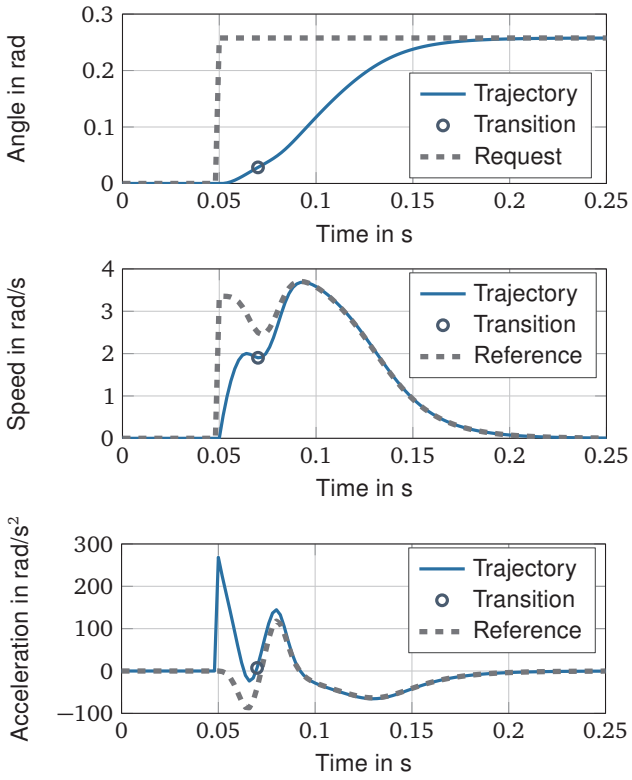

Figure 6.5: Calculated trajectory (y_{traj}, $\dot{y}_{traj}$, $\ddot{y}_{traj}$) for a tip-in from 0 Nm to 80 Nm (solid line) with the transition point (o), the angular position request $\varphi_{12,req}$ (dashed line) and the reference $\dot{y}_{ref}$, $\ddot{y}_{ref}$ (dashed line)

the top, Fig. 6.6(a) and Fig. 6.6(b) display the torque request for tip-in and tip-out respectively. In these maneuvers, two criteria evaluate the controller's performance. The first criteria is $\ddot{\varphi}_{trc}$ to evaluate the strain on components, shown in Fig. 6.6(c) and Fig. 6.6(d). The second criteria is the vehicle's jerk, since the jerk is felt by the driver, illustrated in Fig. 6.6(e) and Fig. 6.6(f). Since the maximum acceleration is the same in all test cases, the reduction of oscillations in the jerk is most important to the driver's perception of the vehicle [30].

Each test case is passed three times and the mean of the results is plotted. Since the initial position of the shaft inside the backlash is unknown, which may affect the impact of the backlash transition, the mean is used to evaluate the general improvement due to the controller. Tab. 6.3 contains the mean values alongside the standard deviations for the significant peaks. Because the experiments focus on high grip conditions, disturbances play a minor role and the

Table 6.3: Result summary for comparison of hard step, first order low pass and the flatness-based controller by their mean peak values with the standard deviation in brackets

	Tip-in			Tip-out		
$\ddot{\varphi}_{trc}$ in rad/s²	Flatness	Filter	Step	Flatness	Filter	Step
Pos. peak	820 (342)	2353 (476)	2394 (1121)	916 (57.2)	1457 (177)	3648 (472)
Neg. peak	-849 (168)	-3113 (722)	-3491 (1295)	-524 (83.3)	-1815 (122)	-3648 (872)
	Tip-in			Tip-out		
Jerk in m/s³	Flatness	Filter	Step	Flatness	Filter	Step
Pos. peak	46.8 (24.1)	164 (83.2)	134 (34.0)	8.50 (2.04)	25.8 (1.13)	100 (11.3)
Neg. peak	-27.5 (0.98)	-109 (66.8)	-113 (47.6)	-48.7 (3.71)	-102 (6.53)	-147 (35.4)

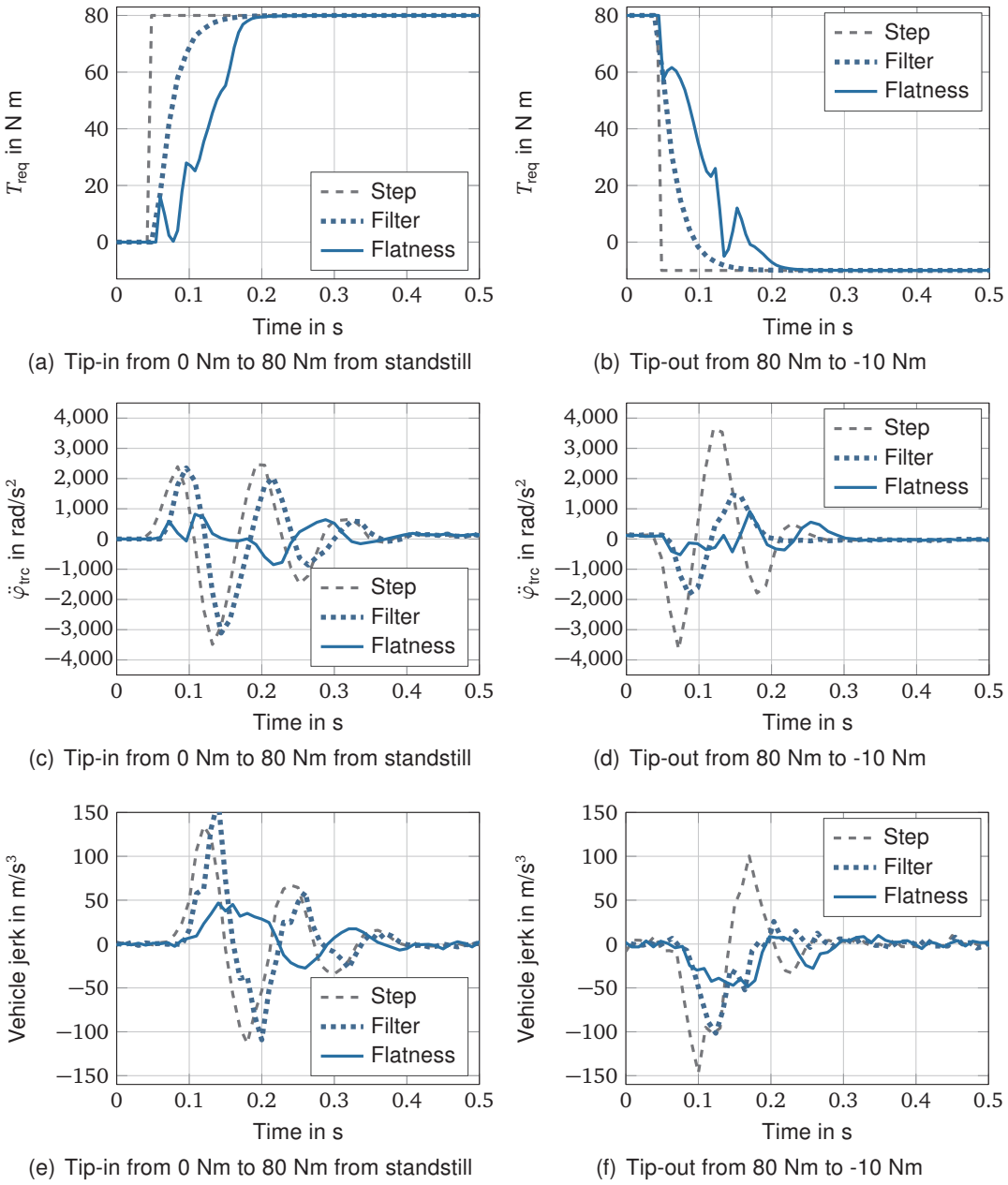

(a) Tip-in from 0 Nm to 80 Nm from standstill

(b) Tip-out from 80 Nm to -10 Nm

(c) Tip-in from 0 Nm to 80 Nm from standstill

(d) Tip-out from 80 Nm to -10 Nm

(e) Tip-in from 0 Nm to 80 Nm from standstill

(f) Tip-out from 80 Nm to -10 Nm

Figure 6.6: Comparison of a hard step (dashed line), a first order low pass (dotted) and the flatness-based controller (solid line)

measurements in general show a limited spread, proven by section 3.2.2.

The tips-ins are analyzed first. The vehicle launches from standstill with a torque step from 0 Nm to 80 Nm. At the top in Fig. 6.6(a), the flatness-based controller shows a first peak of 20 Nm directly after the step request at $t = 0.05$ s, but reduces r back to zero for the transition. Afterwards, r increases with a small peak close to $T = 0.1$ s. Close after the step, r of the flatness-based controller is defined by $\dot{y}_{traj}$ and $\ddot{y}_{traj}$. As y_{traj} increases, the shaft's stiffness progressively dominates the torque calculation and y_{traj} mainly defines r. Since the calculation of the trajectory is executed on the control unit with a sampling rate of 0.002 s but r is transferred via CAN with a rate of 0.006 s, the measured torque curve is not as smooth as the trajectory. The reduction of the gradient in T_{req} by the filter compared to the hard step is also illustrated. However, the simple filter cannot account for the transition and shows the largest gradients at

low torques. But it is in this region that the transition occurs. In Fig. 6.6(c), the curves without and with filter show similar oscillation amplitudes in $\ddot{\varphi}_{\text{trc}}$. Since the filter steadily accelerates the motor it does not significantly soften the backlash transition. The inverter's damping controller has a greater effect than the filter. Therefore, the filter does not produce a noteworthy benefit for the tip-in. However, the flatness-based controller can reduce the positive peaks of $\ddot{\varphi}_{\text{trc}}$ to a third the size and the negative peak even to a quarter. All three strategies reach the steady state at about $t = 0.4$ s with a constant acceleration of about 3.1 m/s^2. At the bottom in Fig. 6.6(e), the jerk shows similar results. The filter exceeds the jerk of the hard because one measurement is extraordinarily larger. The standard deviation further demonstrates this outlier. Analogue to $\ddot{\varphi}_{\text{trc}}$, the flatness-based controller cuts the peaks to about one third.

The tip-outs in Fig. 6.6(b) start in the acceleration phase with 80 Nm and step down to -10 Nm. Because of the step from a high acceleration torque to a modest braking torque, the filter produces much lower gradients in the region of a possible backlash traverse and transition into contact. The flatness-based controller displays a complex torque request caused by the repeated acceleration and deceleration when passing from an acceleration to a braking torque. Since the simple filter acts softly in the backlash, it reduces $\ddot{\varphi}_{\text{trc}}$ significantly in Fig. 6.6(d). However, the flatness-based controller still shows by far the best results. In contrast to the tip-in, the three strategies do not reach the steady state at the same time. The filter has an advantage of about 0.1 s over the flatness-based control. The jerk in Fig. 6.6(f) follows the results in $\ddot{\varphi}_{\text{trc}}$. The filter cuts the jerk down to two thirds whereas the flatness-based controller achieves a reduction to one third of the value for the hard step. The steady state deceleration is 0.6 m/s^2.

6.4 Discussion

This chapter focused on the improvement of backlash compensation in vehicle drivetrains with respect to the vehicle's jerk and motor acceleration. First, a flat model of the drivetrain is presented. It is based on the two-inertia model but incorporates the damping of the tire and the feedback control in an altered shaft damping coefficient $d_{12,\text{flat}}$. The model's stiffness $c_{12,\text{flat}}$ includes the shafts stiffness as well as mounting and tire compliance. The wheel acceleration $\ddot{\varphi}_2$ is assumed to be known. Due to these simplifications, model complexity is small and flatness is achieved. Similar to the arctan backlash approximation, the trajectory is also based on trigonometric functions.

The results show the benefit of a flatness-based feedforward backlash compensation over a first-order filter and no control at all. Regarding the torque request for backlash compensation, Nordin and Gutman [97] identify two concepts, "strong action in the gap" and "weak action in the gap", with the later being the more promising one. Pham [162, p. 89 f.] follows the principle of "strong action in the gap". A large positive torque minimizes the time to pass the backlash gap and a large negative torque, shortly before contact, reduces the impact to a minimum. In simulation, the results are promising. However, if the negative torque is late, the transition into contact occurs without the braking torque and causes a high jerk and strong motor deceleration. Following the impact, the late negative torque disconnects the motor from the load again and creates a second backlash traverse in negative direction. In contrast to Pham [162, p. 89 f.], the trajectory in this dissertation creates a 10 Nm peak torque inside the backlash and reduces the torque to 0 Nm near the contact area. The small initial peak successfully initiates the backlash pass. Because of the small acceleration of the motor no large braking torque is required to soften the transition into contact. Therefore, deviations between estimated backlash position

and true position are not as problematic as for a "strong action in the gap" approach. However, a "too weak action" policy can cause problems as well because the feedback damping controller is tuned for the drivetrain in contact.

For the comparison with the first-order filter, the response time until the feedforward control reaches the set point is important to create a neutral basis for the comparison. However, it is not possible to tune the flatness-based control and the filter to reach the setpoint in tip-ins and tip-outs within the same time. Therefore, the filter has a disadvantage in the tip-out, because it passes the backlash quicker. In addition, the flatness-based controller requires more parameters, which were tuned specifically for these test cases. Evaluating the method's robustness to parameter variations in experiments is a necessary next step, even though the "weak action in the gap" should demonstrate a better robustness than "strong action in the gap" approaches. In addition, the performance in changing conditions remains an open topic, especially if disturbances at the wheel are fed into the feedforward controller through $\ddot{\varphi}_2$. The disturbances in the experiments were small and further tests should be conducted in this regard.

Further improvement in performance may be possible with a state estimator to check the tracking of the trajectory. In this study, a perfect tracking is assumed but deviations are inevitable in reality. As discussed in the introduction, many publications focus on state estimation in drivetrains with backlash. An estimator would add complexity to the control system. However, with a reliable backlash position estimation, stronger action in the gap is possible, which would improve the traverse time. In addition, backlash size estimator was presented in [77] to adapt the feedforward controller to changing backlash size. This could be caused by wear over a vehicle lifespan or changing parts. However, the flatness-based compensation demonstrates good performance even for double or half the backlash size. Appendix C.3 illustrates this.

6.5 Conclusion

The goal of this chapter was the reduction of backlash effects with a flatness-based feedforward control. The required flat drivetrain model was derived from the complex nonlinear model of chapter 3. As Pham et al. [80, 162] already applied flatness based control to drivetrain backlash, the main contribution of this work are the measurements along with the trajectory design. The results demonstrate that the flatness-based approach cuts uncomfortable jerk and component stress to a quarter of the initial values. Therefore, the answer to research question 3 is that a flatness-based backlash compensation is highly effective in reducing jerk and component stress. However, its performance depends strongly on the trajectory, which must be tuned carefully for the application.

For an implementation in production vehicles, identifying the necessary parameters of a flatness-based control scheme may be a challenging task. Therefore, a reduction in complexity could extend the field of application. Pre-filters of higher order, as presented in [91], [129] and [51], could resemble the general behavior of the flatness-based controller with less complexity. However, purely linear controllers cannot recreate the different behavior in contact and in the backlash gap. This could lead to a switching feedforward controller in the style of the feedback control proposed by Nordin and Gutman [192], which is a switching controller based on the input torque.

7 Conclusion

This dissertation focused on the improvement of vehicle dynamics in high and low grip conditions for EVs with TVDs in order to increase the appeal to consumers. The core of vehicle dynamics control is an accurate wheel torque control, which requires sufficient damping of low-frequency oscillations. Among the different EV drivetrains, TVDs demonstrate benefits in the scaling of the motors and in their TV capabilities. However, they are complex mechanical systems and previous studies have focused on the less complex on-board motor topology or standard center differential drivetrains. Since the field of low-frequency oscillations in drivetrains has been widely studied, the main contributions of this dissertation extend previous results in answering three research questions. The subsequent paragraphs summarize the answers to the research questions along with the discussion of related results. Based on this summary, an outlook to future work is given.

Which dynamics of TVD drivetrains are common to vehicle drivetrains in general and which are unique to TVDs?

Chapter 4 addresses the drivetrains' dynamics based on the model and experimental validation of chapter 3. The TVD separates into two independent units, the traction and the TV-unit, which act similar to other drivetrains. Both units are subject to the changes in tire dynamics, which are the most important phenomenon for low-frequency oscillations. In a simplified two-inertia model, these changes relate to changes in load inertia. In this regard, the TVDs are directly linked to other vehicle drivetrain topologies but also to electric drives in general. The choice of the actuator inertia with respect to the load inertia defines the behavior of the system. Even though the two-inertia model requires strong simplifications, the final guidelines of section 4.3 are valid and reasonable for TVDs and other drivetrains. The special effect of the anti-phase wheel oscillations of Prototype Two exist because it deviates strongly from these general design guidelines. The only fundamental difference of a TVD to other drivetrains is that the TV-unit does not couple with the pitch motion of the drivetrain mounting, which is after shaft and tire dynamics possibly the third most important contributor to low-frequency drivetrain oscillations.

In the future, the behavior of a TVD which complies with the design guidelines of section 4.3 should be investigated. If traction and TV-unit satisfy $J_1 = J_{2,0}$, both units would have similar eigenfrequencies. In theory, even in such a case, the TVD is still decoupled. Nevertheless, only experiments can prove that such a design performs well in all relevant driving conditions.

Can simple controllers satisfy performance and robustness goals in a variety of tire operation points?

Chapter 5 addresses this research question. Prior to answering the performance and robustness question, the term "simple controller" is defined more precisely in section 5.1.2 by theoretical considerations based on the two-inertia model. A proportional feedback of the speed difference between actuator and wheel can increase damping. The estimation of the shaft torque with a DT1 transfer function (D-controller) based on the actuator speed yields the potential to increase the system's bandwidth for increased performance with a proportional feedback. Further, an

additional derivative feedback of the estimated shaft torque achieves damping. Therefore, the simple controllers are of first and second order.

The control parameters were optimized for a set of models, which represented the uncertainties of changing tire operation points, with mathematically specified design objectives and constraints. The results of the optimization call for a restricted answer to the research question depending on the actuator inertia J_1 and the zero-grip load inertia $J_{2,0}$. If $J_1 \gg J_{2,0}$, which is the case for the TV-unit of Prototype Two, the controllers are not able to satisfy performance and robustness goals in the face of changing tire operation points. However, with a more balanced inertia distribution, the simple controllers do satisfy performance and robustness goals. The optimization produces the best results with the second order feedback of the actuator speed signal only. This is an important outcome, since such a controller does not rely on additional information from other control units and can be implemented directly on the inverter.

Due to time constraints, it was not possible to test the optimized damping controllers in the vehicles and in combination with ABS, ESP or TRC controllers. Rosenberger [24, p. 107] has demonstrated the benefits of the damping controller in an on-board motor drivetrain for ABS experiments. A TVD drivetrain should perform similarly. However, the superposition of traction and TV-unit could create special challenges. For example, if the required TV torque changes sign quickly and frequently, the backlash could play an important role.

How effective is a flatness-based backlash compensation compared to other feedforward approaches in vehicle experiments?

The results of chapter 6 illustrate that the flatness-based backlash compensation improves comfort by reducing jerk significantly. It also reduced the motor's acceleration limiting component stress. It reduces the jerk and the motor acceleration in tip-in and tip-out experiments. In contrast, the first-order filter can not meet the performance of the flatness-based compensation because it does not acknowledge the switching nature of the backlash. However, the flatness-based feedforward control requires a flat model representation of the drivetrain and a trajectory to pass the backlash. The trajectory mainly defines the torque request by the feedforward control. There are two concepts for the trajectory, namely "strong action in the gap" and "weak action in the gap" [97]. The choice depends on the knowledge about the system. In this dissertation, the trajectory was tuned to follow the concept of "weak action in the gap". Because of the large sampling time of the Visio.M and because there is no information on the true backlash position, it is not possible to stop the motor right before impact. With the "weak action in the gap", such a precise braking torque is not necessary but the traverse time through the backlash is not optimal.

Future work in the area of backlash compensation is possible in two directions. On the one hand, with respect to fast and repeated load changes, for example in the TV-unit of a TVD in critical driving situations, stronger action in the gap could improve the traverse time based on an accurate estimation of the backlash position. A variety of publications exists in this field. However, precise measurements and actuators are essential for a fast and smooth traverse. On the other hand, the main reduction of jerk is caused by the small torque spike followed by a reduction in torque before the final rise to the desired setpoint. Such a behavior could be replicated with less complex switching linear filters. Therefore, a future investigation could follow a similar question as this dissertation did for the feedback control: "Can simple pre-filters create a fast and smooth backlash traverse?".

List of Figures

List of Tables

Bibliography

[1] C. Figueres, H. J. Schellnhuber, G. Whiteman, J. Rockström, A. Hobley and S. Rahmstorf, „Three years to safeguard our climate," *Nature*, vol. 546, no. 7660, pp. 593–595, 2017, DOI: 10.1038/546593a.

[2] „EU transport in figures: Statistical pocketbook 2018," European Commission, Luxembourg, 2018.

[3] L. Guzzella and A. Sciaretta, *Vehicle Propulsion System: Introduction to Modeling and Optimization*, Berlin Heidelberg, Springer, 2007, ISBN: 978-3-540-25195-8.

[4] International Energy Agency, „World Energy Balances 2018: Overview," Paris, 2018. Available: https://webstore.iea.org/world-energy-balances-2018.

[5] International Energy Agency, „Energy Efficiency Indicators 2018: Highlights," Paris, 2018. Available: https://webstore.iea.org/energy-efficiency-indicators-2018-highlights.

[6] R. Colvile, E. Hutchinson, J. Mindell and R. Warren, „The transport sector as a source of air pollution," *Atmospheric Environment*, vol. 35, no. 9, pp. 1537–1565, 2001, DOI: 10.1016/S1352-2310(00)00551-3.

[7] T. R. Hawkins, B. Singh, G. Majeau-Bettez and A. H. Strømman, „Comparative Environmental Life Cycle Assessment of Conventional and Electric Vehicles," *Journal of Industrial Ecology*, vol. 17, no. 1, pp. 53–64, 2013, DOI: 10.1111/j.1530-9290.2012.00532.x.

[8] N. Künzli, R. Kaiser, S. Medina, M. Studnicka, O. Chanel, P. Filliger, M. Herry, F. Horak, V. Puybonnieux-Texier, P. Quénel, J. Schneider, R. Seethaler, J.-C. Vergnaud and H. Sommer, „Public-health impact of outdoor and traffic-related air pollution: A European assessment," *The Lancet*, vol. 356, no. 9232, pp. 795–801, 2000, DOI: 10.1016/S0140-6736(00)02653-2.

[9] J. Woodcock, D. Banister, P. Edwards, A. M. Prentice and I. Roberts, „Energy and transport," *The Lancet*, vol. 370, no. 9592, pp. 1078–1088, 2007, DOI: 10.1016/S0140-6736(07)61254-9.

[10] T. Kuhnimhof, R. Buehler, M. Wirtz and D. Kalinowska, „Travel trends among young adults in Germany: Increasing multimodality and declining car use for men," *Journal of Transport Geography*, vol. 24, pp. 443–450, 2012, DOI: 10.1016/j.jtrangeo.2012.04.018.

[11] J. Woodcock, P. Edwards, C. Tonne, B. G. Armstrong, O. Ashiru, D. Banister, S. Beevers, Z. Chalabi, Z. Chowdhury, A. Cohen, O. H. Franco, A. Haines, R. Hickman, G. Lindsay, I. Mittal, D. Mohan, G. Tiwari, A. Woodward and I. Roberts, „Public health benefits of strategies to reduce greenhouse-gas emissions: Urban land transport," *The Lancet*, vol. 374, no. 9705, pp. 1930–1943, 2009, DOI: 10.1016/S0140-6736(09)61714-1.

[12] S. Campanari, G. Manzolini and F. La Garcia de Iglesia, „Energy analysis of electric vehicles using batteries or fuel cells through well-to-wheel driving cycle simulations," *Journal of Power Sources*, vol. 186, no. 2, pp. 464–477, 2009, DOI: 10.1016/j.jpowsour.2008.09.115.

[13] D. A. Crolla and D. Cao, „The impact of hybrid and electric powertrains on vehicle dynamics, control systems and energy regeneration," *Vehicle System Dynamics*, vol. 50, pp. 95–109, 2012, DOI: 10.1080/00423114.2012.676651.

[14] J. Rauh and D. Ammon, „System dynamics of electrified vehicles: Some facts, thoughts, and challenges," *Vehicle System Dynamics*, vol. 49, no. 7, pp. 1005–1020, 2011, DOI: 10.1080/00423114.2011.582122.

[15] International Energy Agency, „Global EV Outlook 2018," Paris, 2018. Available: https://webstore.iea.org/global-ev-outlook-2018.

[16] W. Sierzchula, S. Bakker, K. Maat and B. van Wee, „The influence of financial incentives and other socio-economic factors on electric vehicle adoption," *Energy Policy*, vol. 68, pp. 183–194, 2014, DOI: 10.1016/j.enpol.2014.01.043.

[17] S. Raszewski, *The International Political Economy of Oil and Gas*, Cham, Springer International Publishing, 2018, DOI: 10.1007/978-3-319-62557-7.

[18] „Global EV Outlook 2019," Paris, 2019. Available: https://webstore.iea.org/global-ev-outlook-2019.

[19] M. Berriri, P. Chevrel and D. Lefebvre, „Active damping of automotive powertrain oscillations by a partial torque compensator," *Control Engineering Practice*, vol. 16, no. 7, pp. 874–883, 2008, DOI: 10.1016/j.conengprac.2007.10.010.

[20] O. Hayat, M. Lebrun and E. Domingues, „Powertrain Driveability Evaluation: Analysis and Simplification of Dynamic Models," *SAE Technical Paper*, no. 2003-01-1328, 2003, DOI: 10.4271/2003-01-1328. Available: https://doi.org/10.4271/2003-01-1328.

[21] G. Götting, „Dynamische Antriebsregelung von Elektrofahrstraßenfahrzeugen unter Berücksichtigung eines schwingungsfähigen Antriebsstrangs," dissertation, RWTH, Aachen, 2003.

[22] V. Ivanov, D. Savitski and B. Shyrokau, „A Survey of Traction Control and Antilock Braking Systems of Full Electric Vehicles With Individually Controlled Electric Motors," *IEEE Transactions on Vehicular Technology*, vol. 64, no. 9, pp. 3878–3896, 2015, DOI: 10.1109/TVT.2014.2361860.

[23] L. de Novellis, A. Sorniotti, P. Gruber, L. Shead, V. Ivanov and K. Hoepping, „Torque Vectoring for Electric Vehicles with Individually Controlled Motors: State of the Art and Future Developments," *EVS International Battery, Hybrid and Fuel Cell Electric Vehicle Symposium*, vol. 26, 2012.

[24] M. Rosenberger, „Regelung radnaher elektrischer Einzelradantriebe während der ABS-Bremsung," dissertation, Institute of Automotive Technology, Technical University of Munich, Munich, 2013.

[25] V. Ivanov, D. Savitski, J. Orus, J. M. R. Fortun, A. Sorniotti and P. Gruber, „All-wheel-drive electric vehicle with on-board motors: Experimental validation of the motion control systems," *Annual Conference of the IEEE Industrial Electronics Society, IECON*, vol. 41st, pp. 001729–001734, 2015, DOI: 10.1109/IECON.2015.7392351.

[26] G. Götting and R. W. de Doncker, „Active drive control of electric vehicles using a modal state observer," *IEEE Annual Power Electronics Specialists Conference*, vol. 35th, pp. 4585–4590, 2004, DOI: 10.1109/PESC.2004.1354810.

[27] K. Z. Yeap and S. Müller, „Characterising the interaction of individual-wheel drives with traction by linear parameter-varying model: A method for analysing the role of traction in torsional vibrations in wheel drives and active damping," *Vehicle System Dynamics*, vol. 54, no. 2, pp. 258–280, 2016, DOI: 10.1080/00423114.2015.1131306.

[28] R. E. Dorey and C. B. Holmes, „Vehicle Driveability - Its Characterisation and Measurement," *SAE Technical Paper*, vol. 1999-01-0949, 1999, DOI: 10.4271/1999-01-0949. Available: https://doi.org/10.4271/1999-01-0949.

[29] R. E. Dorey and E. J. Martin, „Vehicle Driveability - The Development of an Objective Methodology," *SAE Technical Paper*, no. 2000-01-1326, 2000, DOI: 10.4271/2000-01-1326. Available: https://doi.org/10.4271/2000-01-1326.

[30] H. O. List and P. Schoeggl, „Objective Evaluation of Vehicle Driveability," *SAE Technical Paper*, no. 980204, 1998, DOI: 10.4271/980204.

[31] H. Stoffels, „An Approach for the Objective Description of Vehicle Longitudinal Acceleration," *SAE Technical Paper*, no. 24-0166, 2011, DOI: 10.4271/2011-24-0166.

[32] T. E. Marlin, *Process control: Designing processes and control systems for dynamic performance*, (McGraw-Hill chemical engineering series), 2. ed., Boston, Mass., McGraw-Hill, 2000, ISBN: 0070393621.

[33] B. Jacobsen, „Potential of electric wheel motors as new chassis actuators for vehicle manoeuvring," *Proceedings of the Institution of Mechanical Engineers, Part D: Journal of Automobile Engineering*, vol. 216, no. 8, pp. 631–640, 2016, DOI: 10.1177/0954407002 21600801.

[34] S. Murata, „Innovation by in-wheel-motor drive unit," *Vehicle System Dynamics*, vol. 50, no. 6, pp. 807–830, 2012, DOI: 10.1080/00423114.2012.666354.

[35] J. V. Alcantar, F. Assadian and M. Kuang, „Vehicle Dynamics Control of eAWD Hybrid Electric Vehicle Using Slip Ratio Optimization and Allocation," *Journal of Dynamic Systems, Measurement, and Control*, vol. 140, no. 9, p. 091010, 2018, DOI: 10.1115/1.4039486.

[36] P. Gwinner, M. Otto and K. Stahl, „Lightweight Torque-Vectoring Transmission for the Electric Vehicle VISIO.M," *CoFAT*, 2014. Available: https://mediatum.ub.tum.de/doc/1226683/1226683.pdf.

[37] B.-R. Hoehn, C. Wirth and F. Kurth, „Aktives Differential mit Torque-Vectoring-Funktion," *VDI Wissensforum: Automobiltechnisches Kolloquium*, vol. 1. 2009.

[38] B.-R. Hoehn, K. Stahl, P. Gwinner and F. Wiesbeck, „Torque-Vectoring Driveline for Electric Vehicles," *Proceedings of the FISITA World Automotive Congress*, vol. 191, pp. 585–593, 2012, DOI: 10.1007/978-3-642-33777-2_48.

[39] L. de Novellis, A. Sorniotti and P. Gruber, „Wheel Torque Distribution Criteria for Electric Vehicles With Torque-Vectoring Differentials," *IEEE Transactions on Vehicular Technology*, vol. 63, no. 4, pp. 1593–1602, 2014, DOI: 10.1109/TVT.2013.2289371.

[40] J. Park and W. J. Kroppe, „Dana Torque Vectoring Differential Dynamic Trak™," *SAE Technical Paper*, no. 2004-01-2053, 2004, DOI: 10.4271/2004-01-2053. Available: https://doi.org/10.4271/2004-01-2053.

[41] K. Sawase, Y. Ushiroda and T. Miura, „Left-right torque vectoring technology as the core of super all wheel control (S-AWC)," rep. 18, 2006.

[42] B.-R. Hoehn, K. Stahl, C. Wirth, F. Kurth, M. Lienkamp and F. Wiesbeck, „Electromechanical Torque-Vectoring with Active Differential for Maximum Recuperation Capability," *VDI Wissensforum: Automobiltechnisches Kolloquium*, vol. 2. 2011.

[43] J. C. Wheals, H. Baker, K. Ramsey and W. Turner, „Torque Vectoring AWD Driveline: Design, Simulation, Capabilities and Control," *SAE Transactions*, vol. 113, pp. 557–576, 2004. Available: http://www.jstor.org/stable/44724880.

[44] J. C. Doyle, B. A. Francis and A. R. Tannenbaum, *Feedback control theory*, (Dover Books on Electrical Engineering), New York, Macmillan, 1992, ISBN: 0-02-330011-6.

[45] U. Mackenroth, *Robust Control Systems*, Berlin, Heidelberg, Springer Berlin Heidelberg, 2004, DOI: 10.1007/978-3-662-09775-5.

[46] J. Pfleghaar and B. Lohmann, „The Electrical Dual Mass Flywheel -an Efficient Active Damping System," *IFAC Proceedings Volumes*, vol. 46, no. 21, pp. 483–488, 2013, DOI: 10.3182/20130904-4-JP-2042.00046.

[47] J. Pfleghaar, „Energieeffiziente aktive Dämpfung von Torsionsschwingungen im KFZ-Antriebsstrang," Dissertation, Chair of Automatic Control, Technical University of Munich, Munich, 2015.

[48] R. S. Vadamalu and C. Beidl, „MPC for Active Torsional Vibration Reduction of Hybrid Electric Powertrains," *IFAC-PapersOnLine*, vol. 49, no. 11, pp. 756–761, 2016, DOI: 10.1016/j.ifacol.2016.08.110.

[49] A. T. Zaremba and R. I. Davis, „Control design for active engine damping using a starter/alternator," *American Control Conference (ACC)*, pp. 2043–2047, 2000, DOI: 10.1109/ACC.2000.879560.

[50] R. Isermann and M. Münchhof, *Identification of Dynamic Systems: An Introduction with Applications*, (Advanced Textbooks in Control and Signal Processing), Berlin, Heidelberg, Springer-Verlag Berlin Heidelberg, 2011, ISBN: 978-3-540-78878-2. DOI: 10.1007/978-3-540-78879-9.

[51] P. Stewart and P. J. Fleming, „Drive-by-Wire Control of Automotive Driveline Oscillations by Response Surface Methodology," *IEEE Transactions on Control Systems Technology*, vol. 12, no. 5, pp. 737–741, 2004.

[52] N. Amann, J. Böcker, F. Penner, N. Amann, J. Bocker and F. Prenner, „Active Damping of Drive Train Oscillations for an Electrically Driven Vehicle," *IEEE Transactions on Mechatronics*, vol. 9, no. 4, pp. 697–700, 2004, DOI: 10.1109/TMECH.2004.839036.

[53] J.-H. Montonen, N. Nevaranta, T. Lindh, J. Alho, P. Immonen and O. Pyrhonen, „Experimental Identification and Parameter Estimation of the Mechanical Driveline of a Hybrid Bus," *IEEE Transactions on Industrial Electronics*, vol. 65, no. 7, pp. 5921–5930, 2018, DOI: 10.1109/TIE.2017.2782202.

[54] M. C. Best, „Nonlinear optimal control of vehicle driveline vibrations," *UKACC International Conference on CONTROL*, pp. 658–663, 1998, DOI: 10.1049/cp:19980307.

[55] L. Castellazzi, A. Tonoli, N. Amati and E. Galliera, „A study on the role of powertrain system dynamics on vehicle driveability," *Vehicle System Dynamics*, vol. 55, no. 7, pp. 1012–1028, 2017, DOI: 10.1080/00423114.2017.1294699.

[56] D. Killian, J. M. Georg, S. Poltersdorf and M. Lienkamp, „Model-based traction control with friction adaption for preventing drive-train vibration during the power-hop acceleration process of front-wheel drive vehicles," *Symposium of the International Association for Vehicle System Dynamics (IAVSD)*, vol. 24, pp. 533–542, 2015.

[57] M. Menne, „Drehschwingungen im Antriebsstrang von Elektrostraßenfahrzugen - Analyse und aktive Dämpfung," Dissertation, Elektrotechnik und Informationstechnik, RWTH, Aachen, 2001.

[58] M. Batra, J. McPhee and N. L. Azad, „Anti-jerk model predictive cruise control for connected electric vehicles with changing road conditions," *Asian Control Conference (ASCC)*, vol. 11th, pp. 49–54, 2017, DOI: 10.1109/ASCC.2017.8287101.

[59] M. Batra, A. Maitland, J. McPhee and N. L. Azad, „Non-Linear Model Predictive Anti-Jerk Cruise Control for Electric Vehicles with Slip-Based Constraints," *American Control Conference (ACC)*, pp. 3915–3920, 2018, DOI: 10.23919/ACC.2018.8431389.

[60] M. Batra, J. McPhee and N. L. Azad, „Real-time model predictive control of connected electric vehicles," *Vehicle System Dynamics*, vol. 13, no. 10, pp. 1–24, 2018, DOI: 10.1080/00423114.2018.1552004.

[61] U. Angeringer, M. Horn and M. Reichhartinger, „Drive Line Control for Electrically Driven Vehicles Using Generalized Second Order Sliding Modes*," *IFAC Proceedings Volumes*, vol. 45, no. 30, pp. 79–84, 2012, DOI: 10.3182/20121023-3-FR-4025.00027.

[62] G. Götting and M. Kretschmer, „Development and series application of a vehicle drivetrain observer used in hybrid and electric vehicles," *World Electric Vehicle Symposium and Exhibition (EVS)*, pp. 1–9, 2013, DOI: 10.1109/EVS.2013.6914997.

[63] W. Liu, H. He, F. Sun and H. Wang, „Optimal design of adaptive shaking vibration control for electric vehicles," *Vehicle System Dynamics*, vol. 57, no. 1, pp. 134–159, 2018, DOI: 10.1080/00423114.2018.1447676.

[64] C. Lv, J. Zhang and Y. Li, „Extended-Kalman-filter-based regenerative and friction blended braking control for electric vehicle equipped with axle motor considering damping and elastic properties of electric powertrain," *Vehicle System Dynamics*, vol. 52, no. 11, pp. 1372–1388, 2014, DOI: 10.1080/00423114.2014.938663.

[65] C. Lv and Y. Yuan, „Synthesis of a Hybrid-Observer-Based Active Controller for Compensating Powetrain Backlash Nonlinearity of an Electric Vehicle during Regenerative Braking," *SAE International Journal of Alternative Powertrains*, vol. 4, no. 1, 2015.

[66] O. Atabay, M. Ötkür and İ. M. Ereke, „Model based predictive engine torque control for improved drivability," *Proceedings of the Institution of Mechanical Engineers, Part D: Journal of Automobile Engineering*, vol. 232, no. 12, pp. 1654–1666, 2017, DOI: 10.1177/0954407017733867.

[67] J. Baumann, D. D. Torkzadeha, A. Ramstein, U. Kiencke and T. Schlegl, „Model-based predictive anti-jerk control," *Control Engineering Practice*, vol. 14, pp. 259–266, 2006.

[68] M. Bruce, „Powertrain modelling and experimental validation in a heavy duty vehicle," *International Symposium on Advanced Vehicle Control (AVEC)*, vol. 7, 2004.

[69] M. Bruce, B. Egardt and S. Pettersson, „On powertrain oscillation damping using feed-forward and LQ feedback control," *IEEE Conference on Control Applications*, pp. 1415–1420, 2005, DOI: 10.1109/CCA.2005.1507330.

[70] C. F. Caruntu, M. Lazar, S. Di Cairano, R. H. Gielen and P. van den Bosch, „Horizon-1 predictive control of networked controlled vehicle drivetrains," *Proceedings of the World Congress of the International Federation of Automatic Control*, vol. 18. 2011.

[71] C. F. Caruntu, M. Lazar, R. H. Gielen and P. van den Bosch, „Lyapunov based predictive control of vehicle drivetrains over CAN," *Control EngineeringPractice*, vol. 21, pp. 1884–1898, 2013.

[72] J. Fredriksson, H. Weiefors and B. Egardt, „Powertrain Control for Active Damping of Driveline Oscillations," *Vehicle System Dynamics*, vol. 37, no. 5, pp. 359–376, 2002, DOI: 10.1076/vesd.37.5.359.3527.

[73] M. Grotjahn, L. Quernheim and S. Zemke, „Modelling and identification of car driveline dynamics for anti-jerk controller design," *IEEE International Conference on Mechatronics*, pp. 131–136, 2006, DOI: 10.1109/ICMECH.2006.252510.

[74] A. Lagerberg and B. Egardt, „Evaluation of Control Strategies for Automotive Powertrains with Backlash," *International Symposium on Advanced Vehicle Control (AVEC)*, vol. 6, 2002.

[75] A. Lagerberg, „Open-Loop Optimal Control of a Backlash Traverse," Department of Signals and Systems, Chalmers University of Technology, rep. R007/2004, 2004.

[76] A. Lagerberg and B. Egardt, „Model Predictive Control of Automotive Powertrains with Backlash," *IFAC Proceedings Volumes*, vol. 38, no. 1, pp. 1–6, 2005, DOI: 10.3182/20050703-6-CZ-1902.01888.

[77] A. Lagerberg and B. Egardt, „Backlash Estimation With Application to Automotive Powertrains," *IEEE Transactions on Control Systems Technology*, vol. 15, no. 3, pp. 483–493, 2007, DOI: 10.1109/TCST.2007.894643.

[78] M. Pettersson, „Driveline Modeling and Control," Dissertation, Department of Electrical Engineering, Universität, Linköping, 1997.

[79] T. Pham and L. Bushnell, „Two-degree-of-freedom damping control of driveline oscillations caused by pedal tip-in maneuver," *American Control Conference (ACC)*, vol. 49, no. 11, pp. 1425–1432, 2015, DOI: 10.1109/ACC.2015.7170933.

[80] T. Pham, R. Seifried, A. Hock and C. Scholz, „Nonlinear Flatness-Based Control of Driveline Oscillations for a Powertrain with Backlash Traversing," *IFAC-PapersOnLine*, vol. 49, no. 11, pp. 749–755, 2016, DOI: 10.1016/j.ifacol.2016.08.109.

[81] A. Zech, T. Eberl and S. Müller, „Analyse einer neuen kaskadierten Reglerstruktur für die Antriebsschlupfbegrenzung hochdynamischer Fahrzeugantriebe," *VDI Autoreg*, vol. 7. 2017.

[82] S. Zemke, „Analyse und modellbasierte Regelung von Ruckelschwingungen im Antriebsstrang von Kraftfahrzeugen," dissertation, University of Hannover, Hannover, 2012.

[83] F. Bottiglione, A. Sorniotti and L. Shead, „The effect of half-shaft torsion dynamics on the performance of a traction control system for electric vehicles," *Journal of Automobile Engineering*, vol. 226, no. 9, pp. 1145–115, 2012.

[84] J. M. Rodriguez, R. Meneses and J. Orus, „Active Vibration Control for Electric Vehicle Compliant Drivetrains," *Annual Conference of the IEEE Industrial Electronics Society, IECON*, vol. 39th, pp. 2590–2595, 2013.

[85] M. Rosenberger, M. Prof. Lienkamp, P. Kunsch and T. Koch, „Integration der elektrischen Antriebsmotoren in die ABS-Regelung," *VDI Wissensforum: Automobiltechnisches Kolloquium*, vol. 2. 2011.

[86] M. Rosenberger, R. A. Uhlig, T. Koch and M. Lienkamp, „Combining Regenerative Braking and Anti-Lock Braking for Enhanced Braking Performance and Efficiency," *SAE Technical Paper*, no. 2012-01-0234, 2012, DOI: 10.4271/2012-01-0234. [Accessed 06/15/2016].

[87] M. Rosenberger, F. Schindele, T. Koch and M. Lienkamp, „Analyse und aktive Dämpfung von Antriebsstrangschwingungen bei Elektrofahrzeugen während der ABS-Regelung," *Tag des Fahrwerks*, 2012.

[88] M. Foerth, J. Ota and M. Lienkamp, „Sensitivity Analysis of Drivetrain Oscillations in Electric Vehicles," in *ASME 2018 Dynamic Systems and Control Conference*, 2018.

[89] K. Asano, S. Okada and N. Iwama, „Vibration suppression of induction-motor-driven hybrid vehicle using wheel torque observer," *IEEE Transactions on Industry Applications*, vol. 28, no. 2, pp. 441–446, 1992, DOI: 10.1109/28.126754.

[90] D. H. Konig, B. Riemann, M. Bohning, R. Syrnik and S. Rinderknecht, „Robust anti-jerk control for electric vehicles with multi-speed transmission," *IEEE Conference on Decision and Control*, vol. 53, pp. 3298–3303, 2014, DOI: 10.1109/CDC.2014.7039899.

[91] D. Lefebvre, P. Chevrel and S. Richard, „An H-infinity-based control design methodology dedicated to the active control of vehicle longitudinal oscillations," *IEEE Transactions on Control Systems Technology*, vol. 11, no. 6, pp. 948–956, 2003, DOI: 10.1109/TCST.2003.815552.

[92] K. Z. Yeap and S. Müller, „Understanding the influence of traction on the Eigen behaviour of torsional vibrations in individual-wheel drives," *at – Automatisierungstechnik*, vol. 63, no. 6, 2015, DOI: 10.1515/auto-2014-1118.

[93] P. Templin, „Simultaneous estimation of driveline dynamics and backlash size for control design," *IEEE International Conference on Control Applications*, pp. 13–18, 2008, DOI: 10.1109/CCA.2008.4629642.

[94] P. Templin and B. Egardt, „An LQR torque compensator for driveline oscillation damping," *IEEE International Conference on Control Applications*, vol. 18, pp. 352–356, 2009, DOI: 10.1109/CCA.2009.5281020.

[95] P. Templin and B. Egardt, „Experimental Results for a Powertrain LQR-torque Compensator with Backlash Handling," *IFAC Workshop on Engine and Powertrain Control, Simulation and Modeling*, pp. 148–153, 2009.

[96] M. S. Haschka and V. Krebs, „Observing the Torque of a Powertrain with Backlash," *at – Automatisierungstechnik*, vol. 55, no. 3, p. 42, 2007, DOI: 10.1524/auto.2007.55.3.127.

[97] M. Nordin and P.-O. Gutman, „Controlling mechanical systems with backlash—a survey," *Automatica*, vol. 38, pp. 1633–1649, 2002, DOI: 10.1016/S0005-1098(02)00047-X.

[98] G. Brandenburg and U. Schäfer, „Influence and adaptive compensation of simultaneously acting backlash and coulomb friction in elastic two-mass systems of robots and machine tools," *Proceedings of ICCON*, 1989.

[99] D. Liberzon, *Switching in Systems and Control*, Boston, MA, Birkhäuser Boston, 2003, DOI: 10.1007/978-1-4612-0017-8.

[100] M. Nordin, J. Galic and P.-O. Gutman, „New Models for Backlash and Gear Play," *International Journal of Adaptive Control and Signal Processing*, vol. 11, pp. 49–63, 1997.

[101] A. Lagerberg and B. Egardt, „Backlash gap position estimation in automotive powertrains," *European Control Conference (ECC)*, pp. 2292–2297, 2003, DOI: 10.23919/ECC.2003.7085308.

[102] Y. Li, A. Hansen, J. Karl Hedrick and J. Zhang, „A receding horizon sliding control approach for electric powertrains with backlash and flexible half-shafts," *Vehicle System Dynamics*, vol. 55, no. 12, pp. 1823–1841, 2017, DOI: 10.1080/00423114.2017.1335873.

[103] G. Ferrari-Trecate and M. Gati, „Observability analysis and state observers for automotive powertrains with backlash: A hybrid system approach," *International Journal of Control*, vol. 79, no. 5, pp. 496–507, 2007, DOI: 10.1080/00207170600587507.

[104] D. Lefebvre, P. Chevrel and S. Richard, „Control analysis tools for active attenuation of vehicle longitudinal oscillations," *IEEE International Conference on Control Applications (CCA)*, pp. 811–816, 2001, DOI: 10.1109/CCA.2001.973969.

[105] P. J. Antsaklis and Anthony N. Michel, *Linear Systems*, Boston, MA, Birkhäuser, 2006, DOI: 10.1007/0-8176-4435-0.

[106] R. Merzouki, J. C. Cadiou and N. K. M'Sirdi, „Compensation of friction and backlash effects in an electrical actuator," *Proceedings of the Institution of Mechanical Engineers, Part I: Journal of Systems and Control Engineering*, vol. 218, no. 2, pp. 75–84, 2004, DOI: 10.1177/095965180421800202.

[107] R. Merzouki and J. C. Cadiou, „Estimation of backlash phenomenon in the electromechanical actuator," *Control Engineering Practice*, vol. 13, pp. 973–983, 2005.

[108] R. Merzouki, J. A. Davila, J. C. Cadiou and L. Fridman, „Backlash phenomenon observation and identification," *American Control Conference (ACC)*, 2006, DOI: 10.1109/ACC.2006.1657231.

[109] H. B. Pacejka and I. Besselink, *Tire and vehicle dynamics*, 3. ed., Oxford, Butterworth - Heinemann, 2012, ISBN: 978-0-08-097016-5.

[110] A. J. Tuononen, „Onset of frictional sliding of rubber–glass contact under dry and lubricated conditions," *Scientific Reports*, vol. 6, 2016, DOI: 10.1038/srep27951.

[111] S. T. H. Jansen, P. W. A. Zegelaar and H. B. Pacejka, „The Influence of In-Plane Tyre Dynamics on ABS Braking of a Quarter Vehicle Model," *Vehicle System Dynamics*, vol. 32, no. 2-3, pp. 249–261, 1999, DOI: 10.1076/vesd.32.2.249.2086.

[112] H. B. Pacejka and E. Bakker, „The magic formula tyre model," *Vehicle System Dynamics*, vol. 21, pp. 1–18, 1992, DOI: 10.1080/00423110408969994.

[113] A. Higuchi and H. B. Pacejka, „The Relaxation Length Concept at Large Wheel Slip and Camber," *Vehicle System Dynamics*, vol. 27, no. sup001, pp. 50–64, 1997, DOI: 10.1080/00423119708969644.

[114] C. Fang, Z. Cao, M. M. Ektesabi, A. Kapoor and A. Sayem, „Model reference control for active driveability improvement," *Proceedings of the International Conference on Modelling, Identification & Control*, pp. 202–206, 2014, DOI: 10.1109/ICMIC.2014.7020752.

[115] D. Jiang, Y. Huang, D. Hao and P. Dai, „A study on the influence of uncertain factors on vehicle low frequency vibration and control rules," *World Congress on Intelligent Control and Automation (WCICA)*, vol. 12, pp. 3318–3323, 2016, DOI: 10.1109/WCICA.2016.7578811.

[116] P. W. A. Zegelaar, „The dynamic response of tyres to brake torque variations and road unevennesses," dissertation, Delft University of Technology, Delft, 1998.

[117] C. L. Clover and J. E. Bernard, „Longitudinal Tire Dynamics," *Vehicle System Dynamics*, vol. 29, no. 4, pp. 231–260, 1998, DOI: 10.1080/00423119808969374.

[118] S.-L. Koo, H.-S. Tan and M. Tomizuka, „Analysis of Vehicle Longitudinal Dynamics for Longitudinal Ride Comfort," *ASME International Mechanical Engineering Congress and Exposition*, pp. 431–439, 2006, DOI: 10.1115/IMECE2006-15161.

[119] D. Hao, C. Zhao and Y. Huang, „A Reduced-Order Model for Active Suppression Control of Vehicle Longitudinal Low-Frequency Vibration," *Shock and Vibration*, vol. 2018, no. 2, pp. 1–22, 2018, DOI: 10.1155/2018/5731347.

[120] A. J. Tuononen, L. Hartikainen, F. Petry and S. Westermann, „Parameterization of in-plane rigid ring tire model from instrumented vehicle measurements," *International Symposium on Advanced Vehicle Control (AVEC)*, vol. 11, 2012.

[121] L. Castellazzi, A. Tonoli, N. Amati, A. Piu and E. Galliera, „Vehicle Driveability: Dynamic Analysis of Powertrain System Components," *SAE Technical Paper*, no. 2016-01-1124, 2016, DOI: 10.4271/2016-01-1124. Available: https://doi.org/10.4271/2016-01-1124.

[122] A. J. Tuononen and A. Lajunen, „Modal analysis of different drivetrain configurations in electric vehicles," *Journal of Vibration and Control*, 2016, DOI: 10.1177/1077546316635857.

[123] G. F. Franklin, J. D. Powell and M. L. Workman, *Digital control of dynamic systems*, 3rd ed., Menlo Park, Calif., Addison-Wesley, 2002, ISBN: 0-201-33153-5.

[124] T. Pham, R. Seifried and C. Scholz, „Anti-Jerk Control of a Parallel Hybrid Electrified Vehicle with Dead Time," *IFAC-PapersOnLine*, vol. 50, no. 1, pp. 966–971, 2017, DOI: 10.1016/j.ifacol.2017.08.172.

[125] J. Zhang, C. Lv, J. Gou and D. Kong, „Cooperative control of regenerative braking and hydraulic braking of an electrified passenger car," *Proceedings of the Institution of Mechanical Engineers, Part D: Journal of Automobile Engineering*, vol. 226, no. 10, pp. 1289–1302, 2012, DOI: 10.1177/0954407012441884.

[126] R. Prabel and H. Aschemann, „Active oscillation damping for a truck drive train," *International Conference on Methods and Models in Automation and Robotics (MMAR)*, vol. 19th, pp. 486–491, 2014, DOI: 10.1109/MMAR.2014.6957402.

[127] S. Zhao, A. Lasson, O. Wallmark and M. Leksell, „Off-Vehicle Evaluation of Active Oscillation Damping Schemes," *IEEE Journal of Emerging and Selected Topics in Power Electronics*, vol. 2, no. 2, pp. 264–271, 2014, DOI: 10.1109/JESTPE.2013.2291962.

[128] K. Park, J. Lee and J. Park, „Torque control of a vehicle with electronic throttle control using an input shaping method," *International Journal of Automotive Technology*, vol. 14, no. 2, pp. 189–194, 2013, DOI: 10.1007/s12239-013-0021-3. Available: https://doi.org/10.1007/s12239-013-0021-3.

[129] P. Schmidt and T. Rehm, „Notch Filter Tuning for Resonant Frequency Reduction in Dual Inertia Systems," *Industry Applications Conference*, vol. 3, pp. 1730–1734, 1999.

[130] M. A. Valenzuela, J. M. Bentley, A. Villablanca and R. D. Lorenz, „Dynamic Compensation of Torsional Oscillation in Paper Machine Sections," *Annual Pulp and Paper Industry Technical Conference*, 2005.

[131] S. N. Vukosavic and M. R. Stojic, „Suppression of torsional oscillations in a high-performance speed servo drive," *IEEE Transactions on Industrial Electronics*, vol. 45, no. 1, pp. 108–117, 1998, DOI: 10.1109/41.661311.

[132] R. J. Richards, *Solving problems in control*, (Solving problems series), Harlow, Longman, 1993, ISBN: 0582032989.

[133] A. Visioli and Q. Zhong, *Control of Integral Processes with Dead Time*, London, Springer London, 2011, DOI: 10.1007/978-0-85729-070-0.

[134] R. Syrnik, „Untersuchung der fahrdynamischen Potenziale eines elektromotorischen Traktionsantriebs,“ dissertation, Technical University of Munich, Munich, 2015.

[135] Y. Hori, „Disturbance suppression on an acceleration control type DC servo system,“ *IEEE Power Electronics Specialists Conference*, vol. 19th, pp. 222–229, 1988, DOI: 10.1109/PESC.1988.18137.

[136] A. Radke and Z. Gao, „A survey of state and disturbance observers for practitioners,“ *American Control Conference (ACC)*, 6 pp, 2006, DOI: 10.1109/ACC.2006.1657545.

[137] K. Sugiura and Y. Hori, „Vibration suppression in 2- and 3-mass system based on the feedback of imperfect derivative of the estimated torsional torque,“ *IEEE Transactions on Industrial Electronics*, vol. 43, no. 1, pp. 56–64, 1996, DOI: 10.1109/41.481408.

[138] L. de Novellis, A. Sorniotti, P. Gruber, J. Orus, J.-M. Rodriguez Fortun, J. Theunissen and J. de Smet, „Direct yaw moment control actuated through electric drivetrains and friction brakes: Theoretical design and experimental assessment,“ *Mechatronics*, vol. 26, pp. 1–15, 2015, DOI: 10.1016/j.mechatronics.2014.12.003.

[139] M. Green and D. J. N. Limebeer, *Linear robust control*, (Dover Books on Electrical Engineering), Dover ed., Mineola, NY, Dover Publ, 2012, ISBN: 978-0486488363.

[140] J. B. Rawlings, D. Q. Mayne and M. M. Diehl, *Model predictive control: Theory, computation, and design*, 2nd edition, Madison, Wisconsin, Nob Hill Publishing, 2017, ISBN: 0975937731.

[141] D. Simon, *Optimal State Estimation*, Hoboken, NJ, USA, John Wiley & Sons, Inc, 2006, DOI: 10.1002/0470045345.

[142] F. L. Lewis, D. L. Vrabie and V. L. Syrmos, *Optimal control*, 3rd ed., Hoboken, Wiley, 2012, ISBN: 978-0470633496.

[143] J. Doyle and G. Stein, „Robustness with observers,“ *IEEE Transactions on Automatic Control*, vol. 24, no. 4, pp. 607–611, 1979, DOI: 10.1109/TAC.1979.1102095.

[144] A. Lagerberg, „A literature survey on control of automotive powertrains with backlash,“ Department of Signals and Systems, Chalmers University of Technology, rep. R013/2001, 2001.

[145] A. Barreiro and A. Baños, „Input–output stability of systems with backlash,“ *Automatica*, vol. 42, no. 6, pp. 1017–1024, 2006, DOI: 10.1016/j.automatica.2006.02.017. Available: http://www.sciencedirect.com/science/article/pii/S0005109806001105.

[146] A. Balluchi, L. Benvenuti, M. D. Di Benedetto and A. Sangiovanni-Vincentelli, „The design of dynamical observers for hybrid systems: Theory and application to an automotive control problem,“ *Automatica*, vol. 49, no. 4, pp. 915–925, 2013, DOI: 10.1016/j.automatica.2013.01.037.

[147] A. Formentini, A. Oliveri, M. Marchesoni and M. Storace, „A Switched Predictive Controller for an Electrical Powertrain System With Backlash,“ *IEEE Transactions on Power Electronics*, vol. 32, no. 5, pp. 4036–4047, 2017, DOI: 10.1109/TPEL.2016.2587756.

[148] C. F. Caruntu, „Observer-based predictive controller design with network-enhanced time-delay compensation,“ *International Journal of General Systems*, vol. 44, no. 2, pp. 182–197, 2014, DOI: 10.1080/03081079.2014.973731.

[149] C. F. Caruntu, „Predictive control based on piecewise nonlinear models for vehicle drivetrains,“ *IEEE Conference on Emerging Technologies and Factory Automation (ETFA)*, vol. 20, pp. 1–7, 2015, DOI: 10.1109/ETFA.2015.7301442.

[150] C. F. Caruntu, A. E. Balau, M. Lazar, P. P. Bosch and S. Di Cairano, „Driveline oscillations damping: A tractable predictive control solution based on a piecewise affine model," *Nonlinear Analysis: Hybrid Systems*, vol. 19, pp. 168–185, 2016, DOI: 10.1016/j.nahs.2015.10.001.

[151] M. Fliess, J. Lévine, P. Martin and P. Rouchon, „On Differentially Flat Nonlinear Systems," *IFAC Proceedings Volumes*, vol. 25, no. 13, pp. 159–163, 1992, DOI: 10.1016/B978-0-08-041901-5.50031-2.

[152] M. Fliess, J. Levine, P. Martin and P. Rouchon, „Flatness and defect of non-linear systems: Introductory theory and examples," *International Journal of Control*, vol. 61, no. 6, pp. 1327–1361, 1995, DOI: 10.1080/00207179508921959.

[153] G. G. Rigatos, *Nonlinear control and filtering using differential flatness approaches // Nonlinear Control and Filtering Using Differential Flatness Approaches: Applications to electromechanical systems*, (Studies in systems, decision and control). vol. 25, Cham, Springer and Springer International Publishing, 2015, ISBN: 978-3-319-16419-9. DOI: 10.1007/978-3-319-16420-5.

[154] Y. Hori, Y. Toyoda and Y. Tsuruoka, „Traction control of electric vehicle: Basic experimental results using the test EV "UOT electric march"," *IEEE Transactions on Industry Applications*, vol. 34, no. 5, pp. 1131–1138, 1998, DOI: 10.1109/28.720454.

[155] P. Apkarian, P. Gahinet and C. Buhr, „Multi-model, multi-objective tuning of fixed-structure controllers," *European Control Conference (ECC)*, pp. 856–861, 2014, DOI: 10.1109/ECC.2014.6862200.

[156] P. Apkarian, M. N. Dao and D. Noll, „Parametric Robust Structured Control Design," *IEEE Transactions on Automatic Control*, vol. 60, no. 7, pp. 1857–1869, 2015, DOI: 10.1109/TAC.2015.2396644.

[157] D. Karnopp, *System dynamics: Modeling and simulation of mechatronic systems*, 5th ed., Hoboken, Wiley, 2012, ISBN: 9780470889084.

[158] W. Yang, „Entwicklung einer Regelung zur Kompensation der Antriebsstrangschwingungen unter Berücksichtigung des Getriebespiels für Elektrofahrzeuge," Master Thesis, Technical University of Munich, Munich, 2017.

[159] M. Höcher, „Entwicklung eines reduzierten Antriebsstrangmodells für das Elektrofahrzeug Visio.M," Bachelor Thesis, Technical University of Munich, Munich, 2017.

[160] P. A. Grilli, „Modellvalidierung eines Antriebsstrangmodells zur Untersuchung von Schwingungsphänomene," Semester Thesis, Technical University of Munich, Munich, 2018.

[161] D. Pech, „Online-Identifikation des Übertragungsverhaltens von Antriebssträngen," Master Thesis, Technical University of Munich, Munich, 2017.

[162] H. T. Pham, „Control methods of powertrains with backlash and time delay," Dissertation, Institute of Mechanics and Ocean Engineering, Hamburg University of Technology, Hamburg, 2019, DOI: 10.15480/882.2235.

[163] K. Nam, Y. Hori and C. Lee, „Wheel Slip Control for Improving Traction-Ability and Energy Efficiency of a Personal Electric Vehicle," *energies*, vol. 8, no. 7, pp. 6820–6840, 2015, DOI: 10.3390/en8076820.

[164] A. C. Antoulas, *Approximation of Large-Scale Dynamical Systems*, Society for Industrial and Applied Mathematics, 2005, DOI: 10.1137/1.9780898718713.

[165] G. J. Heydinger, W. R. Garrott, J. P. Chrstos and D. A. Guenther, „A Methodology for Validating Vehicle Dynamics Simulations," *SAE Transactions*, vol. 99, pp. 126–146, 1990.

[166] W. L. Oberkampf and M. F. Barone, „Measures of agreement between computation and experiment: Validation metrics," *Journal of Computational Physics*, vol. 217, no. 1, pp. 5–36, 2006, DOI: 10.1016/j.jcp.2006.03.037.

[167] R. E. Skelton, „Model error concepts in control design," *International Journal of Control*, vol. 49, no. 5, pp. 1725–1753, 1989, DOI: 10.1080/00207178908559735.

[168] W. S. Levine, *The control handbook*, (A CRC handbook), Boca Raton, Fla., CRC Press, 1996, ISBN: 0-8493-8570-9.

[169] R. B. Northrop, *Introduction to instrumentation and measurements*, 2. ed., Boca Raton, Taylor & Francis, 2005, ISBN: 0849337739.

[170] D. Schröder, *Elektrische Antriebe - Regelung von Antriebssystemen*, Berlin and Heidelberg, Springer Vieweg, 2015, ISBN: 978-3-642-30095-0. DOI: 10.1007/978-3-642-30096-7.

[171] S.-K. Au, *Operational Modal Analysis*, Singapore, Springer Singapore, 2017, DOI: 10.1007/978-981-10-4118-1.

[172] „Matlab User Guide R2018b," 2018.

[173] M. T. Nair and A. Singh, *Linear Algebra*, Singapore, Springer Singapore, 2018, ISBN: 978-981-13-0925-0. DOI: 10.1007/978-981-13-0926-7.

[174] J. Liesen and V. Mehrmann, *Linear Algebra*, Cham, Springer International Publishing, 2015, DOI: 10.1007/978-3-319-24346-7.

[175] J. R. Kirkwood and B. H. Kirkwood, *Elementary linear algebra*, (Textbooks in mathematics), 1st ed., Boca Raton, London, and New York, CRC Press, 2017, ISBN: 978-1-4987-7846-6.

[176] R. M. Crowder, *Electric drives and electromechanical systems*, 1st ed., Oxford and Burlington, MA, Butterworth-Heinemann, 2011, ISBN: 9780080492643.

[177] J. Larminie and J. Lowry, *Electric vehicle technology explained*, 2nd ed., Hoboken, NJ and Chichester, Wiley, 2012, ISBN: 9781118361146.

[178] P. Lugner, *Vehicle Dynamics of Modern Passenger Cars*. vol. 582, Cham, Springer International Publishing, 2019, ISBN: 9783319790077. DOI: 10.1007/978-3-319-79008-4. Available: http://dx.doi.org/10.1007/978-3-319-79008-4.

[179] J. Berthold, „Entwicklung eines Kalman-Filters zur Zustandsschätzung für den Antriebsstrang des Visio.M," Semester Thesis, Technical University of Munich, Munich, 2018.

[180] C. Bennett, „Electric Vehicle Drivetrain State Estimation by means of Artificial Intelligence," Semester Thesis, Technical University of Munich, Munich, 2018.

[181] F. Himpsl, „Anwendung von LQR/LTR auf die aktive Dämpfung von Antriebsstrangschwingungen," Semester Thesis, Technical University of Munich, Munich, 2017.

[182] S. Hoffmann, „Optimale Regelung zur Bedämpfung von Antriebsstrangschwingungen," Master Thesis, Technical University of Munich, Munich, 2018.

[183] A. Schwarz, „Entwicklung einer modellprädiktiven Regelung zur aktiven Dämpfung von Antriebsstrangschwingungen: Unter Berücksichtigung von Getriebespiel," Master Thesis, Technical University of Munich, Munich, 2018.

[184] M. Wöllhaf, „Aktive Dämpfung von Antriebsstrangschwingungen durch Vorfilter und Ausgangsrückführung," Semester Thesis, Technical University of Munich, Munich, 2017.

[185] J. Mosch, „Adaptive Dämpfung von Antriebsstrangschwingungen durch Vorfilter und Ausgangsrückführung," Semester Thesis, Technical University of Munich, Munich, 2018.

[186] M. Krusch, „Entwicklung eines H∞-Reglers für die aktive Dämpfung von Antriebsstrangschwingungen," Bachelor Thesis, Technical University of Munich, Munich, 2017.

[187] P. Apkarian and D. Noll, „Nonsmooth optimization for multiband frequency domain control design," *Automatica*, vol. 43, no. 4, pp. 724–731, 2007, DOI: 10.1016/j.automatica.2006.08.031.

[188] J. Doyle and G. Stein, „Multivariable feedback design: Concepts for a classical/modern synthesis," *IEEE Transactions on Automatic Control*, vol. 26, no. 1, pp. 4–16, 1981, DOI: 10.1109/TAC.1981.1102555.

[189] J. Vörös, „Modeling and identification of systems with backlash," *Automatica*, vol. 46, no. 2, pp. 369–374, 2010, DOI: 10.1016/j.automatica.2009.11.005.

[190] J. Levine, *Analysis and Control of Nonlinear Systems*, Berlin, Heidelberg, Springer Berlin Heidelberg, 2009, ISBN: 978-3-642-00838-2. DOI: 10.1007/978-3-642-00839-9.

[191] V. Wicke, C. Brace, M. Deacon and N. Vaughan, „Preliminary Results from Driveability Investigations of Vehicles with Continuously Variable Transmissions," *International Congress on Continuously Variable Power Tansmission*, pp. 9–14, 1999.

[192] M. Nordin and P.-O. Gutman, „Non-linear Speed Control of Elastic Systems with Backlash," *IEEE Conference on Decision and Control (CDC)*, vol. 39th, pp. 4060–4065, 2000.

[193] P. Falb and W. Wolovich, „Decoupling in the design and synthesis of multivariable control systems," *IEEE Transactions on Automatic Control*, vol. 12, no. 6, pp. 651–659, 1967, DOI: 10.1109/TAC.1967.1098737.

[194] B. Lohmann, „Vollständige Entkopplung durch dynamische Zustandsrückführung / Complete decoupling by dynamic State feedback," *at - Automatisierungstechnik*, vol. 39, no. 1-12, 1991, DOI: 10.1524/auto.1991.39.112.459.

Prior Publications

For this Ph.D. Thesis the following publication forms the foundation for the chapter 3 and chapter 4. The author wants to thank the other authors for their contribution.

Journals; peer-reviewed

Conferences, Periodicals; peer-reviewed

[88] M. Foerth, J. Ota and M. Lienkamp, „Sensitivity Analysis of Drivetrain Oscillations in Electric Vehicles,“ in *ASME 2018 Dynamic Systems and Control Conference*, 2018.

Patents

Journals, Conferences, Periodicals, Reports, Conference Proceedings and Poster, etc.; not peer-reviewed

Supervised Student's Thesis

Different student theses cover various aspects of the broader topic of this Ph.D. Thesis. The different bachelor-, term- and master-theses originate from the guidance of the author. The author wants to thank the students for their contributions. Hier muss noch eine englische Prenote definiert werden

[158] W. Yang, „Entwicklung einer Regelung zur Kompensation der Antriebsstrangschwingungen unter Berücksichtigung des Getriebespiels für Elektrofahrzeuge," Master Thesis, Technical University of Munich, Munich, 2017.

[159] M. Höcher, „Entwicklung eines reduzierten Antriebsstrangmodells für das Elektrofahrzeug Visio.M," Bachelor Thesis, Technical University of Munich, Munich, 2017.

[160] P. A. Grilli, „Modellvalidierung eines Antriebsstrangmodells zur Untersuchung von Schwingungsphänomene," Semester Thesis, Technical University of Munich, Munich, 2018.

[161] D. Pech, „Online-Identifikation des Übertragungsverhaltens von Antriebssträngen," Master Thesis, Technical University of Munich, Munich, 2017.

[179] J. Berthold, „Entwicklung eines Kalman-Filters zur Zustandsschätzung für den Antriebsstrang des Visio.M," Semester Thesis, Technical University of Munich, Munich, 2018.

[180] C. Bennett, „Electric Vehicle Drivetrain State Estimation by means of Artificial Intelligence," Semester Thesis, Technical University of Munich, Munich, 2018.

[181] F. Himpsl, „Anwendung von LQR/LTR auf die aktive Dämpfung von Antriebsstrangschwingungen," Semester Thesis, Technical University of Munich, Munich, 2017.

[182] S. Hoffmann, „Optimale Regelung zur Bedämpfung von Antriebsstrangschwingungen," Master Thesis, Technical University of Munich, Munich, 2018.

[183] A. Schwarz, „Entwicklung einer modellprädiktiven Regelung zur aktiven Dämpfung von Antriebsstrangschwingungen: Unter Berücksichtigung von Getriebespiel," Master Thesis, Technical University of Munich, Munich, 2018.

[184] M. Wöllhaf, „Aktive Dämpfung von Antriebsstrangschwingungen durch Vorfilter und Ausgangsrückführung," Semester Thesis, Technical University of Munich, Munich, 2017.

[185] J. Mosch, „Adaptive Dämpfung von Antriebsstrangschwingungen durch Vorfilter und Ausgangsrückführung," Semester Thesis, Technical University of Munich, Munich, 2018.

[186] M. Krusch, „Entwicklung eines H∞-Reglers für die aktive Dämpfung von Antriebsstrangschwingungen," Bachelor Thesis, Technical University of Munich, Munich, 2017.

A. Geffel, „Entwicklung einer Anti-Schlupf-Regelung für Elektrofahrzeuge," Master Thesis, Technical University of Munich, Munich, 2018.

P. Werk, „Aufbau und Validierung eines Vertikaldynamikmodells für einen Formula Student Rennwagen zur Optimierung der Feder- und Dämpfereinstellungen," Semester Thesis, Technical University of Munich, Munich, 2018.

Appendix

A Model building and analysis

A.1 Linearization of Braking Slip Dynamics

In order to investigate braking conditions, the linearization has to be conducted with the brake slip definition. Choosing the vehicle speed $\dot{\varphi}_{\text{veh}}$ as the slip reference speed $\dot{\varphi}_{\text{s}}$ yields Eq. A.1.

$$\begin{aligned}\dot{s}_{\text{x}} \approx \frac{r_{\text{w}}}{l_{\sigma,0}}\Bigg[& k_\sigma \left(\dot{\varphi}_{\text{w}} - \dot{\varphi}_{\text{veh}} - \dot{\varphi}_{\text{veh}}\, s_{\text{x}}\right)\Big|_{s_{\text{x,0}},\dot{\varphi}_{\text{veh,0}},\dot{\varphi}_{\text{w,0}}} \left(s_{\text{x}} - s_{\text{x,0}}\right) \\ & - \dot{\varphi}_{\text{veh}}\left(1 + k_\sigma\, s_{\text{x}}\right)\Big|_{s_{\text{x,0}},\dot{\varphi}_{\text{veh,0}}} \left(s_{\text{x}} - s_{\text{x,0}}\right) \\ & - \left(1 + k_\sigma\, s_{\text{x}}\right)\left(1 + s_{\text{x}}\right)\Big|_{s_{\text{x,0}}} \left(\dot{\varphi}_{\text{veh}} - \dot{\varphi}_{veh,0}\right) \\ & + \left(1 + k_\sigma\, s_{\text{x}}\right)\Big|_{s_{\text{x,0}}} \left(\dot{\varphi}_{\text{w}} - \dot{\varphi}_{w,0}\right) \\ & + \left(1 + k_\sigma\, s_{\text{x,0}}\right)\left(\dot{\varphi}_{\text{w,0}} - \dot{\varphi}_{\text{veh,0}} - \dot{\varphi}_{\text{veh,0}}\, s_{\text{x,0}}\right) \Bigg]\end{aligned} \tag{A.1}$$

In order to reduce the large expression of Eq. A.1, two simplifications are possible. First, the constant terms are neglected for the state-space model. Second, Eq. A.2 links $\dot{\varphi}_{\text{w,0}}$ to $\dot{\varphi}_{\text{veh,0}}$ and $s_{\text{x,0}}$ based on the steady-state slip from Eq. 3.20. Inserting Eq. A.2 in Eq. A.1 eliminates the first term $\left(\dot{\varphi}_{\text{w}} - \dot{\varphi}_{\text{veh}} - \dot{\varphi}_{\text{veh}}\, s_{\text{x}}\right)$.

$$\dot{\varphi}_{\text{w,0}} = \dot{\varphi}_{\text{veh,0}} + \dot{\varphi}_{\text{veh,0}}\, s_{\text{x,0}} \tag{A.2}$$

Without the constant terms, Eq. A.3 remains. Further, the factor $\left(1 + k_\sigma\, s_{\text{x,0}}\right)$ is common to all terms and, therefore, taken in front of the brackets to form Eq. A.4. The transient dynamics of Eq. A.4 are implemented into the state-space model.

$$\dot{s}_{\text{x}} \approx \frac{r_{\text{w}}}{l_{\sigma,0}}\left[-\dot{\varphi}_{\text{veh,0}}\left(1 + k_\sigma\, s_{\text{x,0}}\right)s_{\text{x}} - \left(1 + k_\sigma\, s_{\text{x,0}}\right)\left(1 + s_{\text{x,0}}\right)\dot{\varphi}_{\text{veh}} + \left(1 + k_\sigma\, s_{\text{x,0}}\right)\dot{\varphi}_{\text{w}}\right] \tag{A.3}$$

$$\dot{s}_{j,\text{x}} = \frac{r_{\text{w}}\left(1 + k_\sigma\, s_{\text{x,0}}\right)}{l_{\sigma,0}}\left[-\dot{\varphi}_{\text{veh,0}}\, s_{j,\text{x}} + \dot{\varphi}_{j,\text{w}} - \left(1 + s_{\text{x,0}}\right)\dot{\varphi}_{j,\text{veh}}\right] \tag{A.4}$$

In essence, only the viscous damping in the second term changes. The operation point $\dot{\varphi}_{\text{veh,0}}$ is a constant which is predefined, just like the parameter $\dot{\varphi}_{\text{w,0}}$ for the acceleration case.

$$\frac{l_{\sigma,0}}{r_{\text{w}}\,\dot{\varphi}_{\text{veh,0}}\left(1 + k_\sigma\, s_{\text{x,0}}\right)}\dot{s}_{j,\text{x}} + s_{j,\text{x}} = \frac{1}{\dot{\varphi}_{\text{veh,0}}}\left(\dot{\varphi}_{j,\text{w}} - \dot{\varphi}_{j,\text{veh}}\right) - \frac{s_{\text{x,0}}}{\dot{\varphi}_{\text{veh,0}}}\dot{\varphi}_{j,\text{veh}} \tag{A.5}$$

A.2 Decoupling of the TVD model

The first step in the model reduction is the decoupling of in-phase and anti-phase motion into separate drivetrains. The measurement data used for the validation in section 3.2 and Appendix B suggests that in-phase and anti-phase motion are decoupled. In case of the state-space model, the lack of coupling is expressed in the decoupling matrix D^*. In decoupling control of multi-input multi-output (MIMO) systems, D^* and its inverse transform the inputs of the control and, thereby, achieve decoupling. In this context, if D^* is in diagonal form there is no need for a transformation of the inputs to achieve decoupling. This implies the system is decoupled in itself. The calculation of D^* in Eq. A.7 requires the relative degree δ_i or each output, given by Eq. A.6 [193, 194].

$$\delta_i = \min\left\{ j : \boldsymbol{c}_i^T \, A^j \, B \neq \mathbf{0}^T, j = 0, 1, \cdots, n-1 \right\} \tag{A.6}$$

$$D^* = \begin{bmatrix} \boldsymbol{c_i^T} \, \boldsymbol{A^{\delta_1 - 1}} \, \boldsymbol{B} \\ \vdots \\ \boldsymbol{c_m^T} \, \boldsymbol{A^{\delta_m - 1}} \, \boldsymbol{B} \end{bmatrix} \tag{A.7}$$

Prior to the investigation with the two-inertia system, the reduction to an in-phase and an anti-phase system is validated with the decoupling matrix. Equation A.8 holds the decoupling matrix for two systems. On the one hand it shows the result for the input-ouput pair of u_{trc} and u_{tv} to $\dot{\varphi}_{\text{in,w}}$ and $\dot{\varphi}_{\text{in,w}}$. On the other hand it shows the result for u_{trc} and u_{tv} to $T_{\text{l,s}}$ and $T_{\text{r,s}}$. The diagonal structure of the matrix for the first case proves that the system is already decoupled. The in-phase speed is controlled with the u_{trc} while the anti-phase speed is controlled with u_{tv}. The second case shall illustrate what the matrix looks like when the system is not decoupled. It is clear that both motors are required to control the left and right torque individually. This results in the non-diagonal form of the decoupling matrix.

$$D^* = \begin{cases} \begin{bmatrix} 1896.23 & 0 \\ 0 & 156372.63 \end{bmatrix} & \text{for} \begin{bmatrix} u_{\text{trc}} \\ u_{\text{tv}} \end{bmatrix} \rightarrow \begin{bmatrix} \dot{\varphi}_{\text{in,w}} \\ \dot{\varphi}_{\text{anti,w}} \end{bmatrix} \\ \begin{bmatrix} 662.04 & 54594.69 \\ 662.04 & -54594.69 \end{bmatrix} & \text{for} \begin{bmatrix} u_{\text{trc}} \\ u_{\text{tv}} \end{bmatrix} \rightarrow \begin{bmatrix} T_{\text{l,s}} \\ T_{\text{r,s}} \end{bmatrix} \end{cases} \tag{A.8}$$

A.3 Separation of the two-inertia oscillator into two single-inertia oscillators

The two separated springs have to even out their forces in the connection point because there are no external forces. Therefore, the sum of the products of spring stiffness and displacement, $c_1\varphi_1$ and $c_2\varphi_2$, must equal zero in Eq. A.9. This yields an expression for c_2 depending on the

inertias J_1 and J_2 as well as the spring stiffness c_1 given by Eq. A.11.

$$0 = c_1\varphi_1 + c_2\varphi_2 \tag{A.9}$$

$$0 = c_1\varphi_1 - c_2\,\frac{J_1}{J_2}\varphi_1 \tag{A.10}$$

$$c_2 = c_1\frac{J_2}{J_1} \tag{A.11}$$

In addition to the force equilibrium, both separated springs must contain the same potential energy as the original spring, expressed by Eq. A.12. With the previous relation of Eq. A.11, the energy conservation yields the spring stiffness c_1 in Eq. A.16 and c_2 in Eq. A.17 with respect to the original spring stiffness c_{12} and the inertias J_1 and J_2.

$$\frac{1}{2}\,c_{12}(\varphi_1-\varphi_2)^2 = \frac{1}{2}\,c_1\varphi_1^2 + \frac{1}{2}\,c_2\varphi_2^2 \tag{A.12}$$

$$\frac{1}{2}\,c_{12}\left(\varphi_1 + \frac{J_1}{J_2}\varphi_1\right)^2 = \frac{1}{2}\,c_1\varphi_1^2 + \frac{1}{2}\,c_2\left(\frac{J_1}{J_2}\varphi_1\right)^2 \tag{A.13}$$

$$c_{12}\left(\frac{J_1+J_2}{J_2}\right)^2\varphi_1^2 = c_1\varphi_1^2 + c_1\frac{J_2}{J_1}\left(\frac{J_1}{J_2}\varphi_1\right)^2 \tag{A.14}$$

$$c_{12}\frac{(J_1+J_2)^2}{J_2^2} = c_1\frac{J_1+J_2}{J_2} \tag{A.15}$$

$$c_1 = c_{12}\frac{J_1+J_2}{J_2} \tag{A.16}$$

$$c_2 = c_{12}\frac{J_1+J_2}{J_1} \tag{A.17}$$

The same relation holds for damping coefficients

$$d_1 = d_{12}\frac{1}{k_{12}} \tag{A.18}$$

$$d_2 = d_{12}\frac{1}{1-k_{12}} \tag{A.19}$$

B Validation results

B.1 In-phase motion of Prototype Two in straight line driving

Due to constraints imposed by the motor's control unit, the tip-ins for Prototype Two are conducted with the accelerator pedal by the driver. Therefore, the steps are not as precise as with the Visio.M. On high μ, only two measurements are available due to safety concerns. The vehicle launches from standstill with a step on the pedal. This causes a fast rise in u_{trc} up to 180 Nm. However, the motor's control unit cuts of the power to the motor shortly after the start (roughly 10 ms). Therefore, the input is not a step rather than a torque spike. Once the motor is in idle, the backlash has a great effect on the oscillation, which reduces the measured oscillation frequency. On low μ, repeated tip-ins and tip-outs are used to keep the drivetrain in a safe operation region while exciting the oscillations. The initial tip-in exceeds 150 Nm whereas the following tip-ins reach around 50 Nm to limit the spin up of the drivetrain. Twelve measurements were conducted in these conditions. In both test cases white gausian noise is added to the disturbance input $\Delta T_{\text{l,tire}}$ with 0 Nm mean and 20 Nm standard deviation. Since section 3.2.1 proves that the main in-phase oscillation phenomena are visible in $\dot{\varphi}_{\text{trc}}$ and $\dot{\varphi}_{\text{in,w}}$, only these two signals are considered here.

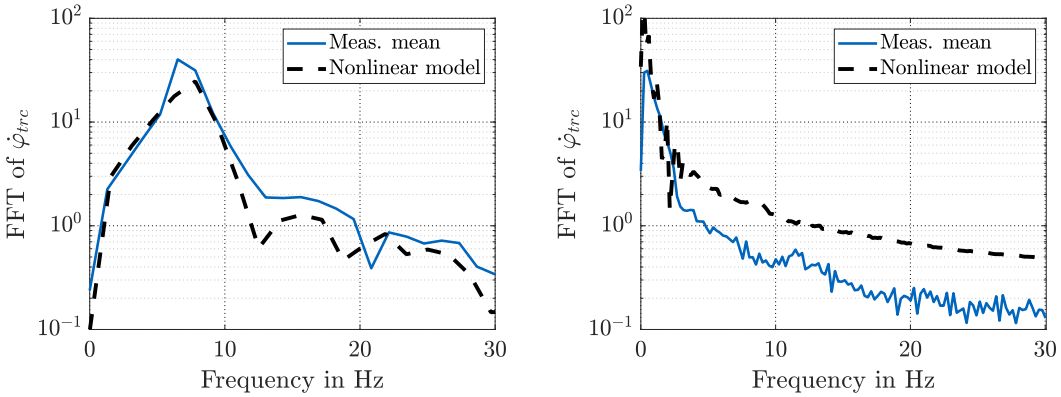

(a) High μ (b) Low μ

Figure B.1: Comparison of frequency response of measurement and nonlinear model for $\dot{\varphi}_{\text{trc}}$ of Prototype Two in tip-in maneuvers with a step input to u_{trc} and white noise in $\Delta T_{\text{l,tire}}$

On high μ in Fig. B.1(a), Prototype Two shows a smoother peak than the Visio.M. This stems from the higher damping but also from the the difference in the torque input and the backlash effects. The numbers in Tab. B.1 show a rather strong difference between model and measurement. However, the difference in frequency results from the peak shape. For the model, the right side of the peak is steeper while the measurement has a steeper rise on the left. Therefore, model and measurement differ by one resolution interval. The difference in magnitude depends on

the T_{trc}, which is filtered by the control unit. Therefore, it is difficult to reenact the exact motor behavior. Nevertheless, the model fits the measurements well in its general behavior. For an oscillation in contact, without backlash effects, the frequency of 7.8 Hz actually appears more realistic than the rather low estimate of 6.5 Hz from the measurement.

On low μ in Fig. B.1(b), there are no distinct peaks visible. The measurement only shows a minor hump slightly above 10 Hz. Compared to the Visio.M, the increased damping in Prototype Two already suppressed in-phase oscillations on low μ sufficiently.

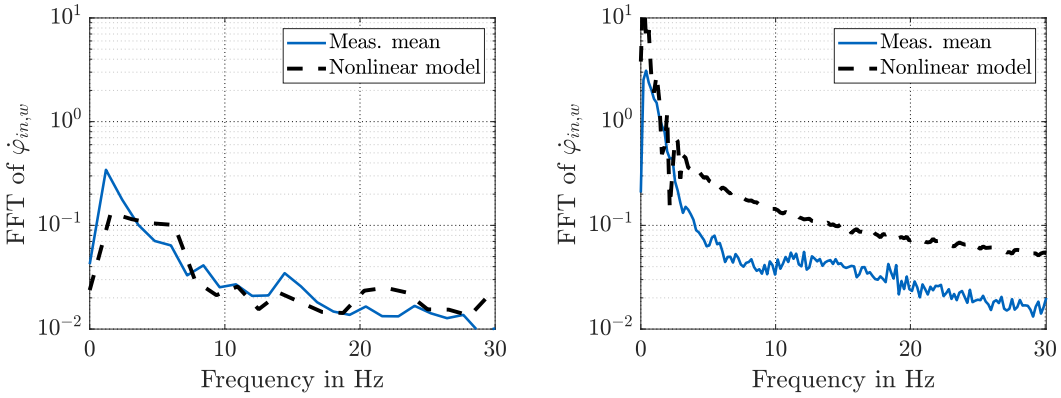

(a) High μ (b) Low μ

Figure B.2: Comparison of frequency response of measurement and nonlinear model for $\dot{\varphi}_{\text{in,w}}$ of Prototype Two in tip-in maneuvers with a step input to u_{trc} and white noise in $\Delta T_{\text{l,tire}}$

Table B.1: Result summary for frequency analysis of $\dot{\varphi}_{\text{trc}}$ for Prototype Two

	Frequency				Magnitude		
Signal	model	mean	std	res.	model	mean	std
High μ	7.8	6.5	0	1.3	25	40	0.23
Low μ	-	-	-	-	-	-	-

B.2 Anti-phase motion of Prototype Two on high mu with cornering by torque vectoring

Due to technical and experimental limitation we only show the response of the anti-phase motion of the drivetrain with Prototype Two on high friction surfaces. In four measurements at a vehicle speed of around 5 m/s, a step from 0 Nm to 20 Nm was fed to u_{tv}.

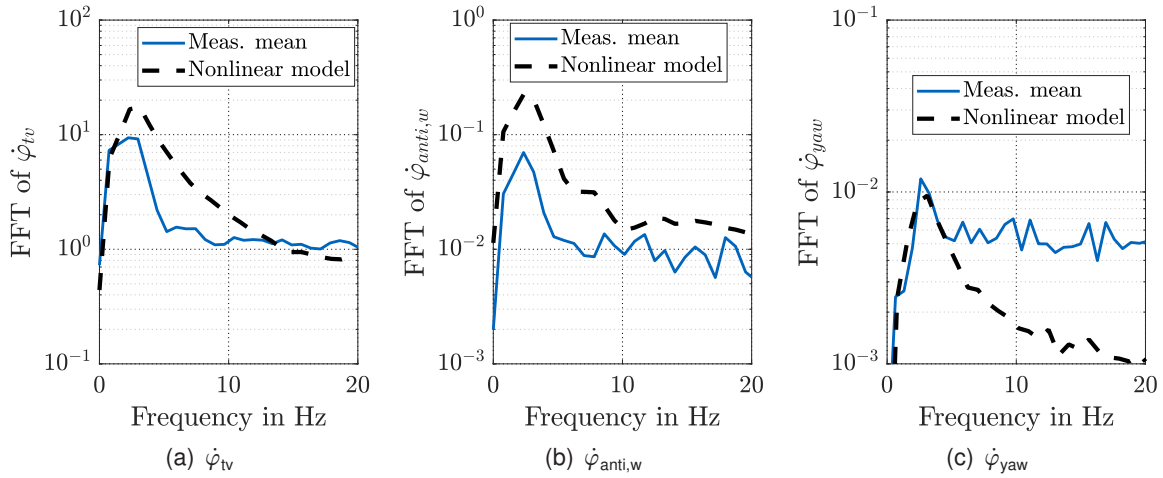

Figure B.3: Comparison of frequency response of measurement and nonlinear model of Prototype Two in tip-in maneuvers with a step input to u_{tv} on high μ

The results in Fig. B.3 and Tab. B.2 demonstrate a similar behavior to the in-phase motion results on high μ of sections 3.2.1 and B.1. The main oscillation occurs at the motor. However, due to the vehicle speed of 5 m/s instead of launching from standstill. A similar peak is visible in Fig. B.3(b) for $\dot{\varphi}_{\text{anti,w}}$. As the modal analysis in Fig. 4.8 demonstrates, increasing speed has a similar effect as a reduced friction coefficient. Therefore, the wheels are not completely locked to the ground anymore and participate in the oscillations. The vehicle experiences only minor yaw oscillations, captured by the small peak in $\dot{\varphi}_{\text{yaw}}$.

The results show that the anti-phase or TV-drivetrain acts like a regular traction drivetrain. Since the oscillations are highly damped, the measurement length is short and the resolution poor, for such low-frequency oscillations. For further analysis, the mean of the different signals is used as the dominant resonance frequency, which is 2.6 Hz.

Table B.2: Result summary for frequency analysis of $\dot{\varphi}_{\text{trc}}$ for Prototype Two

	Frequency				Magnitude		
Signal	model	mean	std	res.	model	mean	std
$\dot{\varphi}_{\text{tv}}$	3.1	2.6	0.43	0.74	17	9.6	0.26
$\dot{\varphi}_{\text{anti,w}}$	2.3	2.3	0	0.78	0.22	0.070	0.0083
$\dot{\varphi}_{\text{yaw}}$	3.1	2.9	0.38	0.65	0.0095	0.012	0.0044

C Feedback control and backlash compensation

C.1 Torque Derivative Feedback

We use $T_1 = u$ because of the fast torque response. We already saw that we can neglect it with the P controller. Analogue to the torque error feedback, the control law is derived.

$$u = r + \left(k_\mathrm{P} + k_\mathrm{D}\ \frac{s}{\tau_\mathrm{DT1}\ s+1}\right)\left(r - u + J_1\ \frac{s}{\tau_\mathrm{DT1}\ s+1}\ \dot{\varphi}_1\right) \tag{C.1}$$

$$u = r + \frac{(k_\mathrm{D} + k_\mathrm{P}\ \tau_\mathrm{DT1})\ s + k_\mathrm{P}}{\tau_\mathrm{DT1}\ s+1}\left(r - u + J_1\ \frac{s}{\tau_\mathrm{DT1}\ s+1}\ \dot{\varphi}_1\right) \tag{C.2}$$

$$\begin{aligned}\frac{(k_\mathrm{D} + k_\mathrm{P}\ \tau_\mathrm{DT1} + \tau_\mathrm{DT1})\ s + k_\mathrm{P} + 1}{\tau_\mathrm{DT1}\ s+1} u = &\frac{(k_\mathrm{D} + k_\mathrm{P}\ \tau_\mathrm{DT1} + \tau_\mathrm{DT1})\ s + k_\mathrm{P} + 1}{\tau_\mathrm{DT1}\ s+1}\ r \\ &+ \frac{(k_\mathrm{D} + k_\mathrm{P}\ \tau_\mathrm{DT1})\ s + k_\mathrm{P}}{\tau_\mathrm{DT1}\ s+1}\frac{J_1\ s}{\tau_\mathrm{DT1}\ s+1}\ \dot{\varphi}_1\end{aligned} \tag{C.3}$$

$$u = r + \frac{(k_\mathrm{D} + k_\mathrm{P}\ \tau_\mathrm{DT1})\ s + k_\mathrm{P}}{(k_\mathrm{D} + k_\mathrm{P}\ \tau_\mathrm{DT1} + \tau_\mathrm{DT1})\ s + k_\mathrm{P} + 1}\frac{J_1\ s}{\tau_\mathrm{DT1}\ s+1}\ \dot{\varphi}_1 \tag{C.4}$$

The feedback law is separated and new gains are defined based on the previous gains for a simpler representation.

$$T_\mathrm{Fb,PD} = \frac{(k_\mathrm{D} + k_\mathrm{P}\ \tau_\mathrm{DT1})\ s + k_\mathrm{P}}{(k_\mathrm{D} + k_\mathrm{P}\ \tau_\mathrm{DT1} + \tau_\mathrm{DT1})\ s + k_\mathrm{P} + 1}\frac{J_1\ s}{\tau_\mathrm{DT1}\ s+1}\ \dot{\varphi}_1 \tag{C.5}$$

C.2 Visio.M's Inverter Damping Controller

In the Visio.M, an internal damping algorithm runs directly on the inverter in order to suppress oscillations in the traction motor's speed $\dot{\varphi}_\mathrm{trc}$. Since it is on the inverter, it does not rely on the CAN Bus and receives the motor speed directly. Because it relies only on $\dot{\varphi}_\mathrm{trc}$, a controller in the form of Eq. 5.36 was fitted to experimental data of nine measurements on high μ, five on low μ and five on the lift. In those measurements, the control effort $T_\mathrm{Fb,PD}$ was calculated as the difference between the step request on u_trc and the measured motor torque T_trc. The result is Eq. C.6 with a normalized root mean squared error (NRMSE) fitness value of 44.8 % [172].

$$T_\mathrm{Fb,PD} = \frac{0.1689 s^2 + 607.8 s}{s^2 + 1097 s + 3.998 * 10^4}\ \dot{\varphi}_1 \tag{C.6}$$

The fitted controller is implemented directly in the linear model. The results for a tip-in on high μ are plotted in Fig. C.1. The torque request is a step from 0 Nm to 40 Nm at 0.1 s. It is clearly visible in Fig. C.1(a) how the controller alters the torque step in model and measurement to

suppress oscillations. The speed signal in Fig. C.1(b) demonstrates the success of the controller. Except for an initial overshoot, the oscillations vanish immediately. The fitted controller in the model resembles the measurement closely even though its performance is slightly worse. One reason could be the simple control structure in the model. The true implementation on the inverter may be more sophisticated, which yields slight improvements in performance.

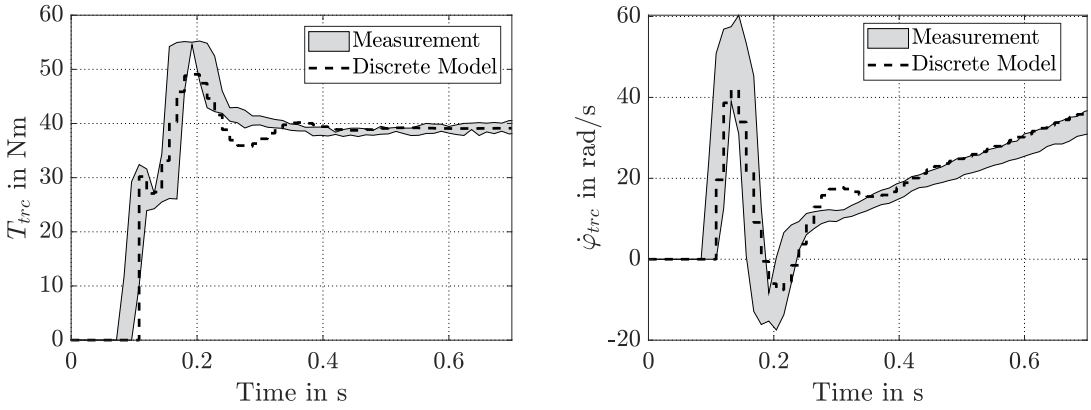

(a) Motor torque in tip-in with damping controller active (b) Motor speed in tip-in with damping controller active

Figure C.1: Validation of the fitted internal damping controller with a tip-in maneuver on high μ

C.3 Performance of flatness-based backlash compensation for different backlash sizes

The flatness-based feedforward backlash compensation roots in a model of the drivetrain. Within this model, the backlash size is specified. It is a key parameter since it determines, when the feedforward control decelerates the motor for a smooth transition. In order to analyze the performance of the flatness-based compensation, three tip-in simulations were conducted with the nonlinear arctan model. The simulation input is the same as presented in Fig. 6.6 and Fig. 6.5. Fig. C.2 contains the results. Reducing the backlash size by half barely has any effect. Twice the backlash size creates a spike in the vehicle's jerk, which is twice as large as for the solid reference curve. Nevertheless, even with 2α the flatness-based compensation performs better than the first-order filter in Fig. 6.6.

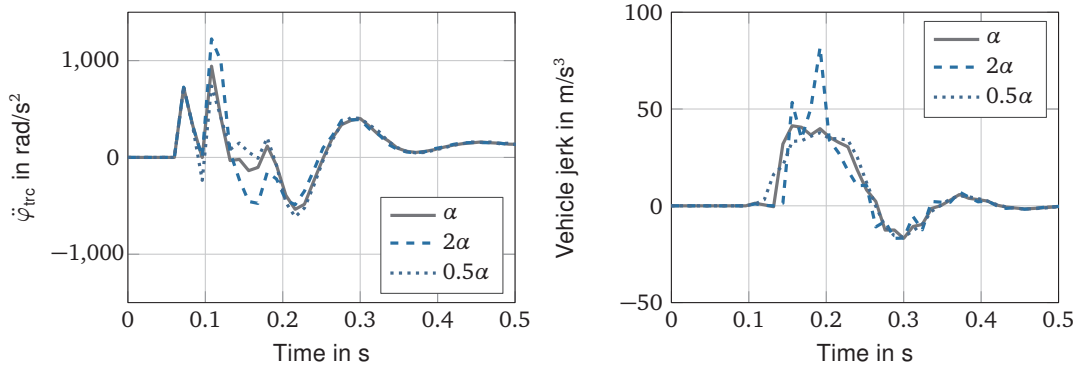

Figure C.2: Comparison of flatness-based backlash compensation for simulations with different backlash sizes α